Theory and Application of PBPK Modelling in Drug Development: The Double-Edged Sword of Complexity



Aleksandra Kmieciak

St Hugh's College

University of Oxford

A thesis submitted for the degree of

Doctor of Philosophy

Michaelmas Term 2022

Acknowledgements

Attributions: Eamonn Gaffney, Mark Coles, Liam Brown and I contributed to the research of every chapter. Jonathan Wagg contributed to the research presented in Chapter 2 and the manuscript for Chapter 2. Alex Phipps assisted in the writing of the manuscript for Chapter 2 and the research presented in Chapters 3 and 4. Likewise, Cristina Santini and Oliver Grimm contributed to the work presented in Chapter 4 and provided advice in the writing of this thesis.

Thanks are due to many people, without whom I would not have been able to complete this journey and genuinely enjoy even the most demanding parts of it. First and foremost, to my academic supervisors, Eamonn Gaffney and Mark Coles, for their incredible hard work, patience and help throughout those four years and for creating the most supportive and welcoming environment I could ever hope for. To Jonathan Wagg, for introducing me to the field of immuno-oncology, sharing his immense knowledge and vision, and guiding me during my first years of the PhD. To Alex Phipps, for his inspiring big-picture thinking, emphasis on precision in speech and writing, and 356 corrections on my first manuscript draft. To Cristina Santini, for the time and continuous effort put into helping me finalise my research, her infectious enthusiasm for science, unspoken mentorship and career guidance. To Oliver Grimm, for providing a pharmacology and industrial perspective that helped shape both my research and professional interests. To my research group, particularly to Liam Brown, for technical and personal advice throughout those last four years. To the EPSRC and Roche, for the financial support to carry out my research. To Stephen Tucker, Jack Miller and John Chalker, for their encouragement and passion, and without whom I would not have considered a PhD in the first place. Finally, to my parents, Krzysztof and Ewa Kmieciak, my siblings, Zuzanna and Oskar Kmieciak, and my friends, especially Pauline Lemaire, for patience, care and support anytime, anywhere and without any reason needed.

Abstract

Physiologically-based pharmacokinetic modelling has become an integral part of model-informed drug development. However, the extensive structure and parameterisation of such models may give rise to issues with model identifiability, parameter estimation and model analysis techniques. In this thesis, we examine the strengths and limitations of whole-body physiologically-based pharmacokinetic models in regard to their complexity by investigating methods of extracting information from such models in clinically relevant applications with limited or no data, as well as how the complexity may be managed in practice. We first address the gaps in the quantitative understanding of the immunological role of the spleen. We do this by assessing how *in silico* splenectomy affects T cell distribution and bioavailability of T cells in the secondary lymphoid tissue in human. Based on the predicted lack of significant difference in the T cell concentration in secondary lymphoid tissue, we conclude that the remaining tissue is predicted to have insufficient cellular and trafficking capacity to compensate for immune functions normally mediated by the spleen. We then discuss the potential limitations of single versus multiple lymph node compartment models in the development of immunotherapeutic modalities. Illustrating the concept by comparing two models with different lymph node compartmentalisation, we show how the choice of the number of lymph node compartments affects the model predictions and, thus, how its application dictates the necessary level of detail in the model. Finally, we propose a model describing the deposition, pharmacokinetics and pharmacodynamics of anti-CD20 monoclonal antibodies administered intravenously and subcutaneously, and analyse the model's identifiability in the context of clinical data format. We fit the model to antibody blood data and show that the model predictions are consistent with the current knowledge on the mechanism of action of anti-CD20 antibodies. We further discuss the data needed for the framework to facilitate consideration of efficacy- and safety-related problems. The thesis concludes with a discussion of the results in the context of model-based drug development, regulatory perspective and the extent to which physiologically-based mathematical models can contribute toward insight and decision support for therapeutic development.

Contents

1 Introduction **1**

1.1 Motivation . . . 2

1.2 Mathematical background . . . 4

1.2.1 Modelling approaches in preclinical and clinical drug development . . . 5

1.2.2 PBPK modelling . . . 7

1.2.3 Variability, uncertainty and sensitivity analysis . . . 8

1.2.4 Model identifiability and parameter estimation . . . 11

1.2.5 Model simplification and model reduction . . . 12

1.3 Biological background . . . 14

1.3.1 The adaptive immune system . . . 14

1.3.2 T cell recirculation and its role in immunosurveillance . . . 16

1.3.3 Structure of lymph nodes and the spleen . . . 17

1.3.4 Cancer immunotherapy: state of the art and current challenges . . . 19

1.4 DPhil objectives . . . 22

2 Modelling T cell distribution post-splenectomy **26**

2.1 Introduction . . . 27

2.2 Methods . . . 29

2.2.1 Model overview . . . 29

2.2.2 Lymph nodes — whole body distribution . . . 38

2.2.3 Parameterisation . . . 39

2.2.4 Exemplar simulation . . . 39

2.2.5 *In silico* splenectomy — model reduction . . . 42

2.2.5.1 *In silico* splenectomy — simulation . . . 50

2.2.5.2 Global sensitivity analysis . . . 51

2.3 Results . . . 53

2.3.1 Post- and pre-splenectomy comparisons . . . 53
2.3.2 Cell localisation and concentration ratios before and after splenectomy 55
2.3.2.1 Sensitivity of cell localisation and concentration ratios pre- and post- splenectomy . . . 55
2.4 Discussion . . . 56
2.4.1 *In silico* splenectomy results in significant reduction in the number of T cells localising to SLT . . . 58
2.4.2 Remarks on model complexity . . . 58
2.4.3 Comparison to previous work . . . 60
2.4.4 Concluding remarks . . . 61

3 Compartmentalisation of lymph nodes in PBPK modelling 62
3.1 Introduction . . . 62
3.2 Methods . . . 66
3.2.1 Single and multiple lymph node trafficking model comparison . . . 66
3.2.1.1 Single lymph node trafficking model . . . 67
3.2.2 Single to multiple lymph node model mapping derivation . . . 71
3.2.2.1 Organ compartments . . . 71
3.2.2.2 Lymph node compartments . . . 73
3.2.2.3 Heart chambers and pulmonary circuit compartments . . . 76
3.2.2.4 Blood mapping variable . . . 77
3.2.3 Parameterisation . . . 78
3.2.4 Mapping variable simulation . . . 80
3.2.5 Single lymph node mapping variable: Local sensitivity analysis . . . 80
3.2.6 Single lymph node mapping variable: eFAST . . . 81
3.2.7 Single lymph node compartment concentration partitioning . . . 83
3.3 Results . . . 86
3.3.1 Main mapping variables: Distributions . . . 86
3.3.2 Lymph nodes mapping variables: Distributions . . . 88
3.3.3 Sensitivity analyses . . . 89
3.3.3.1 Local sensitivity analysis . . . 89
3.3.3.2 Global sensitivity analysis . . . 93
3.3.4 Single lymph node compartment concentration partitioning . . . 95
3.4 Discussion . . . 100
3.4.1 Single lymph node model may be sufficient for predicting whole-body lymph node exposure . . . 101

3.4.2 Mapping framework can support the use of the single lymph node model when specific groups of lymph nodes are of interest 101
3.4.3 Caveats of the mapping framework 102
3.4.4 Concluding remarks 103

4 Choice of delivery route of antibody-based therapies 104
4.1 Introduction 105
4.2 Methods 112
4.2.1 Model overview 112
4.2.1.1 Antibody deposition (PBPK) submodel 113
4.2.1.2 Monoclonal antibody binding and target cell interactions (PK-PD) submodel 119
4.2.2 Parameterisation 122
4.2.2.1 Parameterising lumped compartments 123
4.2.3 Simulating IV and SC administration of antibodies 129
4.2.4 Structural identifiability analysis 130
4.2.5 Local sensitivity analysis 135
4.2.6 Experimental data 136
4.2.7 Data fitting and practical identifiability 136
4.3 Results 138
4.3.1 Structural identifiability 138
4.3.2 Local sensitivity analysis 139
4.3.3 Data fitting and practical identifiability analysis 142
4.4 Discussion 148
4.4.1 The proposed framework can reproduce the antibody blood profile for both administration routes 150
4.4.2 Non-uniqueness of parameters 150
4.4.3 The discrepancy in the total blood volume 151
4.4.4 Predicting tissue exposure 152
4.4.5 Antibody excess regime 153
4.4.6 Remarks on model complexity and comparison to previously developed models 154
4.4.7 Future work and concluding remarks 156

5 Discussion **158**

5.1 Research summary 159

5.2 Research in context: previous and future work 163

5.3 Outlook and concluding remarks 167

A Blood flow changes post-splenectomy **170**

B Effective vs single rate constants **175**

Bibliography **181**

Chapter 1

Introduction

Note: Sections 1.2.2, 1.2.3, 1.3 and 1.4 in this chapter are partially based on a manuscript, where I am a leading author and which was published in Scientific Reports [1].

Complexity is an intuitive yet difficult to precisely define concept. In mathematical models, complexity may refer to different properties of the model in various contexts. The descriptor *complex* may indicate highly dimensional models which are overparameterised relative to available data. It may mean that a model is so elaborate that it is not intuitive or exhibits non-trivial behaviour and, in this case, complexity refers to difficulties in abstraction. Alternatively, the term may also point towards more technical properties like non-linearity in the system of equations that can be computationally intractable. Regardless of which aspect it is, complexity is a potential barrier to gaining a deeper understanding of the modelled system through methods of model analysis [2].

Biological systems are also complex. They comprise a large number of elements (species, populations, cells *etc.*), interactions, and processes, and they often exhibit emergent behaviour or self-organisation. Mathematical models are useful for studying biological systems, as models can shed light on mechanisms, patterns and observations that to the human mind are difficult to understand, notice or explain. In order to exploit the mechanistic exploratory power of mathematical modelling, the framework must contain a sufficient amount of detail to accurately depict the studied system. This often leads to a complex mathematical model, in which complexity can present itself through the high dimensionality of a framework (due to the number of modelled species and processes), interactions between the model elements described by complicated mathematical descriptions, model sensitivity to specific components of the model and evolution over a wide range of time or length scales [2].

Although computational speed used to be a factor limiting the practicality of more complex models, as both dimensionality and numerical stiffness can dramatically increase the computational time, with the advancements in computing power, it has become possible to numerically simulate even highly complex models [2]. The difficulty is that numerical simulations alone do not necessarily provide adequate insight into the model behaviour and model complexity needs to be *managed* somehow to provide insight into the behaviour of the model and the integration of experimental data. As the granularity of a model increases, methods traditionally used in mathematical modelling become progressively less equipped to handle the complexity of a model. In addition, with increasingly larger parameter space, data often becomes too sparse to yield an identifiable model.

1.1 Motivation

The pharmaceutical industry is an example of a field where complex mathematical models are often required. In drug development, complexity is abundant - diseases have complicated pathophysiologies and courses of progression, therapies have novel mechanisms of action, clinical response to drugs is elaborate and highly variable, and clinical data is noisy and usually limited. Mathematical modelling has become an integral part of the preclinical and clinical stages of drug development, where it is used as an indispensable tool aiding better understanding of the novel modalities in the context of biological systems, whether animal species or humans.

The advancements in cancer immunotherapy during the past two decades [3], have shaped the current focus of the pharmaceutical industry on improving the existing therapies, together with expanding and combining the concept of immunotherapies to novel platforms and modalities. Unfortunately, despite the undeniable progress, currently approved immunotherapies only drive efficacious responses in a subgroup of cancer patients and some investigated modalities produced disappointing clinical outcomes despite promising results in preclinical settings [3]. While many immunotherapies are designed to drive immune cell activation that targets abnormal cancerous cells, these therapies often drive inappropriate activation of cells that target normal tissues, leading to immune-related adverse events (irAEs). In addition, the activation of cells targeting biologics, so-called drug immunogenicity, is a major ongoing challenge leading to treatment failure. Due to the complex and variable structures of biological molecules and their manufacturing process, administered biotherapeutics may drive the formation of anti-drug antibodies (ADAs) [4]. As these ADAs can neutralise administered drugs and/or interfere with

the efficacy and/or safety responses evoked by these drugs [5], many pharmaceutical companies have initiated specific activities to reduce the incidence and severity of immune responses targeting their drugs.

The setbacks in designing effective treatments stem in part from a lack of mechanistic understanding of molecular and cellular processes that lead to the emergence of the immune responses, and of how findings based on widely used animal models translate to humans in the clinic. The acknowledged necessity to re-evaluate how scientists conduct biomedical research has resulted in the development and utilisation of theoretical and computational techniques to complement clinical and experimental studies and an increasing amount of experimental data in the quest to achieve practical goals across applications such as combination therapy and scheduling. Although computational simulations are theoretical, they can not only quantitate the existing datasets but can also facilitate the process of experimental design by eliminating hypotheses that are unlikely to be correct. In turn, mathematical and computational approaches can guide the choice of feasible hypotheses and experimental methodologies, and increase the impact of smaller experimental studies.

With the emergence of novel immune therapeutics and the ongoing challenges associated with them, including varying efficacy, toxicity and tolerability, the choice of the optimal route of delivery of an immunotherapeutic modality remains one of the urgent and unanswered questions. T cell-mediated immunotherapies introduce an additional level of complexity to this problem due to the intrinsic interdependence of those therapies on T cell immunity and trafficking. A modelling approach suitable for addressing the problem of the optimal administration route is physiologically-based pharmacokinetic (PBPK) modelling. PBPK models are used to predict systemic and tissue exposure to a drug by integrating the physicochemical properties of the modelled modality with the physiology of the species [6]. As biodistribution of therapy to the target tissue is necessary for sufficient tumour uptake, and, thus, achieving efficacy, while high off-target tissue concentrations may contribute to adverse events (AEs), predicting therapeutic deposition in tissue is an important step in the process of delivering a modality to the clinic. The function PBPK models serve, therefore, allows us to consider the impact of the physiology and anatomy on therapy deposition administered via different delivery routes, and, in turn, the potential impact on therapy efficacy and safety.

Although PBPK modelling offers a mechanistic approach to predicting the deposition of a drug and can provide insight into the underlying biological mechanisms [6], the structure of such models is extensive and they typically comprise a large number of parameters. The aforementioned difficulties associated with the complexity of mathematical models also apply to PBPK models, which may give rise to issues with model identifiability and parameter estimation. The character of preclinical and clinical data further affects the quality of data fitting and

the inability to draw conclusions from the model output and estimated parameters becomes a problem in the context of drug development. In this thesis, we consider the role of PBPK modelling in clinical drug development and examine the extent to which PBPK models can be used in the clinical setting. In particular, we have aimed to understand how the complexity of PBPK models can be managed in practice. We, therefore, applied PBPK models to clinically relevant problems, through which we also sought to quantitatively examine the immunological role of the spleen and establish the foundation for the development of a mechanistic framework that could aid the identification of an administration route potentially resulting in superior efficacy and a more favourable safety profile for immunotherapeutic modalities. The following sections of this chapter provide a mathematical background to the topics related to mathematical modelling and its application in drug development. In particular, we will discuss different modelling approaches utilised in the preclinical and clinical stages of drug development and the role of PBPK modelling within that context. Following the overview of techniques allowing model interrogation, such as sensitivity and identifiability analysis, and parameter estimation, we will provide examples of model simplification and model reduction methods, which can aid the application of such model analysis methods. The second part of this chapter will provide the biological background to the modelling applications considered in the work presented in this thesis. We will start by outlining the key concepts and components of the adaptive immune system and describing how physiological and anatomical features support the generation of the adaptive immune response. We will discuss how the structure of the spleen and lymph nodes, which are major constituents of secondary lymphoid tissue (SLT), reflects their function in immunosurveillance as well as how SLT supports T cell recirculation. We will then outline the state of remaining challenges in immunotherapy development, and summarise the literature examining the effect of altering the administration route on the response to treatment.

1.2 Mathematical background

In order to reduce the risk of failure during the drug development process, pharmaceutical companies employ a wide array of tools to improve the understanding of novel and often complex modalities. Mathematical modelling is one such tool that has become an integral part of drug development, from the early stages focused on understanding disease to delivering effective and safe treatment in the clinic. Modelling and simulation methods play a significant role in the efforts to identify and validate targets, predict efficacy, absorption, distribution, metabolism, excretion, and toxicity (ADMET), assess safety profile, predict first-in-human doses, design clinical trials and guide regulatory and investment decisions. Figure 1.1 shows a

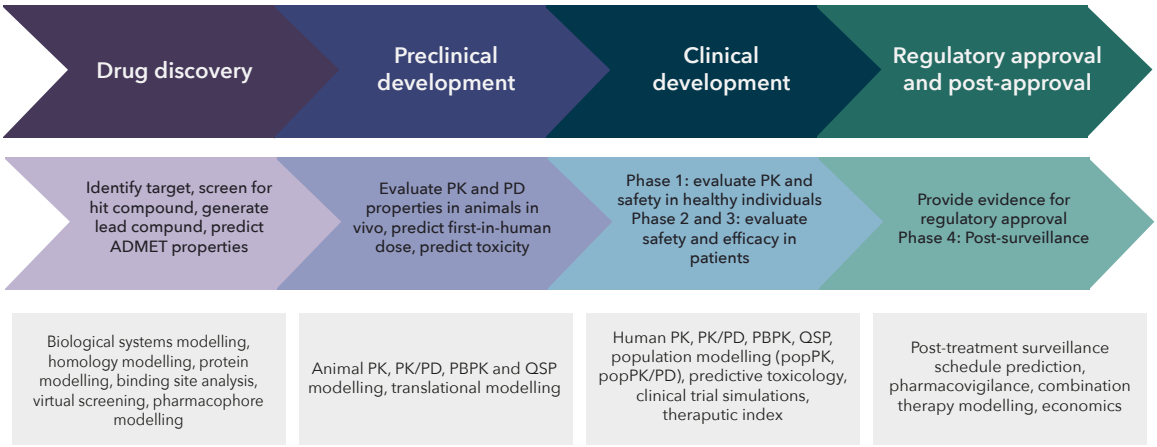


Figure 1.1: Mathematical modelling approaches across the stages of drug discovery and drug development pipeline [8].

schematic of the drug development pipeline and the various modelling applications throughout the process. Mathematical models, therefore, are not only able to predict clinical outcomes, reduce cost and the number of animal studies but they also can provide a mechanistic understanding of the biological and physical processes underlying the observations, thereby, guiding the experimental design and aiding hypothesis testing, which, in turn, can support decision-making. The encouraging impact of mathematical modelling on the quality of the developed drugs, the efficiency of the process and the significant cost reduction has led to increased employment of modelling techniques in the pharmaceutical industry. Model-informed drug development (MIDD) has been further recommended by the regulatory authorities as a means of advancing and integrating various modelling methods with preclinical and clinical data in drug development and the regulatory process [7].

1.2.1 Modelling approaches in preclinical and clinical drug development

Model development typically follows a build-validate-learn-refine cycle [8]. Models are initially built based on all available knowledge about the modality and the biological system if the chosen modelling approach requires it. The model is then used for simulations and comparison with experimental observations (validation). Any discrepancies between the prediction and experiments are considered (learning) and the model is appropriately adjusted (refinement). Having established confidence in the predictive power of a framework, the model is employed throughout the drug development process and can guide the design of further experimental studies.

Various modelling approaches, which differ in their strengths and limitations, are available to modellers and a specific methodology is chosen depending on the research question under

consideration and the available knowledge or experimental data. Empirical or data-driven models are often utilised for exploratory data analysis. However, since such models can be built or refined only after data collection and their parameters lack biological or physical meaning, their application is quite limited. In contrast, mechanistic models are developed to capture the underlying mechanisms in the biological system they represent. In those models parameters, therefore represent biological or physical variables of the system. As mechanistic models can be constructed prior to data collection, they can be used to predict the experimental observations and inform the experimental design.

Compartmental pharmacokinetic (PK) modelling, an empirical or data-driven approach, considers the processes affecting the kinetics of a modality, such as absorption, distribution, metabolism and excretion (ADME). *In vivo* PK data is fitted to the concentration-time profile simulated by a PK model, where decay constants correspond to the rates of ADME processes. Although such models can be easily used to describe the data, they are specific to an application they are constructed for and, thus, offer little potential for extrapolation [8]. As empirical models, they also cannot provide insight into the mechanisms underlying the experimental data, and are, therefore, primarily used in the earlier stages of drug development.

Although PK models typically offer quite a limited benefit, they serve as a helpful foundation for more complex empirical modelling approaches. Population PK (popPK) models, for instance, build on the concept of PK models to capture the sources of the observed variability in drug concentration across target populations due to demographic, pathophysiological and therapeutic characteristics, and are, therefore, of particular importance during the clinical stages of drug development [8]. PK models are also combined with pharmacodynamic (PD) models, which relate the concentration profile of a drug with a measured pharmacodynamic effect at different doses [8]. The resulting PK-PD model describes the dose-response curve, that is the pharmacodynamic effect over time based on the concentration-time profile for a particular dose. As the pharmacodynamic response of a drug most often does not scale linearly with its pharmacokinetic profile [8], PK-PD models are an important tool in drug development for early exploration of the response to a drug.

PK, popPK and PK-PD models all represent a class of top-down modelling approaches, where the structure of a model is determined based on data. In mechanistic modelling, on the other hand, which is categorised as a bottom-up modelling approach, the prior knowledge of the system and the processes that may impact the observations are incorporated into the model structure. An example of a bottom-up approach is physiology-based modelling, which integrates the knowledge of physiological processes with drug-specific information in order to represent complex properties of a drug in a biological setting, *e.g.*, a cell, a tissue, a system of organs or a whole organism. Such models can provide mechanistic insight into the

biological system under consideration, and, thus, are highly beneficial in the context of drug development. By providing a quantitative framework to a descriptive or qualitative biological model, physiological models can facilitate the transition from drug discovery to preclinical and then to clinical drug development. In the clinical stages, in particular, physiology-based modelling can be used to predict the pharmacokinetics of therapy, both systemic and at the organ level, as well as to simulate clinical outcomes [8].

1.2.2 PBPK modelling

Physiologically-Based Pharmacokinetic (PBPK) modelling is one of the major physiology-based modelling approaches used to predict systemic and tissue exposure to a drug [6]. Although the concept of a PBPK model was originally established by Teorell in 1937 [9], due to the complexity of PBPK models and the lack of available data to parameterise them, PBPK modelling remained largely unused for several decades. Nowadays, with the computation power and the advancements in technology facilitating model parameterisation, PBPK models are frequently used to simulate the concentration-time profile of various modalities, both small-molecule drugs and biologics, across many species, by integrating the physicochemical properties of the studied drug or therapy with the physiology of the species. Unlike data-driven empirical models, PBPK modelling offers a mechanistic approach to predicting the deposition of a drug and can provide insight into the underlying biological mechanisms [6]. Further integration of PBPK models with mechanistic PD models (PBPK-PD) provides an additional opportunity for mechanistic insight into the pharmacological response.

A PBPK framework comprises compartments corresponding directly and faithfully to the organs and tissues of the body and connected by the cardiovascular system. Organs that are critical for blood circulation (*e.g.*, heart and lungs), eliminating organs (*e.g.*, liver, kidneys and intestines), large organs that are important for drug distribution (*e.g.*, muscle, skin and adipose tissues) and organs or tissues that are relevant to the pharmacodynamic effect of the modality (*e.g.*, lungs for respiratory drugs, heart for cardiovascular drugs, tumour for oncology drugs) are generally included as (one or more) compartments in a PBPK model. Each compartment is described by the associated physiological parameters, such as volume and blood flow rate, as well as kinetic parameters of a modality determining the resulting tissue distribution. The values for those parameters are typically assumed as being constant in time unless the characteristics of the tissue are expected to vary with time (*e.g.*, for a tumour or a foetus).

Given the chosen compartments defining the structure of a model, PBPK modelling describes the physical and biophysical processes, such as the dynamics of a drug in each tissue,

transport across vascular endothelium, elimination, lymphatic drainage *etc.*, through differential equations, which can be then solved computationally. Although the exact mathematical description depends on the modality the model is applied to, several universal constraints need to be ensured in a PBPK model [8]. Firstly, the sum of blood flow rates to all tissue or organ compartments should be equal to the cardiac output. Secondly, the volumes of individual tissues or organs represented by the compartments should be less than or equal to the total body volume. Finally, the mass balance of the modelled drug should be ensured. That is, the total amount of a drug (and its metabolites, if such are relevant) in the system at any time and the amount of the drug (and its metabolites, if relevant) eliminated from the system by that time should be equal to the initial administered dose.

1.2.3 Variability, uncertainty and sensitivity analysis

Due to the extensive structure of PBPK models, such models typically comprise a large number of physiology- and drug-related input parameters. Physiological parameters generally vary across any population and can also change temporally. Similarly, drug-related parameters are typically based on *in vitro* studies or predicted based on *in silico* approaches and, hence, carry an associated uncertainty. By incorporating parameter variability and uncertainty in input parameters, the resulting variability and uncertainty in the simulated concentration-time profile can be assessed. Given a mean value and variance for a model parameter, a statistical distribution is specified (normal, log-normal, uniform, *etc.*) and model simulations based on multiple sampling from each of the distributions are performed, which can be then statistically summarised (*e.g.*, through 95% confidence intervals).

The impact of the variability in an input parameter on the model output can be also examined through a sensitivity analysis, which provides quantitative information on how sensitive the model output is to changes in each of the model parameters. The analysis can, therefore, identify the parameters that have the most significant impact on the model output and, hence, the values which are the most important for the predictive ability of the model. A local (univariate) sensitivity analysis provides a measure of how sensitive the model output is to changes in a single model parameter. The sensitivity of the model output V_j to the parameter P_i is quantified using a local sensitivity index, S_{ij}, defined in terms of a partial derivative the model output V_j with respect to the varied parameter P_i:

$$S_{ij} = \frac{\partial V_j}{\partial P_i} \Big/ \frac{V_j}{P_i}, \tag{1.1}$$

which describes the relative rate of change in the model output, V_j, due to the varied parameter, P_i, while the remaining parameters remain constant at their baseline values. The normalisation factor, V_j/P_i, allows the comparison of the sensitivity of the model output with respect to several model parameters. A sensitivity index $S_{ij} = 1$ can be interpreted as 1:1 sensitivity of the model output, V_j, to the parameter P_i. For instance, a 5% change in the input parameter, P_i, from its baseline value results in a 5% change in the model output.

Local sensitivity analysis, cannot, by definition, assess the extent of interaction or correlation between the parameters. As a result, a global (multivariate) sensitivity analysis that allows exploration of the entire parameter space is often employed. A large number of global sensitivity methods are available, and, since the review of those methods is beyond the scope of this thesis, we instead introduce one of the variance-based sensitivity analyses, extended Fourier Amplitude Sensitivity Testing (eFAST), that we utilise in Chapters 2 and 3 as an example.

eFAST, developed by Saltelli and Bolado [10], is a variance decomposition method, where the variation in the model output due to variation in input parameters is analysed and partitioned based on what fraction of the variance can be explained by variation in each input parameter, *i.e.*, partial variance. The process of variance partitioning is performed by varying input parameters at different frequencies, which in practice allows encoding the identity of each parameter in the frequency they are varied at [11]. The strength of the frequency of each parameter is then measured in the model output using Fourier analysis, which, in turn, provides a measure of the sensitivity of the model output to the parameter.

The parameter sampling algorithm used in eFAST defines a sinusoidal function of a particular frequency (and integer multiples of this frequency) for each input parameter, called a search curve, $x = f(j)$, where $j = 1,2,...,N_S$ and N_S is the total specified number of samples per search curve. The choice of sinusoidal function depends on the desired distribution of parameter values (uniform, normal, etc.) [11]. For the Fourier analysis to be able to distinguish between input parameters, the algorithm also assigns coprime frequencies in order for the sinusoidal functions of those frequencies to be linearly independent [11, 12], *i.e.*, no non-trivial linear combination of such functions that equals zero exists. A set of one-dimensional sinusoidal functions defined in this way determines a multi-dimensional search curve used to sample different parameter combinations.

A unique and high frequency value, ω_i, is assigned to each parameter, P_i, in turn, and a set of low, and not necessarily unique, frequency values, $\omega_{\sim i}$, to the complementary set parameters, $P_{\sim i}$. The eFAST algorithm developed by Saltelli et al. first evaluates the high frequency, ω_i, depending on the resampling number (N_R, as explained below), the number of parameters (k) and the number of samples per search curve (N_S) [12]. The maximum

allowable frequency for the complementary factors, $P_{\sim i}$, is then evaluated and the frequencies for the complementary set are chosen such that the entire range $[1, \max\{\omega_{\sim i}\}]$ is covered, with (i) the step between two consecutive frequencies as large as possible, and (ii) the number of factors to which the same frequency is assigned as low as possible [12]. Due to the symmetry properties of trigonometric functions, the sampling sinusoidal function eventually repeats the same samples. To avoid this, the sampling algorithm is repeated N_R times with different search curves [12]. The resampling curves are defined by introducing a random phase shift into each sinusoidal function. As a result, the total number of model simulations, N, is given by $N = N_S \cdot k \cdot N_R$.

The analysis yields two indices for each parameter: (i) a first-order sensitivity index, S_i, representing the proportion of an output's variance that is due only to a given parameter (first-order contributions), and (ii) a total-order sensitivity index, S_{Ti}, calculated from the proportion of an output's variance due to all parameters except the one in question (higher-order contributions). The difference between the total-order and the first-order sensitivity indices gives a measure of the impact of the interactions between the parameters. The first-order sensitivity index, S_i, of the parameter P_i, is calculated as the variance at the parameter's unique frequency or multiples thereof divided by the total variance and represents the fraction of the model output variance associated with the variation of a given parameter.

In eFAST, the mentioned advantage of the global sensitivity methods to quantify to what extent the interactions between parameters contribute to the observed sensitivity in the model output is achieved by calculating the total-order sensitivity index for each input parameter. To estimate the total-order sensitivity index, S_{Ti}, of a given parameter P_i, the eFAST method instead varies P_i at a unique, high frequency and the remaining parameters at low, not necessarily unique frequencies. The sensitivity indices of the entire complementary set of parameters (*i.e.*, all parameters except P_i) are then summed to give the contribution of the complementary set, S_{ci}. Hence, eFAST partitions variance into two categories: variance due to the parameter of interest P_i, and variance due to all other parameters (the complementary set to P_i) [11]. The total-order sensitivity index, S_{Ti}, is then obtained as the remaining variance ($S_{Ti} = 1 - S_{ci}$). The total-order sensitivity index, S_{Ti}, therefore, includes higher-order, nonlinear interactions between the parameter P_i and the complementary set of parameters.

When resampling with N_R search curves, first-order and total-order sensitivity indices are calculated for each resample curve j (j = 1,2,...,N_R), and averaged. The eFAST method artificially produces small but non-zero sensitivity indices for parameters of which the model is completely independent [11], due to aliasing effects (the unwanted process of falsely translating a sampled frequency due to the discrete sampling and the symmetric properties of sinusoidal functions) and interference effects (the inability to separate a contribution to the evaluated

variance due to two or more parameters) [13]. A dummy parameter with an arbitrary value range is considered to provide a baseline for statistical comparison, as proposed by Marino et al. [11]. Thus, a total-order sensitivity index less than or equal to that of the dummy parameter is, therefore, not considered substantially different from zero.

1.2.4 Model identifiability and parameter estimation

PBPK models provide a mathematical framework for data integration within a physiological context and, as a modality progresses through the stages of drug development, more available data can be incorporated into the model and the model can be iteratively refined. The process of data fitting, however, requires the estimation of the model parameter values that give the desired model output. An obvious consequence of the high complexity and dimensionality of PBPK models is the problem of parameter identifiability. Identifiability is a fundamental concept relating to parameter estimation or uncertainty, aiming to assess whether it is possible to estimate unique parameter values given the model structure, available data and errors or uncertainties present in the data and the model [14]. While methods such as sensitivity analysis facilitate the characterisation of the model through the *forward problem*, where the model output is simulated given the pre-defined parameter values, identifiability analysis considers the *inverse problem*, where the aim is to estimate parameter values such that the model output depicts the reference data with a satisfactory level of certainty.

Parameter identifiability, therefore, examines whether it is possible to identify a unique set of parameter values for a given model structure or whether multiple parameter values will result in an equally good fit given the available data (parameter non-uniqueness). The former objective is achieved through the structural (*a priori*) identifiability analysis. The model structure (both the conceptualisation of the system represented by the model and equations used to represent it) is one of the possible sources of parameter non-uniqueness [14]. By performing a structural identifiability analysis, usually through algebraic methods [15], structurally non-identifiable parameters can be determined to indicate which variables need to be measured or how the model structure needs to be adjusted to ensure structural identifiability with the type of data available [14].

Parameter non-identifiability can also result from the input data, for instance, through an inappropriate temporal resolution of the data (sparsity or lack of data at a timescale characteristic of specific dynamics present in the model) or observation errors (*e.g.*, due to random noise). This type of non-identifiability is assessed through practical identifiability analysis, which is based on the analysis of the ability to estimate parameters from the observed data. Structural non-identifiability implies practical non-identifiability. If the model structure is the

source of non-identifiability, then it will not be possible to uniquely estimate parameter values in practice, regardless of the amount of data collected, its accuracy or other characteristics. However, structural identifiability does not imply practical identifiability. Even if the model structure theoretically does not preclude parameter estimation, appropriate data is still needed for the parameters to be uniquely estimated.

Parameter estimation methods typically involve optimising an objective function, which quantifies how accurately the model output fits the data. A set of optimal parameter values, then, minimises the objective function. A common and relatively simple objective function is the mean squared error. In many methods, the likelihood that parameter values are *true* given the observations is also used. The parameter estimation process then involves maximising the likelihood and producing the maximum likelihood estimate of the parameter values [14]. Bayesian parameter estimation additionally uses a set of known *a priori* probability distributions of the parameter values, which, combined with the likelihood, yields *a posteriori* probability distributions. As it is almost always difficult to derive an analytical expression for the posterior probability distribution, Markov chain Monte Carlo (MCMC) methods are usually employed to sample from posterior distributions. A wide posterior distribution for a model parameter is indicative of identifiability issues [16].

Analysis of model identifiability is, therefore, an important step in model development. Structural identifiability analysis can help ensure the model structure is appropriate given available data or can aid experimental design. Practical identifiability can also be assessed in the absence of data by using *synthetic* data [14], which are generated using the model to represent the data expected to be obtained in the experiment. Ultimately, however, some level of uncertainty in the estimated parameters is unavoidable due to properties of the data, noise and errors, model structure and equations or a combination of those factors. In the following sections, we will discuss the methods of reducing complexity in PBPK models, which may improve model identifiability and, thus, improve consistency of the model performance when a different dataset or input parameterisation is used (model robustness).

1.2.5 Model simplification and model reduction

Parameter estimation methods become more difficult and their results become less precise as the level of detail and complexity in a model increases. Model simplification and model reduction methods aim to elevate some of the difficulties associated with highly dimensional frameworks while preserving as much as possible the behaviour of the original model. Model simplification methods serve as a tool aiding simplification of the description of a biological

system, which can then, in turn, guide model reduction, through the use of which the number of species, reactions or complexes in the model is reduced [2].

Examples of model simplification methods include conservation analysis, nondimensionalisation and model decomposition [2]. Conservation analysis is most commonly employed in systems, where a subset of variables or a linear combination of model variables remains constant in time (is conserved). Such constraints allow us to reduce the number of differential equations in the model and represent the framework through a new system of differential algebraic equations. Nondimensionalisation technique involves a process of scaling variables in the model in order to represent the system of equations through a new set of dimensionless variables. This method is particularly useful if the behaviour of the system exhibits characteristic timescales, which can be recovered analytically from the nondimensionalised equations using ratios of the parameters and conserved variables. Model decomposition methods can be exploited in systems with distinct model components, where the model can be divided into interacting submodels.

Model reduction methods, although closely related to model simplification methods, can also aid the simplification of a mathematical model but they do so through true reduction of the number of model components (species, reactions, *etc.*) rather than through simplifying the qualitative representation of a system [2]. In simple terms, a model reduction technique can be applied to a physical system described by a system of differential equations to produce a reduced system of differential equations that is simple enough for the available data to be integrated into the model. Although many model reduction methods have been developed, relatively few are applicable to PBPK models. Depending on a specific modelling application, timescale exploitation may be possible if the system exhibits large differences in timescales. In such instances, those differences may be utilised to reduce a model, for example, by assuming that processes occurring at a timescale slower than that of interest are constant or that processes much faster than the timescale of interest equilibrate rapidly. Optimisation and sensitivity methods, the latter of which was described in Section 1.2.3, can help in assessing the relative importance of model components and eliminating the least influential ones given an acceptable level of error. The lumping method is possibly the most widely employed reduction method in PBPK models [17], whereby a reduced system is constructed with new variables corresponding to sums (or *lumps*) of subsets of the original variables. Lumping can be *proper*, where each of the original variables corresponds to only one of the lumped variables, or *improper*, where the original variables can correspond to one or more of the lumped states [2]. In the context of PBPK models, this typically involves a proper lumping of organ compartments to ensure correct interpretability of model results and parameters [18]. As a whole, the choice of a particular reduction or simplification method fundamentally depends on the modelling aim. A method

that is optimal in the sense of preserving the biological meaning of the model variables will most likely be no longer optimal in terms of computational optimisation. Similarly, a method chosen to facilitate the application of another technique that prohibits a large number of parameters or variables may result in too large of an error between the full and reduced models. A certain trade-off with model reduction and simplification is, therefore, to be expected and needs to be carefully considered in the context of the research question.

1.3 Biological background

The aetiology of cancer is complex and heterogeneous, with considerable variability within and between patients. It is acknowledged that immune surveillance and subsequent response play a pivotal role in the mechanism of cancer defence and progression. From a clinical perspective, T cell activation is a crucial event, as it is believed to be a major driver of efficacy across a range of immunotherapeutic modalities that have emerged as an important advance in cancer treatment [19]. The explanation of immunosurveillance in the development of immune therapeutics and vaccines requires an understanding of both T cell activation and the trafficking of T cells. The following sections, therefore, provide the biological and immunological context into the modelling applications considered in the work presented in this thesis [1].

1.3.1 The adaptive immune system

The antigen-specific immune response is known as adaptive immunity. The antigen-specificity is facilitated by lymphocytes, which generate immunological responses through highly variable antigen receptors expressed on their surface. Each lymphocyte bears a unique antigen receptor, which recognises and binds a specific antigen, called a cognate antigen. As a result, a pool of lymphocytes contains a large repertoire of receptors that are highly diverse in their antigen-binding sites, and, hence, are able to generate an adaptive immune response against a wide array of antigens. Until lymphocytes encounter their cognate antigen, they exhibit little functional activity and those cells are known as naive lymphocytes. Upon the recognition and binding to the cognate antigen, naive lymphocytes become activated and differentiate into their fully functional forms, known as effector lymphocytes.

The T lymphocytes (T cells) and B lymphocytes (B cells) comprise two major cell classes of the adaptive immune system. T and B cells differ in the structure of the antigen receptor they express and play distinct roles in the immune system. The antigen receptor expressed on

[1] Much of the biological background described in Sections 1.3.1 - 1.3.3 follows the discussion in the textbook by Murphy et al. [20].

the surface of B cells, called B-cell receptor (BCR), is formed from the same genes encoding antibodies, and, hence, B cell receptors and antibodies are collectively known as immunoglobulins (Ig). Following the binding of the BCR to its cognate antigen, the B cell proliferates and differentiates into plasma cells, which are the effector B lymphocytes secreting antibodies with the same antigen specificity.

Antigen receptors recognise a small portion of an antigen's molecular structure, called an epitope. The antigen receptor expressed on the surface of T cells, T-cell receptor (TCR), however, differs in its structure and recognition mechanism from immunoglobulins. While BCRs can recognise antigens of most chemical structures (*e.g.*, proteins, glycoproteins, polysaccharides), TCRs usually recognise a peptide epitope derived from a partially degraded protein that is bound to specialised cell-surface glycoprotein molecules, called major histocompatibility complexes (MHCs), expressed on the surface of the antigen-presenting cell (APC). Compared to BCRs and antibodies, there are also no secreted forms of the TCR, which serve only the signalling function indicating antigen binding to a T cell. Upon antigen recognition and subsequent binding, the T cell proliferates and differentiates into one of the T cell effector cell types, which characterises its functional activity. The major three classes include cytotoxic, helper and regulatory T cells. Cytotoxic T cells, which express CD8 receptors on their surface and, hence, are also known as $CD8^+$ T cells, kill infected or malignant cells. Effector cells expressing CD4, the regulatory and helper T cells, while not directly involved in the cell-killing mechanisms, regulate the course of the immune response. Helper T cells express cytokines, which provide signals to other cells activating their functions, for instance, the production of antibodies by B cells. Regulatory T cells suppress the immune activity of other lymphocytes, particularly cytotoxic T cells, to prevent the damaging effects of persistent immune response and inflammation state. For the adaptive immune response to be initiated when a T cell encounters its cognate antigen, appropriate inflammatory signals supporting the activation need to be present. As APCs display peptide antigens on the MHC molecules on their surface, they also express cell-surface proteins, called co-stimulatory molecules, which support the ability of the T cells to proliferate and differentiate into their effector form. While BCRs can also bind to free antigens, B cells are more likely to respond to antigens present on the surface of abnormal cells, and additionally require the involvement of activated helper T cells, which highlights the importance of T cell activation in all adaptive immune responses.

Finally, some of the effector T and B cells also differentiate into memory cells, which are long-lasting cells that can differentiate into effector cells upon any further exposure to their cognate antigen. Memory cells are, therefore, responsible for the generation of immunological memory and long-lasting protective immunity. The described processes and cells are summarised in Figure 1.2.

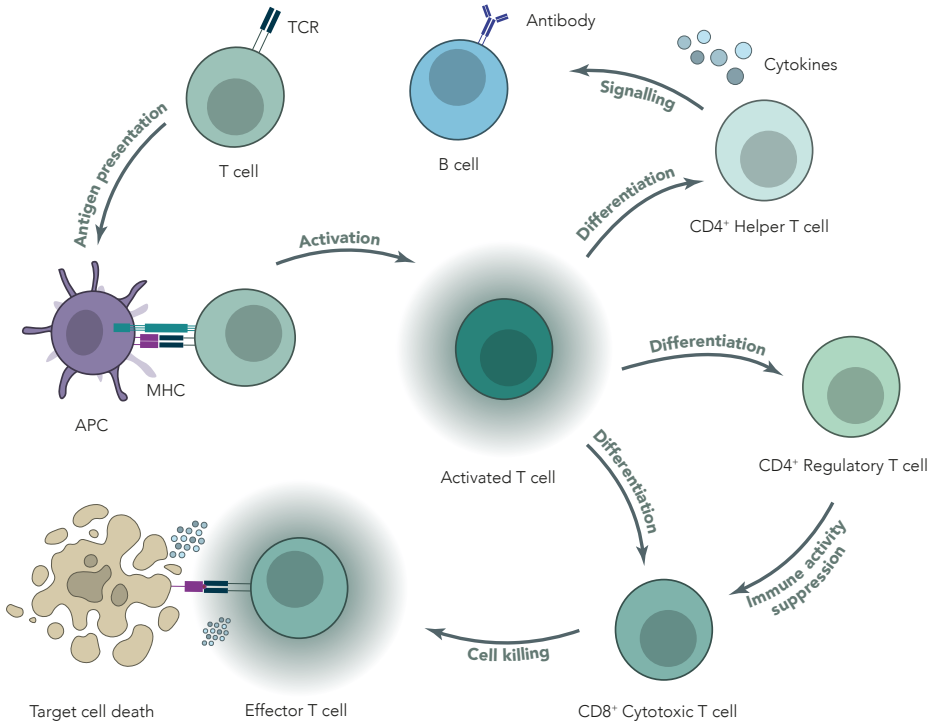


Figure 1.2: T cells and B cells comprise two major cell classes of the adaptive immune system. T and B cells differ in the structure of the antigen receptor they express. B-cell receptor, expressed on the surface of B cells, is formed from the same genes encoding antibodies. The antigen receptor expressed on the surface of T cells, the T-cell receptor (TCR), recognises antigens bound to major histocompatibility complexes (MHCs) expressed on the surface of the antigen-presenting cell (APC). Upon antigen recognition and subsequent binding, the naive T cell becomes activated, proliferates and differentiates into one of the T cell effector cell types: $CD8^+$ cytotoxic cells, $CD4^+$ helper and $CD8^+$ regulatory T cells. Cytotoxic T cells kill infected or malignant cells. Helper T cells express cytokines, which provide signals to other cells activating their functions, such as the production of antibodies by B cells. Regulatory T cells suppress the immune activity of other lymphocytes, particularly cytotoxic T cells, to prevent the damaging effects of persistent immune response and inflammation state.

1.3.2 T cell recirculation and its role in immunosurveillance

T cells recirculate continuously between the vascular and lymphatic systems. As a result, they are found in large numbers in the blood, lymph and lymphoid organs and tissues. The primary lymphoid organs (the bone marrow and thymus) are the sites of lymphocyte generation and maturation. Both T and B cells originate in the bone marrow, where immature B cells complete their development, while immature T cells migrate to the thymus, where they complete their maturation. Once matured, naive T and B cells enter the blood and circulate through the peripheral lymphoid tissues, also called secondary lymphoid tissues (SLTs), which include lymph nodes, the spleen and the mucosal lymphoid tissues in the gut, nasal and respiratory tract, and other mucosae.

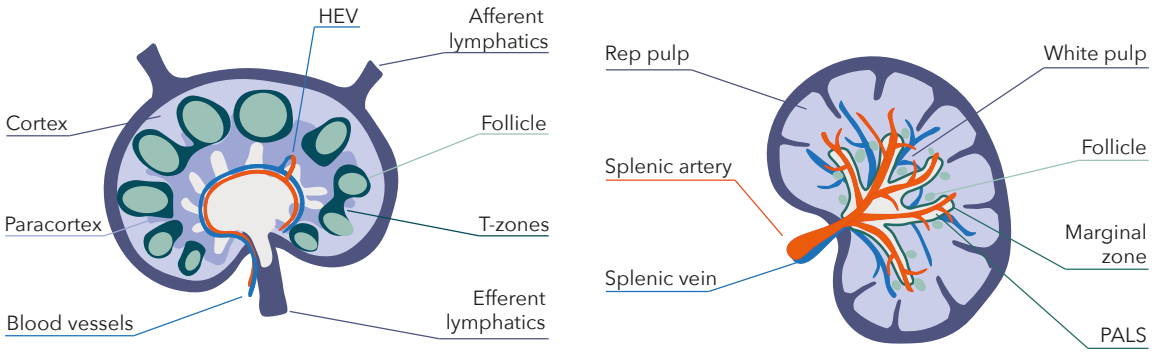
SLTs are the sites of adaptive immune response generation. Cancer antigen, resulting from the destruction of cancer cells within the tumour microenvironment, are collected by APCs,

that have recognised stress signals. APCs carrying cancer antigen then migrate to SLT, where subsequent T cell activation occurs when a naive immune T cell encounters an APC that presents cognate antigen. Such T cell activation events initiate adaptive immune responses, during which the T cell undergoes proliferation and differentiation, generating effector cells, which return to the bloodstream. These T cells migrate to the target site and perform their effector functions. Naive T cells that did not encounter their cognate antigen are also released into the blood and continue to recirculate between the blood, lymph and SLT until the cognate antigen encounter or death. In contrast to effector T cells, which have a rapid turnover rate, naive T cells may recirculate between blood and lymph compartments for prolonged time periods, lasting months in rodents and years in humans [21]. The continuous recirculation of T cells thus facilitates the detection and elimination of any invading pathogens, abnormal cells or foreign particles [22]. The continuous recirculation of T cells between the circulatory and lymphatic systems provides an efficient mechanism for the identification and selective clearance of abnormal cells, further facilitating tumour infiltration, killing of cancer cells and antigen release, thus, generating the tumour-immunity cycle.

The process of lymphocyte tissue entry is not random but rather governed by selective mechanisms based on lymphocyte-endothelial cell interactions [23] that occur whilst these cells are also subject to the hydrodynamic shear stress exerted by flowing blood [24]. Although the lymphocyte-endothelial cell interactions are mediated by several distinct molecular pathways, these interactions are tissue- and lymphocyte-specific, *i.e.*, usually only a single combination of interaction molecules enables efficient migration of a lymphocyte population to a specific target tissue [24]. The migration of a given T cell subset is therefore supported in a specific tissue, while endothelial cells everywhere else permit little or no lymphocyte binding, preventing subsequent extravasation [25]. As a result, the spleen and lymph nodes serve as preferential homing sites for naive lymphocytes.

1.3.3 Structure of lymph nodes and the spleen

Lymph nodes, which are widely present throughout the body and often arranged in chains, drain the interstitial tissues of cells, proteins and surplus tissue fluid (collectively referred to as lymph) via afferent lymphatic vessels. Antigen-bearing APCs and lymphocytes are drained from the peripheral tissues in the lymph, while free antigens diffuse through the extracellular fluid into the lymph node. Dendritic cells and macrophages, which can present antigens and serve as APCs to T cells, on the other hand, actively migrate into the lymph node along the chemokine gradient [20]. Similarly, lymphocytes present in the blood can enter the lymph node



(a) Lymph node (b) Spleen

Figure 1.3: (a) A schematic of lymph node structure. Cells, antigen and tissue fluid are drained from peripheral tissues via afferent lymphatic vessels. Lymphocytes also enter the interstitial space of the lymph node through the blood vessels and high endothelial venules (HEVs). B cells occupy follicles, while T cells are distributed within T-zones, within the paracortex. Immune cells leave the lymph node via the efferent lymphatic vessel. (b) A schematic of spleen structure. Red blood cells are collected and disposed of in the red pulp, which comprises the majority of the splenic tissue. Immune cells enter the spleen directly via the splenic artery and localise in the white pulp, which surrounds the arterioles. T cells form the periarteriolar lymphoid sheath (PALS). B cells localise in follicles, which are distributed along the PALS. Antigen-presenting cells move within the marginal zone towards the PALS, where naive T cells become activated. Lymphocytes leave the white pulp migrating through the marginal zone to the red pulp, and exit via the splenic vein.

attracted by chemokines through high endothelial venules (HEVs), which are highly specialised blood vessels in lymph nodes.

The location of T and B cells within the lymph node is distinct for each cell type and depends on the activation state of each cell [20]. B cells occupy follicles, the circular regions in the outer cortex of the lymph node, while T cells are distributed within T-zones located in the inner region of the cortex, called the paracortex or paracortical area. Lymphocytes entering the lymph node through HEVs, localise in the paracortex together with APCs attracted by the same chemokines and free antigen diffusing from the extracellular fluid. The proximity between T cells and APCs in the T-zones, therefore, facilitates cognate antigen recognition by the naive T cells present in the paracortex and the subsequent T cell activation. Activated T cells then move towards the outer region of the T-zone, closer to the border of the neighbouring follicle. Since activation of B cells relies on the presence of activated helper T cells, as mentioned in Section 1.3.1, this migration of activated T helper cells supports B cell activation. Activated B cells undergo proliferation and differentiation into plasma cells in germinal centres, located within B cell follicles. Components of lymph that may present or contain antigen are removed within the lymph node, whilst activated lymphocytes and other components, such as excess fluid, return to the central circulation via efferent lymphatic vessels [26].

Unlike lymph nodes, the spleen lacks afferent lymphatic vessels, thus all cells and antigens enter the organ directly via the blood [27]. Additionally, the spleen has a key role in haema-

tological functions by regulating iron levels, removal of damaged red blood cells and storage of platelets [28]. Red blood cells are collected and disposed of within the red pulp, which comprises the majority of the tissue. Lymphocytes form isolated regions in the spleen, called the white pulp, which surround the arterioles in the spleen. T cells localise directly around an arteriole, forming a structure called the periarteriolar lymphoid sheath (PALS), composed mainly of T cells. Analogously to lymph nodes, B cells reside in follicles, which, in the spleen, are distributed along the PALS. Each follicle is surrounded by a marginal zone, where APCs are present and blood-borne pathogens, free antigens and antibody-antigen complexes are filtered from the blood. Antigen-bearing cells migrate within the marginal zone towards the PALS, and, subsequently, naive T cells become activated upon antigen presentation. Both effector and naive T cells leave the white pulp migrating through the marginal zone to the red pulp, and rejoin the circulation [27].

The distinct structural differences and the high blood perfusion through the spleen [29] highlight the spleen's immunological role in a wider context – the spleen not only serves a significant role as an anatomical site for lymphocyte activation due to its higher cellular capacity but also performs critical haematological functions, such as clearing the blood of bacteria and aged, antibody-coated or damaged cells [28]. Furthermore, given the high blood flow (for instance, 195 mL/min for the spleen, compared to 110 mL/min for lymph nodes in human [30]) and, consequently, relatively high influx of cells into the spleen, the organ is a crucial site of early exposure to blood-borne pathogens, malignant cells and intravenously administered therapies.

1.3.4 Cancer immunotherapy: state of the art and current challenges

The concept of cancer immunotherapy relies on the idea of deploying the immune system to recognise and kill cancerous cells. This approach to the treatment of neoplastic diseases followed the cancer immunotherapy surveillance hypothesis, conceived more than a century ago, which postulated that tumour-associated antigens (neoantigens) are recognised and eliminated by the immune system through a mechanism similar to that in graft rejection [31]. With the tremendous advancements in the identification and understanding of the mechanisms of tumour-specific responses, immunotherapy emerged as a powerful and innovative line of treatment for many types of cancer, including advanced and refractory diseases [32].

Among the most revolutionising classes of cancer immunotherapeutics are immune checkpoint therapy and adoptive T cell transfer therapy [31]. Immune checkpoint therapy targets molecules which regulate T cell activation (and therefore act as *checkpoint* molecules) to improve the immune response. Cytotoxic T lymphocyte antigen 4 (CTLA-4), programmed

cell death 1 protein (PD-1) and programmed cell death-ligand 1 (PD-L1) represent the most potent examples of T cell immune checkpoint molecules. Adaptive T cell transfer therapy involves an infusion of autologous T cells (*e.g.*, tumour-infiltrating lymphocytes, TILs) or allogenic T cells (*e.g.*, TCR-engineered lymphocytes and chimeric antigen receptor, CAR, therapy). Among the adoptively transferred TILs, TCR- and CAR-based therapies, CAR T cell therapy has shown considerable success in the clinic. A durable response to a TIL-based therapy requires the presence of the tumour-specific effector T cells in the tumour, which is not possible for many types of cancer [31]. The development of such therapies, through expansion of tumour-specific T cells *in vitro* has proven to be a challenge, which led to the investigation of the TCR therapy. TCR-engineered lymphocytes, however, can only respond to neoantigens presented by MHC molecules, which are often further down-regulated by tumours [31]. CARs, on the other hand, are designed to bypass the MHC restriction and can initiate the immune response by recognising neoantigens directly on tumour cells.

Similarly to CAR T cell therapy, bispecific T cell engagers (BiTEs) also bypass the MHC restriction and lead to activation which is independent of the antigen-specificity of the TCR. BiTEs comprise a class of bi-specific antibodies (BsAbs), which are one of the novel immunotherapeutic modalities aiming to reengage effector T cells with tumour cells. The concept of BiTEs utilises an antibody with dual-specificity that binds to antigens specific to T cells and the targeted tumour, thus, promoting immune synapse formation between the effector T cell and a tumour cell. The requirement for dual-binding of the BiTE thereby prevents random T cell activation, while maintaining specificity for the desired antigen [33]. Simultaneous binding drives the formation of an immunological synapse, leading to tumour cell apoptosis [33]. BiTEs further enhance the cytotoxicity of the bound T cell through proliferation and expansion of other T cells, thus, leading to sustained anti-tumour effects [34].

Several strategies have so far yielded promising clinical responses, including CAR T cell therapy and T cell bispecifics being particularly successful in haematological malignancies. Frequent contact of immune and malignant cells in the bloodstream, coupled with malignant cells sharing their cellular origins with those of the immune system, may make haematological malignancies well-suited as targets of immunotherapeutic modalities [35]. Additionally, the initial success of immune checkpoint inhibitor antibodies in melanoma, and lung and renal cell carcinomas, has further reinforced the current focus of the pharmaceutical industry on improving the existing therapies, together with expanding and combining the concept of immunotherapies to novel platforms (*e.g.*, combination therapies) and modalities (*e.g.*, antibody-drug conjugates, ADCs, novel targets for immune checkpoint inhibitors or bispecific antibodies).

Despite the early advancements, currently approved immunotherapies only drive efficacious responses in a subgroup of cancer patients [3]. Similarly, cancer vaccines, which aim to elicit,

expand or boost patients' tumour antigen-specific T cells and antibodies, have shown promising results in preclinical settings but, so far, have produced disappointing clinical outcomes [3]. While many immunotherapies are designed to drive immune cell activation that targets abnormal cancerous cells, these therapies often drive inappropriate activation of cells that target normal tissues, thereby evoking immune-related adverse events (irAEs) that resemble, to some extent, the clinical features of known autoimmune diseases. In addition, the activation of cells targeting biologics, so-called drug immunogenicity, is a major ongoing challenge leading to treatment failure. Due to the complex and variable structures of biological molecules and their manufacturing process, administered biotherapeutics may drive the formation of anti-drug antibodies (ADAs) [4]. As these ADAs can neutralise administered drugs and/or interfere with the efficacy and/or safety responses evoked by these drugs [5], many pharmaceutical companies have initiated specific activities to reduce the incidence and severity of immune responses targeting their drugs.

With the emergence of novel immune therapeutics and the ongoing challenges associated with them, including varying efficacy, toxicity and tolerability, the choice of the optimal route of delivery of an immunotherapeutic modality remains one of the urgent and unanswered questions. T cell-mediated immunotherapies introduce an additional level of complexity to this problem due to the intrinsic interdependence of those therapies on T cell immunity and trafficking. Most cancer immunotherapeutics are administered systemically (via the intravenous route), in line with a commonly held belief that a treatment has to act systemically to eliminate distant metastases [36]. As van Pul et al. argued, this is in contrast with the fact that adaptive immunity is primed locally and yet it provides a systemic response through recirculating effector and memory cells [36]. A local delivery method of an immunotherapeutic near a lesion site, be it through subcutaneous, intradermal or intraperitoneal injection, results in high concentrations of the drug near and potentially within the tumour, as well as the regional lymph nodes, where T cells are primed by the migrating APCs. Local delivery, in turn, allows for the priming of effector and memory T cells, while resulting in a more gradual and lower systemic exposure, and, thus, the associated toxicity [36].

The concept of altering the route of delivery of immunotherapeutics, with the aim to improve efficacy and limit toxicity, has been so far explored in the clinical setting in the context of CAR T cell therapy [37], monoclonal [36, 38, 39] and bispecific antibodies [40, 41, 42]. However, it remains unclear whether the local administration route is feasible for all molecules, not only because of the impact on the drug's bioavailability but the overall safety and tolerability profile. Furthermore, the question of whether a drug administered locally retains efficacy, and if so - how, needs to be considered for each therapeutic with a distinct mechanism of action. Clinical studies investigating the possible mechanisms resulting in the

sustained efficacy of locally administered immunotherapeutics are sporadic. For instance, van Pul et al. evaluated the safety, tolerability and immunomodulatory effects in the peripheral blood and tumour-draining lymph nodes in patients with early-stage melanoma treated with the anti-CTLA-4 monoclonal antibody, tremelimumab [36]. Intradermal delivery of a single dose of antibodies was demonstrated to be safe and well-tolerated. Analyses of lymph node biopsies showed that intradermal delivery induced activation of migratory dendritic cells, the most common type of antigen-presenting cells, in the tumour-draining lymph node. The results also indicated significant and sustained decreases in regulatory T cell frequencies, as well as activation of effector T cells in both the tumour-draining lymph node and peripheral blood. Similarly, preclinical studies demonstrated that local delivery of antibodies targeting CTLA-4 is equally effective in tumour eradication as the systemic delivery and further highlighted the key role of tumour-draining lymph nodes for the efficacy of CTLA-4 inhibitors [43, 44]. Another recent preclinical study by Baharom et al. showed that altering the administration route of cancer vaccination affects the magnitude and quality of tumour-antigen-specific $CD8^+$ T cells. In the study, intravenous vaccination induced a higher proportion of neoantigen-specific $CD8^+$ T cells compared to subcutaneous immunisation [45]. The intravenous immunisation further resulted in a superior anti-tumour response due to the specific characteristics of the generated effector cells. Altogether, the existing scientific evidence, though sparse, suggests that altering the route of administration of immunotherapeutic modalities may indeed lead to a qualitatively and quantitatively different immune response but the problem of the optimal delivery route needs to be considered for each modality with a distinct mechanism of action.

1.4 DPhil objectives

The complexity of PBPK models is a double-edged sword. While it grants the wide applicability of PBPK models through the representation of whole-body physiology and integration of the properties of a drug into the framework, often it can be the source of difficulties. The high dimensionality of those models may limit the applicability of model analysis techniques and the relative size of the parameter space compared to the available data can result in issues with model identifiability and parameter estimation. The goal of this DPhil work is to examine the extent to which PBPK models can be utilised in practice in the clinical setting, where appropriate data is sparse, contains a high level of uncertainty or is often lacking altogether. By considering the role of PBPK modelling in clinical drug development, we aim to understand the strengths and limitations of whole-body PBPK models in regard to their complexity. More specifically, in the thesis, we explore this central objective in two themes: theory and

application. Utilising model reduction and model simplification techniques, we will investigate how such methods can be used to obtain valuable information about the modelled biological system. Furthermore, we aim to understand how the complexity of whole-body PBPK models can be managed in practice. We will apply PBPK models to clinically relevant problems, through which we seek to (i) examine the impact of splenectomy on T cell distribution; (ii) consider lymph node tissue compartmentalisation in PBPK models utilised for applications in immuno-oncology. The first two topics then lead us to the final application, through which we aim to (iii) establish the foundation for the development of a mechanistic framework that could support the process of identifying an administration route that may result in superior efficacy and limited toxicity for immunotherapeutic modalities. As PBPK modelling allows predicting the impact of physiological factors on the deposition of the studied modality, it offers a suitable approach to studying the problem of the optimal administration route, given a very intuitive model structure and physiologically interpretable parameters.

By taking into account the underlying physiological and immunological mechanisms, we aim to identify factors that may determine the bioavailability of a treatment administered via the intravenous and subcutaneous route, and, therefore, potentially impact the treatment efficacy and toxicity. We consider questions such as *What role do physiology and anatomy play in the process of therapy deposition?*, and, *Does the relative importance of the spleen and lymph nodes differ for the intravenous and subcutaneous administration routes?* We will then examine what the implications of our conclusions are for the mathematical modelling approaches that can be used to address the problem of the optimal delivery route. The work presented in this thesis, therefore, aims to investigate methods of extracting information from PBPK models in applications with limited or no data and how the complexity of biological systems, which gives rise to clinical observations, may be handled or countervailed through careful consideration of its representation in a mathematical system.

In Chapter 1, we introduced the two key secondary lymphoid tissues (SLTs), the spleen and lymph nodes, and we discussed their role in the generation of adaptive immune responses. Due to the differences in the functional and physiological characteristics of these organs, distinct administration routes result in different initial exposure levels of each tissue to the administered therapy. We hypothesised that the relative contribution of the spleen and lymph nodes to the resulting efficacy may, therefore, also differ depending on the administration route. For instance, the high blood perfusion through the spleen [29] makes this organ an early site of exposure to a therapy administered intravenously (IV). In contrast, for therapy administered subcutaneously (SC), lymph nodes draining the administration site are initially exposed to much higher concentrations of the immunotherapeutic drug compared to the spleen.

Given the extensive research on lymph nodes and a comparatively better understanding of the role of the tissue, Chapter 2 addresses the gaps in the quantitative understanding of the immunological role of the spleen. Utilising splenectomy as a naturally fitting example, we consider the role of the spleen in the generation of immune responses by examining the clinical effects of the procedure. We illustrate how physiologically-based pharmacokinetic modelling can provide quantitative and mechanistic insight into the observed increase in haematological malignancy risk in asplenic patients. We assess how *in silico* splenectomy affects T cell distribution in humans, and, in particular, the impact of splenectomy on lymph node tissue exposure, in order to estimate to what extent the remaining SLT has the potential capacity to compensate for the loss of spleen-based immune functionality. The first chapter, thereby, highlights the impact of splenectomy on cell trafficking and changes in the bioavailability of an administration of T cells in the SLT, which is relevant to cell-based immunotherapy. Additionally, the work presented in Chapter 2 employs methods of model dimensionality reduction and application of Kirchhoff's laws to physiological circulation systems, through which we aim to highlight that, even in the absence of clinical data, PBPK models can serve as an informative guide to determining the likely effect of changing the physiological status of the body on the trafficking of immune cells and cellular therapies.

In Chapter 3, we turn to the lymph node tissue as the early site of exposure associated with subcutaneous (SC) administration of therapy. Models with a single (lumped) lymph node compartment remain a standard mathematical tool in PBPK modelling, both in clinical pharmacology and drug development, as well as in modelling supporting experimental studies of immune cell trafficking in mice and rats. While the choice of the single lymph node compartment representation is motivated by the reduction of the complexity of a model, the physiological reality, however, is very different. Furthermore, applications with a focus on specific lymph nodes, such as lymph nodes draining the site of SC administration, or indications affecting specific groups of lymph nodes, such as lymphomas, are particularly hard to represent in a single lymph node compartment framework. Consequently, a more detailed description of lymph nodes may be required to model the subcutaneous administration route of any type of therapy.

Since the model structure comprises one of the fundamental assumptions in PBPK modelling, we, therefore, discuss the potential limitations of single lymph node models in clinical applications such as immunotherapies, where the understanding of the immune cell kinetics and dynamics is necessary to control their safety and efficacy. We examine what constitutes a reasonable choice of lymph node compartmentalisation and how such a choice affects the model predictions and, thus, its application. We illustrate these concepts with a comparison of two T cell trafficking models with opposing lymph node compartmentalisation (a single and an

organ-specific lymph node model) and characterise the difference in the predicted cell biodistribution by both models. We further present an analytical method that defines a mapping between models with a different number of lymph node compartments and discuss modelling applications for which single lymph node compartment models may constitute an appropriate level of modelling detail, as well as when additional complexity may be required.

Having considered the aspects of the relative roles of the spleen and lymph nodes in the generation of the adaptive immune response and the impact of lymph node compartmentalisation in a mathematical framework on the framework's predictions, in Chapter 4, we address the question of the optimal delivery route of antibody-based immunotherapies. The chapter aims to assess the feasibility of constructing a mechanistic framework that could support the process of elucidating the mechanism underlying the advantage of one delivery route over the other. We propose a novel physiologically-based framework describing the distribution, pharmacokinetics and pharmacodynamics of intravenously- and subcutaneously-administered monoclonal antibodies. With the use of preclinical data, we examine whether the proposed model can reproduce the observed PK of anti-CD20 monoclonal antibodies administered via the IV and SC route in cynomolgus monkeys.

While computational and mathematical approaches offer a vital tool in elucidating factors maximising therapeutic effectiveness, available physiologically-based models of antibody tissue distribution and kinetics have very limited use in the clinical setting, due to the complexity of the models and the sparsity of the clinical data. We, therefore, also consider the problem of parameterisation in PBPK models based on data typically available in the clinic. Utilising compartment lumping and parameter identifiability analyses, Chapter 4 additionally aims to understand the limitations imposed by the extensive parameterisation of PBPK-type models on the investigation of efficacy- and safety-related aspects of antibody-based therapies.

We conclude the thesis with Chapter 5, where we summarise how the results presented in the previous chapters come together to facilitate the development of mathematical models that could support the process of identifying an optimal delivery route for immunotherapeutic modalities and we outline the scope for future work. Finally, we discuss the presented conclusions in the context of literature, the recent growth of the broader field and the regulatory role in drug development.

Chapter 2

Modelling T cell distribution post-splenectomy

Note: This chapter is based on a manuscript, where I am a leading author and which was published in Scientific Reports [1].

Chapter 1 discussed the role of the secondary lymphoid tissue (SLT), the spleen and lymph nodes, in the generation of adaptive immune responses. In particular, we described the role of SLT as a T cell homing site, which supports the process of T cell recirculation, in turn, driving efficient immunosurveillance. Given the differences between functional and physiological characteristics of those tissues and the studies examining the effect of altering the administration route of immunotherapeutic modalities on the immune response, we hypothesise that the relative contribution of the spleen and lymph nodes to the resulting efficacy of therapy may differ depending on the administration route. In this chapter, we address the gaps in the quantitative understanding of the immunological role of the spleen, utilising splenectomy as a naturally suitable example whilst examining the clinical effects of the procedure. We illustrate how physiologically-based pharmacokinetic (PBPK) modelling, introduced in the previous chapter, can provide quantitative and mechanistic insight into the effect of the splenectomy on T cell distribution in humans, in turn, contributing to those observed effects.

2.1 Introduction

Splenectomy is a relatively common procedure with 22,000 procedures performed annually for all causes in the USA [46]. As the spleen, being a major component of SLT, is an important site of immune response generation, it is possible that splenectomy may compromise the immune system's ability to both prevent and subdue cancer. Two recent cohort studies [47, 48] investigated the association between splenectomy and malignancy. Kristinsson et al. assessed incidence and mortality due to potential complications of splenectomy, including cancer, among 8,149 splenectomised American veterans with a follow-up to 27 years [47]. Sun et al. conducted a nation-wide cohort study of 2,604 splenectomised Taiwanese patients, with a follow-up of up to 11 years [48]. These studies reported analyses based on Standardised Incidence and Mortality Ratios, SIR and SMR, respectively. The ratios estimate the occurrence of an event in a given population relative to a larger comparator population, used as a reference group, thereby giving a statistical measure of what the expected incidence of an analysed condition (SIR) and the expected number of deaths due to a condition (SMR) would be in a population of interest, given a matched cohort [49]. It is worth noting that, while both SIR and SMR are adjusted for factors differentiating the studied and reference groups (age, gender, pre-existing health conditions, etc.), SMR does not account for a changing standard of care and hence necessitates a more careful interpretation.

The studies by Kristinsson et al. and Sun et al. reported an increased overall incidence ratio for any malignancy following splenectomy: 1.51 (95%CI: 1.42 - 1.46) [47] and 2.06 (95%CI: 1.81 - 2.33) [48], respectively. Both analyses also revealed significantly higher incidence ratios with splenectomy for the haematological malignancies, not only compared to an overall cancer incidence but also compared to solid tumour incidence (see Figure 2.1 for visualisation of the data reported by Kristinsson et al. [47]). SIRs were raised across all haematological malignancies in asplenic versus spleen intact populations in both studies, ranging from 1.82 (95%CI: 1.08 - 3.07) for multiple myeloma [47] up to 6.04 (95%CI: 3.92 - 9.29) for acute myeloid leukaemia [47]. Across haematological malignancies, all leukaemias and Non-Hodgkin lymphoma were associated with a statistically significant increase in SMR: 2.45 (1.36 - 4.43) and 4.69 (1.97 - 11.18), respectively [47].

The data highlights the importance of the spleen in immunosurveillance, as the organ plays an essential role, not just for protection against blood-borne bacterial infections, but any kind of abnormal cell carried in the blood. While the process of tumour antigen presentation to T cells is almost completely restricted to the tumour-draining lymph nodes [50, 51], the spleen might be a more efficient anatomical site to mobilise an immune response against blood-borne malignant cells, and potentially associated treatments. As such, the data raises

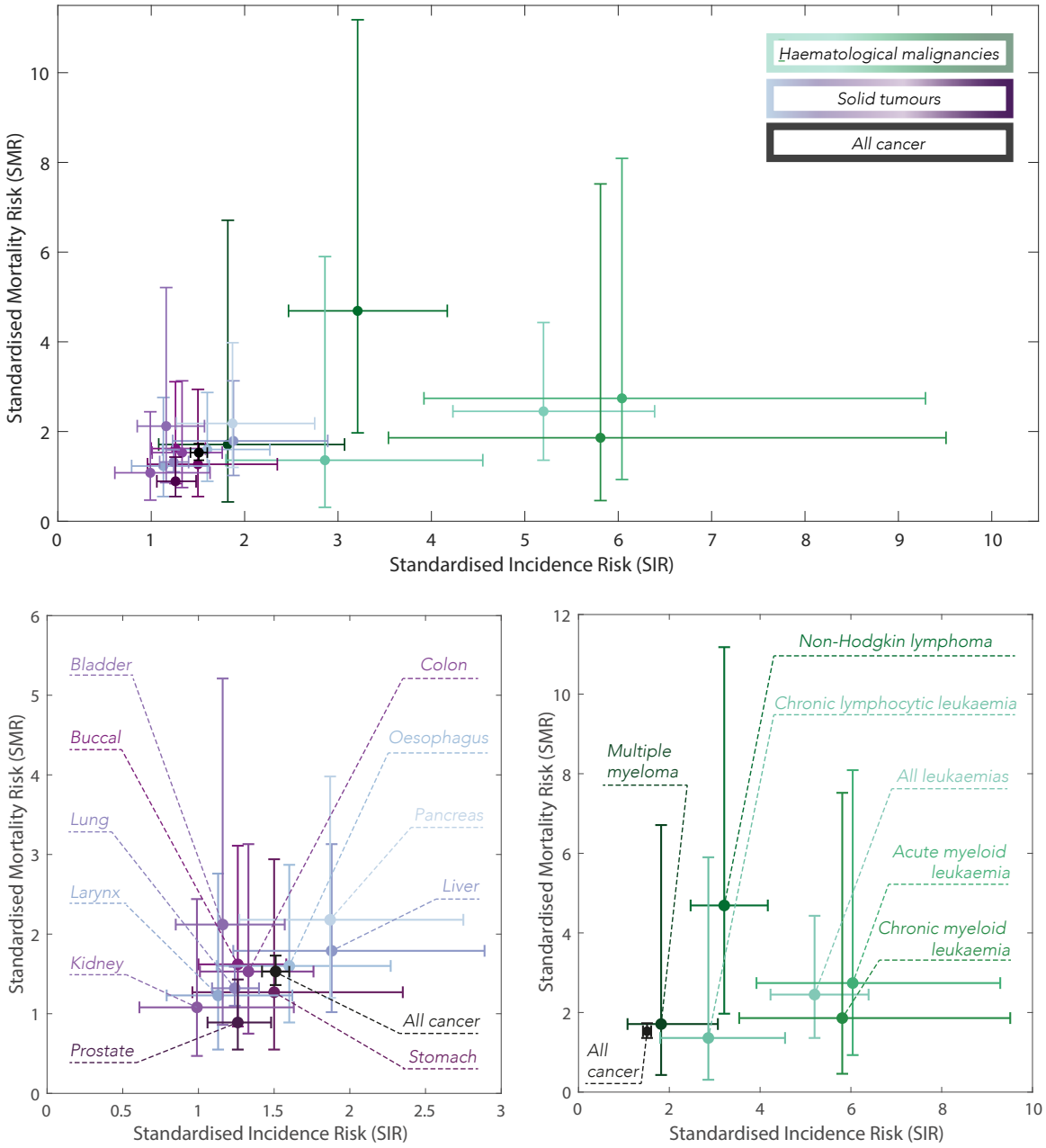


Figure 2.1: Standardised Incidence Ratio (SIR) and Standardised Mortality Ratio (SMR) due to selected malignancies following splenectomy as reported by Kristinsson et al. [47]. Reported malignancies were plotted on one graph (upper plane) to highlight the visible distinction between solid tumours (plotted separately, lower left plane) and haematological malignancies (plotted separately, lower right plane). Cross-lines represent the reported 95% confidence intervals (95%CI). Note the difference in scale.

a question of whether splenectomised patients should undergo cancer immunotherapies, given the associated severe side effects and, effectively, an already impaired immune system due to splenectomy. The splenectomy covariate has so far not been systematically explored for its impact on treatment outcome. At the time of writing, and in the context of asplenic patients, there are no published clinical trial results for two recently approved CAR T cell therapies, Kymriah (tisagenlecleucel) and Yescarta (axicabtagene ciloleucel), and a bispecific T cell engager Blincyto (blinatumomab). Further research is needed to provide input into considerations of the appropriate treatment for splenectomised patients with haematological malignancies. Model-based approaches could facilitate elucidating the impact of splenectomy on T cell trafficking, in particular, the prospect of induced changes in trafficking through lymph nodes to investigate whether a compensation mechanism is even physiologically feasible.

In this chapter, we refine a previously constructed PBPK framework of T cell trafficking [52] to understand the likely distributions of T cells across different secondary lymphoid tissue compartments (the spleen and lymph nodes) in the context of splenectomy. The unique advantages of PBPK modelling, such as anatomically-based model design and incorporation of measurable quantities (*e.g.*, organ volumes, blood flow rates) as model parameters, will be utilised to determine predictions of the immune cell biodistribution in the absence of the spleen. Since, to the best of our knowledge, immune cell trafficking in relation to splenectomy has only been modelled in mice [53], we will assess how *in silico* splenectomy affects T cell distributions in human. In particular, we will investigate the effect of splenectomy on the number (localisation) and concentration of T cells in lymph nodes (exposure), examining the clinically relevant question of to what extent the remaining SLT post-splenectomy may have the capacity to compensate for the lost immunosurveillance, even before differential function between the spleen and lymph nodes is considered. Furthermore, we aim to highlight the impact of splenectomy on cell trafficking and, in particular, changes in the bioavailability of an administration of T cells in the SLT, which is pertinent to cell based immunotherapy.

2.2 Methods

2.2.1 Model overview

A system of ordinary differential equations (ODEs) has been constructed to represent the exchange of any cell population between the heart and organs, with an underlying context in this study of T cell trafficking and T cell immunotherapies. The whole-body physiologically-based model treats the major human organs as compartments connected in an anatomical manner

by the systemic and lymphatic circulation. Figure 2.2 shows a diagram of the circulatory and lymphatic systems (left) and contrasts it with a simplified schematic of the T cell trafficking framework (right). The model contains 20 organs, shown in Figure 2.2, each with a vascular and interstitial compartment, and two additional heart chambers compartments. The blood supply to the heart muscle (coronary circulation) is represented as a separate vascular and interstitial compartment, in addition to a heart chamber compartments due to a distinct anatomy of blood circulation (see Figure 2.2 for further details, including the organs in the model). Similarly, pulmonary circulation and lung tissue blood supply are treated as separate compartments. To provide a more physiologically realistic description, the original model developed by Brown et al. [52] was extended to represent lymph node compartments as multiple compartments distributed across the model. In particular, a separate group of lymph nodes, treated as a single lumped compartment, drains each organ's interstitium, as depicted in Figure 2.2. The exceptions are the blood supply to the lungs and heart, where a single lymph node compartment drains both organs (mediastinal lymph nodes), the spleen, which lacks draining lymphatic vessels, and the pulmonary circuit, where the interstitial subcompartment represents the state of cell entrapment in the pulmonary vasculature [54, 55].

The dependent variables are the number of T cells in each of the compartments as a function of time. The number of T cells in a given compartment of an organ, o, is denoted by N_o, with a rate of change driven by the difference in the rate of flow of these cells into and out of the compartment. The flow of T cells is proportional to the blood flow and cell concentration. For instance, the rate of change in the number of T cells in the vasculature of an organ, o, is given by:

$$\frac{dN_o}{dt} = V_o \frac{dC_o}{dt} = B_o \left(C_{\mathrm{LA\&LV}} - C_o\right), \tag{2.1}$$

where V_o is the blood volume of the organ, o, B_o is the blood flow of the organ, o, C_o is the concentration of T cells in the vasculature of an organ, o, while $C_{\mathrm{LA\&LV}}$ is the concentration of T cells within the left atrium, left ventricle, aorta and large arteries between organs and the heart.

To reflect the fact that a proportion of cells in the vasculature extravasates into the organ's interstitium, a fraction of cells in the vasculature of the organ, o, denoted e_o, flows from that organ's vasculature subcompartment into the interstitial subcompartment (see Figure 2.3). The extravasation factor, e_o, is assumed to be constant for a given organ, o. While the process of extravasation of immune cells can be modified by integrins and other molecular factors [56], it is assumed that the extravasation factor is constant on the timescale of the

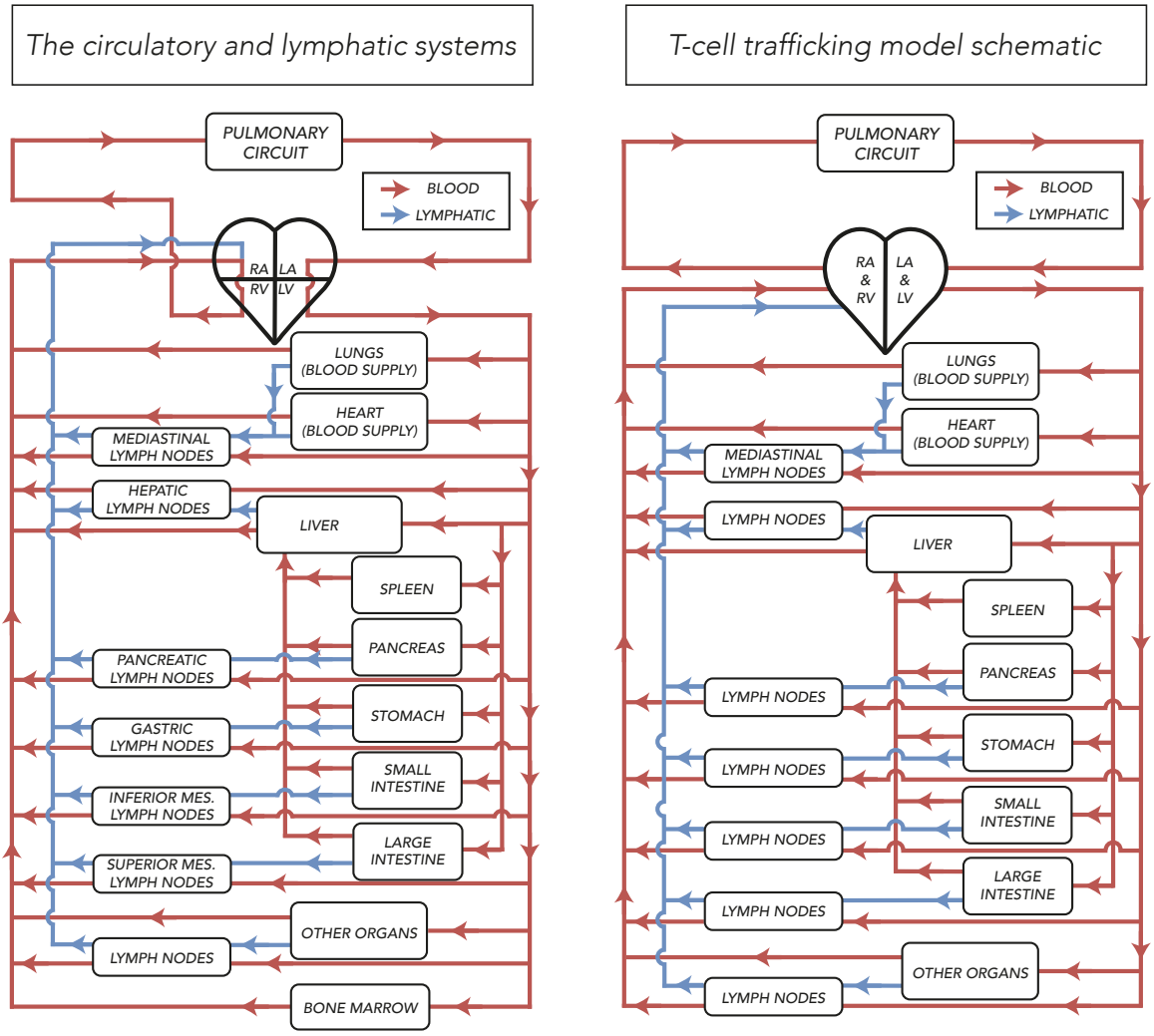


Figure 2.2: Model schematic of the ODE system (right) compared to the simplified schematic of the blood and lymph circulation (left). As a PBPK framework, the T cell trafficking model comprises anatomical compartments corresponding directly and faithfully to the organs and tissues of the body, connected by the cardiovascular and lymphatic system. Such a description of anatomy is used to predict a systemic and tissue exposure to the circulating T cells. Cells flow from the left atrium and left ventricle of the heart to each organ (red lines), via lymphatics (blue lines) into organ-draining lymph nodes and return back to the right atrium and right ventricle of the heart. Each box represents a vasculature and interstitium compartment. Chambers of the heart: *RA* - right atrium, *RV* - right ventricle, *LA* - left atrium, *LV* - left ventricle. *Other organs* compartments include: adrenals, bladder, brain, adipose tissue, gonads, kidneys, skeletal muscles, skeleton, skin and thyroid, which are not shown.

Symbol	Definition	Unit
C_o	T cell vasculature concentration in organ, o	cells / L
$\tilde{C}_o$	T cell interstitial volume concentration in organ, o	cells / L
C_{LN_o}	T cell vasculature concentration in lymph node for organ, o	cells / L
$\tilde{C}_{LN_o}$	T cell interstitial volume concentration in lymph node for organ, o	cells / L
N_o	Number of T cells in the vasculature of organ, o	cells
$\tilde{N}_o$	Number of T cells in the interstitial space of organ, o	cells
N_{LN_o}	Number of T cells in the vasculature of lymph node for organ, o	cells
$\tilde{N}_{LN_o}$	Number of T cells in the interstitial space of lymph node for organ, o	cells
B_o	Blood flow (volume of blood per unit time) in organ, o	L / min
B_{LN_o}	Blood flow (volume of blood per unit time) in lymph node for organ, o	L / min
V_o	Blood volume in organ, o	L
V_{LN_o}	Blood volume in lymph node for organ, o	L
$\tilde{V}_o$	Total volume of organ, o	L
$\tilde{V}_{LN_o}$	Total volume of lymph node for organ, o	L
e_o	Fraction of cells extravasating into the interstitial space of organ, o	-
e_{LN_o}	Fraction of cells extravasating into the interstitial space of lymph node for organ, o	-
μ_o	Fraction of cells leaving the interstitial space of organ, o	-
μ_{LN_o}	Fraction of cells leaving the interstitial space of lymph node for organ, o	-

Table 2.1: Definitions and units of parameters and variables in the model described in Section 2.2.1. Different suffixes, such as *LA&LV* (left atrium, left ventricle, and large arteries), *RA&RV* (right atrium, right ventricle, and large veins), *PC* (pulmonary circuit), *med* (mediastinal lymph nodes) are also used. See Figure 2.3 for a schematic of an exemplar organ and the associated parameters.

simulation of interest. Hence, the rate of extravasation is proportional to the flow of T cells out of the vasculature subcompartment: $e_o B_o C_o$.

From the interstitium of organ, o, T cells flow via lymphatics into its draining group of lymph nodes (see Figure 2.3). A fraction of T cells, μ_o, flows from the interstitial subcompartment of organ, o, into the draining lymph nodes. Similarly to the extravasation factor (e_o), the return factor, μ_o, is assumed to be constant for a given organ, o, and the T cell return rate is proportional to the flow of cells out of interstitium: $e_o \mu_o B_o \tilde{C}_o$, where $\tilde{C}_o$ is the interstitial concentration of T cells. As a result, the number of T cells in the interstitial compartments, $\tilde{N}_o$, changes according to the following equation:

$$\frac{d\tilde{N}_o}{dt} = \tilde{V}_o \frac{d\tilde{C}_o}{dt} = e_o B_o \left(C_o - \mu_o \tilde{C}_o \right), \tag{2.2}$$

where $\tilde{V}_o$ is the volume of the organ.

Each group of organ-draining lymph nodes is represented by a vasculature subcompartment (the blood supply to the lymph node) and the interstitial subcompartment, where T cells from the interstitium of organ, o, are drained via lymphatics (Figure 2.3). The rate of change

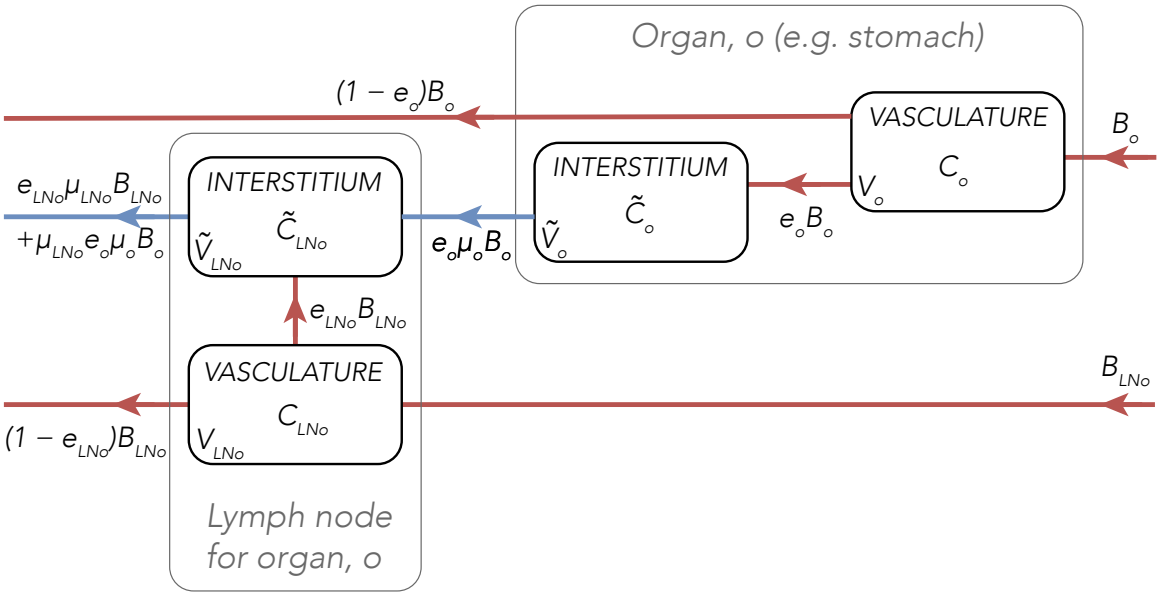


Figure 2.3: Organ, o, and draining lymph nodes for organ, o, are represented in the model as separate vascular and interstitial compartments. T cells flow from the cardiac output compartment (previously defined as left atrium, left ventricle, aorta and large arteries) to each organ, o, with a blood flow B_o, from which a proportion, $e_o B_o$, enters the interstitial space per unit time. A proportion of T cells, $e_o \mu_o B_o$, flows via lymphatics from the interstitial subcompartment of organ, o, into the draining lymph nodes per unit time. T cells also enter organ, o, -draining lymph nodes through the lymph node blood supply, denoted B_{LN_o}. From the lymph node vasculature compartment, a proportion of T cells extravasates into the lymph node interstitial compartment (at a rate $e_{\mathrm{LN}_o} B_{\mathrm{LN}_o}$). T cells drained to organ, o, -draining lymph nodes are returned to the systemic circulation (at a rate $e_{\mathrm{LN}_o} \mu_{\mathrm{LN}_o} B_{\mathrm{LN}_o} + \mu_{\mathrm{LN}_o} e_o \mu_o B_o$). T cells that have not extravasated to the interstitium of organ, o, and organ, o, -draining lymph nodes are, similarly, returned to the systemic circulation (at rates $(1 - e_o)B_o$ and $(1 - e_{\mathrm{LN}_o})B_{\mathrm{LN}_o}$, respectively). Different suffixes, such as *LA&LV* (combined left atrium, left ventricle, and large arteries), *RA&RV* (combined right atrium, right ventricle, and large veins), *PC* (pulmonary circuit), *med* (mediastinal lymph nodes) are also used.

in the number of T cells in the lymph nodes' blood supply compartment, analogously to Equation (2.1), is given by:

$$\frac{dN_{\mathrm{LN}_o}}{dt} = V_{\mathrm{LN}_o}\frac{dC_{\mathrm{LN}_o}}{dt} = B_{\mathrm{LN}_o}\left(C_{\mathrm{LA\&LV}} - C_{\mathrm{LN}_o}\right), \tag{2.3}$$

where V_{LN_o} is the blood volume of lymph nodes draining from an organ, o, B_{LN_o} is the blood flow through these lymph nodes, and $C_{\mathrm{LA\&LV}}$ is the concentration of T cells within the left atrium, left ventricle, aorta and large arteries between organs and the heart. The rate of change of T cells in the interstitial lymph node group compartment accounts for the contribution from the lymph nodes' vasculature and, additionally, the flow of interstitium drained cells through organ, o:

$$\frac{d\tilde{N}_{\mathrm{LN}_o}}{dt} = \tilde{V}_{\mathrm{LN}_o}\frac{d\tilde{C}_{\mathrm{LN}_o}}{dt} = e_{\mathrm{LN}_o}B_{\mathrm{LN}_o}\left(C_{\mathrm{LN}_o} - \mu_{\mathrm{LN}_o}\tilde{C}_{\mathrm{LN}_o}\right) + e_o\mu_o B_o\left(\tilde{C}_o - \mu_{\mathrm{LN}_o}\tilde{C}_{\mathrm{LN}_o}\right), \tag{2.4}$$

where $\tilde{V}_{\mathrm{LN}_o}$ is the volume of draining lymph nodes and μ_{LN_o} is the fraction of cells returning to the systemic circulation per unit blood flow. The first term describes the flow of T cells from the lymph node blood supply subcompartment into the interstitium and the proportion of the T cells that have extravasated leaving the interstitium. The second term represents T cells drained from an organ, o, interstitium and the proportion of the drained T cells being returned to the systemic circulation. Note that mediastinal lymph nodes, which drain both the vasculature of the heart and lungs, are an exception. The rate of change in the number of T cells in the blood supply compartment, analogously to Equation (2.3), is given by:

$$\frac{dN_{\mathrm{LN}_{\mathrm{med}}}}{dt} = V_{\mathrm{LN}_{\mathrm{med}}}\frac{dC_{\mathrm{LN}_{\mathrm{med}}}}{dt} = B_{\mathrm{LN}_{\mathrm{med}}}\left(C_{\mathrm{LA\&LV}} - C_{\mathrm{LN}_{\mathrm{med}}}\right), \tag{2.5}$$

where $V_{\mathrm{LN}_{\mathrm{med}}}$ is the blood volume of lymph nodes draining from the vasculature of the heart and lungs, $B_{\mathrm{LN}_{\mathrm{med}}}$ is the blood flow through these lymph nodes, and $C_{\mathrm{LA\&LV}}$ is the concentration of T cells within the left atrium, left ventricle, aorta and large arteries between organs and the heart. The rate of change of T cells in the interstitial lymph node compartment accounts for the dual drainage of T cells (from the heart and lungs blood supply) in addition to T cells

extravasating from the vasculature lymph node compartment:

$$\frac{d\tilde{N}_{\mathrm{LN_{med}}}}{dt} = \tilde{V}_{\mathrm{LN_{med}}}\frac{d\tilde{C}_{\mathrm{LN_{med}}}}{dt} = e_{\mathrm{LN_{med}}}B_{\mathrm{LN_{med}}}\left(C_{\mathrm{LN_{med}}} - \mu_{\mathrm{LN_{med}}}\tilde{C}_{\mathrm{LN_{med}}}\right) + \sum_{\substack{o\in\{\text{lungs b.s.,}\\ \text{heart b.s.}\}}} e_o\mu_o B_o\left(\tilde{C}_o - \mu_{\mathrm{LN_{med}}}\tilde{C}_{\mathrm{LN_{med}}}\right), \tag{2.6}$$

where $\tilde{V}_{\mathrm{LN_{med}}}$ is the volume of draining lymph nodes, $\mu_{\mathrm{LN_{med}}}$ is the fraction of cells returning to the systemic circulation per unit blood flow, and *b.s.* stands for blood supply. The first term describes the flow of T cells from the lymph node blood supply subcompartment into the interstitium and the proportion of the T cells that have extravasated leaving the interstitium. The second term represents T cells drained from the heart and lungs blood supply interstitium and the proportion of the drained T cells being returned to the systemic circulation.

The liver and liver-draining lymph nodes are further exceptions to Equations (2.1) – (2.4), which need to be modified to capture the specific anatomy of hepatic blood and lymph circulation. The framework treats the hepatic circulation separately from the blood received from the mesentery via the hepatic portal vein, *i.e.,* the blood flow through the liver as the hepatic circulation does not include the contribution from the portal vein. Instead, the liver receives additional blood exiting the mesenteric organs: the stomach, spleen, pancreas, small and large intestines. Note that since the spleen lacks draining lymphatic vessels, the liver's vasculature receives both the T cells that have extravasated into the spleen and those that have not, and hence:

$$\frac{dN_{\mathrm{liver}}}{dt} = V_{\mathrm{liver}}\frac{dC_{\mathrm{liver}}}{dt} = B_{\mathrm{liver}}\left(C_{\mathrm{LA\&LV}} - C_{\mathrm{liver}}\right) + e_{\mathrm{spleen}}\mu_{\mathrm{spleen}}B_{\mathrm{spleen}}\left(\tilde{C}_{\mathrm{spleen}} - C_{\mathrm{liver}}\right) + B_{\mathrm{spleen}}\left(1 - e_{\mathrm{spleen}}\right)\left(C_{\mathrm{spleen}} - C_{\mathrm{liver}}\right) + \sum_{m\in\{\text{mesentery}\}} B_m\left(1 - e_m\right)\left(C_m - C_{\mathrm{liver}}\right), \tag{2.7}$$

where each term respectively describes: (i) T cells from the blood supply to the liver and returning to the systemic circulation; (ii) the flow and exit of T cells that have extravasated into the spleen; (iii) the flow and exit of T cells that have not extravasated into the spleen and have returned through the portal vein; (iv) the flow and exit of T cells that have not extravasated into the mesenteric organs (the stomach, pancreas, small and large intestine) and have returned through the portal vein. The number of T cells in the liver's interstitium,

therefore, changes in time according to:

$$\begin{aligned}\frac{d\tilde{N}_{\text{liver}}}{dt} = \tilde{V}_{\text{liver}}\frac{d\tilde{C}_{\text{liver}}}{dt} &= e_{\text{liver}}B_{\text{liver}}\left(C_{\text{liver}} - \mu_{\text{liver}}\tilde{C}_{\text{liver}}\right) \\ &+ e_{\text{liver}}e_{\text{spleen}}\mu_{\text{spleen}}B_{\text{spleen}}\left(C_{\text{liver}} - \mu_{\text{liver}}\tilde{C}_{\text{liver}}\right) \\ &+ B_{\text{spleen}}\left(1 - e_{\text{spleen}}\right)e_{\text{liver}}\left(C_{\text{liver}} - \mu_{\text{liver}}\tilde{C}_{\text{liver}}\right) \\ &+ \sum_{m\in\{\text{mesentery}\}} B_m\left(1 - e_m\right)e_{\text{liver}}\left(C_{\text{liver}} - \mu_{\text{liver}}\tilde{C}_{\text{liver}}\right),\end{aligned} \tag{2.8}$$

where each term respectively represents: (i) the flow and drainage of T cells that have extravasated from the liver's blood supply; (ii) the flow and drainage of T cells have extravasated in the spleen, returned to the liver's vasculature and subsequently extravasated into the liver interstitium; (iii) the flow and drainage of T cells that have not extravasated in the spleen, returned to the liver's vasculature through the portal vein and subsequently extravasated into the liver interstitium; and (iv) the flow and drainage of T cells that have not extravasated in the mesenteric organs (the stomach, spleen, small and large intestine), returned to the liver's vasculature through the portal vein and subsequently extravasated into the liver interstitium.

The analogous equation for the liver-draining lymph nodes, LN_{liver}, is modified accordingly:

$$\begin{aligned}\frac{d\tilde{N}_{\text{LN}_{\text{liver}}}}{dt} = \tilde{V}_{\text{LN}_{\text{liver}}}\frac{d\tilde{C}_{\text{LN}_{\text{liver}}}}{dt} &= e_{\text{LN}_{\text{liver}}}B_{\text{LN}_{\text{liver}}}\left(C_{\text{LN}_{\text{liver}}} - \mu_{\text{LN}_{\text{liver}}}\tilde{C}_{\text{LN}_{\text{liver}}}\right) \\ &+ e_{\text{LN}_{\text{liver}}}\mu_{\text{LN}_{\text{liver}}}B_{\text{LN}_{\text{liver}}}\left(\tilde{C}_{\text{liver}} - \mu_{\text{LN}_{\text{liver}}}\tilde{C}_{\text{LN}_{\text{liver}}}\right) \\ &+ e_{\text{liver}}\mu_{\text{liver}}e_{\text{spleen}}\mu_{\text{spleen}}B_{\text{spleen}}\left(\tilde{C}_{\text{liver}} - \mu_{\text{LN}_{\text{liver}}}\tilde{C}_{\text{LN}_{\text{liver}}}\right) \\ &+ e_{\text{liver}}\mu_{\text{liver}}(1 - e_{\text{spleen}})B_{\text{spleen}}\left(\tilde{C}_{\text{liver}} - \mu_{\text{LN}_{\text{liver}}}\tilde{C}_{\text{LN}_{\text{liver}}}\right) \\ &+ e_{\text{liver}}\mu_{\text{liver}}\left(\sum_{m\in\{\text{mesentery}\}} B_m\left(1 - e_m\right)\right)\left(\tilde{C}_{\text{liver}} - \mu_{\text{LN}_{\text{liver}}}\tilde{C}_{\text{LN}_{\text{liver}}}\right),\end{aligned} \tag{2.9}$$

where each term respectively represents: (i) the flow of T cells from the lymph node blood supply subcompartment into the interstitium and the proportion of the T cells that have extravasated leaving the interstitium; (ii) the flow of T cells drained from the from the liver's interstitium and the proportion of the drained T cells being returned to the systemic circulation; (iii) the flow and lymphatic drainage of T cells have extravasated in the spleen, returned to the

liver's vasculature and subsequently extravasated into the liver interstitium and the proportion of the T cells being returned to the systemic circulation; (iv) the flow and lymphatic drainage of T cells that have not extravasated in the spleen, returned to the liver's vasculature through the portal vein and subsequently extravasated into the liver interstitium and the proportion of the T cells being returned to the systemic circulation; and (v) the flow and drainage of T cells that have not extravasated in the mesenteric organs (the stomach, spleen, small and large intestine), returned to the liver's vasculature through the portal vein and subsequently extravasated into the liver interstitium and the proportion of the T cells being returned to the systemic circulation. (Note that the blood supply to the vascular compartment of the liver-draining lymph node is in the form of Equation (2.3), analogously to other lymph nodes.)

T cells that have not extravasated from the organ's vasculature return through major veins to the heart's right atrium and right ventricle, *RA&RV*, combined with the lymph node outflow:

$$\begin{aligned}
\tfrac{dN_{\mathrm{RA\&RV}}}{dt} &= V_{\mathrm{RA\&RV}} \tfrac{dC_{\mathrm{RA\&RV}}}{dt} = -B_{\mathrm{TOT}} C_{\mathrm{RA\&RV}} \\
&+ \textstyle\sum_{o \notin \{\mathrm{mesentery}\}} (1 - e_o)\, B_o C_o + \sum_{o \notin \{\mathrm{spleen,PC}\}} (1 - e_{\mathrm{LN}_o})\, B_{\mathrm{LN}_o} C_{\mathrm{LN}_o} \\
&+ \left(e_{\mathrm{spleen}} \mu_{\mathrm{spleen}} B_{\mathrm{spleen}} + \textstyle\sum_{m \in \{\mathrm{mesentery}\}} (1 - e_m)\, B_m \right) (1 - e_{\mathrm{liver}})\, C_{\mathrm{liver}} \\
&+ \textstyle\sum_{\substack{o \notin \{\mathrm{spleen,PC,} \\ \mathrm{heart,lung}\}}} \left(e_{\mathrm{LN}_o} \mu_{\mathrm{LN}_o} B_{\mathrm{LN}_o} + \mu_{\mathrm{LN}_o} e_o \mu_o B_o \right) \tilde{C}_{\mathrm{LN}_o} \\
&+ \left(e_{\mathrm{LN}_{\mathrm{med}}} \mu_{\mathrm{LN}_{\mathrm{med}}} B_{\mathrm{LN}_{\mathrm{med}}} + \mu_{\mathrm{LN}_{\mathrm{med}}} e_{\mathrm{heart}} \mu_{\mathrm{heart}} B_{\mathrm{heart}} + \mu_{\mathrm{LN}_{\mathrm{med}}} e_{\mathrm{lung}} \mu_{\mathrm{lung}} B_{\mathrm{lung}} \right) \tilde{C}_{\mathrm{LN}_{\mathrm{med}}} \\
&+ \mu_{\mathrm{LN}_{\mathrm{liver}}} e_{\mathrm{liver}} \mu_{\mathrm{liver}} \left(e_{\mathrm{spleen}} \mu_{\mathrm{spleen}} B_{\mathrm{spleen}} + B_{\mathrm{spleen}} \left(1 - e_{\mathrm{spleen}} \right) \right) \tilde{C}_{\mathrm{LN}_{\mathrm{liver}}} \\
&+ \mu_{\mathrm{LN}_{\mathrm{liver}}} e_{\mathrm{liver}} \mu_{\mathrm{liver}} \left(\textstyle\sum_{m \in \{\mathrm{mesentery}\}} B_m \left(1 - e_m \right) \right) \tilde{C}_{\mathrm{LN}_{\mathrm{liver}}},
\end{aligned} \tag{2.10}$$

where $B_{\mathrm{TOT}} = \sum_{o \notin \{PC\}} B_o + \sum_{o \notin \{PC, spleen\}} B_{\mathrm{LN}_o}$ is the cardiac output, and the mesentery comprises: the stomach, spleen, pancreas, small and large intestines. Further, each line respectively refers to: (i) the flow of T cells out of the heart's right atrium and right ventricle; (ii) the return of T cells from the non-mesenteric organs; (iii) the return of T cells from the mesentery via the liver; (iv) the return of T cells from the lymph nodes, including (v) mediastinal and (vi, vii) liver-draining lymph nodes.

T cells flow from the right atrium and right ventricle into the pulmonary circuit (PC), where the blood flow is equal to the cardiac output $B_{\mathrm{TOT}} = \sum_{o \notin \{\mathrm{PC}\}} B_o + \sum_{o \notin \{\mathrm{PC,\ spleen}\}} B_{\mathrm{LN}_o}$:

$$\frac{dN_{\mathrm{PC}}}{dt} = B_{\mathrm{TOT}} \left(C_{\mathrm{RA\&RV}} - C_{\mathrm{PC}} \right), \tag{2.11}$$

$$\frac{d\tilde{N}_{\mathrm{PC}}}{dt} = e_{\mathrm{PC}} B_{\mathrm{TOT}} \left(C_{\mathrm{PC}} - \mu_{\mathrm{PC}} \tilde{C}_{\mathrm{PC}} \right). \tag{2.12}$$

Note that the pulmonary circuit lacks lymphatics and the interstitial subcompartment represents the 'trapped' state (functionally equivalent to interstitial space) [54, 55]. Finally, T cells return from the pulmonary circuit to the left atrium and left ventricle of the heart:

$$\frac{dN_{\mathrm{LA\&LV}}}{dt} = (1 - e_{\mathrm{PC}}) B_{\mathrm{TOT}} C_{\mathrm{PC}} + e_{\mathrm{PC}} \mu_{\mathrm{PC}} B_{\mathrm{TOT}} \tilde{C}_{\mathrm{PC}} - B_{\mathrm{TOT}} C_{\mathrm{LA\&LV}}, \tag{2.13}$$

where the last term describes T cells flowing through aorta and major arteries towards vasculature compartments, the subsequent downstream impact of which is captured in Equation (2.1).

2.2.2 Lymph nodes — whole body distribution

To describe the distribution of lymph nodes within the model, certain assumptions have been made due to the lack of detailed literature on lymphatic drainage pathways. It was assumed that lymph nodes each drain a constant volume of tissue. In such a case, the number of lymph nodes draining a particular organ increases with the organ's volume, and lymph nodes were, therefore, partitioned by organ volume. The volume of the group of lymph nodes draining an organ, o, $\tilde{V}_{\mathrm{LN}_o}$, the blood flow, B_{LN_o}, and the blood volume of that lymph node group, V_{LN_o}, were assumed as fractions of the total values of those parameters using the partitioning factor:

$$\begin{aligned}
\tilde{V}_{\mathrm{LN}_o} &= \frac{\tilde{V}_o}{\sum\limits_{\substack{i \notin \{\mathrm{spleen,PC,} \\ \mathrm{RA\&RV,LA\&LV}\}}} \tilde{V}_i} \tilde{V}_{\mathrm{LN}_{\mathrm{TOT}}} \\
B_{\mathrm{LN}_o} &= \frac{\tilde{V}_o}{\sum\limits_{\substack{i \notin \{\mathrm{spleen,PC,} \\ \mathrm{RA\&RV,LA\&LV}\}}} \tilde{V}_i} B_{\mathrm{LN}_{\mathrm{TOT}}} \\
V_{\mathrm{LN}_o} &= \frac{\tilde{V}_o}{\sum\limits_{\substack{i \notin \{\mathrm{spleen,PC,} \\ \mathrm{RA\&RV,LA\&LV}\}}} \tilde{V}_i} V_{\mathrm{LN}_{\mathrm{TOT}}}.
\end{aligned} \tag{2.14}$$

Here $\tilde{V}_o$ is the volume of the drained organ (or sum of organ volumes, for the mediastinal lymph node compartment), and the index i runs over all organs drained by lymph nodes (so that the sum represents the total volume of all organs drained via lymphatics), $\tilde{V}_{\mathrm{LN}_{\mathrm{TOT}}}$, $B_{\mathrm{LN}_{\mathrm{TOT}}}$ and $V_{\mathrm{LN}_{\mathrm{TOT}}}$ are the total volume of lymph nodes, the total blood flow to lymph nodes and the total blood volume in lymph nodes, respectively.

2.2.3 Parameterisation

Extravasation and return parameters for all organs, e_o and μ_o, and organ-draining lymph nodes, e_{LN_o} and μ_{LN_o}, were defined to vary uniformly between 0 and 1. Blood flows, blood and organ volumes in the model were parameterised based on the literature review of relevant physiological reference data carried out by Brown et al. [52]. To avoid using data from different studies, the most complete set of reference data was chosen for baseline parameter values, namely the International Commission on Radiological Protection (ICRP) compilations [30, 57]. The ICRP publications have taken into account age- and gender-related differences in the anatomical and physiological characteristics of reference individuals and have been valued as a standardised set of human data for medical purposes. Since anatomical values vary greatly between and within individuals, the variability between sources compiled by Brown et al. [52] was used as a proxy for anatomical variability. The reported parameter variability was extended by identifying parameters associated with high temporal and inter-individual variability in human [30], *i.e.*, the muscle [58, 59] and fat [60, 61] volumes, the blood flows through organs whose blood flows change as a result of exercise (muscle [62], lungs [63] and pulmonary circuit [63]), meal (mesentery [64]) or temperature change (skin [65]). For each parameter, a wider range was chosen from all reported values and, when only one parameter value was available, we assumed a uniform variability of 25% from the baseline value. A summary of the resulting parameter ranges can be found in Table 2.2.

2.2.4 Exemplar simulation

The ODE system was solved numerically using the Matlab stiff solver ode15s with a variable time step, subject to initial conditions, where T cells of interest are administered intravenously, *i.e.*, to the right atrium, right ventricle and large veins compartment ($RA\&RV$):

$$\begin{gathered} N_{\mathrm{RA\&RV}}(0) = V_{\mathrm{RA\&RV}} C_{\mathrm{RA\&RV}}(0) = N_{\mathrm{TOT}} \\ N_o(0) = V_o C_o(0) = 0 \qquad \tilde{N}_o(0) = \tilde{V}_o \tilde{C}_o(0) = 0 \\ N_{\mathrm{LN}_o}(0) = V_{\mathrm{LN}_o} C\mathrm{LN}_o(0) = 0 \quad \tilde{N}_{\mathrm{LN}_o}(0) = \tilde{V}_{\mathrm{LN}_o} \tilde{C}_{\mathrm{LN}_o}(0) = 0, \end{gathered} \tag{2.15}$$

where N_{TOT} is the total number of T cells of interest in the system. Figure 2.4 shows an example solution for the ODE system.

Organs	Blood flow [L/min]		Blood volume [L]		Organ volume [L]	
Adrenals	0.019 [30]	(0.011 – 0.022) [52]	0.032 [30]	(0.001 – 0.007) [52]	0.017 [30]	(0.014 – 0.017) [52]
Bladder	0.004 [30]	(0.003 – 0.005) [52]	0.001 [30]	(0.0008 – 0.0013) [52]	0.048 [30]	(0.036 – 0.06) [52]
Brain	0.78 [30]	(0.477 – 1.001) [52]	0.064 [30]	(0.019 – 0.593) [52]	1.381 [30]	(1.381 – 1.45) [52]
Fat	0.325 [30]	(0.194 – 0.484) [52]	0.265 [30]	(0.094 – 0.906) [52]	19.791 [30]	(2.249 – 31.5) [60, 61]
Gonads	0.0033 [30]	(0.0016 – 0.0041) [52]	0.0021 [30]	(0.0048 – 0.0026) [52]	0.017 [30]	(0.017 – 0.036) [52]
Heart (blood supply)	0.26 [30]	(0.139 – 0.326) [52]	0.053 [30]	(0.0085 – 0.734) [52]	0.314 [30]	(0.266 – 0.341)[52]
Kidneys	1.235 [30]	(0.704 – 1.464) [52]	0.106 [30]	(0.012 – 0.243) [52]	0.295 [30]	(0.295 – 0.332) [52]
Large Intestine	0.26 [30]	(0.198 – 0.554) [52, 64]	0.53 [30]	(0.006 – 0.262) [52]	0.356 [30]	(0.356 – 0.548) [52]
Liver	0.423 [30]	(0.049 – 0.113) [52, 64]	0.117 [30]	(0.069 – 1.19) [52]	1.714 [30]	(1.687 – 2.143) [52]
Lungs	0.163 [30]	(0.096 – 1) [52, 63]	0.663 [30]	(0.036 – 1.487) [52]	1.142 [30]	(0.519 – 1.169)[52]
Lymph Nodes	0.11 [30]	(0.087 – 0.241) [52]	0.011 [30]	(0.002 – 0.038) [52]	0.709 [30]	(0.274 – 0.709) [52]
Skeletal muscles	1.105 [30]	(0.544 – 35) [52, 62]	0.742 [30]	(0.098 – 10.831) [52]	27.619 [30]	(20 – 45.5) [58, 59]
Pancreas	0.065 [30]	(0.053 – 0.115) [52]	0.032 [30]	(0.004 – 0.071) [52]	0.133 [30]	(0.084 – 0.133) [52]
Small Intestine	0.65 [30]	(0.344 – 1.385) [52, 64]	0.201 [30]	(0.004 – 0.533) [52]	0.625 [30]	(0.385 – 1.652) [52]
Skeleton (bone and bone marrow)	0.325 [30]	(0.159 – 0.333) [52]	0.371 [30]	(0.102 – 1.77) [52]	7.726 [30]	(7.164 – 30.078) [52]
Skin	0.325 [30]	(0.199 – 8) [52, 65]	0.03 [30]	(0.03 – 0.12) [52]	3.562 [30]	(3.408 – 7.77) [52]
Spleen	0.195 [30]	(0.091 – 0.199) [52]	0.074 [30]	(0.011 – 0.167) [52]	0.144 [30]	(0.144 – 0.221) [52]
Stomach	0.065 [30]	(0.03 – 0.138) [52, 64]	0.053 [30]	(0.008 – 0.119) [52]	0.144 [30]	(0.143 – 0.154) [52]
Thyroid	0.098 [30]	(0.033 – 0.121) [52]	0.003 [30]	(0.0011 – 0.0071) [52]	0.019 [30]	(0.019 – 0.02) [52]
Pulmonary Circuit		-	0.557 [30]	(0.417 – 0.696)	0.557 [30]	(0.417 – 0.696)
Right atrium and ventricle		-	1.193 [30]	(0.894 – 1.491)		-
Left atrium and ventricle		-	0.557 [30]	(0.417 – 0.696)		-

Table 2.2: Human anatomical parameter values and variability ranges used for the model parameterisation. The baseline parameter values come from the International Commission on Radiological Protection (ICRP) compilations [30, 57]. The variability ranges were based on the parameter value selection made by Brown *et al.* [52] and additional selected literature sources ([58, 59, 60, 61, 62, 63, 64, 65]). Note that liver row does not include the portal vein, and the pulmonary circuit is listed separately from the lung blood supply parameters. Also note that the parameterisation for the heart chambers includes the blood volume of major blood vessels – superior and inferior vena cavae (for the right ventricle and atrium) and aorta (for the left atrium and ventricle), while the skeleton parameterisation corresponds to an amalgam of bone and bone marrow.

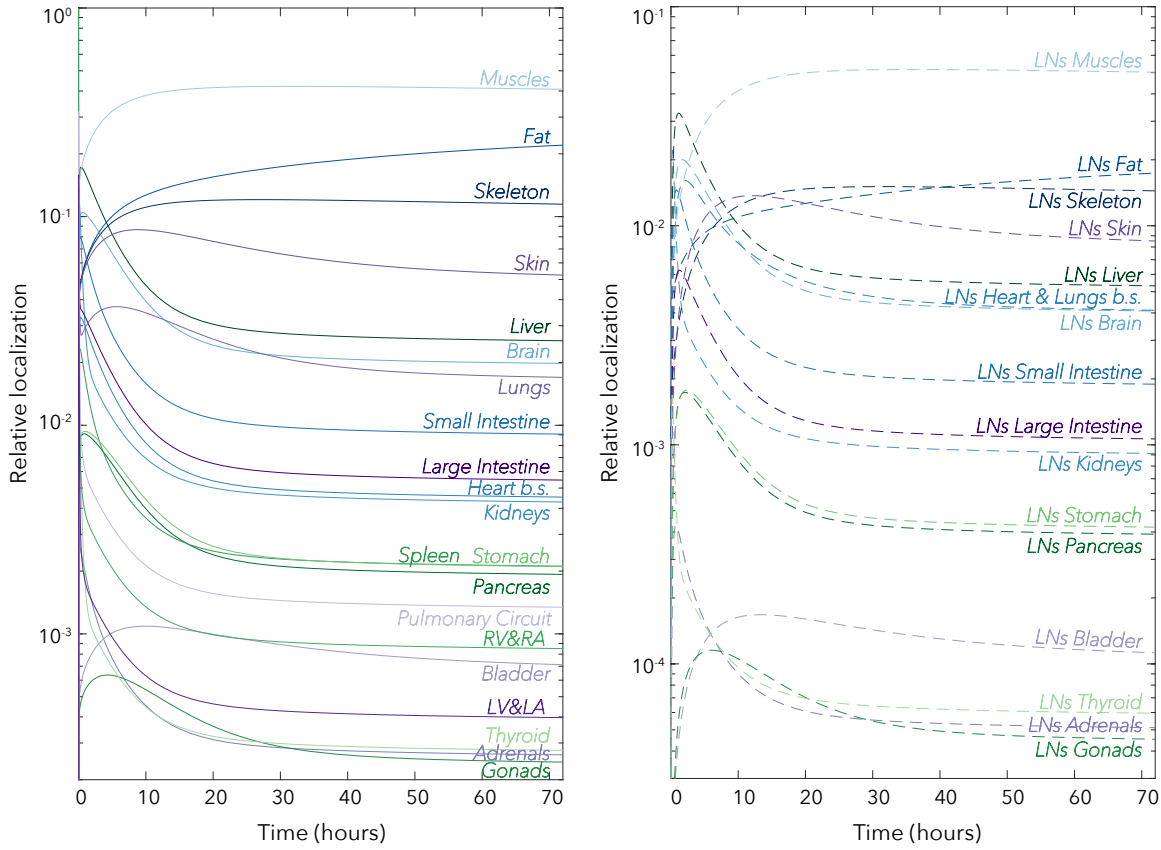


Figure 2.4: Example results from the ODE system, subject to the initial distribution of T cells administered intravenously (Equation (2.15)), with baseline parameter values. Each curve represents the sum of the number of T cells in vascular (N_o) and interstitial localisations ($\tilde{N}_o$) expressed as the fraction of the total number of administered T cells (relative localisation). For all organs (left) and all organ-draining groups of lymph nodes (right), extravasation, e_o, and return parameters, μ_o, were assumed to be equal to 0.25 and 0.05, respectively. Such a choice of parameter values is unlikely to represent a physiologically realistic state, as the extravasation, e_o, and return parameters, μ_o, can be expected to differ between organs and may also change due to other factors, such as inflammation *etc.*. However, the plotted exemplar solution depicts a behaviour of the system that is qualitatively consistent with the expected trafficking of T cells. For instance, the initial T cell localisation peak following intravenous administration of T cells at time $t = 0$ and subsequent T cell distribution across organ compartments. Moreover, given equal extravasation, e_o, and return parameters, μ_o, for all organ compartments, organs and tissues characterised by the highest volumes and blood flows (muscle, fat, skeleton and skin), result in the highest T cell localisation in steady state. Note that the contents of heart chambers (*RA&RV* and *LA&LV*) and the blood supply to the heart (*Heart b.s.*) are plotted separately. Similarly, the lung curve does not include the pulmonary circuit.

2.2.5 In silico splenectomy — model reduction

Trivially neglecting initial transit dynamics, the ratio of post- to pre-splenectomy cell concentration in any compartment can be derived analytically by considering Equations (2.1) – (2.10) in steady state. Denote the pre-splenectomy cell concentration in organ o as C_o and the post-splenectomy cell concentration as C_o^*. The steady state of Equation (2.1) implies $C_o = C_{\text{LA\&LV}}$ and $C_o^* = C_{\text{LA\&LV}}^*$ for all organs $o \notin \{\text{liver, PC}\}$, meaning the steady-state cell concentration is equal to the cell concentration in the left atrium and ventricle of the heart, $C_{\text{LA\&LV}}$ pre-splenectomy and $C_{\text{LA\&LV}}^*$ post-splenectomy for all organs, except the liver. We can therefore define a dimensionless constant κ such that:

$$C_o^* = \kappa C_o \text{ and } C_{\text{LA\&LV}}^* = \kappa C_{\text{LA\&LV}}, \tag{2.16}$$

and an expression for κ will be derived below. Similarly, by considering Equation (2.2) the steady-state cell concentration in the interstitium of organ, o, can be related to the steady-state concentration in the corresponding vasculature compartment: $\mu_o \tilde{C}_o = C_o$ (pre-splenectomy) and $\mu_o \tilde{C}_o^* = C_o^*$ (post-splenectomy). The interstitial cell concentrations pre- and post-splenectomy in organ, o, are related by the same constant κ analogously to Equation (2.16):

$$\tilde{C}_o^* = \kappa \tilde{C}_o. \tag{2.17}$$

Equations (2.16) and (2.17) imply that ratios of post- to pre-splenectomy cell concentration, and consequently cell numbers, are equal for both the vasculature and interstitial compartments of organ, o, and the ratios are equal for all organs. The exception is the liver, for which the equations are modified to capture the anatomy of hepatic blood and lymph circulation. By considering Equation (2.7) in steady state and substituting $C_{\text{LA\&LV}} = C_{\text{spleen}} = C_m = C_o$ (where $m \in \{$ stomach, pancreas, small intestine, large intestine$\}$), $\tilde{C}_{\text{spleen}} = \frac{1}{\mu_{\text{spleen}}} C_{\text{spleen}} = \frac{1}{\mu_{\text{spleen}}} C_o$, the steady-state cell concentration C_{liver} can be solved for, resulting in:

$$\begin{aligned} C_{\text{liver}} &= \frac{B_{\text{liver}} + e_{\text{spleen}} B_{\text{spleen}} + B_{\text{spleen}}(1-e_{\text{spleen}}) + \sum_{m\in\{\text{mesentery}\}} B_m(1-e_m)}{B_{\text{liver}} + e_{\text{spleen}}\mu_{\text{spleen}} B_{\text{spleen}} + B_{\text{spleen}}(1-e_{\text{spleen}}) + \sum_{m\in\{\text{mesentery}\}} B_m(1-e_m)} C_o \\ &= \left(1 + \frac{e_{\text{spleen}} B_{\text{spleen}}(1-\mu_{\text{spleen}})}{B_{\text{liver}} + e_{\text{spleen}}\mu_{\text{spleen}} B_{\text{spleen}} + B_{\text{spleen}}(1-e_{\text{spleen}}) + \sum_{m\in\{\text{mesentery}\}} B_m(1-e_m)}\right) C_o \\ &= \lambda C_o, \end{aligned} \tag{2.18}$$

where mesentery refers to the small and large intestines, stomach and pancreas and the variable λ has been introduced to simplify the notation. Equation (2.18) implies that the steady-state cell concentration in the liver vasculature is larger than in the remaining organs. Note that post-splenectomy $\lambda^* = 1$, since $B_{\text{spleen}} = 0$ and Equation (2.18) simplifies to:

$$C^*_{\text{liver}} = C^*_o, \tag{2.19}$$

indicating the cell concentration in the liver's vasculature post-splenectomy is the same as in the remaining organs. The ratio of post- to pre-splenectomy cell concentration in the liver vasculature is, therefore:

$$\frac{C^*_{\text{liver}}}{C_{\text{liver}}} = \frac{\kappa}{1 + \frac{e_{\text{spleen}} B_{\text{spleen}}(1-\mu_{\text{spleen}})}{B_{\text{liver}} + e_{\text{spleen}}\mu_{\text{spleen}} B_{\text{spleen}} + B_{\text{spleen}}(1-e_{\text{spleen}}) + \sum_{m\in\{\text{mesentery}\}} B_m(1-e_m)}} = \frac{\kappa}{\lambda}. \tag{2.20}$$

Since $\lambda > 1$, the expected post-to pre-splenectomy cell concentration ratio is predicted to be lower than for the remaining compartments. Analogously, considering the steady state of Equation (2.8) and substituting $C_{\text{liver}} = \lambda C_o$ (Equation (2.18)), the steady-state cell concentration in the liver interstitium, $\tilde{C}_{\text{liver}}$, can be expressed as:

$$\tilde{C}_{\text{liver}} = \frac{C_{\text{liver}}}{\mu_{\text{liver}}} = \frac{\lambda}{\mu_{\text{liver}}} C_o. \tag{2.21}$$

Since $\lambda^* = 1$ in the absence of the spleen, the ratio of post- to pre-splenectomy cell concentration in the liver interstitium is given by:

$$\frac{\tilde{C}^*_{\text{liver}}}{\tilde{C}_{\text{liver}}} = \frac{C^*_o}{\lambda C_o} = \frac{\kappa}{\lambda}, \tag{2.22}$$

resulting in equal post- to pre-splenectomy ratios in both the vasculature and the interstitial liver compartments.

The post- to pre-splenectomy cell concentration ratio for organ, o, -draining lymph nodes can be derived in the same manner. Note that the lymph node blood supply compartment follows the same scaling as vasculature of organ, o, with:

$$C^*_{\text{LN}_o} = \kappa C_{\text{LN}_o}, \tag{2.23}$$

which follows from Equation (2.3). Consider Equation (2.4) for the interstitium compartment of organ, o, -draining lymph nodes in steady state. Substituting the known steady-state cell concentration relations ($C_{\mathrm{LN}_o} = C_o$ and $\tilde{C}_o = \frac{1}{\mu_o} C_o$) and solving for $\tilde{C}_{\mathrm{LN}_o}$ gives:

$$\tilde{C}_{\mathrm{LN}_o} = \frac{e_{\mathrm{LN}_o} B_{\mathrm{LN}_o} + e_o B_o}{e_{\mathrm{LN}_o} B_{\mathrm{LN}_o} + e_o \mu_o B_o} \frac{C_o}{\mu_{\mathrm{LN}_o}}. \tag{2.24}$$

Similarly, the steady-state cell concentration post-splenectomy, $\tilde{C}^*_{\mathrm{LN}_o}$, is given by:

$$\tilde{C}^*_{\mathrm{LN}_o} = \frac{e_{\mathrm{LN}_o} B^*_{\mathrm{LN}_o} + e_o B^*_o}{e_{\mathrm{LN}_o} B^*_{\mathrm{LN}_o} + e_o \mu_o B^*_o} \frac{C^*_o}{\mu_{\mathrm{LN}_o}} = \frac{e_{\mathrm{LN}_o} B_{\mathrm{LN}_o} + e_o B_o}{e_{\mathrm{LN}_o} B_{\mathrm{LN}_o} + e_o \mu_o B_o} \frac{C^*_o}{\mu_{\mathrm{LN}_o}}, \tag{2.25}$$

where $C^*_{\mathrm{LN}_o} = C^*_o$ and $\tilde{C}^*_o = \frac{1}{\mu_o} C^*_o$ were substituted and B^*_o denotes the blood flow post-splenectomy. Since all pre-splenectomy blood flows are scaled by the same factor $1 + \theta$ (Equation (A.7)), the post- to pre-splenectomy cell concentration ratio is simply given by:

$$\frac{\tilde{C}^*_{\mathrm{LN}_o}}{\tilde{C}_{\mathrm{LN}_o}} = \frac{C^*_o}{C_o} = \kappa, \tag{2.26}$$

where κ is the post- to pre-splenectomy cell concentration ratio for all compartments, except the liver. Note that Equation (2.26) also holds for mediastinal lymph nodes, which drain both the heart and lung blood supply compartments. The ratio of the steady-state cell concentration in the mediastinal lymph node compartment post-splenectomy:

$$\begin{aligned} \tilde{C}^*_{\mathrm{LN}_{\mathrm{med}}} &= \frac{e_{\mathrm{LN}_{\mathrm{med}}} B^*_{\mathrm{LN}_{\mathrm{med}}} + e_{\mathrm{heart}} B^*_{\mathrm{heart}} + e_{\mathrm{lung}} B^*_{\mathrm{lung}}}{e_{\mathrm{LN}_{\mathrm{med}}} B^*_{\mathrm{LN}_{\mathrm{med}}} + e_{\mathrm{heart}} \mu_{\mathrm{heart}} B^*_{\mathrm{heart}} + e_{\mathrm{lung}} \mu_{\mathrm{lung}} B^*_{\mathrm{lung}}} \frac{C^*_o}{\mu_{\mathrm{LN}_{\mathrm{med}}}} \\ &= \frac{e_{\mathrm{LN}_{\mathrm{med}}} B_{\mathrm{LN}_{\mathrm{med}}} + e_{\mathrm{heart}} B_{\mathrm{heart}} + e_{\mathrm{lung}} B_{\mathrm{lung}}}{e_{\mathrm{LN}_{\mathrm{med}}} B_{\mathrm{LN}_{\mathrm{med}}} + e_{\mathrm{heart}} \mu_{\mathrm{heart}} B_{\mathrm{heart}} + e_{\mathrm{lung}} \mu_{\mathrm{lung}} B_{\mathrm{lung}}} \frac{C^*_o}{\mu_{\mathrm{LN}_{\mathrm{med}}}}, \end{aligned} \tag{2.27}$$

and pre-splenectomy:

$$\tilde{C}_{\mathrm{LN}_{\mathrm{med}}} = \frac{e_{\mathrm{LN}_{\mathrm{med}}} B_{\mathrm{LN}_{\mathrm{med}}} + e_{\mathrm{heart}} B_{\mathrm{heart}} + e_{\mathrm{lung}} B_{\mathrm{lung}}}{e_{\mathrm{LN}_{\mathrm{med}}} B_{\mathrm{LN}_{\mathrm{med}}} + e_{\mathrm{heart}} \mu_{\mathrm{heart}} B_{\mathrm{heart}} + e_{\mathrm{lung}} \mu_{\mathrm{lung}} B_{\mathrm{lung}}} \frac{C_o}{\mu_{\mathrm{LN}_{\mathrm{med}}}}, \tag{2.28}$$

yields the same post- to pre-splenectomy cell concentration ratio, κ:

$$\frac{\tilde{C}^*_{\mathrm{LN_{med}}}}{\tilde{C}_{\mathrm{LN_{med}}}} = \frac{C^*_o}{C_o} = \kappa. \tag{2.29}$$

Also note that the post- to pre-splenectomy ratio remains the same independent of the number of drained organs, with the exception of the liver. The post- to pre-splenectomy cell concentration ratio in lymph nodes that do not drain from the liver are, therefore, equal to the ratio for all other organs, except the liver.

Due to the anatomy of hepatic circulation, the liver-draining lymph nodes differ from the remaining lymph nodes. Consider Equation (2.9) in steady state:

$$\begin{aligned}
\frac{d\tilde{N}_{\mathrm{LN_{liver}}}}{dt} &= \tilde{V}_{\mathrm{LN_{liver}}} \frac{d\tilde{C}_{\mathrm{LN_{liver}}}}{dt} = e_{\mathrm{LN_{liver}}} B_{\mathrm{LN_{liver}}} \left(C_{\mathrm{LN_{liver}}} - \mu_{\mathrm{LN_{liver}}} \tilde{C}_{\mathrm{LN_{liver}}}\right) \\
&+ e_{\mathrm{LN_{liver}}} \mu_{\mathrm{LN_{liver}}} B_{\mathrm{LN_{liver}}} \left(\tilde{C}_{\mathrm{liver}} - \mu_{\mathrm{LN_{liver}}} \tilde{C}_{\mathrm{LN_{liver}}}\right) \\
&+ e_{\mathrm{liver}} \mu_{\mathrm{liver}} e_{\mathrm{spleen}} \mu_{\mathrm{spleen}} B_{\mathrm{spleen}} \left(\tilde{C}_{\mathrm{liver}} - \mu_{\mathrm{LN_{liver}}} \tilde{C}_{\mathrm{LN_{liver}}}\right) \\
&+ e_{\mathrm{liver}} \mu_{\mathrm{liver}} (1 - e_{\mathrm{spleen}}) B_{\mathrm{spleen}} \left(\tilde{C}_{\mathrm{liver}} - \mu_{\mathrm{LN_{liver}}} \tilde{C}_{\mathrm{LN_{liver}}}\right) \\
&+ e_{\mathrm{liver}} \mu_{\mathrm{liver}} \left(\textstyle\sum_{m \in \{\mathrm{mesentery}\}} B_m (1 - e_m)\right) \left(\tilde{C}_{\mathrm{liver}} - \mu_{\mathrm{LN_{liver}}} \tilde{C}_{\mathrm{LN_{liver}}}\right) \\
&= 0.
\end{aligned}$$

Recall that pre-splenectomy, in steady state $C_{\mathrm{LN_{liver}}} = C_o$ and $\tilde{C}_{\mathrm{liver}} = \frac{\lambda}{\mu_{\mathrm{liver}}} C_o$, where λ is given by Equation (2.18). Substituting those steady-state cell concentrations and solving for $\tilde{C}_{\mathrm{LN_{liver}}}$ in steady state:

$$\begin{aligned}
\tilde{C}_{\mathrm{LN_{liver}}} &= \frac{e_{\mathrm{LN_{liver}}} B_{\mathrm{LN_{liver}}} + \lambda e_{\mathrm{liver}} \left(B_{\mathrm{liver}} + e_{\mathrm{spleen}} \mu_{\mathrm{spleen}} B_{\mathrm{spleen}} + B_{\mathrm{spleen}} (1 - e_{\mathrm{spleen}}) + \sum_m B_m (1 - e_m)\right)}{e_{\mathrm{LN_{liver}}} B_{\mathrm{LN_{liver}}} + e_{\mathrm{liver}} \mu_{\mathrm{liver}} \left(B_{\mathrm{liver}} + e_{\mathrm{spleen}} \mu_{\mathrm{spleen}} B_{\mathrm{spleen}} + B_{\mathrm{spleen}} (1 - e_{\mathrm{spleen}}) + \sum_m B_m (1 - e_m)\right)} \frac{C_o}{\mu_{\mathrm{LN_{liver}}}} \\
&= \sigma \frac{C_o}{\mu_{\mathrm{LN_{liver}}}},
\end{aligned} \tag{2.30}$$

which defines σ, where summation over m runs over mesenteric organs (the, stomach, small and large intestine, and pancreas). Similarly, for the post-splenectomy steady-state cell con-

centration $\tilde{C}^*_{\mathsf{LN}_{\mathsf{liver}}}$:

$$\begin{aligned}\tilde{C}^*_{\mathsf{LN}_{\mathsf{liver}}} &= \frac{e_{\mathsf{LN}_{\mathsf{liver}}} B_{\mathsf{LN}_{\mathsf{liver}}} + e_{\mathsf{liver}} \left(B_{\mathsf{liver}} + \sum_m B_m(1-e_m)\right)}{e_{\mathsf{LN}_{\mathsf{liver}}} B_{\mathsf{LN}_{\mathsf{liver}}} + e_{\mathsf{liver}} \mu_{\mathsf{liver}} \left(B_{\mathsf{liver}} + \sum_m B_m(1-e_m)\right)} \frac{C_o}{\mu_{\mathsf{LN}_{\mathsf{liver}}}} \\ &= \sigma^* \frac{C^*_o}{\mu_{\mathsf{LN}_{\mathsf{liver}}}},\end{aligned} \tag{2.31}$$

which defines σ^*, where summation over m runs over mesenteric organs (the stomach, small and large intestine, and pancreas). The post- to pre-splenectomy cell concentration ratio can be then expressed as

$$\frac{\tilde{C}^*_{\mathsf{LN}_{\mathsf{liver}}}}{\tilde{C}_{\mathsf{LN}_{\mathsf{liver}}}} = \frac{\sigma^*}{\sigma}\frac{C^*_o}{C_o} = \frac{\sigma^*\kappa}{\sigma}, \tag{2.32}$$

where the parameter groupings σ and σ^* were derived above.

Finally, it can be shown that the post- to pre-splenectomy cell concentration ratio for the three remaining compartments, the pulmonary circuit (PC), the right (RA&RV) and left heart chambers (LA&LV), is equal to κ. By considering Equation (2.10) in steady state pre-splenectomy (post-splenectomy) we have:

$$C_{\mathsf{PC}} = C_{\mathsf{RA\&RV}} \quad \left(C^*_{\mathsf{PC}} = C^*_{\mathsf{RA\&RV}}\right), \tag{2.33}$$

and similarly Equation (2.12) gives:

$$\tilde{C}_{\mathsf{PC}} = \frac{1}{\mu_{\mathsf{PC}}} C_{\mathsf{PC}} \quad \left(\tilde{C}^*_{\mathsf{PC}} = \frac{1}{\mu_{\mathsf{PC}}} C^*_{\mathsf{PC}}\right). \tag{2.34}$$

Substituting the above relations into Equation (2.13) in steady state yields:

$$C_{\mathsf{LA\&LV}} = C_{\mathsf{PC}} = C_{\mathsf{RA\&RV}} \quad \left(C^*_{\mathsf{LA\&LV}} = C^*_{\mathsf{PC}} = C^*_{\mathsf{RA\&RV}}\right), \tag{2.35}$$

and, by Equation (2.16), the post- to pre-splenectomy cell concentration ratios in the pulmonary circuit (PC) and heart chambers compartments (RA&RV and LA&LV) are:

$$\frac{C^*_{\mathsf{LA\&LV}}}{C_{\mathsf{LA\&LV}}} = \frac{C^*_{\mathsf{RA\&RV}}}{C_{\mathsf{RA\&RV}}} = \frac{C^*_{\mathsf{PC}}}{C_{\mathsf{PC}}} = \frac{\tilde{C}^*_{\mathsf{PC}}}{\tilde{C}_{\mathsf{PC}}} = \kappa. \tag{2.36}$$

An expression for the post- to pre-splenectomy concentration ratio κ in organs other

than the liver and liver-draining lymph nodes (Equation (2.16) and (2.17)) is derived from the constraint that the total number of cells in the system is conserved pre- and post-splenectomy: $N_{\mathrm{TOT}} = N^*_{\mathrm{TOT}}$. Expressing the constraint via a summation of the number of cells in each compartment in steady state:

$$N_{\mathrm{TOT}} = \sum_o V_o C_o + \sum_{\substack{o\notin\{\mathrm{RA\&RV}\\ \mathrm{PC,LA\&LV}\}}} \tilde{V}_o \tilde{C}_o + \sum_{\substack{o'\notin\{\mathrm{spleen,RA\&RV,}\\ \mathrm{PC,LA\&LV}\}}} \left(V_{\mathrm{LN}_{o'}} C_{\mathrm{LN}_{o'}} + \tilde{V}_{\mathrm{LN}_{o'}} \tilde{C}_{\mathrm{LN}_{o'}}\right), \quad (2.37)$$

$$N^*_{\mathrm{TOT}} = \sum_{o\notin\{\mathrm{spleen}\}} V_o C^*_o + \sum_{\substack{o\notin\{\mathrm{spleen,RA\&RV,}\\ \mathrm{PC,LA\&LV}\}}} \tilde{V}_o \tilde{C}^*_o + \sum_{\substack{o'\notin\{\mathrm{spleen,RA\&RV,}\\ \mathrm{PC,LA\&LV}\}}} \left(V_{\mathrm{LN}_{o'}} C^*_{\mathrm{LN}_{o'}} + \tilde{V}_{\mathrm{LN}_{o'}} \tilde{C}^*_{\mathrm{LN}_{o'}}\right). \quad (2.38)$$

Substituting the derived expressions for the cell concentration pre- and post-splenectomy in the liver and lymph nodes compartments one can write N_{TOT} in the form $N_{\mathrm{TOT}} = AC_o$, where

$$A = \sum_{o\notin\{\mathrm{liver}\}} V_o + \sum_{\substack{o\notin\{\mathrm{liver,RA}\\ \mathrm{\&RV,LA\&LV}\}}} \frac{\tilde{V}_o}{\mu_o} + \lambda\left(V_{\mathrm{liver}} + \frac{\tilde{V}_{\mathrm{liver}}}{\mu_{\mathrm{liver}}}\right) + \sum_{\substack{o'\notin\{\mathrm{spleen,RA\&RV,}\\ \mathrm{PC,LA\&LV,liver}\}}} \left(V_{\mathrm{LN}_{o'}} + \frac{\tilde{V}_{\mathrm{LN}_{o'}}}{\mu_{\mathrm{LN}_{o'}}}\right) + V_{\mathrm{LN}_{\mathrm{liver}}} + \sigma\frac{\tilde{V}_{\mathrm{LN}_{\mathrm{liver}}}}{\mu_{\mathrm{LN}_{\mathrm{liver}}}}, \quad (2.39)$$

using, for example, $C_{\mathrm{LN}_o} = C_o$ for all organs including liver, and $\tilde{C}_{\mathrm{LN}_o} = \frac{1}{\mu_{\mathrm{LN}_o}} C_o$ for all organs but the liver, where $\tilde{C}_{\mathrm{LN}_{\mathrm{liver}}} = \frac{\sigma}{\mu_{\mathrm{LN}_{\mathrm{liver}}}} C_o$. With analogous identities and algebra post-splenectomy we have $N^*_{\mathrm{TOT}} = BC^*_o$, where

$$B = \sum_{o\notin\{\mathrm{spleen}\}} V_o + \sum_{\substack{o\notin\{\mathrm{spleen,RA}\\ \mathrm{\&RV,LA\&LV}\}}} \frac{\tilde{V}_o}{\mu_o} + \sum_{\substack{o'\notin\{\mathrm{spleen,RA\&RV,}\\ \mathrm{PC,LA\&LV,liver}\}}} \left(V_{\mathrm{LN}_{o'}} + \frac{\tilde{V}_{\mathrm{LN}_{o'}}}{\mu_{\mathrm{LN}_{o'}}}\right) + V_{\mathrm{LN}_{\mathrm{liver}}} + \sigma^*\frac{\tilde{V}_{\mathrm{LN}_{\mathrm{liver}}}}{\mu_{\mathrm{LN}_{\mathrm{liver}}}}. \quad (2.40)$$

Hence with $N_{\mathrm{TOT}} = N^*_{\mathrm{TOT}}$, we have $AC_o = BC^*_o$ and thus:

$$\kappa = \frac{\sum_{o\notin\{\mathrm{liver}\}} V_o + \sum_{\substack{o\notin\{\mathrm{liver,RA}\\ \mathrm{\&RV,LA\&LV}\}}} \frac{\tilde{V}_o}{\mu_o} + \lambda\left(V_{\mathrm{liver}} + \frac{\tilde{V}_{\mathrm{liver}}}{\mu_{\mathrm{liver}}}\right) + \sum_{\substack{o'\notin\{\mathrm{spleen,RA\&RV,}\\ \mathrm{PC,LA\&LV,liver}\}}} \left(V_{\mathrm{LN}_{o'}} + \frac{\tilde{V}_{\mathrm{LN}_{o'}}}{\mu_{\mathrm{LN}_{o'}}}\right) + V_{\mathrm{LN}_{\mathrm{liver}}} + \sigma\frac{\tilde{V}_{\mathrm{LN}_{\mathrm{liver}}}}{\mu_{\mathrm{LN}_{\mathrm{liver}}}}}{\sum_{o\notin\{\mathrm{spleen}\}} V_o + \sum_{\substack{o\notin\{\mathrm{spleen,RA}\\ \mathrm{\&RV,LA\&LV}\}}} \frac{\tilde{V}_o}{\mu_o} + \sum_{\substack{o'\notin\{\mathrm{spleen,RA\&RV,}\\ \mathrm{PC,LA\&LV,liver}\}}} \left(V_{\mathrm{LN}_{o'}} + \frac{\tilde{V}_{\mathrm{LN}_{o'}}}{\mu_{\mathrm{LN}_{o'}}}\right) + V_{\mathrm{LN}_{\mathrm{liver}}} + \sigma^*\frac{\tilde{V}_{\mathrm{LN}_{\mathrm{liver}}}}{\mu_{\mathrm{LN}_{\mathrm{liver}}}}}. \quad (2.41)$$

Using the derived parameter groupings, two ratios of interest can be constructed: the post- to pre-splenectomy total T-cell localisation to SLT ratio, $N^*_{\mathrm{SLT}}/N_{\mathrm{SLT}}$, and post- to pre-splenectomy net T-cell concentration in SLT ratio, $C^*_{\mathrm{SLT}}/C_{\mathrm{SLT}}$. The total T-cell localisation ratio is taken as a ratio of the total number of cells localising to all lymph nodes

post-splenectomy, N^*_{SLT}:

$$\begin{aligned} N^*_{\text{SLT}} &= \sum_{\substack{o\notin\{\text{spleen,RA\&RV,}\\ \text{PC,LA\&LV}\}}} \left(N^*_{\text{LN}_o} + \tilde{N}^*_{\text{LN}_o}\right) = \sum_{\substack{o\notin\{\text{spleen,RA\&RV,}\\ \text{PC,LA\&LV}\}}} \left(V_{\text{LN}_o} C^*_{\text{LN}_o} + \tilde{V}_{\text{LN}_o} \tilde{C}^*_{\text{LN}_o}\right) \\ &= \sum_{\substack{o\notin\{\text{spleen,RA\&RV,}\\ \text{PC,LA\&LV,liver}\}}} \left(V_{\text{LN}_o} C^*_o + \tilde{V}_{\text{LN}_o} \frac{C^*_o}{\mu_{\text{LN}_o}}\right) + V_{\text{LN}_{\text{liver}}} C^*_o + \tilde{V}_{\text{LN}_{\text{liver}}} \frac{\sigma}{\mu_{\text{LN}_{\text{liver}}}} C^*_o \\ &= \sum_{\substack{o\notin\{\text{spleen,RA\&RV,}\\ \text{PC,LA\&LV, liver}\}}} \left(V_{\text{LN}_o} \kappa C_o + \tilde{V}_{\text{LN}_o} \frac{\kappa C_o}{\mu_{\text{LN}_o}}\right) + V_{\text{LN}_{\text{liver}}} \kappa C_o + \tilde{V}_{\text{LN}_{\text{liver}}} \frac{\kappa\sigma^*}{\mu_{\text{LN}_{\text{liver}}}} C_o, \end{aligned} \tag{2.42}$$

to the total number of T-cells localising to all lymph nodes and the spleen pre-splenectomy,

$$\begin{aligned} N_{\text{SLT}} &= N_{\text{spleen}} + \tilde{N}_{\text{spleen}} + \sum_{\substack{o\notin\{\text{spleen,RA\&RV,}\\ \text{PC,LA\&LV}\}}} \left(N_{\text{LN}_o} + \tilde{N}_{\text{LN}_o}\right) \\ &= V_{\text{spleen}} C_{\text{spleen}} + \tilde{V}_{\text{spleen}} \tilde{C}_{\text{spleen}} + \sum_{\substack{o\notin\{\text{spleen,RA\&RV,}\\ \text{PC,LA\&LV}\}}} \left(V_{\text{LN}_o} C_{\text{LN}_o} + \tilde{V}_{\text{LN}_o} \tilde{C}_{\text{LN}_o}\right) \\ &= V_{\text{spleen}} C_o + \tilde{V}_{\text{spleen}} \frac{C_o}{\mu_{\text{spleen}}} + \sum_{\substack{o\notin\{\text{spleen,RA\&RV,}\\ \text{PC,LA\&LV,liver}\}}} \left(V_{\text{LN}_o} C_o + \tilde{V}_{\text{LN}_o} \frac{C_o}{\mu_{\text{LN}_o}}\right) \\ &\quad + V_{\text{LN}_{\text{liver}}} C_o + \tilde{V}_{\text{LN}_{\text{liver}}} \frac{\sigma C_o}{\mu_{\text{LN}_{\text{liver}}}}. \end{aligned} \tag{2.43}$$

Hence the total SLT T-cell localisation ratio is

$$\frac{N^*_{\text{SLT}}}{N_{\text{SLT}}} = \kappa \frac{\sum_{\substack{o\notin\{\text{spleen,RA\&RV,}\\ \text{PC,LA\&LV,liver}\}}} \left(V_{\text{LN}_o} + \tilde{V}_{\text{LN}_o} \frac{1}{\mu_{\text{LN}_o}}\right) + V_{\text{LN}_{\text{liver}}} + \tilde{V}_{\text{LN}_{\text{liver}}} \frac{\sigma^*}{\mu_{\text{LN}_{\text{liver}}}}}{V_{\text{spleen}} + \tilde{V}_{\text{spleen}} \frac{1}{\mu_{\text{spleen}}} + \sum_{\substack{o\notin\{\text{spleen,RA\&RV,}\\ \text{PC,LA\&LV,liver}\}}} \left(V_{\text{LN}_o} + \tilde{V}_{\text{LN}_o} \frac{1}{\mu_{\text{LN}_o}}\right) + V_{\text{LN}_{\text{liver}}} + \tilde{V}_{\text{LN}_{\text{liver}}} \frac{\sigma}{\mu_{\text{LN}_{\text{liver}}}}}, \tag{2.44}$$

where κ, σ, σ^* are given by Equation (2.41), (2.30), (2.31), respectively. The net SLT T-cell concentration ratio, $C^*_{\text{SLT}}/C_{\text{SLT}}$, can then be defined as the ratio of the total number of T-cells

in SLT per unit volume of SLT post- to pre-splenectomy:

$$\frac{\bar{C}^*_{\text{SLT}}}{\bar{C}_{\text{SLT}}} = \frac{N^*_{\text{SLT}}}{N_{\text{SLT}}} \Bigg/ \frac{\sum_{o\notin\{\text{spleen,RA\&RV,}\atop\text{PC,LA\&LV}\}} \tilde{V}_{\text{LN}_o}}{\tilde{V}_{\text{spleen}} + \sum_{o\notin\{\text{spleen,RA\&RV,}\atop\text{PC,LA\&LV}\}} \tilde{V}_{\text{LN}_o}} \,. \tag{2.45}$$

Assuming identical return parameters for all organ-draining lymph nodes, μ_{LN}, Equations (2.44) and (2.45) can be rewritten in the form used in the global sensitivity analysis eFAST

$$\frac{N^*_{\text{SLT}}}{N_{\text{SLT}}} = \kappa \frac{V_{\text{LN}_{\text{TOT}}} + \frac{1}{\mu_{\text{LN}}}\tilde{V}_{\text{LN}_{\text{TOT}}} \left(1 + (\sigma^* - 1)\frac{\tilde{V}_{\text{liver}}}{\sum_{i\notin\{\text{spleen,PC,}\atop\text{RA\&RV,LA\&LV}\}} \tilde{V}_i}\right)}{V_{\text{spleen}} + \frac{1}{\mu_{\text{spleen}}}\tilde{V}_{\text{spleen}} + V_{\text{LN}_{\text{TOT}}} + \frac{1}{\mu_{\text{LN}}}\tilde{V}_{\text{LN}_{\text{TOT}}} \left(1 + (\sigma - 1)\frac{\tilde{V}_{\text{liver}}}{\sum_{i\notin\{\text{spleen,PC,}\atop\text{RA\&RV,LA\&LV}\}} \tilde{V}_i}\right)}, \tag{2.46}$$

$$\frac{C^*_{\text{SLT}}}{C_{\text{SLT}}} = \frac{N^*_{\text{SLT}}}{N_{\text{SLT}}} \Bigg/ \frac{\tilde{V}_{\text{LN}_{\text{TOT}}}}{\tilde{V}_{\text{LN}_{\text{TOT}}} + \tilde{V}_{\text{spleen}}} \,, \tag{2.47}$$

where $V_{\text{LN}_{\text{TOT}}}$ and $\tilde{V}_{\text{LN}_{\text{TOT}}}$ is the total blood and organ volume of lymph nodes, respectively. The derivation follows in a straightforward manner. For example, note the liver is excluded in the summation in the numerator of Equation (2.44). Reinstating the liver in this summation by adding the liver contribution to the summation and subtracting it from the remaining terms entails this numerator can be written as

$$\begin{aligned} &\sum_{o\notin\{\text{spleen,RA\&RV,}\atop\text{PC,LA\&LV }\}} \left(V_{\text{LN}_o} + \tilde{V}_{\text{LN}_o}\frac{1}{\mu_{\text{LN}}}\right) + (\sigma^* - 1)\frac{\tilde{V}_{\text{LN}_{\text{liver}}}}{\mu_{\text{LN}}} \\ &= V_{\text{LN}_{\text{TOT}}} + \frac{1}{\mu_{\text{LN}}}\tilde{V}_{\text{LN}_{\text{TOT}}} + (\sigma^* - 1)\frac{\tilde{V}_{\text{LN}_{\text{liver}}}}{\mu_{\text{LN}}} \\ &= V_{\text{LN}_{\text{TOT}}} + \frac{1}{\mu_{\text{LN}}}\tilde{V}_{\text{LN}_{\text{TOT}}} + \frac{(\sigma^* - 1)}{\mu_{\text{LN}}}\tilde{V}_{\text{LN}_{\text{TOT}}}\frac{\tilde{V}_{\text{liver}}}{\sum_{i\notin\{\text{spleen,PC,}\atop\text{RA\&RV,LA\&LV}\}} \tilde{V}_i}, \end{aligned} \tag{2.48}$$

where the final line arises by application of the partitioning of Equation (2.14). Furthermore this final line gives the numerator of Equation (2.46) and the equivalence of the denominator

Parameter grouping	Definition
κ	Post- to pre-splenectomy T cell concentration ratio (except the liver and the liver-draining lymph nodes)
$\frac{\kappa}{\lambda}$	Liver post- to pre-splenectomy T cell concentration ratio
$\frac{\sigma^*\kappa}{\sigma}$	Liver-draining lymph nodes post- to pre-splenectomy T cell concentration ratio
λ	Liver pre-splenectomy T cell concentration with respect to other organs
σ	Liver-draining lymph nodes pre-splenectomy T cell concentration with respect to other organs (to within a factor of $\mu_{\mathrm{LN}_{\mathrm{liver}}}$)
σ^*	Liver-draining lymph node post-splenectomy T cell concentration with respect to other organs (to within a factor of $\mu_{\mathrm{LN}_{\mathrm{liver}}}$)
$\frac{N^*_{\mathrm{SLT}}}{N_{\mathrm{SLT}}}$	Total SLT post- to pre-splenectomy T cell localisation ratio
$\frac{C^*_{\mathrm{SLT}}}{C_{\mathrm{SLT}}}$	Net SLT post- to pre-splenectomy T cell concentration ratio

Table 2.3: Summary of the derived post- to pre-splenectomy T cell concentration ratios κ (Equation (2.41)), κ/λ (Equations (2.20) and (2.22)) and $\sigma^*\kappa/\sigma$ (Equation (2.32)); parameter groupings λ (Equation (2.18)), σ (Equation (2.30)) and σ^* (Equation (2.31)); and the post- to pre-splenectomy total T cell localisation ratio, $N^*_{\mathrm{SLT}}/N_{\mathrm{SLT}}$ (Equation (2.44)) and the net T cell concentration ratio in the SLT, $C^*_{\mathrm{SLT}}/C_{\mathrm{SLT}}$ (Equation (2.45)). See Section 2.2.5 for derivation.

in Equations (2.44) and (2.46) follows analogously.

2.2.5.1 In silico splenectomy — simulation

The effect of *in silico* splenectomy on T cell distribution across organs can be evaluated in two ways. Firstly, the ODE system can be solved explicitly for a set of chosen input parameters to compare the resulting pre- and post-splenectomy T cell distribution across all organs. To evaluate the post-splenectomy T cell distribution, *in silico* splenectomy can be simulated by setting the blood flow through the spleen, B_{spleen}, to zero, and adjusting the blood flow values for the remaining organs, according to the expected blood flow scaling (the derivation of blood flow changes post-splenectomy can be found in Appendix A, but is not necessary to follow the remaining text).

Alternatively, the steady-state model reduction (Section 2.2.5) can be utilised to evaluate the post- to pre-splenectomy cell concentration ratios, κ, κ/λ and $\sigma^*\kappa/\sigma$, which also accommodates blood flow changes, as well as considering the parameter groupings, λ, σ and σ^*. We present the analytically derived distributions in Section 2.2.5 to highlight the advantage of model reduction given the prohibitively high dimensionality of PBPK models.

The post- to pre-splenectomy cell concentration ratios, κ, κ/λ and $\sigma^*\kappa/\sigma$, and the parameter groupings, λ, σ and σ^*, were computed varying the input parameters B_o, V_o, $\tilde{V}_o$, e_o, μ_o for each organ, and $B_{\mathrm{LN}_{\mathrm{TOT}}}$, $V_{\mathrm{LN}_{\mathrm{TOT}}}$, $\tilde{V}_{\mathrm{LN}_{\mathrm{TOT}}}$, e_{LN_o}, μ_{LN_o} for lymph node compartments.

Variability ranges for the anatomical parameters (B_o, V_o, $\tilde{V}_o$, $B_{\mathrm{LN}_{\mathrm{TOT}}}$, $V_{\mathrm{LN}_{\mathrm{TOT}}}$, $\tilde{V}_{\mathrm{LN}_{\mathrm{TOT}}}$) were defined as described in Section 2.2.3, while extravasation and return parameters (e_o, μ_o, e_{LN_o}, μ_{LN_o}) were varied uniformly between 0 and 1. Extravasation, e_{LN_o}, and return parameters, μ_{LN_o}, were assumed identical across all lymph node compartments for each parameter sampling iteration. Results with no restrictions on those parameters did not differ significantly, and are, therefore, not presented. This parameter space was sampled 1,000,000 times by randomly sampling each input parameter value from a uniform probability distribution, defined by those variability ranges. For each iteration, the post- to pre-splenectomy cell concentration ratios, κ, κ/λ and $\sigma^*\kappa/\sigma$, and the parameter groupings, λ, σ and σ^*, were calculated based on the randomly sampled parameter set. Means and 95% confidence intervals were computed for each resulting distribution.

To ensure convergence, all ratios and parameter groupings were evaluated for different numbers of sampling points in the parameter space, starting from 1,000, and increasing the number of sample points by a factor of 10. All ratios and parameter grouping exhibited convergence in their means and confidence intervals for 1,000,000 sampling points. While this number is relatively small compared to the number of model parameters, the convergence stems from diminished sensitivity due to the structure of the considered functions (see Equation (2.44) as an example), and the number of parameter samples is thus observed to be sufficient.

2.2.5.2 Global sensitivity analysis

A global sensitivity analysis was performed on the post- to pre-splenectomy total T cell localisation ratio (Equation (2.46)) and the post- to pre-splenectomy net T cell concentration ratio (Equation (2.47)), to identify the most influential parameters. A variance-based method, extended Fourier amplitude sensitivity testing (eFAST), was implemented using the Matlab code developed and made available online by Kirschner Lab, University of Michigan [66].

Due to eFAST scaling constraints with respect to the number of parameters, simply sampling from all parameters in the model is far from feasible; instead we take advantage of the fact the ratios of interest in Equations (2.46) and (2.47) can be written in terms of the lumped parameters κ, σ and σ^* together with a relatively small number of other parameters to be varied: the spleen return parameter μ_{spleen}, the spleen organ and blood volumes, the total lymph node volume and lymph node blood volume and the liver organ volume. As previously, the lymph node return rates for each organ, μ_{LN_o}, were assumed identical across all lymph node compartments, as was the sum of lymph node draining organ volumes.

The sensitivity analysis is thus considered with a sampling of the lumped parameters, κ, σ, σ^*, from their distributions in Figure 2.5(a), cut off at the 95% confidence interval, together with the other parameters to be varied sampled uniformly, as detailed in Section 2.2.3 and Table 2.2. However, the eFAST algorithm is designed for uniform sampling, in contrast to the distribution of the lumped parameters κ, σ and σ^*. Thus for example, we uniformly sampled $\kappa_U := f(\kappa)$, within eFAST rather than κ, where the continuous bijection $f(\cdot)$ is defined uniquely by the constraint that when κ_U is uniform then κ is distributed as in Figure 2.5(a). Then by applying the function inverse f^{-1} to the the precursor, κ_U, where κ is generated according to its distribution in Figure 2.5(a), with analogous procedures for the lumped parameters σ, σ^*. In particular parameter value sets for the uniform precursors of the lumped parameters κ, σ, σ^* and the other parameters of interest in Equations (2.46) and (2.47) were generated using Fourier frequency curves through the variability ranges. Each of these parameters was sampled $N_S = 1920$ times with a frequency of $\omega_i = 49$ from a uniform probability distribution [12]. Due to the symmetry properties of trigonometric functions, the sampling sinusoidal function eventually repeats the same samples. To avoid this, the sampling algorithm was repeated $N_R = 5$ times [12]. The resampling produced 5 different search curves, specified by introducing a random phase shift into each sinusoidal function.

By assigning a unique frequency to each input parameter, the eFAST algorithm calculates the unique contribution of each parameter in determining the model output. The analysis yields two indices for each parameter: (i) a first-order sensitivity index, S_i, representing the proportion of an output's variance that is due only to a given parameter (first-order contributions), and (ii) total-order sensitivity index, S_{Ti}, calculated from the proportion of an output's variance due to all parameters except the one in question (higher-order contributions). The difference between the total-order and the first-order sensitivity indices gives a measure of the impact of the interactions between the parameters.

The eFAST method artificially produces small but non-zero sensitivity indices for parameters which the model is completely independent of, due to aliasing and interference effects, as well as assumptions used to calculate total-order sensitivity indices [11]. A dummy parameter with an arbitrary value range was considered to provide a baseline for statistical comparison, as proposed by Marino et al. [11]. Thus, a total-order sensitivity index less than or equal to that of the dummy parameter is, therefore, not considered substantially different from zero.

The resampling of search curves, which is originally used for more efficient parameter sampling, produces different combinations of parameter values for each curve, and, hence, slightly different sensitivity measures S_i and S_{Ti}. The repeated measures were used to perform a two-sample t-test to compare the sensitivity indices of each parameter with the corresponding indices assigned to the dummy parameter [11]. The t-test method assigns a p-value to each

sensitivity index, which provides an additional way to determine whether the index is significantly different from the index calculated from the dummy parameter, and, thus, whether there is sensitivity to the parameter.

Finally, we note a caveat with this procedure: the lumped parameters σ and σ^* depend on μ_{spleen}, but σ, σ^* and μ_{spleen} are varied independently during the sensitivity analysis. However, σ and σ^* depend on μ_{spleen} very weakly with an error on the scale of the reciprocal of the number of organs as μ_{spleen} only occurs in additive combination of a summation over the organs. Hence the impact of not accommodating this correlation in the sampling is also weak. An analogous caveat applies for κ and its dependence on parameters that are also varied in the sensitivity analysis. That this is a weak effect is not immediately observed *a priori*, as with σ and σ^*, but it can be confirmed *a posteriori* as we briefly consider in the presentation of results.

2.3 Results

The immune cell trafficking model was used to examine predicted distributions of T cells across different SLT compartments — lymph nodes and the spleen. Since the spleen comprises a major part of the SLT, we sought to investigate how splenectomy affects the T cell distribution in other organs, particularly, the lymph nodes.

2.3.1 Post- and pre-splenectomy comparisons

The response of the system to splenectomy can be qualitatively and quantitatively analysed by considering a reduced framework. Despite the high complexity of the trafficking model (101 parameters), the steady-state model reduction demonstrated that post- to pre-splenectomy cell concentration ratios across all organ compartments can be described by four parameter lumpings. It further showed that, upon the removal of the spleen, all but two organ compartments result in the same relative change in the steady-state T cell concentration. The exceptions were the liver and liver- draining lymph node compartments, where a lower relative increase in cell concentration is expected, due to the fact that all T cells exiting the spleen flow directly to the liver.

The expected post- to pre-splenectomy cell concentration ratios were expressed as functions of the model input parameters and the distributions of the computed ratios and parameter groupings were plotted as histograms in Figure 2.5(a). The obtained post- to pre-splenectomy

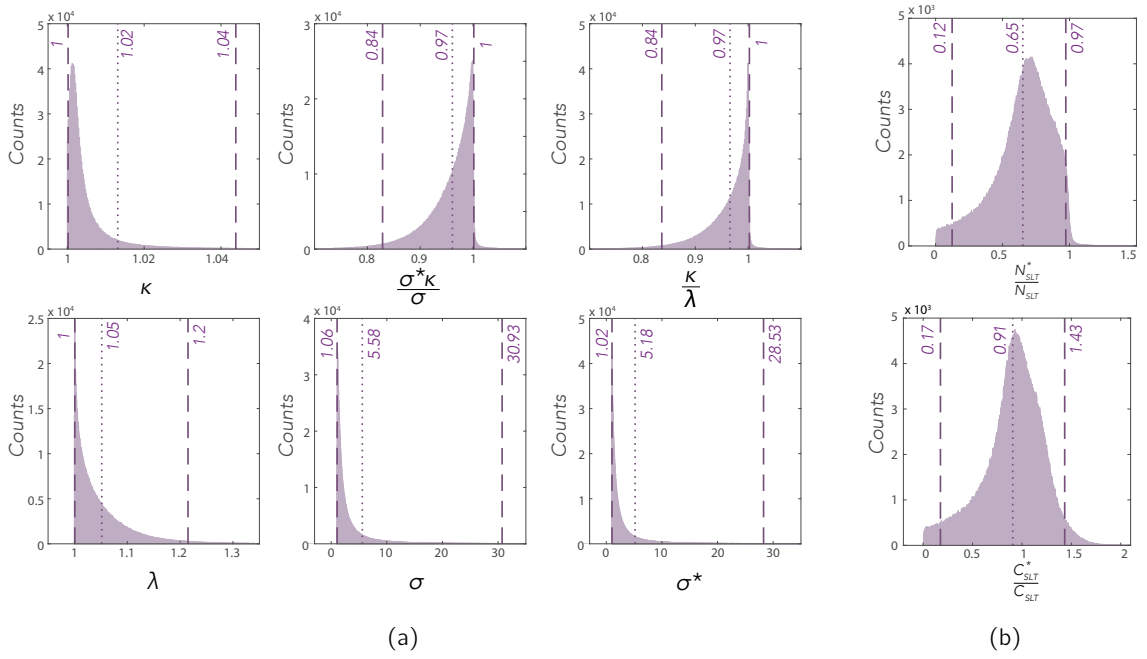


Figure 2.5: Distributions of (a) post- to pre-splenectomy cell concentration ratios: κ, $\sigma^*\kappa/\sigma$ and κ/λ, as well as the parameter groupings: λ, σ and σ^*; and (b) the post- to pre-splenectomy total T cell localisation ratio and the net T cell concentration ratio in the SLT. Dotted and dashed lines correspond to means and 95% confidence intervals of the plotted distributions. See Table 2.3 for definitions of the cell concentration ratios and the parameter groupings.

T cell concentration ratios were characterised by relatively narrow distributions. This was quantitatively illustrated by the 95% confidence intervals (Figure 2.5(a)) and demonstrates that the simulated relative change in T cell exposure post-splenectomy in different tissues can be estimated despite the unknown tissue-specific entry and exit rates, as well as the large interpersonal and temporal variability in the physiological parameters. For instance, the volume of muscle mass can vary significantly between individuals (muscle mass can reach 65.1% of body mass in athletes and bodybuilders [59]), and blood flow to muscles and blood volume in the tissue increases significantly during exercise (the total blood flow can reach 30-35 L/min in elite endurance athletes [62], roughly 6 times higher than the baseline [30]). Yet the relative change in T cell exposure post-splenectomy in the majority of organ and organ-draining lymph node compartments, κ, resulted in the mean of 1.02 and 95% confidence interval of $1-1.04$. The predicted T cell exposure ratio was more broadly distributed for the two remaining compartments, the liver (κ/λ) and liver-draining lymph node compartments ($\sigma^*\kappa/\sigma$), both with the means of 0.97 and 95% confidence intervals of $0.84-1$.

The negligibly low mean relative increase of T cell exposure, κ, suggests little to no change in the lymph node cellular capacity post-splenectomy to account for the loss of the spleen. The post- to pre-splenectomy total cell localisation in SLT was evaluated as a ratio of the

total number of T cells localising to all lymph node compartments post-splenectomy to the total number of cells localising to both the spleen and all lymph node compartments pre-splenectomy (Equation (2.44)). Since a quantity of concentration is often used in the clinic, a similar ratio of net T cell concentration in SLT was evaluated (Equation (2.45)). However, as concentrations are not additive, the net T cell concentration in SLTs pre-splenectomy (post-splenectomy) has been defined as the number of T cells localising to all lymph node compartments and the spleen (all lymph node compartments) per unit volume of secondary lymphoid tissue: lymph nodes and the spleen (lymph nodes). As a result, a ratio defined in this manner can be interpreted as a relative change in the number of T cells per unit mass of SLT.

2.3.2 Cell localisation and concentration ratios before and after splenectomy

The localisation and concentration ratio distributions were plotted as histograms in Figure 2.5(b). *In silico* splenectomy resulted in an average post- to pre-splenectomy total T cell localisation ratio of 0.65 (95%CI: $0.12 - 0.97$), indicating a statistically significant 35% reduction in T cells localising to SLT post-splenectomy. The distribution has been characterised by a wide 95% confidence interval compared to the standard T cell concentration ratio, such as κ (see Figure 2.5(a)). The corresponding distribution of the net SLT T cell concentration ratio was characterised by a mean of 0.91, with a confidence interval of $0.17 - 1.43$. Contrasting the results of localisation ratio with the concentration ratio shows that, although, on average, the net concentration in SLT is reduced, the resulting relative concentration decrease is not statistically significant. Consequently, the analysis showed a considerable difference in the T cell localisation but no substantial difference in the net concentration post-splenectomy.

2.3.2.1 Sensitivity of cell localisation and concentration ratios pre- and post- splenectomy

A variance-based global sensitivity analysis, eFAST, was performed to identify the parameters driving the wide distributions of the post- to pre-splenectomy total T cell localisation ratio (Equation (2.44)) and the post- to pre-splenectomy net T cell concentration ratio (Equation (2.45)) (Figure 2.6). Both the post- to pre-splenectomy total T cell localisation ratio and the post- to pre-splenectomy net T cell concentration ratio were primarily dependent on the return parameters of the spleen and lymph nodes, μ_{spleen} and μ_{LN} (varied separately). The strong sensitivity of the localisation and concentration ratios to the return parameters, μ_{spleen} and μ_{LN}, stems from the definition of these parameters, which determine the rate at which T

cells leave the associated interstitial compartments (see Equation (2.2)). As such, the return parameters, μ_{spleen} and μ_{LN}, are the primary parameters affecting the accumulation of T cells in steady state in SLT compartments and, thus, the resulting relative T cell concentration SLT following the redistribution of T cells from the spleen. The eFAST analysis also indicated slight sensitivity to the parameter groupings σ and σ^*, which, to within a factor of $\mu_{\text{LN}_{\text{liver}}}$, define the steady-state T cell concentration in liver-draining lymph nodes relative to the steady-state vasculature concentration (equal for all organs except the liver) pre- and post-splenectomy, respectively. Although small, the statistically significant sensitivity indices associated with the parameter groupings σ and σ^* highlight the relevance of the specific anatomical structure of hepatic circulation in lymphocyte trafficking modelling. As a whole, both the localisation and net concentration ratio yielded consistent and comparable sensitivity indices, with the net concentration ratio being moderately less sensitive to the spleen and total lymph nodes volumes, as expected from the ratio of Equations 2.44 and 2.45.

Finally, as mentioned in Section 2.2.5.2, the dependence of the parameter grouping κ on the other sampled parameters has been neglected. However, this neglect serves to increase the variation of κ (*e.g.*, fixing a parameter within κ reduces, or at least does not increase, the range it can acquire compared to the distribution in Figure 2.5(a), where the same parameter was free to vary in its sampling). However even with an artifact of increased variation the sensitivity scores of κ in Figure 2.6 are small compared to the scores of the more sensitive parameters and do not exceed those associated with the dummy parameter. Thus the results show that the impact of the parameter grouping κ is below the level of meaningful classification in this sensitivity analysis regardless of the above-mentioned caveat in its sampling.

2.4 Discussion

Recent cohort study data reporting a marked increase in the haematological malignancies risk in splenectomised subjects [47, 48], suggests that splenectomy leads to a loss of effective immunosurveillance of blood-borne malignant cells, as the remaining secondary lymphoid tissue has been predicted to not have the sufficient capacity to compensate. Given the natural trafficking pattern of T cells to the spleen and lymph nodes, the primary aim of this chapter has been to examine how splenectomy affects T cell distribution across secondary lymphoid tissue in human.

Using a PBPK modelling approach, we adopted a previously developed immune cell trafficking framework [52], refined and specialised to predict T cell biodistribution in the presence and absence of the spleen. The effect of *in silico* splenectomy on lymph node tissue exposure

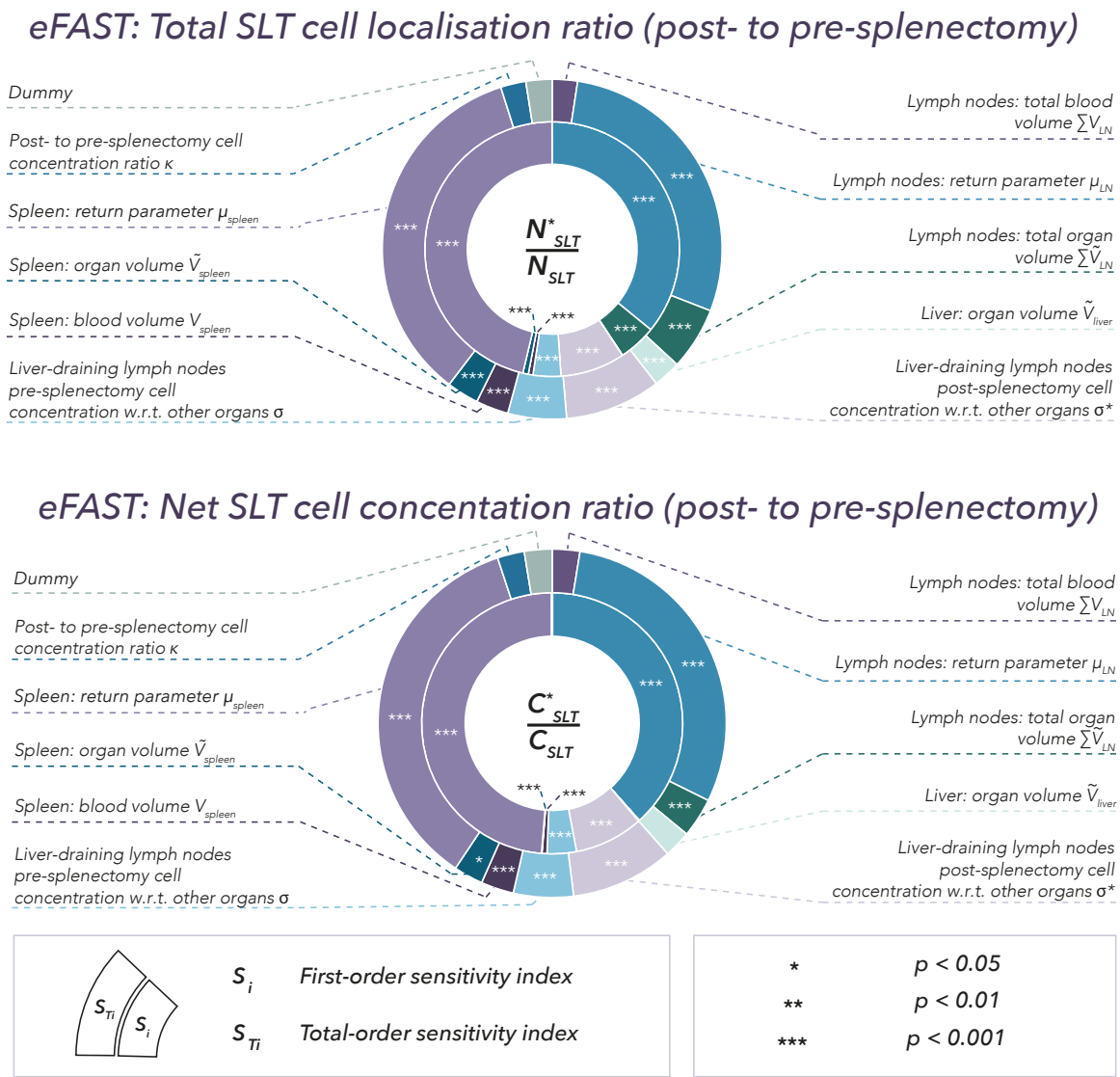


Figure 2.6: Results of the global sensitivity analysis eFAST on the post- to pre-splenectomy total T cell localisation to SLT ratio (upper) and the post- to pre-splenectomy net T cell concentration in SLT ratio (lower). The inner (outer) ring indicates the proportional size of individual sensitivity indices (total sensitivity indices). A dummy parameter is used as a baseline for statistical comparison and a p-value was assigned to each sensitivity index using a two-sample t-test [11]. Parameters with statistically significant sensitivity indices were labelled according to the assigned p-value (*,**,***). The eFAST sensitivity analysis considered with a sampling of the parameter groupings κ, σ, σ^* from their distributions in Figure 2.5(a), cut off at the 95% confidence interval, together with the other parameters to be sampled uniformly, as detailed in Section 2.2.5.2, with further details on parameter distributions in Sections 2.2.3 and 2.2.5.1.

was investigated to estimate to what extent the remaining secondary lymphoid tissue has the potential capacity to compensate for the loss of immune functionality, normally mediated by the spleen. By utilising the model's structure, we analytically derived post- to pre-splenectomy cell concentration ratios and simulated them across the parameter space. The variability in the input parameters was carefully considered to account for possible values of entry and exit rates of T cells across all tissues, as well as interpersonal and temporal differences in anatomical and physiological characteristics.

2.4.1 In silico splenectomy results in significant reduction in the number of T cells localising to SLT

The resulting simulations of the relative changes in the organ T cell concentration were characterised by narrow distributions, despite large variability in the input parameters. All tissues and tissue-specific groups of lymph nodes, except the liver and the liver-draining lymph nodes, exhibited an equal post- to pre-splenectomy cell exposure, κ, with a mean of 1.02 (95%CI: 1 – 1.04). Since the mean relative increase in lymph node cell exposure was negligibly low, the post- to pre-splenectomy total T cell localisation and net T cell concentration in secondary lymphoid tissue were also evaluated. Given the uniform sampling across parameter space, the net concentration of T cells in secondary lymphoid tissue had a mean of 91% in asplenic patients compared to normal patients (0.91, 95%CI: 0.17 — 1.43) and the net localisation of T cells in secondary lymphoid tissue was reduced by 35% (0.65, 95%CI: 0.12 — 0.97). This indicates that, while *in silico* splenectomy produces a minimal change in the secondary lymphoid tissue exposure (concentration), it significantly reduces the total number of T cells localising to secondary lymphoid tissue and, thus, possible activation events. In turn, this suggests that remaining lymph nodes do not have sufficient trafficking thoroughfare to compensate for lost T cell traffic within the spleen, even before detailed functional differences in the spleen and lymph nodes are considered. These results appear to corroborate the clinical data that asplenic patients may be more susceptible to haematological malignancies or do worse with the conditions than patients with full spleen function [47, 48]. The results further highlight that compensatory pathways to mitigate the loss of the spleen are unlikely.

2.4.2 Remarks on model complexity

As with all models, the immune cell trafficking model was constructed based on certain assumptions, which impose limitations on the interpretation of results. Firstly, the model treats

lymph node tissue as 18 separate organ-specific groups of lymph nodes, and each group is represented as a lumped compartment. In reality, lymph nodes are widely present throughout the human body and often arranged in chains, which can drain more than one organ (particularly in mesentery). Secondly, lymph nodes were partitioned into groups across the body based on the volume of the organ they drain from. The data on lymph node whole-body distribution and lymphatic drainage pathways is limited, largely relying on 19th-century cadaver studies [67], which have been reported to contrast with some recent clinical data [26]. Further data on the lymphatic system anatomy is needed, but the current state of knowledge suggests that both the size and number of lymph nodes increases with the body mass between different species [68]. The assumption that the number of lymph nodes, and consequently the total volume of lymph nodes, will scale with organ volume has therefore been chosen as a parsimonious working approximation. To the best of our knowledge, no previously published PBPK model of immune cell trafficking contained more than three lymph node compartments [69, 70]. Integrating organ-specificity into a framework provides a more physiologically accurate description, albeit still being a significant simplification of the anatomy of the lymphatic system. We will consider whether such complexity is necessary to accurately depict T cell dynamics in Chapter 3.

Although the impact of splenectomy on T cell distribution could, in theory, be modelled with a smaller, though reasonable, trafficking framework, the use of a large mathematical model, as presented here, does in fact offer several advantages, given it dramatically simplifies. The complexity of the model affords the possibility of examining the research question without *a priori* simplifying components of the model, which might be necessary for understanding the mechanism of splenectomy but would not otherwise be captured using a simpler framework, for instance, the anatomy of the hepatic circulation. The steady-state model reduction approach additionally provides structural and biological insight that is not feasible from numerical simulations only. Noting the reduction in the size of the parameter space on model simplification, with the concomitant removal of the curse of dimensionality, the computational advantage is substantial. For example, it renders a global sensitivity analysis feasible and allows a verification that sufficient sampling of the parameter space has been performed, in turn enabling a comprehensive survey of the prospective features that may, or may not, have an impact on the T cell redistribution post-splenectomy, while fully accommodating physiological features such as the hepatic circulation.

2.4.3 Comparison to previous work

The impact of splenectomy on T cell trafficking has so far been addressed experimentally across different species (mice [53], rats [71], sheep [72], pigs [73]) and across different time periods of observation. Experimental and theoretical distribution profiles of primed T cells from five tissues in tumour-bearing non-splenectomised and splenectomised mice suggested a compartmental shift in lymphocyte distribution following splenectomy [53]. Similarly to our model's predictions, the retention of transferred cells in the liver was greater in non-splenectomised mice compared to splenectomised animals [53].

Despite the relatively high retention of cells within the spleen, splenectomy had a negligible effect on tumour lymphocyte recruitment [53]. Another short timescale experiment, with splenectomised pigs, showed that labelled lymphocytes exit the peripheral blood at much slower rate than in non-splenectomised animals [73]. The data collected from isolated perfused pig spleen demonstrated that lymphocytes recirculate through the spleen at a rapid rate of up to 270×10^9 lymphocytes per day in living pigs [73], highlighting the role of the spleen for recirculating T cells.

However, a shorter time period between splenectomy and data collection may highlight many transient effects, including trauma, which we are not accommodating, and we similarly do not directly consider the presence of a tumour in this study. Hence, we only consider how the overall framework and quantitative predictions compare with relatively longer experiments. One instance is a study of rats, with a follow-up of 15 months after the removal of the spleen. While there was a differential effect on different subsets of T cells, the overall numbers of T cells were comparable in splenectomised and control group of animals [71]. Similarly, a study on two-year-old neaonatally-splenectomised sheep did not identify significant changes in the blood profile [72]. These results appear in agreement with the qualitative features of the model's predictions across parameter space in that the relative predicted increase of T cells within the vasculature compartments is very modest and may not be resolvable in practice. While consistent, these qualitative comparisons of model prediction and observation need to be interpreted with suitable caution, particularly in the light of difficulties with interspecies translation and the question of whether the number of T cells in the blood reflects the whole pool of recirculating T cells. Furthermore, while, to the best of our knowledge, no clinical or preclinical data has been published suggesting a potential long-term compensatory mechanism affecting T cell numbers or trafficking dynamics post-splenectomy, such a mechanism cannot be ruled out.

2.4.4 Concluding remarks

The spleen plays an important role in the generation of adaptive immune responses, but the impact of splenectomy on immunocompetence has not been fully understood yet. The predicted lack of significant relative difference in the T cell concentration in secondary lymphoid tissue upon virtual removal of the spleen predicts an insufficient cellular and trafficking capacity of the tissue to compensate for immune functions normally mediated by the spleen. The implied deficit is particularly noteworthy given the clinical data suggesting that asplenic patients are at higher risk of incidence and mortality of haematological malignancies [47, 48]. Although the direct link between splenectomy and cancer is yet to be established, detailed statistical analyses of the clinical data revealed that the risk of malignancies remained significantly elevated in analyses limited to trauma patients as well as those excluding patients with an autoimmune disease prior to splenectomy [47].

The mechanisms for splenectomy increasing the risk of many haematological malignancies over solid tumours [47, 48] are not scientifically demonstrated. The physiological characteristics of the spleen may make the organ a more suitable site for the detection of malignant cells persisting in the bloodstream, as would be the case for haematological malignancies. The relatively higher perfusion of the spleen ($0.87\,\mathrm{min}^{-1}$ [52]) compared to lymph nodes ($0.41\,\mathrm{min}^{-1}$ [52]) also contributes to the noticeably higher estimated maximal cell delivery rate to the spleen ($27.9\,\mathrm{cells\,min}^{-1}\,\mathrm{mm}^{-3}$ [52]) in comparison to lymph nodes ($13\ \ \mathrm{cells\,min}^{-1}\,\mathrm{mm}^{-3}$ [52]), and thus enhanced immunosurveillance with a spleen. The physiological and anatomical differences between the SLT components underlie the predicted reduction in the mean number of T cells localising in the SLT in the absence of the spleen. Differences in spleen versus lymph node lymphocyte activation may additionally play a more crucial role in the context of specific disease pathophysiologies or processes, such as the recognition and clearance of blood-borne leukaemic or metastatic cells from the blood compartment, as opposed to abnormal cells comprising solid tumours. In the absence of further clinical data, however, PBPK models can serve as a guide to determining the likely effect of changing the physiological status of the body on the trafficking of not only T cells, but also other types of cells, such as B, NK cells, and cellular therapies. Such cell-kinetic modelling frameworks, in turn, allow the simulation of clinical scenarios of interest and quantifying the relative exposure of therapy to the spleen, lymph nodes or a tumour, which may lead to further insight into the improved design of immunotherapies, while highlighting the potential impact of confounding factors, such as the case of splenectomy studied here.

Chapter 3

Compartmentalisation of lymph nodes in PBPK modelling

The model structure comprises one of the fundamental assumptions in physiologically-based pharmacokinetic (PBPK) modelling. Chapter 2 showcased an application of the T cell trafficking PBPK model which integrated organ-specific lymph node compartmentalisation. A question that is natural to ask is: *is such detailed lymph node compartmentalisation necessary?* While in Chapter 2 the complexity of the model aided structural and biological insight without the necessity of imposing any *a priori* assumptions, in the context of data fitting, for instance, such complexity would generally be prohibitive. For this reason, PBPK models with a single (lumped) lymph node compartment remain a standard tool in the preclinical and clinical stages of drug development. However, modelling applications concerning specific subsets of lymph nodes are particularly hard to represent a single lymph node compartment framework. More specifically, a more detailed description of lymph nodes may be required to model the subcutaneous administration route of any type of therapy. In this chapter, we, therefore, examine what constitutes a reasonable choice of lymph node compartmentalisation and how such a choice affects the model predictions and, thus, its application.

3.1 Introduction

Over the past decade, physiologically-based pharmacokinetic (PBPK) modelling has become an integral part of the drug discovery and development process. The potential of PBPK simu-

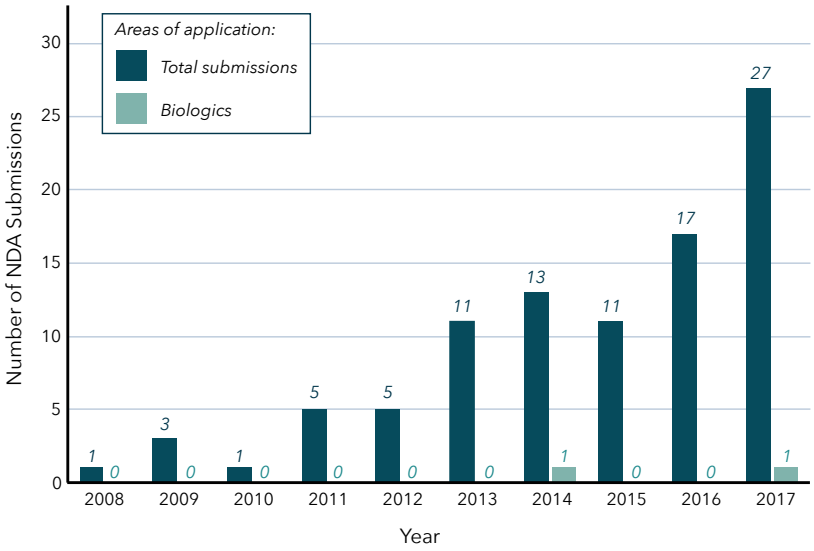


Figure 3.1: Number of New Drug Application (NDA) submissions per year containing PBPK analyses in the period of 2008 to 2017, with the number of NDA submissions with PBPK analyses applied to biologics presented separately. Data from Grimstein et al. [78]

lations to streamline clinical development has been acknowledged by the regulatory authorities, the U.S. Food and Drug Administration (FDA) and the European Medicines Agency (EMA), in a series of guidelines on using PBPK modelling in the development of an investigational drug [74, 75, 76, 77]. The published guidelines require the drug manufacturer to submit a PBPK report for the regulatory bodies to assess the predictive performance of the framework used in the development of the drug. While those guidelines do not address methodological considerations and best practices for conducting PBPK modelling and simulations, the manufacturer is expected to provide a description of key model assumptions that may impact the model's application [74]. Those assumptions include biological and/or pharmacological rationale, patient- or disease-related assumptions, and mathematical representations of the biological systems. Such a report is further required to discuss the validity of model assumptions, the plausibility of input parameter values, and uncertainty around the model prediction.

The number of New Drug Application (NDA) submissions to the FDA that included PBPK analyses has continued to grow significantly over the past years [78]. However, only two submissions supported with PBPK modelling were reported in application to biologics between 2008 and 2017 (see Figure 3.1) [78]. Given the recent progress in the development of immune cell-based therapies, the statistic highlights the potential of further integrating PBPK modelling into the clinical development within those areas.

Examples of applications of PBPK modelling existing in the literature, including CAR T cells [52, 79], adoptively transferred cells [53, 69, 80] and bifunctional antibodies [81], demonstrate the versatility of the physiologically-based modelling approach beyond small-molecule

Study	Application	Model lymph node description
Zhu et al. (1996) [80]	Modelling biodistribution of adoptively transferred cells in rodents.	A lumped whole-body peripheral lymph node compartment.
Friedrich et al. (2002) [81]	Modelling distribution of bifunctional antibodies in tumour-bearing mice.	A lumped whole-body peripheral lymph node compartment.
Melder et al. (2002) [53]	Modelling distribution of adoptively transferred effector lymphocytes in normal, tumour-bearing, and tumour bearing and splenectomised mice.	A lumped whole-body peripheral lymph node compartment.
Ganusov and Auerbach (2014) [70]	Modelling the dynamics of thoracic duct lymphocytes recirculation by estimating lymphocyte migration rates and residence times within major tissues in mice.	Lymph nodes represented as two compartments: mesenteric and subcutaneous lymph nodes; Different numbers of subcompartments in lymph nodes were considered.
Khot et al. (2019) [69]	Modelling the pharmacokinetics of exogenously administered T cells in tumour-bearing mice.	Lymph nodes represented as three compartments: a tumour-draining lymph node, a non-tumour draining lymph node, and the remaining lymph nodes as a single, lumped compartment.
Singh et al. (2020) [79]	An integration of PBPK and PD models to characterise expansion of CAR T cells and tumour inhibition in xenograft mouse model.	A lumped whole-body peripheral lymph node compartment.
Brown et al. (2021) [52]	Quantification of the maximum delivery rates of CAR T cells across organs and species.	A lumped whole-body peripheral lymph node compartment, with vascular and interstitial subcompartments.

Table 3.1: Summary of PBPK modelling approaches utilised in the lymphocyte trafficking research area and the number of compartments used to describe the lymph node tissue within frameworks.

drugs. The same nature of PBPK models that grants their wide applicability can also at times be a source of difficulties, however, particularly when integrating experimental data into the modelling process. As PBPK models tend to depict whole-body physiology and are sometimes further combined with tissue-level PK-PD submodels [79], they usually contain a large number of parameters. Since fitting a PBPK model to measured time-concentration profiles is a fundamental step in most modelling applications, the high dimensionality of a model, both in absolute terms and relative to the data available, may give rise to issues with model identifiability and parameter estimation. Many parameter fitting techniques are not able to manage the high dimensionality of PBPK systems and, even when the process is in theory tractable, unidentifiable parameters can lead to problems with numerical procedures in parameter estimation. The character of real-life data (noisy, sparse, non-longitudinal) further affects the quality of data fitting and the inability to draw conclusions from the model output and estimated parameters becomes an issue for modelling applications where the biological meaning of parameters is of importance.

The aforementioned difficulties associated with the complexity of PBPK models, as a result,

render the prospect of having a model with a simplified structure highly valuable. A single (lumped) lymph node compartment model has remained the established standard for PBPK modelling in preclinical and clinical pharmacology. Although most of the published PBPK models assume a single lymph node compartment model structure to quantify experimental data [52, 53, 79, 80, 81], examples of a more detailed lymph node compartmentalisation can also be found in literature [69, 70] (see Table 3.1). While the choice of the single lymph node compartment representation is motivated by the reduction of uncertainty in the physiological parameters and overall complexity of a model, it is not physiologically realistic. Additionally, indications affecting specific groups of lymph nodes, such as lymphomas, or applications with a focus on single lymph nodes, for instance, tumour-draining lymph nodes, are particularly hard to represent in a single lymph node compartment framework. Furthermore, it is unclear whether single lymph node models are sufficient for clinical applications where the efficacy of therapy relies on immune cell activation, and, thus, where understanding the immune cell kinetics and dynamics is crucial to controlling both the safety and efficacy of the therapy, in question.

The choice of lymph node tissue compartmentalisation in a PBPK model comprises one of the primary assumptions, as it can drastically affect the complexity of the resulting model. While model simplifications generally aid the application of mathematical and modelling techniques, the potential implications of such simplifications on the model output should be examined critically. In this study, we consider if and to what extent the choice of lymph node tissue compartmentalisation in a PBPK model impacts the model's predictions in the context of recirculating immune cells and cell-based therapies. Utilising two previously published frameworks with opposing descriptions of lymph node compartments, a single lymph node T cell trafficking model developed by Brown et al. [52] and its extended version, with multiple, organ-specific lymph node compartments, introduced in Chapter 2, we will analyse the difference in the predicted biodistributions of modelled cells between the two models. By considering a mapping between the steady-state biodistributions predicted by the models, we will derive a framework that allows direct comparison of the two models without the necessity to develop the more complex lymph node model explicitly. We will further investigate whether models with a lumped lymph node compartment can still serve as useful tools when specific lymph node groups are of interest. Sensitivity analyses will be used to identify the most influential parameters in the derived mapping framework, and we will examine when the framework can be used in place of a many-compartment lymph node model. As such, we hope the study provides a better contextual understanding of what constitutes a reasonable choice of lymph node compartmentalisation and how such a choice affects the model application.

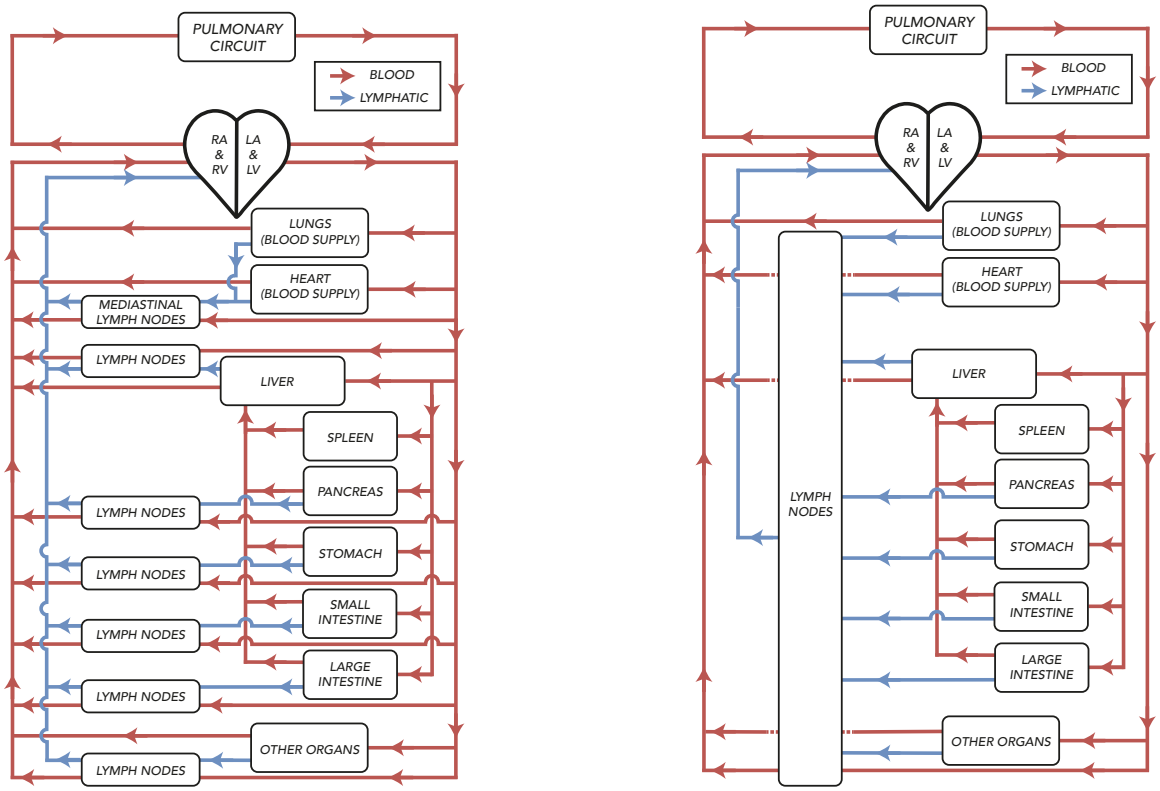


Figure 3.2: Model schematics of (a) the multiple and (b) the single lymph node trafficking models. Cells flow from the left atrium and left ventricle of the heart to each organ (red lines), via lymphatics (blue lines) into (a) organ-draining or (b) single lymph node compartments and return back to the right atrium and right ventricle of the heart. Each box represents a vasculature and interstitium compartment. Chambers of the heart: *RA* - right atrium, *RV* - right ventricle, *LA* - left atrium, *LV* - left ventricle. *Other organs* compartments include: adrenals, bladder, brain, adipose tissue, gonads, kidneys, skeletal muscles, skeleton, skin and thyroid.

3.2 Methods

3.2.1 Single and multiple lymph node trafficking model comparison

The single and multiple lymph node models, shown in Figure 3.2, represent two versions of a T cell trafficking model, with two counter descriptions of lymph nodes. The single lymph node model (Figure 3.2(b)), as the name implies, depicts lymph nodes as a single lumped compartment with a collective inflow of T cells from all organs drained by lymphatics. In contrast, the multiple lymph node model (Figure 3.2(a)), compartmentalises the lymph node tissue into organ-specific groups of lymph nodes, analogously to its anatomical description. Accordingly, two systems of ordinary differential equations (ODEs) represent the exchange of any population of recirculating cells between the heart and organs, originally applied in the context of T cell immunotherapies [52] and T cell trafficking [1].

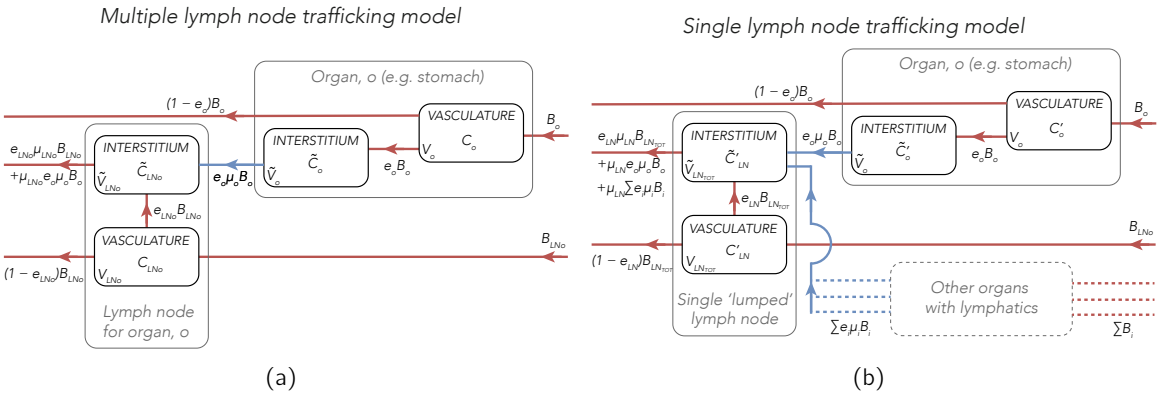


Figure 3.3: Organs and lymph nodes are represented in (a) the multiple and (b) the single lymph node trafficking model as separate vascular and interstitial compartments. Cells flow from the cardiac output compartment (previously defined as left atrium, left ventricle, aorta and large arteries) to each organ, o, with a blood flow B_o, from which a proportion, $e_o B_o$, enters the interstitial space per unit time. A proportion of cells, $e_o \mu_o B_o$, flows via lymphatics from the interstitial subcompartment of organ, o, into (a) the draining lymph nodes and (b) the single lymph node per unit time. Cells also enter (a) organ, o, -draining lymph nodes and (b) the single lymph node through the lymph node blood supply, denoted B_{LN_o} and $B_{\mathrm{LN}_{\mathrm{TOT}}}$, respectively. From the lymph node vasculature compartment, a proportion of cells extravasates into the lymph node interstitial compartment (at a rate $e_{\mathrm{LN}_o} B_{\mathrm{LN}_o}$ and $e_{\mathrm{LN}_{\mathrm{TOT}}} B_{\mathrm{LN}_{\mathrm{TOT}}}$). Cells drained to organ, o, -draining lymph nodes and the single lymph node are returned to the systemic circulation (at rates $e_{\mathrm{LN}_o} \mu_{\mathrm{LN}_o} B_{\mathrm{LN}_o} + \mu_{\mathrm{LN}_o} e_o \mu_o B_o$ and $e_{\mathrm{LN}_{\mathrm{TOT}}} \mu_{\mathrm{LN}_{\mathrm{TOT}}} B_{\mathrm{LN}_{\mathrm{TOT}}} + \mu_{\mathrm{LN}_{\mathrm{TOT}}} e_o \mu_o B_o + \sum_i \mu_{\mathrm{LN}_{\mathrm{TOT}}} e_i \mu_i B_i$, respectively). Cells that have not extravasated to the interstitium of organ, o, organ, o, -draining lymph nodes and the single lymph node are, similarly, returned to the systemic circulation (at rates $(1 - e_o) B_o$, $(1 - e_{\mathrm{LN}_o}) B_{\mathrm{LN}_o}$ and $(1 - e_{\mathrm{LN}_{\mathrm{TOT}}}) B_{\mathrm{LN}_{\mathrm{TOT}}}$, respectively). Different suffixes, such as *LA&LV* (combined left atrium, left ventricle, and large arteries), *RA&RV* (combined right atrium, right ventricle, and large veins), *PC* (pulmonary circuit), *med* (mediastinal lymph nodes) are also used.

The differences in the lymph node compartmentalisation between the models result in a distinct structure of the ODE equations describing the systems (see Figure 3.3). As the multiple lymph node model was described in detail in Section 2.2.1, the following provides an overview of the single lymph node trafficking model and the comparison of the two ODE systems. As a reminder for the reader, organ compartments in both models are parameterised by the following input parameters: blood flow (B_o), blood volume (V_o), total organ volume ($\tilde{V}_o$), extravasation parameter (e_o) and return parameter (μ_o), the definitions and units of which can be found in Table 2.1.

3.2.1.1 Single lymph node trafficking model

The single lymph node model, based on Figure 3.2(b) represents the exchange of a cell population between the heart and organs analogously to the multiple lymph node model, with the exception of lymph nodes, which are represented with a single lumped compartment, as opposed to 16 organ-specific lymph node group compartments, as described in Section 2.2.1. The model variables in the single lymph node model, the number of cells and the cell concentration in each compartment are denoted with a prime, *i.e.*, N'_o, $\tilde{N}'_o$ and C'_o, $\tilde{C}'_o$, respectively.

The number of cells in the vascular compartment of organ, o, N'_o, in the single lymph node model, changes in time analogously to Equation (2.1):

$$\frac{dN'_o}{dt} = V_o \frac{dC'_o}{dt} = B_o \left(C'_{\text{LA\&LV}} - C'_o\right), \tag{3.1}$$

where the first and the second term describe cells flowing from the heart into the organ's vasculature and cells leaving the vasculature of organ, o, respectively. C'_o is the cell concentration in the vascular compartment of organ, o, while $C'_{\text{LA\&LV}}$ is the concentration of T-cells within the left atrium, left ventricle, aorta and large arteries between organs and the heart, in the single lymph node model. A fraction of cells (e_o) in the vasculature subsequently extravasates into the organ's interstitium and a proportion of cells (μ_o) flows via lymphatics into the lymph node compartment. The number of cells in the interstitial compartment of organ, o, N'_o and $\tilde{N}'_o$, in the single lymph node model, changes in time analogously to Equation (2.2):

$$\frac{d\tilde{N}'_o}{dt} = \tilde{V}_o \frac{d\tilde{C}'_o}{dt} = e_o B_o \left(C'_o - \mu_o \tilde{C}'_o\right), \tag{3.2}$$

where $\tilde{C}'_o$ is the cell concentration in the interstitial compartment of organ, o,

Similarly, the equations for the rate of change of cells in the vascular and interstitial liver compartments remain unchanged:

$$\begin{aligned}\frac{dN'_{\text{liver}}}{dt} = V_{\text{liver}} \frac{dC'_{\text{liver}}}{dt} = B_{\text{liver}} \left(C'_{\text{LA\&LV}} - C'_{\text{liver}}\right) + e_{\text{spleen}} \mu_{\text{spleen}} B_{\text{spleen}} \left(\tilde{C}'_{\text{spleen}} - C'_{\text{liver}}\right) \\ + \sum_{o \in \{\text{mesentery}\}} B_o \left(1 - e_o\right) \left(C'_o - C'_{\text{liver}}\right),\end{aligned} \tag{3.3}$$

where each term respectively describes: (i) cells from the blood supply to the liver and returning to the systemic circulation; (ii) the flow and exit of cells that have extravasated into the spleen; and (iii) the flow and exit of cells that have not extravasated from the mesenteric organs (the stomach, spleen, pancreas, small and large intestine) and have returned through the portal vein. The number of cells in the liver's interstitium, changes in time according to:

$$\begin{aligned}\frac{d\tilde{N}'_{\text{liver}}}{dt} = \tilde{V}_{\text{liver}}\frac{d\tilde{C}'_{\text{liver}}}{dt} &= e_{\text{liver}}B_{\text{liver}}\left(C'_{\text{liver}} - \mu_{\text{liver}}\tilde{C}'_{\text{liver}}\right) \\ &+ \sum_{o\in\{\text{mesentery}\}} B_o\left(1-e_o\right)e_{\text{liver}}\left(C'_{\text{liver}} - \mu_{\text{liver}}\tilde{C}'_{\text{liver}}\right) \\ &+ e_{\text{liver}}\left(C'_{\text{liver}} - \mu_{\text{liver}}\tilde{C}'_{\text{liver}}\right)e_{\text{spleen}}\mu_{\text{spleen}}B_{\text{spleen}},\end{aligned} \tag{3.4}$$

where each term respectively represents: (i) the flow and drainage of cells that have extravasated from the liver's blood supply; (ii) the flow and drainage of cells that have not extravasated in the mesentery, returned to the liver's vasculature through the portal vein and subsequently extravasated into the liver interstitium (where mesentery refers to: the stomach, spleen, pancreas, small and large intestines); and (iii) the flow and drainage of cells have extravasated in the spleen, returned to the liver's vasculature and subsequently extravasated into the liver interstitium.

Similarly to the organ-specific lymph node compartments in the multiple lymph node model, the lumped lymph node compartment in the single lymph node model is represented by a vasculature subcompartment (the blood supply to the lymph node) and the interstitial subcompartment, where cells from organs are drained via lymphatics. The rate of change in the number of cells in the blood supply compartment of the single lymph node is given by:

$$\frac{dN'_{\text{LN}}}{dt} = V_{\text{LN}_{\text{TOT}}}\frac{dC'_{\text{LN}}}{dt} = B_{\text{LN}_{\text{TOT}}}\left(C'_{\text{LA\&LV}} - C'_{\text{LN}}\right), \tag{3.5}$$

where $V_{\text{LN}_{\text{TOT}}}$ is the total blood volume of lymph nodes, $B_{\text{LN}_{\text{TOT}}}$ is the total blood flow through lymph nodes, and $C'_{\text{LA\&LV}}$ is the concentration of cells within the left atrium, left ventricle, aorta and large arteries between organs and the heart in the single lymph node model. The rate of change of cells in the interstitial lymph node group compartment accounts for the contribution from the vasculature of the single lymph node and, additionally, the flow of cells from all organs drained by the lymphatics:

$$\begin{aligned}\tfrac{d\tilde{N}'_{\text{LN}_{\text{TOT}}}}{dt} &= \tilde{V}_{\text{LN}_{\text{TOT}}}\tfrac{d\tilde{C}'_{\text{LN}_{\text{TOT}}}}{dt} = e_{\text{LN}_{\text{TOT}}}B_{\text{LN}_{\text{TOT}}}\left(C'_{\text{LN}_{\text{TOT}}} - \mu_{\text{LN}_{\text{TOT}}}\tilde{C}'_{\text{LN}_{\text{TOT}}}\right) \\ &+ \textstyle\sum_{\substack{o\notin\{\text{liver,spleen,PC}\\ \text{RA\&RV,LA\&LV}\}}} e_o\mu_o B_o\left(\tilde{C}'_o - \mu_{\text{LN}_{\text{TOT}}}\tilde{C}'_{\text{LN}_{\text{TOT}}}\right) \\ &+ e_{\text{liver}}\mu_{\text{liver}}\left(e_{\text{spleen}}\mu_{\text{spleen}}B_{\text{spleen}} + \textstyle\sum_{o\in\{\text{mesentery}\}} B_o\left(1-e_o\right)\right)\left(\tilde{C}'_{\text{liver}} - \mu_{\text{LN}_{\text{TOT}}}\tilde{C}'_{\text{LN}_{\text{TOT}}}\right),\end{aligned} \tag{3.6}$$

where $\tilde{V}_{\text{LN}_{\text{TOT}}}$ is the total volume of lymph nodes and $\mu_{\text{LN}_{\text{TOT}}}$ is the fraction of cells returning to the systemic circulation per unit blood flow. The term in the first line of Equation (3.6)

describes the flow of cells from the lymph node blood supply subcompartment into the interstitium and the proportion of the cells that have extravasated leaving the interstitium. The term in the second line represents cells drained from organs with lymphatics, except the liver, and the proportion of the drained cells being returned to the systemic circulation. The term in the final line represents cells drained from the liver and the proportion of those cells being returned to the systemic circulation.

Finally, Equation (2.10) is modified to account for the change in the lymph node outflow of cells into the heart's right atrium and right ventricle, *RA&RV*:

$$\begin{aligned}\frac{dN'_{\text{RA\&RV}}}{dt} &= V_{\text{RA\&RV}}\frac{dC'_{\text{RA\&RV}}}{dt} = -B_{\text{TOT}}C'_{\text{RA\&RV}} \\ &+\textstyle\sum_{o\notin\{\text{mesentery}\}}(1-e_o)\,B_oC_o + \left(1-e_{\text{LN}_{\text{TOT}}}\right)B_{\text{LN}_{\text{TOT}}}C'_{\text{LN}_{\text{TOT}}} \\ &+\left(e_{\text{spleen}}\mu_{\text{spleen}}B_{\text{spleen}} + \textstyle\sum_{o\in\{\text{mesentery}\}}(1-e_o)\,B_o\right)(1-e_{\text{liver}})\,C'_{\text{liver}} \\ &+e_{\text{LN}_{\text{TOT}}}\mu_{\text{LN}_{\text{TOT}}}B_{\text{LN}_{\text{TOT}}}\tilde{C}'_{\text{LN}_{\text{TOT}}} + \textstyle\sum_{o\notin\{\text{spleen,PC,liver, RA\&RV,LA\&LV}\}}\mu_{\text{LN}_{\text{TOT}}}e_o\mu_oB_o\tilde{C}'_{\text{LN}_{\text{TOT}}} \\ &+\mu_{\text{LN}_{\text{TOT}}}e_{\text{liver}}\mu_{\text{liver}}\tilde{C}'_{\text{LN}_{\text{TOT}}}\left(e_{\text{spleen}}\mu_{\text{spleen}}B_{\text{spleen}} + \textstyle\sum_{o\in\{\text{mesentery}\}}B_o\,(1-e_o)\right),\end{aligned} \tag{3.7}$$

where $B_{\text{TOT}} = \sum_{o\notin\{PC\}}B_o + \sum_{o\notin\{PC,spleen\}}B_{\text{LN}_o}$ is the cardiac output, and the mesentery comprises: the stomach, spleen, pancreas, small and large intestines. Further, each line respectively refers to: (i) the flow of cells out of the heart's right atrium and right ventricle; (ii) the return of cells from the non-mesenteric organs; (iii) the return of cells from the mesentery via the liver; (iv, v) the return of cells from the single lymph node compartment.

Equations (2.11) and (2.12) remain unchanged and cells flow from the right atrium and right ventricle into the pulmonary circuit (PC), where the blood flow is equal to the cardiac output $B_{\text{TOT}} = \sum_{o\notin\{\text{PC}\}}B_o + \sum_{o\notin\{\text{PC, spleen}\}}B_{\text{LN}_o}$:

$$\frac{dN'_{\text{PC}}}{dt} = B_{\text{TOT}}\left(C'_{\text{RA\&RV}} - C'_{\text{PC}}\right), \tag{3.8}$$

$$\frac{d\tilde{N}'_{\text{PC}}}{dt} = e_{\text{PC}}B_{\text{TOT}}\left(C'_{\text{PC}} - \mu_{\text{PC}}\tilde{C}'_{\text{PC}}\right). \tag{3.9}$$

Finally, cells return from the pulmonary circuit to the left atrium and left ventricle of the heart, analogously to Equation (2.13):

$$\frac{dN'_{\text{LA\&LV}}}{dt} = (1-e_{\text{PC}})B_{\text{TOT}}C'_{\text{PC}} + e_{\text{PC}}\mu_{\text{PC}}B_{\text{TOT}}\tilde{C}'_{\text{PC}} - B_{\text{TOT}}C'_{\text{LA\&LV}}, \tag{3.10}$$

where the last term describes cells flowing through aorta and major arteries towards vasculature compartments, the subsequent downstream impact of which is captured in Equation (3.1).

3.2.2 Single to multiple lymph node model mapping derivation

Different choices of lymph node compartmentalisation in a model, such as that described in Section 3.2.1, are reflected in the structure of the ODE systems describing them. While the ODEs describing the rate of change of the number of cells in the vasculature and interstitium of an organ, o (Equations (2.1), (2.2) and (3.1), (3.2)), are equivalent for both models, the steady-state cell localisation in those compartments will generally be distinct for a given choice of input parameters.

The difference in the steady-state cell localisation and concentration across compartments between the two models can be shown and derived analytically by considering an equal number of cells in both systems, expressing this constraint as a summation of the number of cells in each compartment in steady state and solving for the number of cells in each compartment. This can be used to characterise the difference in the predicted biodistribution of cells between the two models, by constructing a mapping between the steady-state biodistribution in the single and the multiple lymph node model. For each organ and lymph node compartment, a mapping variable, which is a function of the model parameters, is defined as a ratio of the steady-state cell concentration in the considered compartment in the multiple lymph node model to the corresponding steady-state cell concentration in the single lymph node model. For instance, a mapping variable for the vascular compartment if an organ, o, is defined as C_o/C'_o. $C_{\mathrm{LN}_o}/C'_{\mathrm{LN}}$ and $C_{\mathrm{LN}}/C'_{\mathrm{LN}}$ denote mapping variables for the lymph node compartments. The variable, $C_{\mathrm{LN}_o}/C'_{\mathrm{LN}}$, refers to the ratio of organ, o, -draining lymph node concentration in the multiple lymph node model to the cell concentration in the lumped lymph node compartment in the single lymph node model. The variable, $C_{\mathrm{LN}}/C'_{\mathrm{LN}}$, is defined as the net cell concentration across the lymph node compartments in the multiple lymph node model with respect to the cell concentration in the lumped lymph node compartment in the single lymph node model. The following sections present an outline of the derivation of the mapping variables within this framework.

3.2.2.1 Organ compartments

Denote the steady-state cell concentration in the vasculature of organ, o, in the multiple lymph node model as C_o and the steady-state cell concentration in the single lymph node model as C'_o. The steady state of Equations (2.1) and (3.1) imply $C_o = C_{\mathrm{LA\&LV}}$ and $C'_o = C'_{\mathrm{LA\&LV}}$

for all organs $o \notin \{\text{liver}\}$, meaning the steady-state cell concentration in the vasculature of organ, o, is equal to the cell concentration in the left atrium and ventricle of the heart, $C_{\text{LA\&LV}}$ in the multiple lymph node model and $C'_{\text{LA\&LV}}$ in the single lymph node model for all organs, except the liver. The steady-state cell concentrations C_o and C'_o are, therefore, equal across all vascular compartments, except for the liver, within each model and we will refer to C_o and C'_o as steady-state blood concentrations for simplicity. The mapping variable from the single to multiple lymph node model for the vasculature of organ, o, is then equal to the ratio of steady-state blood concentrations C_o/C'_o, which we show below can be determined analytically in terms of model parameters (Equation (3.38)).

Similarly, consider Equations (2.2) and (3.2), which describe the change in the number of cells in the interstitial compartments of organ, o, in steady state. The interstitial steady-state cell concentration can be expressed in relation to the steady-state vascular cell concentration as $\mu_o \tilde{C}_o = C_o$ and $\mu_o \tilde{C}'_o = C'_o$, in the multiple and the single lymph node model, respectively. The mapping variable from the single to multiple lymph node model for the interstitium of organ, o, is, therefore, also equal to the ratio of steady-state blood concentrations, C_o/C'_o.

The exception is the liver, for which the ODEs in both models differ to capture the anatomy of hepatic blood and lymph circulation. By considering Equation (2.7) in steady state and substituting $C_{\text{LA\&LV}} = C_o$, $\tilde{C}_{\text{spleen}} = \frac{1}{\mu_{\text{spleen}}} C_{\text{spleen}} = \frac{1}{\mu_{\text{spleen}}} C_o$, the steady-state cell concentration, C_{liver}, can be solved for, resulting in:

$$\begin{aligned} C_{\text{liver}} &= \frac{B_{\text{liver}} + e_{\text{spleen}} B_{\text{spleen}} + \sum_{o \in \{\text{mesentery}\}} B_o (1 - e_o)}{B_{\text{liver}} + e_{\text{spleen}} \mu_{\text{spleen}} B_{\text{spleen}} + \sum_{o \in \{\text{mesentery}\}} B_o (1 - e_o)} C_o \\ &= \left(1 + \frac{e_{\text{spleen}} B_{\text{spleen}} (1 - \mu_{\text{spleen}})}{B_{\text{liver}} + e_{\text{spleen}} \mu_{\text{spleen}} B_{\text{spleen}} + \sum_{o \in \{\text{mesentery}\}} B_o (1 - e_o)} \right) C_o \\ &= \lambda C_o, \end{aligned} \tag{3.11}$$

where mesentery refers to the spleen, small and large intestines, stomach and pancreas and the variable λ has been introduced to simplify the notation:

$$\lambda = 1 + \frac{e_{\text{spleen}} B_{\text{spleen}} (1 - \mu_{\text{spleen}})}{B_{\text{liver}} + e_{\text{spleen}} \mu_{\text{spleen}} B_{\text{spleen}} + \sum_{o \in \{\text{mesentery}\}} B_o (1 - e_o)}. \tag{3.12}$$

An analogous expression follows after considering the corresponding equation in single lymph node model, Equation (3.3):

$$C'_{\text{liver}} = \lambda C'_o, \tag{3.13}$$

where λ was introduced above. The mapping variable from the single to multiple lymph node model for the liver vasculature compartment is, therefore, equal to the blood mapping variable:

$$\frac{C_{\text{liver}}}{C'_{\text{liver}}} = \frac{C_o}{C'_o}. \tag{3.14}$$

Similarly, considering Equation (2.8) in steady state and substituting $C_{\text{liver}} = \lambda C_o$ (Equation (3.11)), the steady-state cell concentration in the liver interstitium, $\tilde{C}_{\text{liver}}$, can be expressed as:

$$\tilde{C}_{\text{liver}} = \frac{C_{\text{liver}}}{\mu_{\text{liver}}} = \frac{\lambda}{\mu_{\text{liver}}} C_o. \tag{3.15}$$

An analogous expression also applies to the liver interstitium compartment in the single lymph node model:

$$\tilde{C}'_{\text{liver}} = \frac{\lambda}{\mu_{\text{liver}}} \tilde{C}'_o, \tag{3.16}$$

where λ is given by Equation (3.12). The mapping variable from the single to multiple lymph node model for the liver interstitium is, as a result, also equal to the blood mapping variable:

$$\frac{\tilde{C}_{\text{liver}}}{\tilde{C}'_{\text{liver}}} = \frac{C_o}{C'_o}. \tag{3.17}$$

3.2.2.2 Lymph node compartments

The steady-state cell concentration ratio for organ, o, -draining lymph node group and the single lymph node can be derived in the same manner. Consider the multiple lymph node model first. Note that the lymph node blood supply compartments follow the same equation as the vasculature of organ, o (Equation (2.3)). This implies that the steady-state cell concentration in the vasculature compartments of all lymph nodes, except the liver-draining lymph nodes, is equal to the steady-state cell concentration of all vascular compartments (except the liver):

$$C_{\text{LN}_o} = C_o. \tag{3.18}$$

Next, consider Equation (2.4) for the interstitial compartment of organ, o, -draining lymph nodes in steady state. Substituting the known steady-state cell concentration relations ($C_{\text{LN}_o} =$

C_o and $\tilde{C}_o = \frac{1}{\mu_o} C_o$) and solving for $\tilde{C}_{\mathrm{LN}_o}$ gives:

$$\tilde{C}_{\mathrm{LN}_o} = \frac{e_{\mathrm{LN}_o} B_{\mathrm{LN}_o} + e_o B_o}{e_{\mathrm{LN}_o} B_{\mathrm{LN}_o} + e_o \mu_o B_o} \frac{C_o}{\mu_{\mathrm{LN}_o}} = \frac{\alpha_o}{\mu_{\mathrm{LN}_o}} C_o, \tag{3.19}$$

where the parameter α_o has been introduced to simplify the notation. For mediastinal lymph nodes, which drain both the heart and lung blood supply compartments (see Equation (2.6)), the above equation is modified as:

$$\tilde{C}_{\mathrm{LN}_{\mathrm{med}}} = \frac{e_{\mathrm{LN}_{\mathrm{med}}} B_{\mathrm{LN}_{\mathrm{med}}} + e_{\mathrm{heart}} B_{\mathrm{heart}} + e_{\mathrm{lung}} B_{\mathrm{lung}}}{e_{\mathrm{LN}_{\mathrm{med}}} B_{\mathrm{LN}_{\mathrm{med}}} + e_{\mathrm{heart}} \mu_{\mathrm{heart}} B_{\mathrm{heart}} + e_{\mathrm{lung}} \mu_{\mathrm{lung}} B_{\mathrm{lung}}} \frac{C_o}{\mu_{\mathrm{LN}_{\mathrm{med}}}} = \frac{\alpha_{\mathrm{med}}}{\mu_{\mathrm{LN}_o}} C_o, \tag{3.20}$$

where the parameter α_{med} has been defined above, analogously to α_o.

Due to the anatomy of hepatic circulation, the steady-state cell concentration in the liver-draining lymph node compartment also differs. Consider Equation (2.9) in steady state. Substituting known steady-state cell concentrations ($C_{\mathrm{LN}_{\mathrm{liver}}} = C_o$, $\tilde{C}_{\mathrm{liver}} = \frac{\lambda}{\mu_{\mathrm{liver}}} C_o$) and solving for $\tilde{C}_{\mathrm{LN}_{\mathrm{liver}}}$ gives:

$$\tilde{C}_{\mathrm{LN}_{\mathrm{liver}}} = \frac{e_{\mathrm{LN}_{\mathrm{liver}}} B_{\mathrm{LN}_{\mathrm{liver}}} + \lambda e_{\mathrm{liver}} \left(B_{\mathrm{liver}} + e_{\mathrm{spleen}} \mu_{\mathrm{spleen}} B_{\mathrm{spleen}} + \sum_{o \in \{\mathrm{mesentery}\}} B_o (1 - e_o) \right)}{e_{\mathrm{LN}_{\mathrm{liver}}} B_{\mathrm{LN}_{\mathrm{liver}}} + e_{\mathrm{liver}} \mu_{\mathrm{liver}} \left(B_{\mathrm{liver}} + e_{\mathrm{spleen}} \mu_{\mathrm{spleen}} B_{\mathrm{spleen}} + \sum_{o \in \{\mathrm{mesentery}\}} B_o (1 - e_o) \right)} \frac{C_o}{\mu_{\mathrm{LN}_{\mathrm{liver}}}} = \frac{\alpha_{\mathrm{liver}}}{\mu_{\mathrm{LN}_{\mathrm{liver}}}} C_o, \tag{3.21}$$

which defines α_{liver}.

For the single lymph node model, consider Equation (3.6) in steady state. Substituting known steady-state concentration relations ($\tilde{C}'_o = \frac{1}{\mu_o} C'_o$, $C'_{\mathrm{LN}_{\mathrm{TOT}}} = C'_o$ and $\tilde{C}'_{\mathrm{liver}} = \frac{\lambda}{\mu_{\mathrm{liver}}} C'_o$) and solving for $\tilde{C}'_{\mathrm{LN}_{\mathrm{TOT}}}$ gives:

$$\tilde{C}'_{\mathrm{LN}_{\mathrm{TOT}}} = \frac{1}{\mu_{\mathrm{LN}_{\mathrm{TOT}}}} \frac{e_{\mathrm{LN}_{\mathrm{TOT}}} B_{\mathrm{LN}_{\mathrm{TOT}}} + \sum_o e_o B_o + e_{\mathrm{liver}} \lambda (e_{\mathrm{spleen}} \mu_{\mathrm{spleen}} B_{\mathrm{spleen}} + \sum_{o \in \{\mathrm{mesentery}\}} B_o (1 - e_o))}{e_{\mathrm{LN}_{\mathrm{TOT}}} B_{\mathrm{LN}_{\mathrm{TOT}}} + \sum_o e_o \mu_o B_o + e_{\mathrm{liver}} \mu_{\mathrm{liver}} (e_{\mathrm{spleen}} \mu_{\mathrm{spleen}} B_{\mathrm{spleen}} + \sum_{o \in \{\mathrm{mesentery}\}} B_o (1 - e_o))} C'_o = \frac{\alpha}{\mu_{\mathrm{LN}_{\mathrm{TOT}}}} C'_o, \tag{3.22}$$

which defines α:

$$\alpha = \frac{e_{\mathrm{LN}_{\mathrm{TOT}}} B_{\mathrm{LN}_{\mathrm{TOT}}} + \sum_o e_o B_o + e_{\mathrm{liver}} \lambda (e_{\mathrm{spleen}} \mu_{\mathrm{spleen}} B_{\mathrm{spleen}} + \sum_{o \in \{\mathrm{mesentery}\}} B_o (1 - e_o))}{e_{\mathrm{LN}_{\mathrm{TOT}}} B_{\mathrm{LN}_{\mathrm{TOT}}} + \sum_o e_o \mu_o B_o + e_{\mathrm{liver}} \mu_{\mathrm{liver}} (e_{\mathrm{spleen}} \mu_{\mathrm{spleen}} B_{\mathrm{spleen}} + \sum_{o \in \{\mathrm{mesentery}\}} B_o (1 - e_o))}. \tag{3.23}$$

The mapping variable for lymph nodes can be defined in two ways. Firstly, a mapping between the total number of cells in all lymph node compartments in the multiple lymph node model and the number of cells in the lumped lymph node compartment in the single lymph node model, $C_{\mathrm{LN}}/C'_{\mathrm{LN}}$, can be considered. Expressing the total number of cells in lymph node

compartments in the multiple lymph node model in steady state as:

$$N_{\mathrm{LN}} = \sum_{\substack{o \notin \{\text{spleen,PC} \\ \text{RA\&RV,LA\&LV}\}}} \left(N_{\mathrm{LN}_o} + \tilde{N}_{\mathrm{LN}_o}\right) = \sum_{\substack{o \notin \{\text{spleen,PC} \\ \text{RA\&RV,LA\&LV}\}}} \left(V_{\mathrm{LN}_o} C_{\mathrm{LN}_o} + \tilde{V}_{\mathrm{LN}_o} \tilde{C}_{\mathrm{LN}_o}\right), \tag{3.24}$$

and the total number of cells in the lumped lymph node compartment in the single lymph node model as:

$$N'_{\mathrm{LN}} = N'_{\mathrm{LN_{TOT}}} + \tilde{N}'_{\mathrm{LN_{TOT}}} = V_{\mathrm{LN_{TOT}}} C'_{\mathrm{LN_{TOT}}} + \tilde{V}_{\mathrm{LN_{TOT}}} \tilde{C}'_{\mathrm{LN_{TOT}}}, \tag{3.25}$$

gives the ratio of cell localisations, which is equivalent to the ratio of the net lymph node cell concentration in the multiple lymph node model to the cell concentration in the single lymph node model due to identical total volumes of the lymph node compartments in both models. Substituting know steady-state cell concentrations ($C_{\mathrm{LN}_o} = C_o$, $\tilde{C}_{\mathrm{LN}_o} = \frac{\alpha_o}{\mu_{\mathrm{LN}_o}} C_o$, $C_{\mathrm{LN_{med}}} = C_o$, $\tilde{C}_{\mathrm{med}} = \frac{\alpha_{\mathrm{med}}}{\mu_{\mathrm{med}}} C_o$, $C_{\mathrm{LN_{liver}}} = C_o$, $\tilde{C}_{\mathrm{liver}} = \frac{\alpha_{\mathrm{liver}}}{\mu_{\mathrm{liver}}} C_o$, $C'_{\mathrm{LN_{TOT}}} = C'_o$, $\tilde{C}'_{\mathrm{LN_{TOT}}} = \frac{\alpha}{\mu_{\mathrm{LN_{TOT}}}} C'_o$), the total lymph node mapping variable is given as:

$$\frac{C_{\mathrm{LN}}}{C'_{\mathrm{LN}}} = \frac{\sum_{\substack{o \notin \{\text{spleen,liver, heart} \\ \text{lungs,RA\&RV,LA\&LV}\}}} \left(V_{\mathrm{LN}_o} + \frac{\alpha_o}{\mu_{\mathrm{LN}_o}} \tilde{V}_{\mathrm{LN}_o}\right) + V_{\mathrm{LN_{med}}} + \frac{\alpha_{\mathrm{med}}}{\mu_{\mathrm{med}}} \tilde{V}_{\mathrm{LN_{med}}} + V_{\mathrm{LN_{liver}}} + \frac{\alpha_{\mathrm{liver}}}{\mu_{\mathrm{liver}}} \tilde{V}_{\mathrm{LN_{liver}}}}{V_{\mathrm{LN_{TOT}}} + \frac{\alpha}{\mu_{\mathrm{LN_{TOT}}}} \tilde{V}_{\mathrm{LN_{TOT}}}} \frac{C_o}{C'_o} = \alpha_{\mathrm{LN_{TOT}}} \frac{C_o}{C'_o}, \tag{3.26}$$

which defines $\alpha_{\mathrm{LN_{TOT}}}$ and the parameters α_o, α_{med}, α_{liver} and α were defined in Equations (3.19), (3.20), (3.21) and (3.23), respectively.

In addition, a mapping variable between each lymph node compartment in the multiple lymph node model and the lumped lymph node compartment, $C_{\mathrm{LN}_o}/C'_{\mathrm{LN}}$, can be constructed, by taking a ratio of Equations (3.19) and (3.22):

$$\frac{C_{\mathrm{LN}_o}}{C'_{\mathrm{LN}}} = \frac{\alpha_o}{\alpha} \frac{\frac{1}{\mu_{\mathrm{LN}_o}}}{\frac{1}{\mu_{\mathrm{LN_{TOT}}}}} \frac{C_o}{C'_o}. \tag{3.27}$$

A mapping variable defined in this manner expresses the cell concentration in a lymph node compartment in the multiple lymph node model as a fraction of the cell concentration in the lumped lymph node in the single lymph node model.

Equation (3.27) applies to all organ-specific lymph node compartments, with the exception of the liver-draining and mediastinal lymph nodes. Taking a ratio of Equations (3.21)

and (3.22), the mapping variable for the liver-draining lymph nodes can be defined as:

$$\frac{C_{\mathrm{LN}_{\mathrm{liver}}}}{C'_{\mathrm{LN}}} = \frac{\alpha_{\mathrm{liver}}}{\alpha} \frac{\frac{1}{\mu_{\mathrm{LN}_{\mathrm{liver}}}}}{\frac{1}{\mu_{\mathrm{LN}_{\mathrm{TOT}}}}} \frac{C_o}{C'_o}, \tag{3.28}$$

where α_{liver} was defined in Equation (3.21). Analogously, the mapping variable for the mediastinal lymph nodes is given by the ratio of Equations (3.20) and (3.22):

$$\frac{C_{\mathrm{LN}_{\mathrm{med}}}}{C'_{\mathrm{LN}}} = \frac{\alpha_{\mathrm{med}}}{\alpha} \frac{\frac{1}{\mu_{\mathrm{LN}_{\mathrm{med}}}}}{\frac{1}{\mu_{\mathrm{LN}_{\mathrm{TOT}}}}} \frac{C_o}{C'_o}, \tag{3.29}$$

where α_{liver} was defined in Equation (3.20).

3.2.2.3 Heart chambers and pulmonary circuit compartments

Finally, it can be shown the mapping variables for the steady state pulmonary circuit (PC), the right atrium and ventricle ($RA\&RV$), left atrium and ventricle ($LA\&LV$) compartments are also equal to the blood mapping variable, C_o/C'_o. By considering Equations (2.10) and (3.7) in steady state we have:

$$C_{\mathrm{PC}} = C_{\mathrm{RA\&RV}} \quad \text{and} \quad C'_{\mathrm{PC}} = C'_{\mathrm{RA\&RV}}, \tag{3.30}$$

and, similarly, Equation (2.11) and the corresponding expression for the pulmonary circuit compartment in the single lymph node model, given by Equation (3.8):

$$\tilde{C}_{\mathrm{PC}} = \frac{1}{\mu_{\mathrm{PC}}} C_{\mathrm{PC}} \quad \text{and} \quad \tilde{C}'_{\mathrm{PC}} = \frac{1}{\mu_{\mathrm{PC}}} C'_{\mathrm{PC}}. \tag{3.31}$$

Substituting the above relations into Equation (2.13) in steady state and its corresponding version in the single lymph node model (Equation (3.10)) yields:

$$C_{\mathrm{LA\&LV}} = C_{\mathrm{PC}} = C_{\mathrm{RA\&RV}} \quad \text{and} \quad C'_{\mathrm{LA\&LV}} = C'_{\mathrm{PC}} = C'_{\mathrm{RA\&RV}}. \tag{3.32}$$

The steady-state cell concentrations in the heart chambers and pulmonary circuit compartments are, therefore, equal to the blood concentration in each model:

$$\begin{aligned} C_o &= C_{\text{LA\&LV}} = C_{\text{PC}} = C_{\text{RA\&RV}} \\ C'_o &= C'_{\text{LA\&LV}} = C'_{\text{PC}} = C'_{\text{RA\&RV}}, \end{aligned} \tag{3.33}$$

resulting in the mapping variables equal to the blood mapping variable, similarly to other organs:

$$\frac{C_{\text{PC}}}{C'_{\text{PC}}} = \frac{\tilde{C}_{\text{PC}}}{\tilde{C}'_{\text{PC}}} = \frac{C_{\text{LA\&LV}}}{C'_{\text{LA\&LV}}} = \frac{C_{\text{RA\&RV}}}{C'_{\text{RA\&RV}}} = \frac{C_o}{C'_o}. \tag{3.34}$$

3.2.2.4 Blood mapping variable

An expression for the blood and organ mapping variable, C_o/C'_o, which equals the ratio of the cell concentration in the vascular and interstitial organ compartments other than lymph nodes, is derived from the constraint that the total number of cells in both systems is conserved: $N_{\text{TOT}} = N'_{\text{TOT}}$. Expressing the constraint via a summation of the number of cells in each compartment in steady state yields:

$$\begin{aligned} N_{\text{TOT}} &= \sum_o V_o C_o + \sum_{\substack{o \notin \{\text{RA\&RV} \\ \text{PC,LA\&LV}\}}} \tilde{V}_o \tilde{C}_o + \sum_{\substack{o' \notin \{\text{spleen,RA\&RV,} \\ \text{PC,LA\&LV}\}}} \left(V_{\text{LN}_{o'}} C_{\text{LN}_{o'}} + \tilde{V}_{\text{LN}_{o'}} \tilde{C}_{\text{LN}_{o'}} \right) \\ N'_{\text{TOT}} &= \sum_o V_o C'_o + \sum_{\substack{o \notin \{\text{RA\&RV,} \\ \text{PC,LA\&LV}\}}} \tilde{V}_o \tilde{C}'_o + V_{\text{LN}_{\text{TOT}}} C'_{\text{LN}_{\text{TOT}}} + \tilde{V}_{\text{LN}_{\text{TOT}}} \tilde{C}'_{\text{LN}_{\text{TOT}}}. \end{aligned} \tag{3.35}$$

Substituting the derived expressions for the steady-state cell concentrations in the multiple lymph node model (Equations (3.13), (3.16), (3.22) and (3.33)), one can write $N_{\text{TOT}} = AC_o$, where

$$A = \sum_{o \notin \{\text{liver}\}} V_o + \sum_{\substack{o \notin \{\text{liver,RA} \\ \&\text{RV,LA}\&\text{LV}\}}} \frac{\tilde{V}_o}{\mu_o} + \lambda \left(V_{\text{liver}} + \frac{\tilde{V}_{\text{liver}}}{\mu_{\text{liver}}} \right) + \sum_{\substack{o' \notin \{\text{spleen,heart,lung} \\ \text{RA}\&\text{RV,PC,LA}\&\text{LV,liver}\}}} \left(V_{\text{LN}_{o'}} + \frac{\alpha_{o'}}{\mu_{\text{LN}_{o'}}} \tilde{V}_{\text{LN}_{o'}} \right) + V_{\text{LN}_{\text{liver}}} + \frac{\alpha_{\text{liver}}}{\mu_{\text{LN}_{\text{liver}}}} \tilde{V}_{\text{LN}_{\text{liver}}} + V_{\text{LN}_{\text{med}}} + \frac{\alpha_{\text{med}}}{\mu_{\text{LN}_{\text{med}}}} \tilde{V}_{\text{LN}_{\text{med}}}, \tag{3.36}$$

using, for example, $C_{LN_o} = C_o$ and $\tilde{C}_o = \frac{1}{\mu_o} C_o$ for all organs, with the exception of the liver and lymph nodes. With analogous identities in the single lymph node model (Equations (3.11), (3.15), (3.18), (3.19), (3.20), (3.21) and (3.33)) and algebra, we have $N'_{\text{TOT}} = BC'_o$, where

$$B = \sum_{o \notin \{\text{liver}\}} V_o + \sum_{\substack{o \notin \{\text{liver,RA} \\ \&\text{RV,LA}\&\text{LV}\}}} \frac{\tilde{V}_o}{\mu_o} + \lambda \left(V_{\text{liver}} + \frac{\tilde{V}_{\text{liver}}}{\mu_{\text{liver}}} \right) + V_{\text{LN}_{\text{TOT}}} + \frac{\alpha}{\mu_{\text{LN}_{\text{TOT}}}} \tilde{V}_{\text{LN}_{\text{TOT}}}. \tag{3.37}$$

Hence, with $N_{\text{TOT}} = N'_{\text{TOT}}$, we have $AC_o = BC'_o$, and thus:

$$\frac{C_o}{C'_o} = \frac{\sum_{o \notin \{\text{liver}\}} V_o + \sum_{\substack{o \notin \{\text{liver,RA} \\ \&\text{RV,LA}\&\text{LV}\}}} \frac{\tilde{V}_o}{\mu_o} + \lambda \left(V_{\text{liver}} + \frac{\tilde{V}_{\text{liver}}}{\mu_{\text{liver}}} \right) + V_{\text{LN}_{\text{TOT}}} + \frac{\alpha}{\mu_{\text{LN}_{\text{TOT}}}} \tilde{V}_{\text{LN}_{\text{TOT}}}}{\sum_{o \notin \{\text{liver}\}} V_o + \sum_{\substack{o \notin \{\text{liver,RA} \\ \&\text{RV,LA}\&\text{LV}\}}} \frac{\tilde{V}_o}{\mu_o} + \lambda \left(V_{\text{liver}} + \frac{\tilde{V}_{\text{liver}}}{\mu_{\text{liver}}} \right) + V_{\text{LN}_{\text{TOT}}} + \sum_{\substack{o' \notin \{\text{spleen,heart} \\ \text{lung,RA}\&\text{RV,} \\ \text{PC,LA}\&\text{LV,liver}\}}} \frac{\alpha_{o'}}{\mu_{\text{LN}_{o'}}} \tilde{V}_{\text{LN}_{o'}} + \frac{\alpha_{\text{liver}}}{\mu_{\text{LN}_{\text{liver}}}} \tilde{V}_{\text{LN}_{\text{liver}}} + \frac{\alpha_{\text{med}}}{\mu_{\text{LN}_{\text{med}}}} \tilde{V}_{\text{LN}_{\text{med}}}}. \tag{3.38}$$

A summary of the derived mapping variables and steady-state cell concentrations is shown in Table 3.2.

3.2.3 Parameterisation

Multiple and single lymph node model were parameterised based on the human reference data as described in Section 2.2.3. Extravasation and return parameters for all organs, e_o and μ_o, and lymph node compartments, $e_{\text{LN}_{\text{TOT}}}$ and $\mu_{\text{LN}_{\text{TOT}}}$ (for the lumped lymph node compartment in the single lymph node model), e_{LN_o} and μ_{LN_o} (for organ-draining lymph node compartments in the multiple lymph node model), were defined to vary uniformly between 0 and 1. The variability ranges for the model parameters are summarised in Table 2.2.

Compartments	Multiple lymph node model	Single lymph node model	Mapping variable
Organ, o, except liver	C_o	C'_o	C_o/C'_o (as given by Equation (3.38))
	$\tilde{C}_o = \frac{1}{\mu_o} C_o$	$\tilde{C}'_o = \frac{1}{\mu_o} C'_o$	C_o/C'_o
Liver	$C_{\text{liver}} = \lambda C_o$	$C'_{\text{liver}} = \lambda C'_o$	C_o/C'_o
	$\tilde{C}_{\text{liver}} = \frac{\lambda}{\mu_{\text{liver}}} C_o$	$\tilde{C}'_{\text{liver}} = \frac{\lambda}{\mu_{\text{liver}}} C'_o$	C_o/C'_o
Organ, o, -draining lymph nodes, except liver-draining and mediastinal lymph nodes	$C_{\text{LN}_o} = C_o$	—	C_o/C'_o
	$\tilde{C}_{\text{LN}} = \frac{1}{\mu_{\text{LN}_o}} C_o$	—	$\frac{C_{\text{LN}_o}}{C'_{\text{LN}}} = \frac{\alpha_o}{\alpha} \frac{\frac{1}{\mu_{\text{LN}_o}}}{\frac{1}{\mu_{\text{LN}_{\text{TOT}}}}} \frac{C_o}{C'_o}$
Liver-draining lymph nodes	$C_{\text{LN}_{\text{liver}}} = C_o$	—	C_o/C'_o
	$\tilde{C}_{\text{LN}_{\text{liver}}} = \frac{\alpha_{\text{liver}}}{\mu_{\text{LN}_{\text{liver}}}} C_o$	—	$\frac{C_{\text{LN}_{\text{liver}}}}{C'_{\text{LN}}} = \frac{\alpha_{\text{liver}}}{\alpha} \frac{\frac{1}{\mu_{\text{LN}_{\text{liver}}}}}{\frac{1}{\mu_{\text{LN}_{\text{TOT}}}}} \frac{C_o}{C'_o}$
Mediastinal lymph nodes	$C_{\text{LN}_{\text{med}}} = C_o$	—	C_o/C'_o
	$\tilde{C}_{\text{LN}_{\text{med}}} = \frac{\alpha_{\text{med}}}{\mu_{\text{LN}_{\text{med}}}} C_o$	—	$\frac{C_{\text{LN}_{\text{med}}}}{C'_{\text{LN}}} = \frac{\alpha_{\text{med}}}{\alpha} \frac{\frac{1}{\mu_{\text{LN}_{\text{med}}}}}{\frac{1}{\mu_{\text{LN}_{\text{TOT}}}}} \frac{C_o}{C'_o}$
Single (all) lymph node(s)	—	$C_{\text{LN}_{\text{TOT}}} = C'_o$	$\frac{C_{\text{LN}}}{C'_{\text{LN}}} = \alpha_{\text{LN}_{\text{TOT}}} \frac{C_o}{C'_o}$
	—	$\tilde{C}_{\text{LN}_{\text{TOT}}} = \frac{\alpha}{\mu_{\text{LN}_{\text{TOT}}}} C'_o$	

Table 3.2: Summary of the derived steady-state cell concentrations in the multiple (second column) and single lymph node models (third column) and mapping variables in all model compartments (last column). The ratio C_o/C'_o is given by Equation (3.38), and the parameters λ, α_o, α_{med}, α_{liver}, α and $\alpha_{\text{LN}_{\text{TOT}}}$ are given by Equations (3.12), (3.19), (3.20), (3.21), (3.23) and (3.26), respectively.

3.2.4 Mapping variable simulation

The mapping variables: the blood and organ mapping variable, C_o/C'_o, the total lymph node mapping variable, $C_{\text{LN}}/C'_{\text{LN}}$, and single lymph node mapping variables, $C_{\text{LN}_o}/C'_{\text{LN}}$, $C_{\text{LN}_{\text{liver}}}/C'_{\text{LN}}$ and $C_{\text{LN}_{\text{med}}}/C'_{\text{LN}}$, were computed varying the input parameters B_o, V_o, $\tilde{V}_o$, e_o, μ_o for each organ, and $B_{\text{LN}_{\text{TOT}}}$, $V_{\text{LN}_{\text{TOT}}}$, $\tilde{V}_{\text{LN}_{\text{TOT}}}$, e_{LN_o}, μ_{LN_o} for lymph node compartments. Variability ranges for the anatomical parameters (B_o, V_o, $\tilde{V}_o$, $B_{\text{LN}_{\text{TOT}}}$, $V_{\text{LN}_{\text{TOT}}}$, $\tilde{V}_{\text{LN}_{\text{TOT}}}$) were defined as described in Section 3.2.3, while extravasation and return parameters (e_o, μ_o, $e_{\text{LN}_{\text{TOT}}}$, $\mu_{\text{LN}_{\text{TOT}}}$, e_{LN_o}, μ_{LN_o}) were varied uniformly between 0 and 1. Lymph node extravasation, $e_{\text{LN}_{\text{TOT}}}$ and e_{LN_o}, and return parameters, $\mu_{\text{LN}_{\text{TOT}}}$ and μ_{LN_o}, were assumed identical across all lymph node compartments in both models for each parameter sampling iteration. This parameter space was sampled 1,000,000 times by randomly sampling each input parameter value from a uniform probability distribution, defined by those variability ranges. For each iteration, the blood and organ mapping variable, C_o/C'_o, the total lymph node mapping variable, $C_{\text{LN}}/C'_{\text{LN}}$, and single lymph node mapping variables, $C_{\text{LN}_o}/C'_{\text{LN}}$ (for lymph nodes other than the liver-draining and mediastinal), $C_{\text{LN}_{\text{liver}}}/C'_{\text{LN}}$ (for the liver-draining lymph nodes) and $C_{\text{LN}_{\text{med}}}/C'_{\text{LN}}$ (for mediastinal lymph nodes), were calculated based on the randomly sampled parameter set. Means and 95% confidence intervals were computed for each resulting distribution. The summary statistics of the computed distributions, shown in Figure 3.4(b), was represented with a box plot using the in-built Matlab function *boxplot*. For each distribution, the central mark on the box indicates the median, and the edges of the box represent the 25th and 75th percentiles, respectively. The whiskers extend to the most extreme points not considered outliers and defined as values that are more than 1.5 times the interquartile range away from the edges of the box.

To ensure convergence, the mapping variables were evaluated for different numbers of sampling points in the parameter space, starting from 1,000, and increasing the number of sample points by a factor of 10. All mapping variables exhibited convergence in their means and confidence intervals for 1,000,000 sampling points. While this number is relatively small compared to the number of model parameters, the convergence stems from diminished sensitivity due to the structure of the considered functions (see Equation (3.38) as an example), and the number of parameter samples was thus observed to be sufficient.

3.2.5 Single lymph node mapping variable: Local sensitivity analysis

A local sensitivity analysis was performed on the single lymph node mapping variables (Equations (3.27), (3.28) and (3.29)) to identify the most influential parameters governing the behaviour of the variables. The parameters tested in the local sensitivity analysis included the blood flow, B_o, blood volume, V_o, organ volume, $\tilde{V}_o$, extravasation and return parameters, e_o

and μ_o, respectively, for each organ, and the total blood flow, $B_{\mathrm{LN_{TOT}}}$, total blood volume, $V_{\mathrm{LN_{TOT}}}$, total volume, $\tilde{V}_{\mathrm{LN_{TOT}}}$, extravsation and return parameters, e_{LN_o} and μ_{LN_o}, respectively, for lymph node compartments. Extravasation, e_{LN_o}, and return parameters, μ_{LN_o}, were assumed identical across all lymph node compartments in both models.

A local one-at-a-time (OAT) method was performed by varying one of the input parameters by $\pm 25\%$, while keeping the rest of the parameters at their baseline levels, as described in Section 3.2.3. The parameter value was then returned to its baseline value and the step was repeated for each of the input parameters. Sensitivity of each of the 16 single lymph node mapping variables was measured by monitoring the change in the mapping variable using a local sensitivity index, S_{ij}, defined in terms of a partial derivative of each mapping variable, here denoted V_j for clarity, with respect to the varied parameter P_i:

$$S_{ij} = \frac{\partial V_j}{\partial P_i} \Big/ \frac{V_j}{P_i}, \tag{3.39}$$

where i and j run over all parameters and single lymph node mapping variables, respectively. The derivatives were normalised for dimensional and scaling reasons.

3.2.6 Single lymph node mapping variable: eFAST

A global sensitivity analysis was performed on the single lymph node mapping variables (Equations (3.27), (3.28) and (3.29)) to identify the most influential parameters across the parameters space. A variance-based method, extended Fourier amplitude sensitivity testing (eFAST), was implemented using the Matlab code developed and made available online by Kirschner Lab, University of Michigan [66].

Since sampling all parameters in both models is not feasible, due to eFAST scaling constraints with respect to the number of parameters, we utilised the fact that the single lymph node mapping variables in Equations (3.27), (3.28) and (3.29) can be written in terms of the lumped parameters and a relatively small number of other parameters to be varied. For instance, Equation (3.27), defining the single lymph node mapping variable for lymph nodes other than the mediastinal and liver-draining lymph nodes, can be expressed as follows:

$$\begin{aligned}\frac{C_{\mathrm{LN}_o}}{C'_{\mathrm{LN}}} &= \frac{\alpha_o}{\alpha}\frac{\frac{1}{\mu_{\mathrm{LN}_o}}}{\frac{1}{\mu_{\mathrm{LN}_{\mathrm{TOT}}}}}\frac{C_o}{C'_o} \\ &= \frac{\frac{e_{\mathrm{LN}_o}B_{\mathrm{LN}_o}+e_oB_o}{e_{\mathrm{LN}_o}B_{\mathrm{LN}_o}+e_o\mu_oB_o}}{\frac{e_{\mathrm{LN}_{\mathrm{TOT}}}B_{\mathrm{LN}_{\mathrm{TOT}}}+\sum_o e_oB_o+e_{\mathrm{liver}}\lambda(e_{\mathrm{spleen}}\mu_{\mathrm{spleen}}B_{\mathrm{spleen}}+\sum_{o\in\{\mathrm{mesentery}\}}B_o(1-e_o))}{e_{\mathrm{LN}_{\mathrm{TOT}}}B_{\mathrm{LN}_{\mathrm{TOT}}}+\sum_o e_o\mu_oB_o+e_{\mathrm{liver}}\mu_{\mathrm{liver}}(e_{\mathrm{spleen}}\mu_{\mathrm{spleen}}B_{\mathrm{spleen}}+\sum_{o\in\{\mathrm{mesentery}\}}B_o(1-e_o))}}\frac{\frac{1}{\mu_{\mathrm{LN}_o}}}{\frac{1}{\mu_{\mathrm{LN}_{\mathrm{TOT}}}}}\frac{C_o}{C'_o} \\ &= \frac{\frac{e_{\mathrm{LN}_o}B_{\mathrm{LN}_o}+e_oB_o}{e_{\mathrm{LN}_o}B_{\mathrm{LN}_o}+e_o\mu_oB_o}}{\frac{e_{\mathrm{LN}_{\mathrm{TOT}}}B_{\mathrm{LN}_{\mathrm{TOT}}}+e_oB_o+\Delta_{\mathrm{ex}_o}}{e_{\mathrm{LN}_{\mathrm{TOT}}}B_{\mathrm{LN}_{\mathrm{TOT}}}+e_o\mu_oB_o+\Delta_{\mathrm{dr}_o}}}\frac{\frac{1}{\mu_{\mathrm{LN}_o}}}{\frac{1}{\mu_{\mathrm{LN}_{\mathrm{TOT}}}}}\frac{C_o}{C'_o},\end{aligned} \tag{3.40}$$

where the expressions for α_o and α introduced in the second line were simplified using lumped parameters Δ_{ex_o}, describing the rate of cells that have extravasated into organs with lymphatics other than the organ drained by the lymph node group of interest:

$$\Delta_{\mathrm{ex}_o} = \sum_{i\neq o} e_iB_i + e_{\mathrm{liver}}\lambda(e_{\mathrm{spleen}}\mu_{\mathrm{spleen}}B_{\mathrm{spleen}} + \sum_{m\in\{\mathrm{mesentery}\}} B_m(1-e_m)), \tag{3.41}$$

and Δ_{dr_o}, describing the rate of cells that have extravasated into and have been drained by organs with lymphatics other than the organ drained by the lymph node group of interest:

$$\Delta_{\mathrm{dr}_o} = \sum_{i\neq o} e_i\mu_iB_i + e_{\mathrm{liver}}\mu_{\mathrm{liver}}(e_{\mathrm{spleen}}\mu_{\mathrm{spleen}}B_{\mathrm{spleen}} + \sum_{m\in\{\mathrm{mesentery}\}} B_m(1-e_m)), \tag{3.42}$$

where $m \in \{\mathrm{mesentery}\}$ includes the spleen, stomach, pancreas, small and large intestine. Given Equation (3.40) and the fact that B_{LN_o} is related to $B_{\mathrm{LN}_{\mathrm{TOT}}}$ as given by Equation (2.14), the parameter groupings varied in eFAST included the blood mapping variable, C_o/C'_o, the ratio of drained organ's volume to the sum of volumes of all organs with lymphatics, $\tilde{V}_o/\sum_i \tilde{V}_i$, and the parameter groupings Δ_{ex_o} and Δ_{dr_o}, introduced above. The remaining single parameters were the lymph node extravasation parameters, e_{LN_o} and $e_{\mathrm{LN}_{\mathrm{TOT}}}$ (assumed to be identical across all lymph node compartments in both models), total blood flow to lymph node compartments, $B_{\mathrm{LN}_{\mathrm{TOT}}}$, extravasation parameter for the drained organ, e_o, return parameter of the drained organ, μ_o and the blood flow to the drained organ, B_o. As previously, the lymph node return rates for each organ, μ_{LN_o} and $\mu_{\mathrm{LN}_{\mathrm{TOT}}}$, were assumed identical across all lymph node compartments in both models and varied in eFAST simulation.

The sensitivity analysis was considered with a sampling of the lumped parameters from their distributions obtained as described in Section 3.2.4, cut off at the 95% confidence interval. However, the eFAST algorithm is designed for uniform sampling, in contrast to the distribution

of the lumped parameters, C_o/C'_o, $\tilde{V}_o/\sum_i \tilde{V}_i$, Δ_{ex_o} and Δ_{dr_o}. We, therefore, uniformly sampled, for example, $\Delta_{\mathrm{dr,U}} := f(\Delta_{\mathrm{dr}_o})$ within eFAST rather than Δ_{dr_o}, where the continuous bijection $f(\cdot)$ is defined uniquely by the constraint that, when $\Delta_{\mathrm{dr,U}}$ is uniform then Δ_{dr_o} is distributed according to the method described in Section 3.2.4. By applying the function inverse f^{-1} to the the precursor, $\Delta_{\mathrm{dr,U}}$, Δ_{dr_o} is generated according to its distribution across the parameter space, with analogous procedures for the other lumped parameters.

The parameter value sets for the uniform precursors of the lumped parameters C_o/C'_o, $\tilde{V}_o/\sum_i \tilde{V}_i$, Δ_{ex_o} and Δ_{dr_o} and the other parameters of interest in Equations (3.27), (3.28) and (3.29) were generated using using Fourier frequency curves through the variability ranges. Each of these parameters was sampled $N_S = 3000$ times with a frequency of $\omega_i = 374$ from a uniform probability distribution [12], and $N_R = 6$ re-sampling curves. Similarly to the methodology discussed in Section 2.2.5.2, the lumped parameter C_o/C'_o depends on some of the parameters varied independently during the analysis. However, having investigated the dependence of C_o/C'_o on those parameters using local sensitivity analysis and principal component analysis, the dependence was shown to be weak, given the number of parameters in the expression (see Equation (3.38)). Therefore, the impact of not accommodating this correlation in the sampling is minimal.

3.2.7 Single lymph node compartment concentration partitioning

The derived single lymph node mapping variables can be used in conjunction with the single lymph node model steady-state solution to estimate the steady-state cell concentrations in specific lymph node group compartments, without the need to solve the multiple lymph node trafficking model explicitly. Based on the results of the local and global sensitivity analyses (Section 3.3.3), which indicated the return parameter of a drained organ, o, μ_o, as the most influential parameters determining the single lymph node mapping variable (Equations (3.27), (3.28) and (3.29)), the single lymph node mapping variables can be approximated in terms of the reciprocal of the return parameter, μ_o, and an appropriate proportionality factor, β_o:

$$\frac{C_{\mathrm{LN}_o}}{C'_{\mathrm{LN}}} \approx \beta_o \frac{1}{\mu_o}. \tag{3.43}$$

The inverse proportionality of the single mapping variable and the return parameter, μ_o, can

be obtained by considering the expression for the parameter α_o (Equation (3.19)):

$$\alpha_o = \frac{e_{\mathrm{LN}_o} B_{\mathrm{LN}_o} + e_o B_o}{e_{\mathrm{LN}_o} B_{\mathrm{LN}_o} + e_o \mu_o B_o} = \frac{\frac{e_{\mathrm{LN}_o} B_{\mathrm{LN}_o}}{e_o B_o} + 1}{\frac{e_{\mathrm{LN}_o} B_{\mathrm{LN}_o}}{e_o B_o} + \mu_o} = \frac{\epsilon_o + 1}{\epsilon_o + \mu_o}, \tag{3.44}$$

which defines the variable ϵ_o, describing the ratio of the rate of extravasation in the organ, o, -draining lymph node group and the rate of extravasation in the organ drained by that lymph node group. Therefore we get:

$$\alpha_o \approx \frac{1}{\mu_o} \iff \epsilon_o \ll 1, \epsilon_o \ll \mu_o \,. \tag{3.45}$$

As $B_{\mathrm{LN}_{\mathrm{TOT}}} \ll B_o$ (see Table 2.2), and $\frac{B_{\mathrm{LN}_o}}{B_{\mathrm{LN}_{\mathrm{TOT}}}} = \frac{\tilde{V}_o}{\sum_i \tilde{V}_i} < 1$ (Equation (2.14)), therefore $B_{\mathrm{LN}_o} \ll B_o$. Hence, Equation (3.45) is a reasonable assumption and the single lymph node cell concentration partitioning factor, $\mathrm{PF}_{\mathrm{LN}_o}$ is then defined as:

$$\mathrm{PF}_{\mathrm{LN}_o} = \bar{\beta}_o \frac{1}{\mu_o}, \tag{3.46}$$

where the constant $\bar{\beta}_o$ is the mean over parameter space samples of the proportionality factor β_o, evaluated as:

$$\beta_o = \frac{C_{\mathrm{LN}_o}}{C'_{\mathrm{LN}}} \Big/ \frac{1}{\mu_o}. \tag{3.47}$$

For the mediastinal lymph node group, the parameter α_{med}, defined via Equation (3.20), is rewritten as:

$$\alpha_{\mathrm{med}} = \frac{\epsilon_{\mathrm{med}} + 1}{\epsilon_{\mathrm{med}} + \mu_{\mathrm{heart}} \left(\frac{e_{\mathrm{heart}} B_{\mathrm{heart}}}{e_{\mathrm{heart}} B_{\mathrm{heart}} + e_{\mathrm{lung}} B_{\mathrm{lung}}} \right) + \mu_{\mathrm{lung}} \left(\frac{e_{\mathrm{lung}} B_{\mathrm{lung}}}{e_{\mathrm{heart}} B_{\mathrm{heart}} + e_{\mathrm{lung}} B_{\mathrm{lung}}} \right)}, \tag{3.48}$$

where the parameter ϵ_{med} is defined to be:

$$\epsilon_{\mathrm{med}} = \frac{e_{\mathrm{LN}_{\mathrm{med}}} B_{\mathrm{LN}_{\mathrm{med}}}}{e_{\mathrm{heart}} B_{\mathrm{heart}} + e_{\mathrm{lung}} B_{\mathrm{lung}}}. \tag{3.49}$$

As a result, the partitioning factor accounts for the dual drainage of T cells from the heart

and lungs blood supply and takes the form:

$$\mathrm{PF}_{\mathrm{LN}_{\mathrm{med}}} = \bar{\beta}_{\mathrm{med}} \frac{1}{\mu_{\mathrm{heart}} + \mu_{\mathrm{lungs}}}. \tag{3.50}$$

Similarly, the parameter $\epsilon_{\mathrm{liver}}$ is rewritten for the liver-draining lymph nodes to highlight the anatomy of the hepatic circulation, through which cell from the mesenteric organs traffic:

$$\epsilon_{\mathrm{liver}} = \frac{e_{\mathrm{LN}_{\mathrm{liver}}} B_{\mathrm{LN}_{\mathrm{liver}}}}{e_{\mathrm{liver}} \left(B_{\mathrm{liver}} + \lambda \left(e_{\mathrm{spleen}} \mu_{\mathrm{spleen}} B_{\mathrm{spleen}} + \sum_{o \in \{\mathrm{mesentery}\}} B_o (1 - e_o) \right) \right)}. \tag{3.51}$$

The parameter α_{liver} defined in Equation (3.21) can be rewritten as:

$$\alpha_{\mathrm{liver}} = \frac{\epsilon_{\mathrm{liver}} + 1}{\epsilon_{\mathrm{liver}} + \mu_{\mathrm{liver}} \frac{B_{\mathrm{liver}} + \left(e_{\mathrm{spleen}} \mu_{\mathrm{spleen}} B_{\mathrm{spleen}} + \sum_{o \in \{\mathrm{mesentery}\}} B_o (1 - e_o) \right)}{B_{\mathrm{liver}} + \lambda \left(e_{\mathrm{spleen}} \mu_{\mathrm{spleen}} B_{\mathrm{spleen}} + \sum_{o \in \{\mathrm{mesentery}\}} B_o (1 - e_o) \right)}}. \tag{3.52}$$

The additional terms in the the expressions for α_{med} (Equation (3.48)) and α_{liver} (Equation (3.52), see Equation (3.44)), imply the approximation in Equation (3.45) will be less accurate for those lymph node groups, even for negligibly small values of the parameter ϵ_o.

The single lymph node steady-state concentration partitioning factor given in Equation (3.46), therefore, is defined as a fraction of the steady-state cell concentration in the lumped lymph node compartment. Given an estimate of the drained organ's return parameter, μ_o, and the lymph node steady-state concentration in the single lymph node model, the partitioning factor can be used to approximate the steady-state cell concentration in the specific lymph node group. The proportionality factor, $\bar{\beta}_o$, necessary for the approximation of the partitioning factor and the median of the variable ϵ_o, quantifying the quality of the approximation in Equation (3.46), were computed varying the input parameters B_o, V_o, $\tilde{V}_o$, e_o, μ_o for each organ, and $B_{\mathrm{LN}_{\mathrm{TOT}}}$, $V_{\mathrm{LN}_{\mathrm{TOT}}}$, $\tilde{V}_{\mathrm{LN}_{\mathrm{TOT}}}$, e_{LN_o}, μ_{LN_o} for lymph node compartments. Variability ranges for the anatomical parameters (B_o, V_o, $\tilde{V}_o$, $B_{\mathrm{LN}_{\mathrm{TOT}}}$, $V_{\mathrm{LN}_{\mathrm{TOT}}}$, $\tilde{V}_{\mathrm{LN}_{\mathrm{TOT}}}$) were defined as described in Section 3.2.3, while extravasation and return parameters (e_o, μ_o, e_{LN_o}, μ_{LN_o}) were varied uniformly between 0 and 1. Extravasation, e_{LN_o}, and return parameters, μ_{LN_o}, were assumed identical across all lymph node compartments in both models for each parameter sampling iteration. This parameter space was sampled 1,000,000 times by randomly sampling each input parameter value from a uniform probability distribution, defined by those variability ranges. For each iteration, the proportionality factor, β_o (Equation (3.47)), and the parameter, ϵ_o (Equation (3.44)), were calculated based on the randomly sampled parameter set. Medians,

means and 95% confidence intervals were computed for each resulting distribution. The accuracy of the approximation was assessed by comparing the single lymph node cell concentration as predicted by Equation (3.46) and the exact solution (Equations (3.19), (3.20) and (3.21)). The relative difference between the prediction and the exact solution for each lymph node group, Δ_{rel_o}, was evaluated for each iteration:

$$\Delta_{\text{rel}_o} = \frac{C_{\text{LN}_o} - \text{PF}_{\text{LN}_o} C'_{\text{LN}}}{C_{\text{LN}_o}} = \frac{C_{\text{LN}_o} - \bar{\beta}_o \frac{1}{\mu_o} C'_{\text{LN}}}{C_{\text{LN}_o}}, \tag{3.53}$$

where C_{LN_o} is the exact steady-state cell concentration in an organ, o, -draining lymph node group and the proportionality factor, $\bar{\beta}_o$, is the evaluated mean slope of the single lymph node concentration partitioning factor for an organ, o, -draining lymph node group, given in Equation (3.46).

3.3 Results

Two PBPK frameworks describing the trafficking and distribution of circulating immune cells and cellular therapies in humans were used to compare the impact of the compartmentalisation of lymph node tissue on the models' predictions. By considering steady-state biodistributions in the trafficking model with multiple (Figure 3.2(a)) and a single lumped lymph node compartments (Figure 3.2(b)), we characterised the difference in the resulting biodistributions utilising a derived mapping between the two sets of solutions to the ODE systems representing the multiple and single lymph node trafficking models. Given the clear advantage of the single lymph node trafficking model in the reduced number of parameters (101 vs 176) and compartments in the model (22 vs 37), compared to the multiple lymph node trafficking model, we sought to investigate whether the single lymph node trafficking model combined with the derived mapping framework can serve as a tool to estimate the steady-state cell concentration in specific lymph node groups, without the need to rely on the highly more complex multiple lymph node trafficking model.

3.3.1 Main mapping variables: Distributions

The derived mapping framework constitutes a set of functions describing the relative difference in the steady-state biodistribution between the single and multiple lymph node trafficking models. For each organ within both models, a mapping variable is defined by a function of model parameters and gives the ratio of the steady-state cell concentration in the compartment

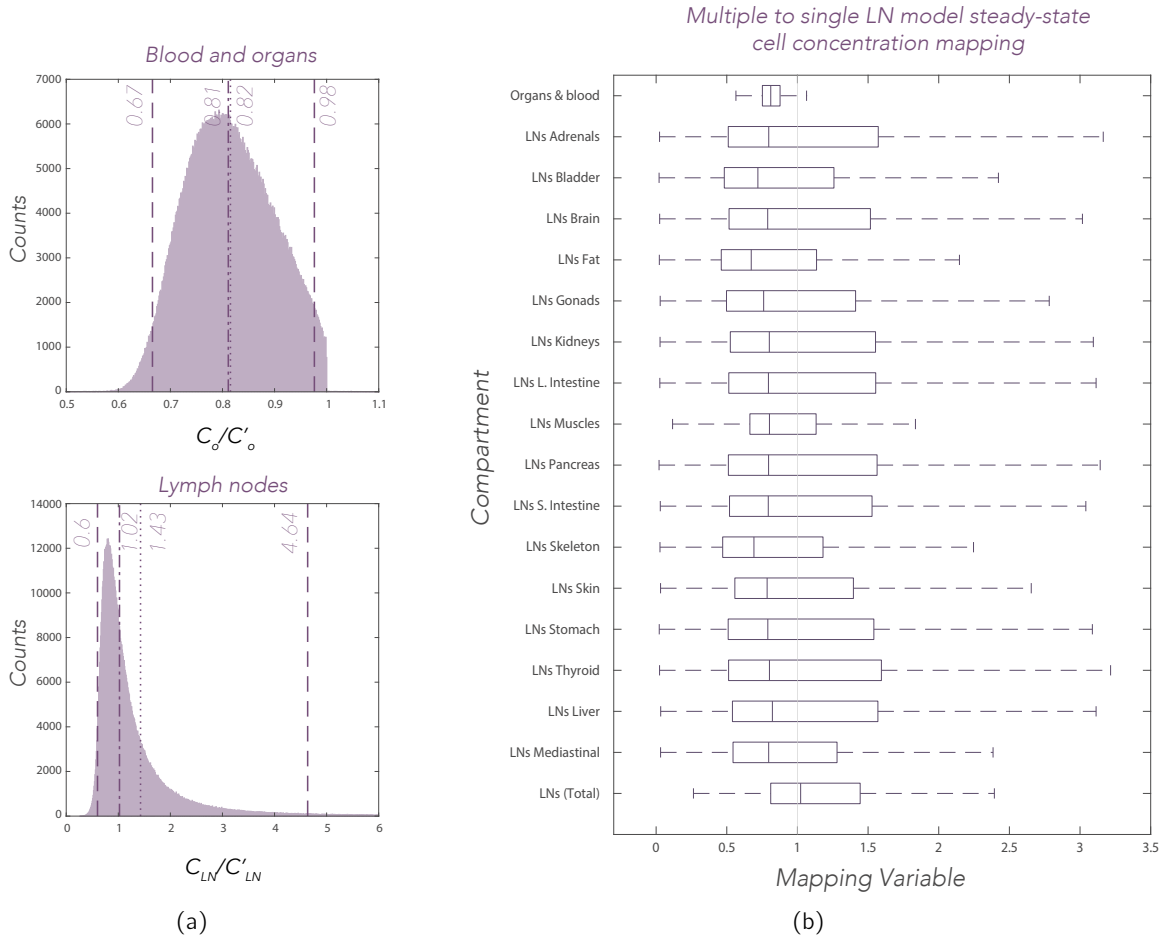


Figure 3.4: (a) Distributions of the blood and organ mapping variable (upper) and the total lymph node mapping variable (lower). Dotted, dash-dot and dashed lines correspond to means, medians and 95% confidence intervals of the plotted distributions, respectively. (b) A box plot visualising the summary statistics of the blood and organ, single and total lymph node mapping variables. On each box, the central mark indicates the median, and the edges of the box represent the 25th and 75th percentiles, respectively. The whiskers extend to the most extreme data points not considered outliers. Outliers were defined as values that are more than 1.5 times the interquartile range away from the edges of the box. See Sections 3.2.3 and 3.2.4 for details on parameters.

of interest in the multiple lymph node trafficking model to the corresponding steady-state cell concentration in the single lymph node trafficking model. See Section 3.2.2 for the full derivation and Section 3.2.3 for the parameterisation.

Despite the high dimensionality of the trafficking models, the steady state mapping framework demonstrated that the relative difference in the predicted steady-state cell concentrations across all organs can be described by two mapping variables. The derivation further showed that, when comparing the steady-state cell concentrations between the single and multiple lymph node models in any organ compartment that is not a lymph node compartment, all organ compartments result in the same steady-state cell concentration ratio. This ratio, referred to as the blood and organ mapping variable, C_o/C'_o (Equation (3.38)), therefore, describes

the relative change in the steady-state cell concentration in the multiple lymph node model with respect to the corresponding concentration in the single lymph node model, in all vascular and interstitial organ compartments (see Table 3.2). The exceptions are the lymph node compartments, where an analogous variable has to be redefined to account for the lymph node compartmentalisation in the multiple lymph node model. As a result, the cell biodistribution in the lymph node compartments between the two models is compared using the total lymph node mapping variable, $C_{\mathrm{LN}}/C'_{\mathrm{LN}}$. The total lymph node mapping variable (Equation (3.26)) was defined as the ratio of the sum of steady-state cell localisations over the lymph node compartments in the multiple lymph node model to the steady-state cell localisation in the single lymph node model. This is also equivalent to the ratio of the net steady-state cell concentration in the lymph node compartments in the multiple lymph node model to the steady-state cell concentration in the lumped lymph node compartment in the single lymph node model.

The distributions of the blood and organs mapping variable, C_o/C'_o, and the total lymph node mapping variable, $C_{\mathrm{LN}}/C'_{\mathrm{LN}}$, were were plotted as histograms in Figure 3.4(a). The blood and organs mapping variable, C_o/C'_o, was characterised by a relatively symmetric distribution, centred around the median and mean values of 0.81 and 0.82, respectively, and a 95% confidence interval of 0.67 – 0.98. The total lymph node mapping variable, $C_{\mathrm{LN}}/C'_{\mathrm{LN}}$, resulted in a distribution centered very close to 1 (median of 1.02). In contrast to the blood and organ mapping variable, C_o/C'_o, the total lymph node mapping variable, $C_{\mathrm{LN}}/C'_{\mathrm{LN}}$, distribution was visibly asymmetrical, with a positive skew and 95% confidence interval of 0.6 – 4.64, resulting in a distribution mean of 1.43. The results indicate that, on average, the multiple lymph node trafficking model predicts organ and blood cell concentration reduced by about 20% compared to the single lymph node trafficking model, but, on average, comparable lymph node cell concentration. This, in turn, suggests that, if the overall lymph node tissue exposure is of interest, increasing the complexity of a trafficking model by compartmentalising lymph nodes into organ-specific compartments might not be necessary.

3.3.2 Lymph nodes mapping variables: Distributions

The comparable cell concentration predicted across the multiple lymph node compartments and in the single lumped lymph node compartment indicates the single lymph node trafficking model might be a more appropriate modelling tool for applications where the overall lymph node cell exposure is of relevance. However, it remains unclear what level of lymph node compartmentalisation is appropriate for modelling applications where a particular group of lymph nodes is of interest, rather than the whole-body lymph node tissue. For instance, the progression of lymphoma initially usually occurs within distinct lymph node groups.

The derived mapping framework allows constructing mapping variables for each organ-draining lymph node compartment, similarly to the blood and organs, C_o/C'_o, and total lymph node, $C_{\mathrm{LN}}/C'_{\mathrm{LN}}$, mapping variables. A set of such single lymph node mapping variables then consists of a set of functions of input parameters (one function per each lymph node compartment in the multiple lymph node model) and each function expresses the cell concentration in each of the lymph node group compartments as a fraction of the cell concentration in the lumped lymph node compartment in the single lymph node model. A single lymph node mapping variable defined in such a way, therefore, functions as a partitioning factor that can be used to estimate the cell concentration in a specific lymph node group compartment based on a single lymph node trafficking model steady-state solution.

The distributions of the single lymph node mapping variables were evaluated for each lymph node compartment and the statistics of the resulting distributions were summarised using a box plot, shown in Figure 3.4(b). All single lymph node mapping variables evaluated over the parameter space resulted in comparable distributions with similar medians (roughly 0.8) and the 25th to 75th percentile ranges. The whiskers, indicating the spread and the degree of the extremity of the distributions, were more variable among different lymph node compartments, with the muscle- and adipose tissue-draining lymph node groups resulting in the most narrow mapping variables distributions. Compared to the blood and organ mapping variable, C_o/C'_o (included in the box plot in Figure 3.4(b) for comparison), the single lymph node mapping variables were characterised by noticeably wider distributions, resembling more the total lymph node, $C_{\mathrm{LN}}/C'_{\mathrm{LN}}$, mapping variable distribution, although with still more variability in computed values than the total lymph node mapping variable.

3.3.3 Sensitivity analyses

Local and global sensitivity analyses were performed to identify the parameters driving the comparatively wider distributions of the single lymph node mapping variables (Equations (3.27), (3.28) and (3.29)).

3.3.3.1 Local sensitivity analysis

A local, one-at-a-time, sensitivity analysis was performed by varying one of the input parameters and keeping the rest of the parameters at their baseline values. Sensitivity to each parameter for all single lymph node mapping variables was measured by monitoring the change in the single lymph node mapping variable with respect to the change in each parameter, and expressed as a normalised sensitivity index, as defined by Equation (3.39) in Section 3.3.3.1. Local sensitivity

analysis yielded a set of 101 sensitivity indices for each of the 16 single lymph node mapping variables, listed in Table 3.3. All 16 single lymph node mapping variables showed primary sensitivity to the return parameter associated with the organ drained by the corresponding lymph node group. For instance, the mapping variable of the adrenal-draining lymph node group compartment (see the second column in Table 3.3) was noticeably more sensitive to the adrenal return parameter, μ_{adrenals}, than to all the remaining parameters. The strong sensitivity of the single lymph node mapping variables to the corresponding organ's return parameters follows from the definition of the return parameter. The parameter μ_o determines the rate at which cells leave the associated organ's interstitium, are subsequently drained by the lymphatics and accumulate in the organ-specific lymph node compartment. The return parameter thus affects directly the resulting steady-state concentration in the organ-specific lymph node compartment.

Table 3.3: Results of the local sensitivity analysis on the single lymph node mapping variable for each lymph node group compartment. Sensitivity of the single lymph node mapping variables associated with each lymph node group (Equations (3.27), (3.28) and (3.29)) to each input parameter (first column) in turn was measured using a normalised sensitivity index, as defined in Equation (3.39). Sensitivity indices resulting in absolute values smaller than 0.01 were indicated with 0 in the table. *Med.* - mediastinal, *L. Int.* - large intestine, *S. Int.* - small intestine.

	Lymph node group															
Parameter	Adrenals	Bladder	Brain	Fat	Gonads	Med.	Kidneys	L. Int.	Liver	Muscles	Pancreas	S. Int.	Skeleton	Skin	Stomach	Thyroid
e_{adrenals}	0.03	0	0	0	0	0	0	0	0	0	0	0	0	0	0	0
e_{bladder}	0	0.28	0	0	0	0	0	0	0	0	0	0	0	0	0	0
e_{brain}	-0.02	-0.02	0.04	-0.02	-0.02	-0.02	-0.02	-0.02	-0.02	-0.02	-0.02	-0.02	-0.02	-0.02	-0.02	-0.02
e_{fat}	-0.02	-0.02	-0.02	0.56	-0.02	-0.02	-0.02	-0.02	-0.02	-0.02	-0.02	-0.02	-0.02	-0.02	-0.02	-0.02
e_{gonads}	0	0	0	0	0.15	0	0	0	0	0	0	0	0	0	0	0
e_{heart}	-0.01	-0.01	-0.01	-0.01	-0.01	0.06	-0.01	-0.01	-0.01	-0.01	-0.01	-0.01	-0.01	-0.01	-0.01	-0.01
e_{kidneys}	-0.03	-0.03	-0.03	-0.03	-0.03	-0.03	-0.02	-0.03	-0.03	-0.03	-0.03	-0.03	-0.03	-0.03	-0.03	-0.03
$e_{\text{l.int.}}$	-0.01	-0.01	-0.01	-0.01	-0.01	-0.01	-0.01	0.04	-0.01	-0.01	-0.01	-0.01	-0.01	-0.01	-0.01	-0.01
e_{liver}	-0.04	-0.04	-0.04	-0.04	-0.04	-0.04	-0.04	-0.04	0.02	-0.04	-0.04	-0.04	-0.04	-0.04	-0.04	-0.04
e_{lung}	0	0	0	0	0	0.03	0	0	0	0	0	0	0	0	0	0
e_{muscles}	-0.05	-0.05	-0.05	-0.05	-0.05	-0.05	-0.05	-0.05	-0.05	0.38	-0.05	-0.05	-0.05	-0.05	-0.05	-0.05
e_{pancreas}	0	0	0	0	0	0	0	0	0	0	0.06	0	0	0	0	0
$e_{\text{s.int.}}$	-0.01	-0.01	-0.01	-0.01	-0.01	-0.01	-0.01	-0.01	-0.02	-0.01	-0.01	0.02	-0.01	-0.01	-0.01	-0.01
e_{skeleton}	-0.01	-0.01	-0.01	-0.01	-0.01	-0.01	-0.01	-0.01	-0.01	-0.01	-0.01	-0.01	0.40	-0.01	-0.01	-0.01
e_{skin}	-0.01	-0.01	-0.01	-0.01	-0.01	-0.01	-0.01	-0.01	-0.01	-0.01	-0.01	-0.01	-0.01	0.25	-0.01	-0.01
e_{spleen}	0	0	0	0	0	0	0	0	0.03	0	0	0	0	0	0	0
e_{stomach}	0	0	0	0	0	0	0	0	0	0	0	0	0	0	0.07	0
e_{thyroid}	0	0	0	0	0	0	0	0	0	0	0	0	0	0	0	0
e_{LN}	0.20	-0.04	0.18	-0.36	0.09	0.13	0.22	0.19	0.17	-0.19	0.17	0.20	-0.18	-0.02	0.16	0.22
e_{PC}	0	0	0	0	0	0	0	0	0	0	0	0	0	0	0	0
μ_{adrenals}	-1.03	0	0	0	0	0	0	0	0	0	0	0	0	0	0	0

Continuation of Table 3.3

	Lymph node group															
Parameter	Adrenals	Bladder	Brain	Fat	Gonads	Med.	Kidneys	L. Int.	Liver	Muscles	Pancreas	S. Int.	Skeleton	Skin	Stomach	Thyroid
μ_{bladder}	0	-0.73	0	0	0	0	0	0	0	0	0	0	0	0	0	0
μ_{brain}	0.08	0.08	-0.92	0.08	0.08	0.08	0.08	0.08	0.08	0.08	0.08	0.08	0.08	0.08	0.08	0.08
μ_{fat}	0.04	0.04	0.04	-0.29	0.04	0.04	0.04	0.04	0.04	0.04	0.04	0.04	0.04	0.04	0.04	0.04
μ_{gonads}	0	0	0	0	-0.89	0	0	0	0	0	0	0	0	0	0	0
μ_{heart}	0.03	0.03	0.03	0.03	0.03	-0.53	0.03	0.03	0.03	0.03	0.03	0.03	0.03	0.03	0.03	0.03
μ_{kidneys}	0.12	0.12	0.12	0.12	0.12	0.12	-0.93	0.12	0.12	0.12	0.12	0.12	0.12	0.12	0.12	0.12
$\mu_{\text{l.int.}}$	0.03	0.03	0.03	0.03	0.03	0.03	0.03	-0.99	0.03	0.03	0.03	0.03	0.03	0.03	0.03	0.03
μ_{liver}	0.13	0.13	0.13	0.13	0.13	0.13	0.13	0.13	-0.86	0.13	0.13	0.13	0.13	0.13	0.13	0.13
μ_{lungs}	0.02	0.02	0.02	0.02	0.02	-0.33	0.02	0.02	0.02	0.02	0.02	0.02	0.02	0.02	0.02	0.02
μ_{muscles}	0.13	0.13	0.13	0.13	0.13	0.13	0.13	0.13	0.13	-0.42	0.13	0.13	0.13	0.13	0.13	0.13
μ_{pancreas}	0.01	0.01	0.01	0.01	0.01	0.01	0.01	0.01	0.01	0.01	-0.98	0.01	0.01	0.01	0.01	0.01
$\mu_{\text{s.int.}}$	0.06	0.06	0.06	0.06	0.06	0.06	0.06	0.06	0.06	0.06	0.06	-0.96	0.06	0.06	0.06	0.06
μ_{skeleton}	0.04	0.04	0.04	0.04	0.04	0.04	0.04	0.04	0.04	0.04	0.04	0.04	-0.53	0.04	0.04	0.04
μ_{skin}	0.04	0.04	0.04	0.04	0.04	0.04	0.04	0.04	0.04	0.04	0.04	0.04	0.04	-0.72	0.04	0.04
μ_{spleen}	0	0	0	0	0	0	0	0	0	0	0	0	0	0	0	0
μ_{stomach}	0.01	0.01	0.01	0.01	0.01	0.01	0.01	0.01	0.01	0.01	0.01	0.01	0.01	0.01	-0.98	0.01
μ_{thyroid}	0.01	0.01	0.01	0.01	0.01	0.01	0.01	0.01	0.01	0.01	0.01	0.01	0.01	0.01	0.01	-1.05
μ_{LN}	-0.04	-0.04	-0.04	-0.04	-0.04	-0.04	-0.04	-0.04	-0.04	-0.04	-0.04	-0.04	-0.04	-0.04	-0.04	-0.04
μ_{PC}	0	0	0	0	0	0	0	0	0	0	0	0	0	0	0	0
B_{adrenals}	0.03	0	0	0	0	0	0	0	0	0	0	0	0	0	0	0
B_{bladder}	0	0.28	0	0	0	0	0	0	0	0	0	0	0	0	0	0
B_{brain}	-0.02	-0.02	0.04	-0.02	-0.02	-0.02	-0.02	-0.02	-0.02	-0.02	-0.02	-0.02	-0.02	-0.02	-0.02	-0.02
B_{fat}	-0.02	-0.02	-0.02	0.56	-0.02	-0.02	-0.02	-0.02	-0.02	-0.02	-0.02	-0.02	-0.02	-0.02	-0.02	-0.02
B_{gonads}	0	0	0	0	0.15	0	0	0	0	0	0	0	0	0	0	0
B_{heart}	-0.01	-0.01	-0.01	-0.01	-0.01	0.06	-0.01	-0.01	-0.01	-0.01	-0.01	-0.01	-0.01	-0.01	-0.01	-0.01
B_{kidneys}	-0.03	-0.03	-0.03	-0.03	-0.03	-0.03	-0.02	-0.03	-0.03	-0.03	-0.03	-0.03	-0.03	-0.03	-0.03	-0.03
$B_{\text{l.int.}}$	-0.01	-0.01	-0.01	-0.01	-0.01	-0.01	-0.01	0.03	-0.01	-0.01	-0.01	-0.01	-0.01	-0.01	-0.01	-0.01
B_{liver}	-0.01	-0.01	-0.01	-0.01	-0.01	-0.01	-0.01	-0.01	-0.02	-0.01	-0.01	-0.01	-0.01	-0.01	-0.01	-0.01
B_{lung}	0	0	0	0	0	0.03	0	0	0	0	0	0	0	0	0	0
B_{muscles}	-0.05	-0.05	-0.05	-0.05	-0.05	-0.05	-0.05	-0.05	-0.05	0.38	-0.05	-0.05	-0.05	-0.05	-0.05	-0.05
B_{pancreas}	0	0	0	0	0	0	0	0	0	0	0.06	0	0	0	0	0
$B_{\text{s.int.}}$	-0.03	-0.03	-0.03	-0.03	-0.03	-0.03	-0.03	-0.03	-0.01	-0.03	-0.03	0	-0.03	-0.03	-0.03	-0.03
B_{skeleton}	-0.01	-0.01	-0.01	-0.01	-0.01	-0.01	-0.01	-0.01	-0.01	-0.01	-0.01	-0.01	0.40	-0.01	-0.01	-0.01
B_{skin}	-0.01	-0.01	-0.01	-0.01	-0.01	-0.01	-0.01	-0.01	-0.01	-0.01	-0.01	-0.01	-0.01	0.25	-0.01	-0.01
B_{spleen}	-0.01	-0.01	-0.01	-0.01	-0.01	-0.01	-0.01	-0.01	0.03	-0.01	-0.01	-0.01	-0.01	-0.01	-0.01	-0.01
B_{stomach}	0	0	0	0	0	0	0	0	0	0	0	0	0	0	0.07	0
B_{thyroid}	0	0	0	0	0	0	0	0	0	0	0	0	0	0	0	0
$B_{\text{LN}_{\text{TOT}}}$	0.19	0.19	0.19	0.19	0.19	0.19	0.19	0.19	0.19	0.19	0.19	0.19	0.19	0.19	0.19	0.19
V_{adrenals}	0	0	0	0	0	0	0	0	0	0	0	0	0	0	0	0
V_{bladder}	0	0	0	0	0	0	0	0	0	0	0	0	0	0	0	0
V_{brain}	0	0	0	0	0	0	0	0	0	0	0	0	0	0	0	0

Continuation of Table 3.3

Parameter	Lymph node group															
	Adrenals	Bladder	Brain	Fat	Gonads	Med.	Kidneys	L. Int.	Liver	Muscles	Pancreas	S. Int.	Skeleton	Skin	Stomach	Thyroid
V_{fat}	0	0	0	0	0	0	0	0	0	0	0	0	0	0	0	0
V_{gonads}	0	0	0	0	0	0	0	0	0	0	0	0	0	0	0	0
V_{heart}	0	0	0	0	0	0	0	0	0	0	0	0	0	0	0	0
$V_{kidneys}$	0	0	0	0	0	0	0	0	0	0	0	0	0	0	0	0
$V_{l.int.}$	0	0	0	0	0	0	0	0	0	0	0	0	0	0	0	0
V_{liver}	0	0	0	0	0	0	0	0	0	0	0	0	0	0	0	0
V_{lung}	0	0	0	0	0	0	0	0	0	0	0	0	0	0	0	0
$V_{muscles}$	0	0	0	0	0	0	0	0	0	0	0	0	0	0	0	0
$V_{pancreas}$	0	0	0	0	0	0	0	0	0	0	0	0	0	0	0	0
$V_{s.int.}$	0	0	0	0	0	0	0	0	0	0	0	0	0	0	0	0
$V_{skeleton}$	0	0	0	0	0	0	0	0	0	0	0	0	0	0	0	0
V_{skin}	0	0	0	0	0	0	0	0	0	0	0	0	0	0	0	0
V_{spleen}	0	0	0	0	0	0	0	0	0	0	0	0	0	0	0	0
V_{skin}	0	0	0	0	0	0	0	0	0	0	0	0	0	0	0	0
$V_{thyroid}$	0	0	0	0	0	0	0	0	0	0	0	0	0	0	0	0
$V_{LN_{TOT}}$	0	0	0	0	0	0	0	0	0	0	0	0	0	0	0	0
V_{PC}	0	0	0	0	0	0	0	0	0	0	0	0	0	0	0	0
V_{CO}	0	0	0	0	0	0	0	0	0	0	0	0	0	0	0	0
$\tilde{V}_{adrenals}$	0	0	0	0	0	0	0	0	0	0	0	0	0	0	0	0
$\tilde{V}_{bladder}$	0	0	0	0	0	0	0	0	0	0	0	0	0	0	0	0
$\tilde{V}_{brain}$	0	0	0	0	0	0	0	0	0	0	0	0	0	0	0	0
$\tilde{V}_{fat}$	-0.01	-0.01	-0.01	-0.01	-0.01	-0.01	-0.01	-0.01	-0.01	-0.01	-0.01	-0.01	-0.01	-0.01	-0.01	-0.01
$\tilde{V}_{gonads}$	0	0	0	0	0	0	0	0	0	0	0	0	0	0	0	0
$\tilde{V}_{heart}$	0	0	0	0	0	0	0	0	0	0	0	0	0	0	0	0
$\tilde{V}_{kidneys}$	0	0	0	0	0	0	0	0	0	0	0	0	0	0	0	0
$\tilde{V}_{l.int.}$	0	0	0	0	0	0	0	0	0	0	0	0	0	0	0	0
$\tilde{V}_{liver}$	0	0	0	0	0	0	0	0	0	0	0	0	0	0	0	0
$\tilde{V}_{lung}$	0	0	0	0	0	0	0	0	0	0	0	0	0	0	0	0
$\tilde{V}_{muscles}$	-0.02	-0.02	-0.02	-0.02	-0.02	-0.02	-0.02	-0.02	-0.02	-0.02	-0.02	-0.02	-0.02	-0.02	-0.02	-0.02
$\tilde{V}_{pancreas}$	0	0	0	0	0	0	0	0	0	0	0	0	0	0	0	0
$\tilde{V}_{s.int.}$	0	0	0	0	0	0	0	0	0	0	0	0	0	0	0	0
$\tilde{V}_{skeleton}$	-0.01	-0.01	-0.01	-0.01	-0.01	-0.01	-0.01	-0.01	-0.01	-0.01	-0.01	-0.01	-0.01	-0.01	-0.01	-0.01
$\tilde{V}_{skin}$	0	0	0	0	0	0	0	0	0	0	0	0	0	0	0	0
$\tilde{V}_{spleen}$	0	0	0	0	0	0	0	0	0	0	0	0	0	0	0	0
$\tilde{V}_{stomach}$	0	0	0	0	0	0	0	0	0	0	0	0	0	0	0	0
$\tilde{V}_{thyroid}$	0	0	0	0	0	0	0	0	0	0	0	0	0	0	0	0
$\tilde{V}_{LN_{TOT}}$	0.14	0.14	0.14	0.14	0.14	0.14	0.14	0.14	0.14	0.14	0.14	0.14	0.14	0.14	0.14	0.14
$\tilde{V}_{PC}$	0	0	0	0	0	0	0	0	0	0	0	0	0	0	0	0

The local sensitivity analysis also highlighted two distinct sensitivity patterns across the

lymph node groups. While all lymph node groups exhibited primary sensitivity in their mapping variable to the corresponding organ's return parameter, μ_o, the level of sensitivity to the remaining input parameters differed. The first category of lymph node groups showed minor sensitivity in their mapping variable to parameters associated with the lymph node tissue itself (lymph nodes extravasation, e_{LN}, and return parameter, μ_{LN}, total blood flow, $B_{\mathrm{LN}_{\mathrm{TOT}}}$, and total lymph node volume, $\tilde{V}_{\mathrm{LN}_{\mathrm{TOT}}}$) and negligible sensitivity to all remaining parameters. The lymph node groups characterised by this sensitivity pattern included: adrenal-, brain-, gonad- kidney-, small and large intestine-, liver-, pancreas-, stomach- and thyroid-draining lymph nodes. On the other hand, the second category of lymph node compartments showed noticeable sensitivity in their mapping variables to various input parameters, which was comparable to the sensitivity to the lymph node parameters, in addition to the dominating sensitivity to the corresponding organ's return parameter, μ_o. This category of lymph node compartments included: bladder-, fat-, muscle-, skeleton-, skin-draining and mediastinal lymph nodes. The latter category included lymph nodes draining the largest organs in the body (*i.e.*, fat, muscle, skeleton), an organ with the most notable variability in the blood flow parameter (*i.e.*, skin), as well as the lymph node group with dual organ drainage pathway (*i.e.*, mediastinal lymph nodes). Those two distinct patterns in sensitivity were exemplified using the results of the local sensitivity analysis on the single lymph node mapping variable of two lymph node groups: the kidney- and the skin-draining lymph node compartments in Figure 3.5(a) and 3.5(b), respectively.

3.3.3.2 Global sensitivity analysis

To validate the results of the local sensitivity analysis and identify the most influential parameters across the parameter space, a variance-based global sensitivity analysis, eFAST, was performed on the single lymph node mapping variables (Equations (3.27), (3.28) and (3.29)). The sensitivity of a mapping variable to each parameter or parameter grouping in the corresponding expression (see Section 3.2.6 was measured using a first-order, S_i, and total-order sensitivity indices, S_{Ti}, yielded by the eFAST algorithm. The results of the analysis for all 16 single lymph node mapping variables are shown in Table 3.4, with the statistically significant indices indicated according to the assigned p-value. Similarly to the results of the local sensitivity analysis, all single lymph nodes mapping variables showed strong sensitivity to the return parameter associated with the organ drained by the corresponding lymph node group, μ_o. Both the first-order, S_i, and total-order sensitivity indices, assigned to the μ_o parameter were statistically significant across all lymph node groups.

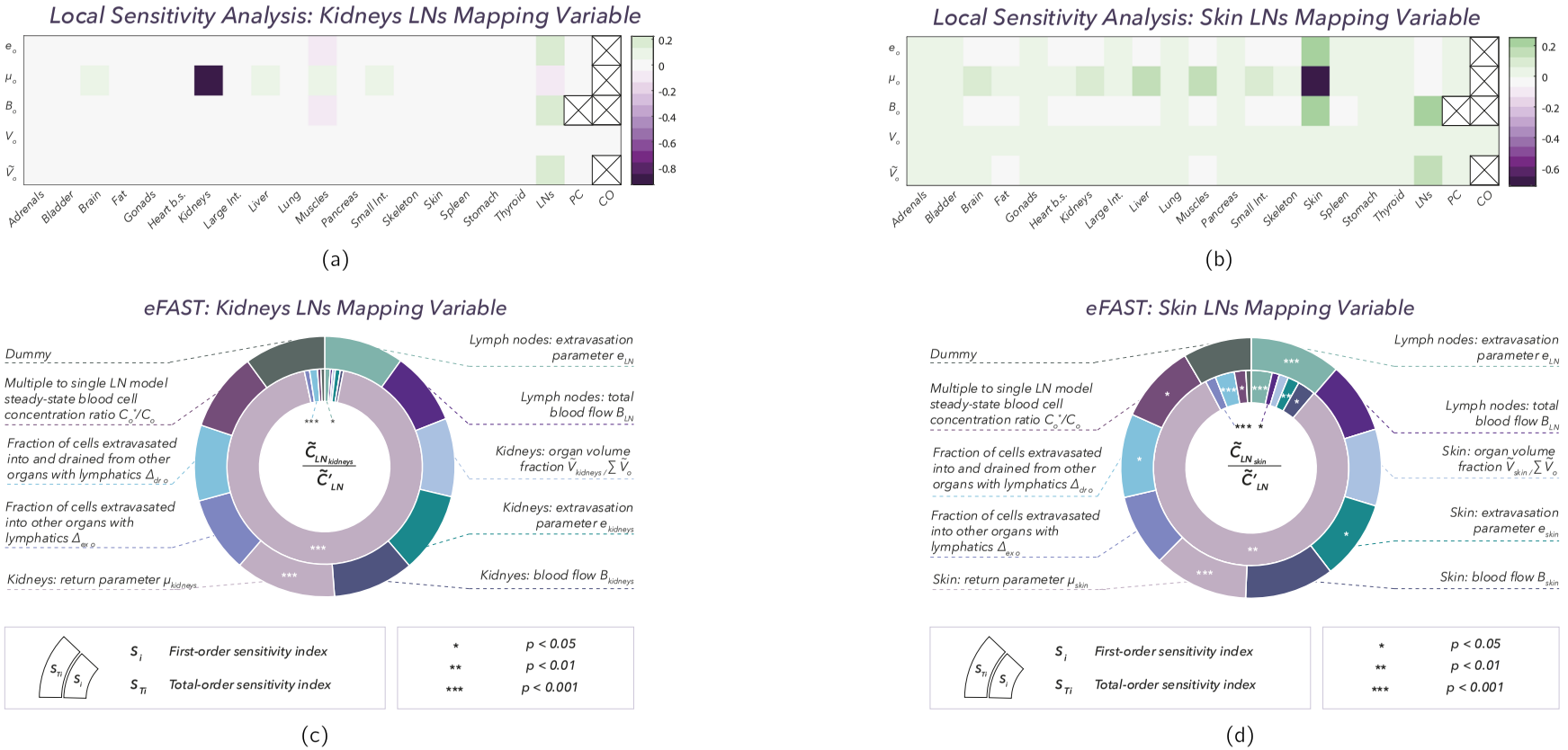


Figure 3.5: Results of the sensitivity analyses on the single lymph node mapping variables of two lymph node compartments, kidney- (a,c) and skin-draining lymph nodes (b,d), serving as examples of two groups of lymph node compartments, with distinct sensitivities to model parameters. (a -b) Results of the local sensitivity analysis on the single lymph node mapping variables for (a) the kidney- and (b) skin-draining lymph node compartments. The heatmaps display the values of the local sensitivity indices, defined by Equation (3.39), measuring the change in the mapping variable with respect to all parameters in the single and multiple lymph node trafficking models. The x- and y-axis represent the compartments and the associated parameters, respectively. Crossed-out heatmap elements stand for parameters that do not exist in the models. (c - d) Results of the global sensitivity analysis eFAST on the single lymph node mapping variables for (c) the kidney- and (d) skin-draining lymph node compartments. The inner (outer) ring indicates the proportional size of individual sensitivity indices (total sensitivity indices). A dummy parameter is used as a baseline for statistical comparison and a p-value was assigned to each sensitivity index using a two-sample t-test [11]. Parameters with statistically significant sensitivity indices were labelled according to the assigned p-value (*,**,***). The eFAST sensitivity analysis considered with a sampling of the lumped parameters C_o/C_o', $\tilde{V}_o/\sum_i \tilde{V}_i$, Δ_{ex_o} and Δ_{dr_o} from their distributions (see Section 3.2.4), cut off at the 95% confidence interval, together with the other parameters to be sampled uniformly, as detailed in Section 3.3.3.2, with further details on parameter distributions in Sections 3.2.3 and 3.3.3.2.

In addition, the eFAST analysis indicated the two distinct sensitivity patterns across the lymph node groups, also demonstrated in the local sensitivity analysis (see Figure 3.5). While all lymph node groups showed primary sensitivity to the return parameter associated with the organ drained by the corresponding lymph node group, μ_o, the sensitivity to the remaining input parameters varied between the lymph node groups and was consistent with the categories of lymph node groups inferred in Section 3.3.3.1. Mapping variables of the lymph node groups in the first category were significantly less sensitive to the remaining parameters than mapping variables of the lymph node groups in the second category. Figures 3.5(a), 3.5(c) and Figures 3.5(b), 3.5(d) illustrate the differences in the results for single lymph node mapping variables of two lymph node groups with different sensitivity patterns: the kidney- (the first group) and the skin-draining lymph nodes (the second group), respectively.

The observed varying levels of sensitivity of the single lymph node mapping variables to parameters other than the corresponding return parameters, μ_o, correlated with the median of the parameter ϵ_o (see Table 3.5). The parameter grouping, ϵ_o (Equation (3.44)), which gives a measure of the relative ratio of the extravasation rate in a given lymph node group with respect to the extravasation rate in the drained organ, determines the degree of linearity between the single lymph node mapping variable, $C_{\mathrm{LN}_o}/C'_{\mathrm{LN}}$, and the reciprocal of the return parameter, μ_o. As a result, single lymph node mapping variables of lymph node compartments characterised by values of $\epsilon_o \ll 1$ exhibit strongly linear dependence in $1/\mu_o$ (see Equation (3.45)). This dependence is weaker in the case of single lymph node mapping variables of the lymph node compartments with non-negligible values of the variable ϵ_o, and, consequently, higher levels of sensitivity to parameters other than μ_o are observed for those lymph node groups.

3.3.4 Single lymph node compartment concentration partitioning

The single lymph node mapping variables, $C_{\mathrm{LN}_o}/C'_{\mathrm{LN}}$, defined as ratios of the steady-state cell concentration in an organ, o, - draining lymph node group in the multiple lymph node model to the steady-state cell concentration in the lumped lymph node compartment in the single lymph node model, were used to derive a function (a partitioning factor, $\mathrm{PF}_{\mathrm{LN}_o}$) estimating the steady-state cell concentration in partitioned lymph node groups (see Equation (3.46)) based on a solution to the single lymph node ODE system. Given the results of the sensitivity analyses indicating the return parameter, μ_o, as the most significant parameter for each of the single lymph node mapping variables (see Section 3.3.3), a partitioning factor for each lymph node group was expressed as a linear function of the reciprocal of the return parameter, μ_o, with a proportionality factor, $\bar{\beta}_o$ (Equation (3.46)).

		Parameters									
LN Group		e_{LN}	$B_{LN_{TOT}}$	$\tilde{V}_o/\sum\tilde{V}_i$	e_o	B_o	μ_o	Δ_{ex_o}	Δ_{dr_o}	C_o/C'_o	Dummy
LNs Adrenals	S_i	0.002	0.002	0.001	0.002	0.002	0.186***	0.002	0.002	0.001	0.002
	S_{Ti}	0.769	0.846	0.759	0.734	0.780	0.896***	0.734	0.736	0.695	0.842
LNs Bladder	S_i	0.007***	0.002*	0.002	0.007***	0.006***	0.194*	0.005**	0.004**	0.001	0.001
	S_{Ti}	0.534	0.525	0.506	0.507	0.469	0.893***	0.503	0.547	0.479	0.528
LNs Brain	S_i	0.003	0.002	0.001	0.002*	0.002	0.097**	0.003**	0.003*	0.002	0.003
	S_{Ti}	0.788	0.693	0.735	0.646	0.855	0.886**	0.763	0.623	0.707	0.848
LNs Fat	S_i	0.008***	0.001	0.002**	0.004**	0.002	0.206**	0.005**	0.004*	0.001	0.001
	S_{Ti}	0.479	0.450	0.652	0.710	0.476	0.895***	0.666	0.575	0.430	0.565
LNs Gonads	S_i	0.004**	0.002	0.001	0.003***	0.002*	0.097**	0.004**	0.003*	0.002	0.001
	S_{Ti}	0.677	0.642	0.556	0.814	0.534	0.885***	0.521	0.767	0.527	0.569
LNs Kidneys	S_i	0.002*	0.001	0.001	0.002	0.001	0.232***	0.002	0.003***	0.001	0.002
	S_{Ti}	0.712	0.655	0.700	0.721	0.722	0.901***	0.679	0.677	0.705	0.723
LNs L. Int.	S_i	0.002*	0.002	0.002	0.002	0.001	0.207***	0.003*	0.002**	0.001	0.001
	S_{Ti}	0.762	0.776	0.754	0.812	0.715	0.898***	0.721	0.696	0.705	0.735
LNs Liver	S_i	0.003***	0.002	0.002	0.009***	0.003**	0.115**	0.005**	0.006***	0.001	0.001
	S_{Ti}	0.860	0.385	0.791	0.504*	0.746	0.885***	0.401*	0.505*	0.431	0.339
LNs Muscles	S_i	0.002***	0.001*	0.002*	0.002***	0.002**	0.098**	0.002***	0.002***	0.001***	0.001
	S_{Ti}	0.562	0.620*	0.758**	0.547	0.605	0.886***	0.541	0.576	0.607	0.545
LNs Pancreas	S_i	0.002	0.002	0.002	0.002	0.002	0.190***	0.002	0.002	0.001	0.002
	S_{Ti}	0.743	0.761	0.773	0.752	0.781	0.897**	0.793	0.719	0.710	0.814
LNs S. Int.	S_i	0.002	0.001	0.002	0.001	0.001	0.128**	0.003	0.002	0.002	0.002
	S_{Ti}	0.781	0.749	0.811	0.753	0.754	0.890**	0.840	0.774	0.778	0.853
LNs Skeleton	S_i	0.015***	0.001	0.001	0.012***	0.002*	0.212**	0.007***	0.008***	0.001	0.001
	S_{Ti}	0.453	0.307	0.407	0.418	0.419	0.892***	0.475	0.324	0.426	0.321
LNs Skin	S_i	0.003***	0.001*	0.001	0.001**	0.002*	0.060**	0.001***	0.002***	0.001*	0.001
	S_{Ti}	0.852***	0.667	0.717	0.743***	0.833	0.882***	0.673	0.780*	0.736*	0.638
LNs Stomach	S_i	0.002	0.002	0.002	0.002**	0.002	0.166**	0.002*	0.002	0.001	0.002
	S_{Ti}	0.742	0.836	0.718	0.647	0.649	0.894***	0.729	0.735	0.634	0.776
LNs Thyroid	S_i	0.002	0.002	0.002	0.001	0.001	0.143**	0.002*	0.002*	0.001	0.002
	S_{Ti}	0.852	0.852	0.816	0.776	0.787	0.891***	0.818	0.819	0.793	0.856

		Parameters						
LNs Med.		e_{LN}	$B_{LN_{TOT}}$	$\tilde{V}_o/\sum\tilde{V}_i$	e_{heart}	B_{heart}	μ_{heart}	Δ_{ex_o}
	S_i	0.001	0.001	0.000	0.004***	0.001	0.078***	0.007***
	S_{Ti}	0.456	0.394	0.370	0.548**	0.406	0.643***	0.514*
		Δ_{dr_o}	C_o/C'_o	e_{lung}	B_{lung}	μ_{lung}	Dummy	
	S_i	0.010***	0.001	0.001**	0.001*	0.214***	0.000	
	S_{Ti}	0.445*	0.405	0.414	0.341	0.783**	0.340	

Table 3.4: Results of the global sensitivity analysis eFAST on the single lymph node mapping variable for each lymph node group compartment. Sensitivity of the single lymph node mapping variables associated with each lymph node group (Equations (3.27), (3.28) and (3.29)) to each of the parameters was measured with a first-order sensitivity index, S_i, representing the proportion of an output's variance that is due only to a given parameter, and total-order sensitivity index, S_{Ti}, calculated from the proportion of an output's variance due to all parameters except the one in question. A dummy parameter was used as a baseline for statistical comparison and a p-value was assigned to each sensitivity index using a two-sample t-test [11]. Parameters with statistically significant sensitivity indices were labelled according to the assigned p-value ($p < 0.05$ as *, $p < 0.01$ as **, $p < 0.001$ as ***). The eFAST sensitivity analysis considered with a sampling of the lumped parameters C_o/C'_o, $\tilde{V}_o/\sum_i\tilde{V}_i$, Δ_{ex_o} and Δ_{dr_o} from their distributions (see Section 3.2.4), cut off at the 95% confidence interval, together with the other parameters to be sampled uniformly, as detailed in Section 3.3.3.2, with further details on parameter distributions in Sections 3.2.3 and 3.3.3.2. *Med.* - mediastinal, *L. Int.* - large intestine, *S. Int.* - small intestine.

LN group	Sensitivity	$1/\mu_o$-linearity determiner, ϵ_o		Proportionality factor, $\bar{\beta}_o$		Relative difference, Δ_{rel_o}	
	group	Median	95%CI	Mean	95%CI	Median	95%CI
LNs Adrenals	1	0.002	0.0001 – 0.05	0.39	0.13 – 0.67	-0.27%	-204.3% – 41.3%
LNs Bladder	2	0.05	0.002 – 1.4	0.35	0.06 – 0.64	-0.09%	-428.6% – 45.6%
LNs Brain	1	0.004	0.0002 – 0.09	0.39	0.12 – 0.66	-0.16%	-215.7% – 41.6%
LNs Fat	2	0.1	0.004 – 2.4	0.33	0.05 – 0.60	0.36%	-528.1% – 46.01%
LNs Gonads	1	0.02	0.001 – 0.5	0.37	0.09 – 0.65	-0.10%	-295% – 43.6%
LNs Kidneys	1	0.001	0.00003 – 0.01	0.40	0.14 – 0.67	-0.27%	-194.4% – 40.95%
LNs L. Int.	1	0.003	0.0001 – 0.06	0.39	0.13 – 0.67	-0.23%	-207.8% – 41.4%
LNs Liver	-	0.0001	0.000002 – 0.001	0.40	0.13 – 0.70	-0.60%	-222.8% – 41.9%
LNs Mediastinal	-	0.0001	0.000003 – 0.0004	0.89	0.26 – 2.10	-12.01%	-241.3% – 57.6%
LNs Muscles	2	0.005	0.0002 – 0.2	0.39	0.11 – 0.68	-0.34%	-247.7% – 42.7%
LNs Pancreas	1	0.003	0.0001 – 0.07	0.39	0.13 – 0.67	-0.25%	-208.2% – 41.4%
LNs S. Int.	1	0.003	0.0001 – 0.07	0.39	0.13 – 0.67	-0.19%	-207.4% – 41.4%
LNs Skeleton	2	0.08	0.004 – 1.8	0.33	0.06 – 0.61	0.19%	-475.4% – 45.7%
LNs Skin	2	0.004	0.0001 – 0.1	0.39	0.12 – 0.66	-0.04%	-223.1% – 41.5%
LNs Stomach	1	0.004	0.0002 – 0.1	0.39	0.12 – 0.67	-0.24%	-217.03% – 41.7%
LNs Thyroid	1	0.001	0.00003 – 0.01	0.40	0.14 – 0.68	-0.29%	-193.9% – 41%

Table 3.5: Means, medians and 95% confidence intervals of the variables within the single lymph node concentration partitioning approximation: the $1/\mu_o$-linearity determiner, ϵ_o (Equation (3.44)), the proportionality factor, β_o (Equation (3.47)) and the relative difference, Δ_{rel_o}, between the exact steady-state solution and the single lymph node concentration partitioning approximation (Equation (3.53)). For each lymph node group, the variable ϵ_o determines the degree of linearity between the single lymph node mapping variable for that lymph node group, $C_{\text{LN}_o}/C'_{\text{LN}}$, and the reciprocal of the return parameter, μ_o. Given the linear relationship, the reciprocal of the return parameter, μ_o, together with the mean of the proportionality factor, $\bar{\beta}_o$, serve as a partitioning factor that can be used to approximate the steady-state cell concentration in the specific lymph node group based on the solution of the single lymph node trafficking model. The accuracy of the approximation is measured by the relative difference, Δ_{rel_o} between the exact steady-state solution and the partitioning factor used as the cell concentration approximation.

For each lymph node group, a variable ϵ_o was introduced as a measure determining the degree of linearity between the single lymph node mapping variable for each lymph node group, $C_{\text{LN}_o}/C'_{\text{LN}}$, and the reciprocal of the return parameter, μ_o (see Equation (3.45)). The variable ϵ_o, therefore, can act as a predictor of the quality of the proportionality factor (Equation (3.46)) as a single lymph node cell concentration approximation. The accuracy of the approximation was further assessed by evaluating the relative difference between the exact solution for the steady-state cell concentration and the corresponding value predicted by the partitioning factor, Δ_{rel_o} (Equation (3.53)). For each lymph node group, the mean proportionality factor, $\bar{\beta}_o$, the median of the $1/\mu_o$-linearity determiner, ϵ_o and the relative difference, Δ_{rel_o}, were evaluated based on 1,000,000 uniform samplings in the parameter space, varying the input parameters, as described in Section (3.2.7). The resulting means, medians and 95% confidence intervals of the variables within the single lymph node concentration partitioning approximation as well as the distributions of the relative difference, Δ_{rel_o}, are shown in Table 3.5.

The sample means and 95% confidence intervals of the evaluated proportionality factors, $\bar{\beta}_o$, resulted in comparable values for the majority of the lymph node groups. The means varied

between 0.33, for the fat- and skeleton-draining, and 0.4, for the kidney-, liver- and thyroid-draining lymph node groups, while the confidence intervals were similar across the majority of the lymph node compartments and the lower and upper confidence interval bounds ranged between 0.05 and 0.14, and 0.6 and 0.7, respectively. The exception was the mediastinal lymph node compartment, for which the mean proportionality factor, $\bar{\beta}_{\text{med}}$, was 0.89, with the 95% confidence interval of 0.26 – 2.1. Despite the width of the distributions, the use of a single value of the proportionality constant, $\bar{\beta}_o$, as the slope value in the expression for the cell concentration partitioning factor (Equation (3.46)), the approximation was shown to be accurate for the majority of the lymph node groups. The distributions of the relative difference, Δ_{rel_o}, between the exact and predicted cell concentrations in each lymph node group were characterised by medians very close to 0, indicating that the derived approximation framework is, on average, able to accurately predict cell biodistribution in all single lymph node groups based on the single lymph node trafficking model solutions.

The distributions of the relative difference, Δ_{rel_o}, for all lymph node groups displayed a negatively skewed shape (see the means and 95%CI values of Δ_{rel_o} in Table 3.5), in agreement with the distributions of the single lymph node mapping variable, which showed positive skewness (see Figure 3.4). Incidentally, we verified that the values of the relative difference, Δ_{rel_o}, on the left ends of the distributions corresponded to the points in the parameter space resulting in very small steady-state cell concentrations in the lumped lymph node compartment. In such instances, a relatively small absolute difference between the exact value of the solution and the value predicted by the approximation is exaggerated in relative terms.

The width of the relative difference distributions, indicated by the 95% confidence intervals, varied across the lymph node groups, with the fat-draining lymph node compartment resulting in the largest difference between the exact and predicted cell concentration (-530.5% – 46.1%). Other lymph node compartments with noticeably wider distributions included bladder -, gonads -, kidneys -, muscles -, skeleton -, skin -draining and mediastinal lymph nodes. The noted deviation of the resulting values from the approximation variables of the remaining lymph node groups was expected based on the much weaker linear relationship of the single lymph node mapping variables for the mentioned lymph node compartments and the inverse of the return parameter, μ_o. This can be seen by comparing the simulated values of the $1/\mu_o$-linearity determiner parameter, ϵ_o, and the Δ_{rel_o} distribution summary statistic in Table 3.5, where higher median values of the parameter ϵ_o tend to be associated with wider confidence intervals of the corresponding relative difference distributions, Δ_{rel_o}. Cell concentration estimates in the lymph node groups characterised by higher values of the variable ϵ_o (*e.g.*, fat-draining lymph nodes) were less accurate (in terms of the distribution width) than in the lymph node compartments with relatively negligible values of ϵ_o (*e.g.*, kidneys-draining lymph nodes). The

exception was the mediastinal lymph node compartment, with ϵ_o of 0.0001. Although the noted deviation in the relative difference distribution, Δ_{rel_o}, was expected based on the structure of the single lymph node mapping variable, $C_{\text{LN}_{\text{med}}}/C'_{\text{LN}}$, which accounts for the dual lymphatic drainage to mediastinal lymph nodes in the model, the difference in the median and confidence interval of the Δ_{rel_o} distribution was relatively minor in practice (12%). Considering Equation (3.49), this may be in part due to the blood flow to the heart and lung blood supply compartments being of a similar order of magnitude (0.26 L/min [30] and 0.16 L/min [30] at baseline, respectively) and it is possible that the approximation applied lymph nodes draining organs with more prominent differences in the physiological characteristics would result in more substantial deviations.

In all the above-mentioned cases, however, the accuracy of the approximation can be improved by correcting the partitioning factor function (Equation (3.46)) with the parameter ϵ_o for the lymph node compartment of interest. For instance, the corrected steady-state concentration partitioning factor for the mediastinal lymph nodes, $\text{PF}'_{\text{LN}_{\text{med}}}$, can be rewritten as:

$$\text{PF}'_{\text{LN}_{\text{med}}} = \bar{\beta}_{\epsilon_{\text{med}}} \frac{\tilde{\epsilon}_{\text{med}} + 1}{\tilde{\epsilon}_{\text{med}} + \mu_{\text{heart}} + \mu_{\text{lung}}}, \tag{3.54}$$

where $\tilde{\epsilon}_{\text{med}}$ is the median of the parameter ϵ_{med}, given by Equation (3.49), and the correction is based on the approximate form of the parameter α_{med} (Equation (3.48)):

$$\alpha_{\text{med}} \approx \frac{\epsilon_{\text{med}} + 1}{\epsilon_{\text{med}} + \mu_{\text{heart}} + \mu_{\text{lung}}}. \tag{3.55}$$

This can be further generalised to a lymph node compartment draining m organ compartments (LN_m), so that the corrected partitioning factor, PF'_{LN_o}, can be defined as:

$$\text{PF}'_{\text{LN}_m} = \bar{\beta}_{\epsilon_m} \frac{\tilde{\epsilon}_m + 1}{\tilde{\epsilon}_m + \sum_{i=1}^{m} \mu_i}, \tag{3.56}$$

where $\bar{\beta}_{\epsilon_m}$ is the new proportionality factor, and $\tilde{\epsilon}_m$ is the median of the parameter ϵ_m given by:

$$\epsilon_m = \frac{e_{\text{LN}_m} B_{\text{LN}_m}}{\sum_{i=1}^{m} e_i B_i}, \tag{3.57}$$

where the summation runs over all m organs drained by the lymph node compartment, LN_m.

3.4 Discussion

Whole-body mechanistic PBPK models are often characterised by high complexity due to a large number of parameters, which can lead to issues with model identifiability and parameter estimation. Structurally simpler models are for this reason deemed more useful and single lymph node compartment models have remained an established standard, as representing the lymph node tissue through a lumped compartment greatly reduces the model complexity and uncertainty. Encouraging progress in immunotherapy has highlighted the potential to further integrate PBPK modelling in the development of novel treatments, which, in turn, necessitates consideration of whether such a simple mathematical description of the tissue that is central to immune cell kinetics and dynamics is sufficient. The primary aim of this chapter has been to examine the impact of the choice of lymph node compartmentalisation on the predictions of a PBPK model, here applied in the context of recirculating immune cells and cell-based therapies, by contrasting two previously published models with opposing descriptions of lymph node compartments: a single and a multiple lymph node trafficking models.

Given the difference in the number of parameters between the single and multiple lymph node models (101 vs 176, respectively), the single lymph node trafficking model pertains as a more favourable modelling tool. Certain assumptions imposed on the multiple lymph node trafficking model, such as (i) identical extravasation and return cell rates of the organ-specific lymph node compartments, and (ii) compartmentalisation of the lymph node tissue based on the drained organ volume, can result in a substantial reduction of the number of parameters in the model (from 176 to 101 parameters). While those steps may offer a considerable advantage in terms of reducing the parameter dimensionality, the number of compartments in the multiple lymph node model (37, compared to 22 in the single lymph node model) continues to render the multiple lymph node model disadvantageous in real-life applications with practical limitations. The risk of parameters' unidentifiability in larger models combined with limited or imperfect data further complicates the process of data fitting. On the other hand, depending on the research question, cell or drug concentrations in all lymph nodes may not always be of interest, calling into question the suitability of both the lumped and compartmentalised representation of lymph nodes in a PBPK model.

The framework presented in this study was formulated to characterise the difference between the biodistribution of recirculating cells predicted by the single and multiple lymph node trafficking models. By considering two identically parameterised trafficking models with opposing lymph node compartmentalisation [1, 52], a mapping between the steady-state solutions of the two models was derived, allowing direct comparison of the models' outputs across the parameter space. The resulting framework comprises mapping variables defined as the ratios

of the steady-state cell concentration in each compartment in the multiple lymph node model to the steady-state cell concentration in the corresponding compartment in the single lymph node model for a given set of input parameter values.

3.4.1 Single lymph node model may be sufficient for predicting whole-body lymph node exposure

The mapping variables were simulated across the parameter space, varying the input parameters, with variability considered to account for the interpersonal and temporal differences in anatomical and physiological characteristics, as well as the possible values of entry and exit rates of cells across all tissues. The resulting simulations indicated that, compared to the single lymph node model, the multiple lymph node model, on average, would yield comparable steady-state cell concentration in lymph nodes (median 1.02, 95%CI: 0.6 – 4.64), with the cell concentration across the remaining organ compartments reduced by roughly 20% (median 0.81, 95%CI: 0.67 – 0.98). The similarity in the overall lymph node tissue cell concentration, therefore, suggests that if predicting the whole-body lymph node exposure is the primary goal of the modelling work, a lumped lymph node compartment is sufficient and introducing lymph node compartmentalisation, and thus increasing the complexity of the model, is not necessary.

3.4.2 Mapping framework can support the use of the single lymph node model when specific groups of lymph nodes are of interest

The mapping framework was further explored as a potential tool facilitating the estimation of the steady-state cell concentration in organ-specific lymph node compartments. Utilising local and global sensitivity techniques, the steady-state cell concentration across lymph node compartments was shown to be well approximated with a simple linear function of the reciprocal of the associated drained organ's cell exit rate. For each organ-specific lymph node compartment, an appropriate proportionality factor was evaluated and the accuracy of the resulting approximation was demonstrated by comparing the exact solution from the multiple lymph node model and the value estimated with the approximation. In turn, we have illustrated that the single lymph node model combined with the estimating function can be used to predict cell concentration in organ-specific lymph node compartments. Based on a single lymph node model solution for a chosen set of input parameters, estimating cell concentration in a lymph node group of interest simply requires the proportionality factor associated with that lymph node group and the cell exit rate from the organ drained by that lymph node group. The

exit rate of cells from an organ associated with the lymph node group of interest, represented by the organ's return parameter, μ_o, can be either directly measured experimentally or estimated by comparing the cell concentration in the organ and the blood at steady state (see Section 3.2.2.1 and Equation (2.2)). Furthermore, the high dependence of the cell concentration in the specific lymph node group on the μ_o parameter suggests that if one anticipates a modality to exhibit different kinetics and dynamics within a particular lymph node group (*e.g.*, tumour-draining, administration site-draining, lesion-bearing lymph nodes), it naturally follows that the model should depict that distinction. The lymph node or lymph node group expected to differ from the remaining tissue should, therefore, be compartmentalised as a distinct compartment in order to allow meaningful interpretation of the model results, while the remaining lymph nodes can be depicted as a lumped compartment. Such a description then minimises the complexity of the model, while providing a suitable mathematical structure to address the research question at hand.

3.4.3 Caveats of the mapping framework

The mapping framework presented in this study was derived based on a specific choice of lymph node compartmentalisation, with the lymph node tissue defined as 16 separate organ-specific groups of lymph nodes in the multiple lymph node model. In the human body, lymph nodes are known to be widely present and often arranged in chains, which can drain more than one organ [67, 82], however, our current knowledge on the lymphatic system anatomy and lymphatic drainage pathways is still relatively limited (see Section 2.4.2 for further discussion on the choice of lymph node tissue compartmentalisation in the multiple lymph node model). The employed method of mapping steady-state solutions between two ODE systems demonstrates the advantage of the framework, as it allows generalisation of the framework to a lymph node compartmentalisation of choice. The lymph node cell concentration partitioning approach can be extended to estimate cell concentrations across lymph nodes draining cells from multiple organs. This is exemplified here by the mediastinal lymph node compartment, defined in the multiple lymph node model as a lymph node group draining cells from the heart and lung blood supply, for which the approximation performed comparably to the remaining lymph node groups with single organ cell drainage. While such generalisation requires the existence of a unique steady-state solution to an ODE system that can be obtained analytically, the vast majority of PBPK models tend to be linear and based on the mass conservation law [52, 53, 69, 79, 80, 81], and, hence a similar derivation approach could, in theory, be applied.

3.4.4 Concluding remarks

Model-informed drug development, which includes PBPK modelling strategies, has been recognised as a potentially critical area in the future of immuno-oncology, particularly when addressing a question through a clinical study is not feasible for ethical or economic reasons [83]. Context- (disease- and/or patient-) specific assumptions characterising PBPK modelling offer a unique advantage to generate physically meaningful results that can enhance our understanding of immune cell trafficking and cell-based therapy distribution. With relatively simple compartmental models utilised so far to describe the biodistribution of cell-based therapies [52, 79], the PBPK modelling approach may offer a useful tool to answer more complex questions, such as the activity of modelled cells and tumour infiltration. The amount of mechanistic detail in PBPK models, and, thus, often over-parameterisation and related identifiability issues, has been a major focus of the criticism towards this modelling approach [83]. The intricacy of PBPK models, and thus rightfully, a potential limitation, necessitates consideration of what constitutes an appropriate level of detail for a given modelling purpose and application. Understanding the expected outcomes of proposed models and their simplified versions is vital to fully utilise the predictive potential of PBPK models and to allow insight into more meaningful predictions of therapy deposition and patient responses in the future.

Chapter 4

Choice of delivery route of antibody-based therapies

In Chapter 3, we considered how compartmentalisation of lymph node tissue in PBPK modelling impacts the model predictions depending on the model application. We have shown that a PBPK model with a single lumped lymph node compartment, on average, predicts the same cell concentration in the lymph node tissue as a model with much more complex lymph node compartmentalisation. We also argued that if the modelled modality is expected to exhibit distinct dynamics in different lymph node groups and its dynamics is relevant to the research question, those lymph nodes should be accordingly depicted in a model as separate compartments. In this chapter, we employ the previously drawn conclusions in the process of developing a PBPK-based framework to facilitate addressing the question of the optimal delivery route for immunotherapeutic modalities. We propose an ODE-based framework that describes the deposition and mechanism of action of monoclonal antibodies delivered via two routes: intravenous and subcutaneous. The chosen structure of the model enables simulation of the subcutaneous administrations by depicting the subcutaneous administration site and the lymph nodes draining that region as individual compartments, while distal lymph nodes are represented as a lumped compartment, which minimises the model complexity. This chapter further considers the problem of parameterisation in PBPK models in the clinical setting, where available data that could facilitate model development is much more limited compared to preclinical studies. We strategically utilise preclinical data from a study on cynomolgus monkeys, comparing the intravenous and subcutaneous administration of monoclonal antibodies. Anti-

body blood measurements, which would typically be the only type of data available in the clinic, are used for model fitting. Data on target cells in the blood and lymph nodes, which would very rarely be available in the clinical setting, are, in contrast, used to qualitatively verify the predicted behaviour of the model. As the additional target cell data is not directly employed in the process of model fitting, this method allows us to examine the usability of the proposed framework with data availability similar to that in the clinic, while also granting a possibility of a better understanding of the model behaviour. In summary, this final research chapter, therefore, will assess the feasibility of constructing a mechanistic framework to support the process of elucidating the mechanism underlying the advantages of one delivery route over the other in the context of antibody-based therapies.

4.1 Introduction

Establishing the route of administration is an important stage in the development of any new therapeutic agent, and can be particularly challenging when the mechanism via which the therapeutic exerts its effects are complex or not fully understood [84]. The choice is governed by the principles of safety, efficacy, pharmacoeconomics and patient preference, where safety and efficacy must be regarded as dominant [84]. Subcutaneous (SC) delivery of biotherapeutics has become a valuable alternative to intravenous (IV) administration across several disease areas, including diabetes, rheumatoid arthritis, multiple sclerosis and primary immunodeficiency [85]. The established approach was extended to SC monoclonal antibodies (mAbs) in oncology with the European approval of SC formulations of trastuzumab (Herceptin) and rituximab (Rituxan) in 2013 and 2014, respectively [85]. While most biotherapeutics for cancer treatment are administered IV, SC administration for certain drugs has proven effective, safe, less invasive and preferable in terms of healthcare costs and resources [84, 85]. Comparative studies of optimal choice of administration route have been sporadically conducted, and literature reviewing the advantages and disadvantages of various routes of injection is even more limited within the area of oncology (see Table 4.1) [84, 86, 87].

The development of therapeutic antibodies has expanded considerably during the past 20 years and, currently, between 6 and 10 novel antibody-based drugs are approved each year [88, 89]. While the IV route remains the most common delivery method for therapeutic antibodies, the alternative routes, and especially the SC route, have been explored more frequently due to their potential efficacy, safety and cost benefits [89]. SC and IV administrations of the same therapeutic protein may differ in efficacy, safety and immunogenicity [85]. The two routes of injections are generally associated with distinct pharmacokinetic (PK) profiles: a

'SC better than IV'	'IM better than IV'	'SC better than IM'
rituximab (CD20 mAb) trastuzumab (HER2 mAb) TNF inhibitors (mAb, small molecules) bortezomib (proteosome inhibitor, small molecule) rhGM-CSF (haematopoietic growth factor) G-CSF (haematopoietic growth factor) IL-2 (growth factor)	none reported	methotrexate (small molecule)
'IV better than SC'	**'IV better than IM'**	**'IM better than SC'**
none reported	none reported	pegaspargase (protein-based)

Table 4.1: Medications and classes of drugs that have been observed with advantages of one route of administration over the other in oncology, in terms of efficacy, safety, cost and/or patient preference. In this context, the word *better* implies which administration method is regarded as more optimal in the clinic. Data was selected from a review of comparative studies by Jin et al. [84]. SC - subcutaneous; IV - intravenous; IM - intramuscular; rhGM-CSF - recombinant human granulocyte-macrophage colony-stimulating factor; G-CSF - granulocyte colony-stimulating factor; IL-2 - interleukin-2.

biotherapeutic injected directly into the bloodstream is typically characterised by an immediate maximum serum concentration (C_{max}), while the slower absorption rate of the SC injection leads to a more gradual but also comparatively lower C_{max} level. For this reason, SC dosing may reduce C_{max}-related adverse events (AEs) of biotherapeutics compared to IV. Additionally, it has been hypothesised that a higher concentration of the antibody near the target site could, in theory, lead to improved therapeutic response, while reducing the exposure to the therapeutic of the neighbouring healthy tissues, and, thereby, lowering the probability of off-target AEs [89]. However, it remains unclear whether the SC administration route is feasible for all molecules, not only because of the impact on the drug's bioavailability but the overall safety and tolerability profile (particularly the formation of anti-drug antibodies, ADAs) [85]. Furthermore, the question of whether SC administration of a biotherapeutic retains efficacy, and if so - how, needs to be considered individually for each therapeutic with a distinct mechanism of action.

Model-based approaches have been increasingly supporting decision-making in the drug development process and, in the context of antibody-based therapies, have been applied at various stages: predicting PK through translational modelling, informing the processes of modality and target selection, candidate optimisation and supporting pharmacology-based decisions [90]. Indeed, mathematical modelling has been extensively applied to describe the deposition, pharmacodynamics and pharmacokinetics of both endogenous and therapeutic antibodies. Due to the number of factors controlling the antibody biodistribution and mechanism of action, mathematical and computational approaches have also proven beneficial in elucidat-

ing the relative importance of the physiological and cellular processes affecting the observed behaviour in a given experimental setting [91]. Most commonly used modelling approaches, in order of increasing complexity, include: non-compartmental analyses, compartmental models (in particular, 2-compartment models, with central and peripheral tissue compartments), target-mediated deposition (TMD) models and physiologically-based pharmacokinetic (PBPK) models [91].

Similarly to small-molecule and immune-cell applications, the use of PBPK modelling to describe antibody deposition offers the advantage of putting the processes governing the deposition in the context of physiologically relevant spaces. This allows a more intuitive interpretation of the parameters describing those processes than in the case of classical compartment models and, in turn, facilitates interspecies translation. Available PBPK models for antibody deposition, however, differ substantially from each other with respect to their representation of physiology and parameterisation of the depicted mechanisms involved in antibody deposition [92]. The most notable differences concern: (i) defining the relevant tissue spaces; (ii) depicting the processes of antibody extravasation from the vasculature; (iii) the relevance of interactions with neonatal Fc receptors (FcRns), which is responsible for the transfer of humoral immunity from the mother to the newborn and, later on, contributes to maintaining antibody levels in the blood through a process denoted antibody recycling [93], and the description of this dynamics; (iv) the explicit representation of the endogenous antibodies; (v) the description of antibody clearance; and (vi) the presence of a lymph node compartment in the model, as elegantly summarised by Fronton et al. [92]. Tables 4.2 and 4.3 provide an overview of several antibody deposition PBPK models and highlight the vast diversity of the modelling approaches available in the literature [81, 92, 96, 97, 98, 99, 100, 101, 102, 94, 95].

Study	Significance	Relevant tissue spaces	Extravasation	FcRn	Endogenous IgG	Clearance	Lymph node compartment
Covell et al. (1986) [99]	First PBPK model for IgG and its fragments	6 organs, each with vascular, interstitial and cell-associated subcompartments	Transcapillary exchange through convective and diffusive pathways, using vascular reflection and diffusion coefficient description	Not included	Not included	Catabolism of bound antibody in extravascular spaces, linear elimination rate	Not included
Baxter et al. (1994) [101]	Based on [99], expanded to describe mAb-specific binding and a two-pore formalism for extravasation	10 organs (including tumour), each with vascular and extravascular subcompartments	Transcapillary exchange through convective and diffusive pathways, using a two-pore formalism proposed by Rippe and Haraldsson [103]	Not included	Not included	Catabolism of antibody in cell-associated compartments, linear elimination rate	Included
Friedrich et al. (2002) [81]	First PBPK model for bifunctional antibodies	11 organs (including tumour), each with vascular and interstitial compartments	Transcapillary exchange through convective and diffusive pathways, using a two-pore formalism	Not included	Not included	Elimination of unbound antibody in kidneys and antibody-effector cell complexes in vascular spaces, linear elimination rate	Included
Ferl et al. (2005) [102]	First PBPK model to incorporate the effect of FcRn-mediated antibody recycling	10 organs (including tumour), each with vascular and interstitial compartments (and intracellular subcompartments for muscle and skin)	Transcapillary exchange through convective and diffusive pathways, using a two-pore formalism	FcRn-mediated antibody recycling in the skin and muscle compartments	Not included	Elimination of free antibody in the liver, skin and muscle, linear elimination rate	Not included
Garg and Balthasar (2007) [94]	Equilibrium model of FcRn binding to describe antibody tissue distribution	9 organs, each with vascular, endosomal and interstitial subcompartments	Transcapillary exchange through convective transport, using vascular reflection coefficient description	Binding to FcRn in endosomal compartments, with assumed equilibrium kinetics	Not included	Catabolic elimination of the unbound antibody from all organs and tissues, linear elimination rate	Not included
Urva et al. (2010) [95]	First PBPK model to incorporate endogenous antibody levels to model the effect on the FcRn-mediated transport of therapeutic antibodies	10 organs (including tumour), each with vascular, endosomal and interstitial subcompartments	Transcapillary exchange through convective transport, using vascular reflection coefficient description	Binding to FcRn in endosomal compartments, with assumed equilibrium kinetics	Included, steady-state levels of endogenous antibodies incorporated to describe the competitive binding to FcRn with therapeutic antibodies	Catabolic elimination of the unbound antibody from all organs and tissues, linear elimination rate	Included

Table 4.2: Examples of PBPK modelling approaches applied in the context of antibody tissue distribution.

Study	Significance	Relevant tissue spaces	Extravasation	FcRn	Endogenous IgG	Clearance	Lymph node compartment
Abuqayyas and Balthasar (2012) [96]	Based on [95], applied to investigate the impact of target antigen expression level and antibody specificity on plasma, tissue and tumour deposition	10 organs (including tumour), each with vascular, endosomal and interstitial subcompartments	Transcapillary exchange through convective transport, using vascular reflection coefficient description	Binding to FcRn in endosomal compartments, with assumed equilibrium kinetics	Included, steady-state levels of endogenous antibodies incorporated to describe the competitive binding to FcRn with therapeutic antibodies	Catabolic elimination of the unbound antibody from all organs and tissues, linear elimination rate	Included
Chen and Balthasar (2012) [97]	Based on [96], expanded to include pH-dependent FcRn binding	10 organs (including tumour), each with vascular, (multiple) endosomal and interstitial subcompartments	Transcapillary exchange through convective transport, using vascular reflection coefficient description	Binding to FcRn in 5 endosomal compartments representing different pH levels, with non-equilibrium kinetics	Included, steady-state levels of endogenous antibodies incorporated to describe the competitive binding to FcRn with therapeutic antibodies	Catabolic elimination of the unbound antibody from all organs and tissues, linear elimination rate	Included
Shah and Betts (2012) [98]	First "platform" PBPK model of antibody deposition in mouse, rat, monkey, and man, applied to infer tissue concentrations of antibody from plasma data alone	18 tissues (including tumour), each with vascular, endosomal, interstitial and cellular subcompartments	Transcapillary exchange through convective transport, using vascular reflection coefficient description, first use of different vascular reflection coefficients for different tissues	Binding to FcRn in endosomal compartments, with non-equilibrium kinetics	Not included	Catabolic elimination of the unbound antibody in endosomal compartments, linear elimination rate	Included
Fronton et al. (2014) [92]	Demonstrated equivalence of complex and simplified PBPK models for antibody deposition under relevant conditions and timescale assumptions	10 organs, each with vascular and interstitial subcompartments	Transcapillary exchange through convective transport, using tissue partition coefficient description	Considered implicitly, illustrated that under commonly encountered conditions, the clearance of mAbs in the endosomal space can be expected to be linear, regardless of the level of saturation of FcRn that protect antibodies from degradation.	Considered implicitly, assumed constant fraction of unbound antibody in endosomal compartments	Catabolic elimination of antibody in all tissues, linear elimination rate	Not included
Eigenmann et al. (2017) [100]	First PBPK model to provide a tissue-specific compartment description, demonstrated how to account for the residual plasma and cellular contents in total tissue measurements	11 organs, with vascular and interstitial subcompartments/ lumped vascular and interstitial subcompartment/ solely vascular compartment, depending on the tissue-specific structure of capillaries)	Transcapillary exchange through convective transport for tissues with distinguished interstitial compartment	Not included	Not included	Catabolic elimination of antibody in all tissues, linear elimination rate, based on previously quantified fractional clearance contributions [104]	Not included

Table 4.3: Continuation of Table 4.2: Examples of PBPK modelling approaches applied in the context of antibody tissue distribution.

The models reviewed in Tables 4.2 and 4.3, however, have all been developed and validated with the use of preclinical data and animal models. The usability of such complex frameworks remains very limited in the clinical stages of drug development, where the format of the collected data largely restricts the possible scope of modelling work. Data sets from clinical studies typically include data obtainable from a blood draw, meaning only serum antibody concentration data would usually be available. For membrane-bound targets, serum target occupancy can sometimes be collected, if the target antigen is present in the peripheral blood. PK tissue-specific data are very rarely available, and the decreasing levels of antibodies in serum often serve as an indicator for the antibody interaction with antigen in the target tissue(s). In contrast, preclinical studies offer the possibility to collect temporal measurements of antibody levels in specific tissues. Most of the reviewed models (all but Eigenmann et al. [100] and Fronton et al. [92]), therefore, incorporate a rather complex description of the transport of antibodies from the blood to tissues, as such data supports the development of a more detailed framework. Furthermore, multiple models reviewed Tables 4.2 and 4.3 depict the interactions of the therapeutic antibodies with the Fc receptor [96, 97, 98, 102, 94, 95] and the competitive binding with endogenous IgG antibodies in the model [95, 96, 97]. Parameterisation of those processes is generally difficult, and requires introduction of additional assumptions into the model. Finally, as neither of the models listed in Tables 4.2 and 4.3 were developed to facilitate the simulation of different administration routes, all of the reviewed frameworks would require further extension to depict the processes relevant to the SC administration of antibodies.

In this chapter, we, therefore, propose a novel and minimal physiologically-based model describing the distribution, pharmacokinetics and pharmacodynamics of intravenously- and subcutaneously-administered monoclonal antibodies. The main aim of this chapter is to assess whether the constructed model structure is appropriate to study the problem of the choice of administration route in the clinical setting based on typically available blood data. We further aim to understand the limitations imposed by the need for extensive parameterisation of PBPK-type models on the investigation of efficacy- and safety-related aspects of mAb therapeutics.

We will start by presenting the developed physiologically-based pharmacokinetic-pharmacodynamic (PBPK-PD) model, which combines the features of PBPK modelling with the traditional compartmental pharmacokinetic-pharmacodynamic (PK-PD) approaches, and is intended to allow the simulation of IV and SC administration of antibodies. Antibodies perform two distinct functions: antigen recognition and effector functions, which are represented by the characteristic Y-shaped structure of the antibody molecule [20]. The two arms of the antibody are the specialised parts that allow the antibody to bind specifically to the target antigen. Those regions vary significantly between different antibodies and are referred to as *variable*

regions. The stem region of the Y shape, on the other hand, does not exhibit similar variability. The constant region, as it is referred to, is involved in the interaction of the antibody with effector cells and molecules, thus, mediating the destruction of the target antigen.

In particular, we focus on the anti-CD20 monoclonal antibody rituximab. The CD20 antigen is a transmembrane protein expressed by most B cells (from pre-B to the mature germinal centre B cells, but not pro-B cells) and most malignant cells that derive from these B cells. The mean elimination half-life of rituximab is about 19 days in humans, however, rituximab, in general, exhibits a wide inter-individual variability in its PK characteristics in the clinic [105]. Following administration, rituximab diffuses in most organs and tissues. Upon contact with a $CD20^+$ B cell, the variable domain of the antibody molecule binds to the CD20 antigen on the cell surface and the constant region recruits immune effector functions to mediate cell lysis. While the exact effector mechanisms are challenging to study *in vivo*, several mechanisms are thought to be responsible for the cellular destruction of bound B cells: antibody-dependent cell cytotoxicity (ADCC), complement-mediated cytotoxicity (CDC) and antibody-dependent phagocytosis [106].

Given the complexity of whole-body PBPK models depicting multiple tissues and organs as separate compartments, which may be prohibitive in the light of the limited data needed to parameterise them, the proposed model depicts tissues and organs that are not directly relevant to the mechanism of action of anti-CD20 therapies as a lumped compartment. We, therefore, consider the problem of parameterisation of lumped compartments representing multiple organs and how parameters associated with lumped compartments can be mapped onto single organ parameters.

The structural identifiability and local sensitivity analyses of the mAb PBPK-PD framework are then performed to assess the applicability of the model and to guide the process of data fitting. We will further investigate the practical identifiability of the framework with the use of published preclinical data by Mao et al. [107], which compared the PK and PD for IV and SC administration of rituximab. More specifically, the aim of the study has been to determine the feasibility of achieving equivalent B cell depletion and sustained CD20 target coverage of the SC formulation of rituximab compared to the intravenous dosing in cynomolgus monkeys. We deliberately employ a preclinical data set in this process, as the study offers a rich set of temporal data on antibody concentration and B cell depletion levels, both in the serum and in lymph nodes. As antibody concentration measurements are the typically collected data type in the clinical setting, this part of the data set is utilised in the model fitting and practical identifiability. Measurements on B cell depletion in the blood and lymph nodes, which would very rarely be available in the clinic, are used for qualitative model validation and comparison. As the additional B cell data is not directly incorporated into the process of model fitting, this

method allows us to examine the usability of the proposed framework with data availability similar to that in the clinic, while also granting a possibility of a better understanding of the model behaviour.

With the implementation of analyses of the proposed model we, therefore, firstly aim to understand whether the minimal structure of the model can accurately depict both the IV and SC administration routes of anti-CD20 antibodies. Secondly, we will investigate whether a non-uniqueness of parameters occurs in data fitting and what the consequences of parameter non-identifiability are in the context of use in the clinical setting. Particularly, we are interested in the ability of the model to predict the resulting antibody distribution across model compartments. As the distribution of antibodies to the target tissue is a prerequisite for sufficient tumour uptake and, thus, achieving efficacy, while high off-target tissue concentrations may contribute to AEs, we, therefore, will investigate whether the model can facilitate further research on the impact of the delivery method on efficacy and safety by predicting antibody biodistribution based on solely antibody blood concentration data.

4.2 Methods

4.2.1 Model overview

The PBPK-PD antibody framework combines the features of PBPK and PK-PD models to describe the mechanisms involved in antibody deposition and target binding. The PBPK part of the model captures the physiological processes governing antibody tissue distribution: (i) IV and SC administration of antibodies; (ii) transport of antibodies between the main blood vessels and tissue vasculature; (iii) tissue uptake by convection through pores in the vascular endothelium; (iv) lymphatic clearance from tissues into lymph nodes; (v) return of antibodies into the main blood pool via the afferent lymph; and (vi) non-specific elimination of antibodies in tissues. The PD component of the model incorporates the interactions of antibody and its target, and the processes directly associated with specific binding. For monoclonal antibodies in oncology, those elements include: (i) reversible binding of the antibody to a malignant cell; (ii) target production and degradation; and (iii) the elimination of target cell-antibody complexes.

The following sections provide a more detailed description of the ODE system constructed to represent the monoclonal antibody transport, pharmacokinetics and pharmacodynamics. The full model, comprising of 54 ODEs and 81 parameters, is represented in Figures 4.1–4.4 with definitions and units of parameters and variables in the model shown in Table 4.4.

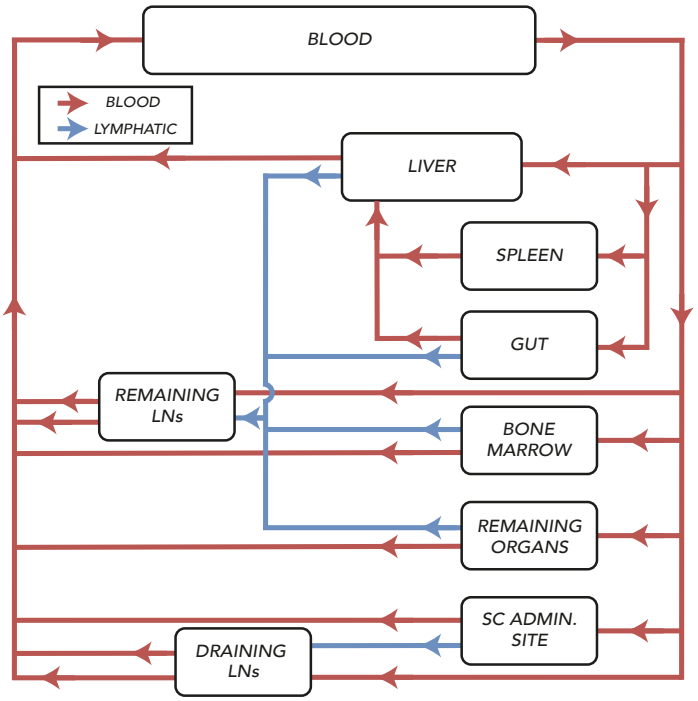


Figure 4.1: Whole-body model schematic of the ODE system describing the PBPK-PD framework of antibody deposition and target kinetics. The PBPK submodel comprises 9 compartments connected by the cardiovascular and lymphatic systems: blood, liver, spleen, bone marrow, SC administration site, draining lymph nodes, remaining lymph nodes and remaining organs. Each compartment is further depicted by a vascular and interstitial subcompartment. Such a description of the anatomy is used to predict systemic and tissue concentrations of the administered antibody. Antibodies administered IV flow from the extra-organ blood compartment (denoted by *blood*) to each organ (red lines), via lymphatics (blue lines) into lymph node compartments and return back to the blood compartment. SC administration of antibodies is modelled through the SC administration site compartment, from where antibodies flow directly into draining lymph nodes and then to the blood compartment. SC administered antibodies then distribute into the remaining model compartments (red lines), flow via lymphatics (blue lines) into lymph node compartments and again return back to the blood compartment.

Figure 4.1 depicts a whole-body level description of the model. Individual organs are modelled as shown in Figure 4.2. Figure 4.3 highlights the structure and mathematical representation of the site of subcutaneous administration and the draining lymph node compartment. The binding kinetics of the monoclonal antibody is shown in the schematic in Figure 4.4. The parameterisation of the model is discussed in detail in Section 4.2.2.

4.2.1.1 Antibody deposition (PBPK) submodel

The PBPK submodel, depicted in Figure 4.1, contains 9 tissue compartment: extra-organ blood, liver, spleen, gut, bone marrow, remaining organs, draining and remaining lymph nodes, in addition to the subcutaneous administration site depot compartment, all connected in an anatomical manner through the circulatory and lymphatic systems. The *remaining organs* compartment represents tissues not specifically accounted for in the model structure (adrenals,

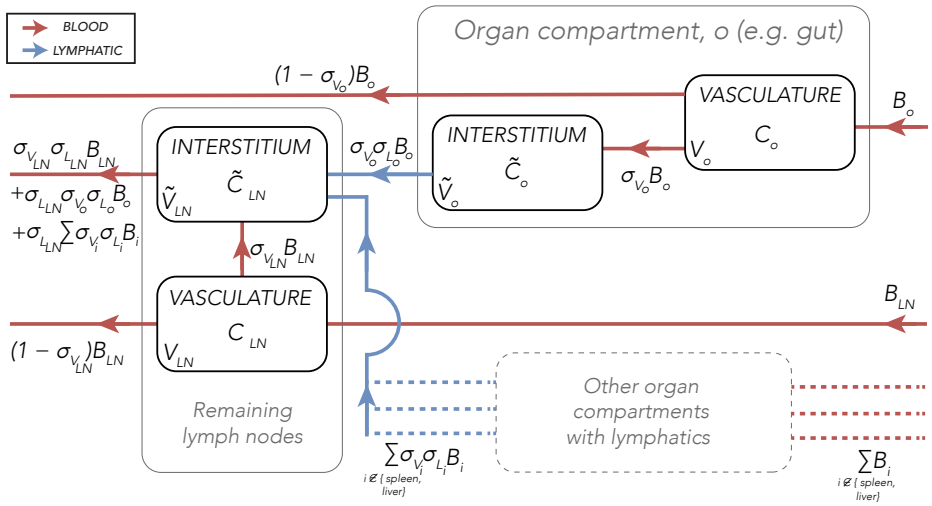


Figure 4.2: Antibodies flow from the extra-organ blood compartment (denoted by *blood*) to the vascular space of each organ, o, with a blood flow B_o and intra-organ blood volume V_o. Antibodies enter the interstitial space from the vascular subcompartment at a rate $\sigma_{V_o}B_o$ per unit time per unit concentration. Antibodies further flow via lymphatics from the interstitial subcompartment of organ, o, into the lymph node compartment at a rate $\sigma_{V_o}\sigma_{L_o}B_o$ per unit time per unit concentration. Antibodies from organ compartments with lymphatics are then drained into the lumped lymph node compartment, at a rate $\sum_i \sigma_{V_i}\sigma_{L_i}B_i$ per unit time per unit concentration, where the summation over i denotes the remaining drained organs not explicitly depicted in the figure. Antibodies also enter the lymph node compartment through the lymph node blood supply, denoted B_{LN}. From the lymph node vasculature compartment, molecules extravasate into the lymph node interstitial compartment (at a rate $\sigma_{V_{\text{LN}}}B_{\text{LN}}$ per unit time per unit concentration). Antibodies drained to the lymph nodes are returned to the systemic circulation (at a rate $\sigma_{V_{\text{LN}}}\sigma_{L_{LN}}B_{\text{LN}}+\sigma_{L_{\text{LN}}}\sigma_{V_o}\sigma_{L_o}B_o+\sum_i \sigma_{V_i}\sigma_{L_i}B_i$). Molecules that have not extravasated to the interstitium of organ, o, and lymph nodes are, similarly, returned to the systemic circulation (at rates $(1-\sigma_{V_o})B_o$ per unit time per unit concentration and $(1-\sigma_{V_{\text{LN}}})B_{\text{LN}}$ per unit time per unit concentration, respectively).

bladder, brain, adipose tissue, gonads, kidneys, skeletal muscles, skin, lung blood supply, heart blood supply, thyroid). Similarly, the *gut* compartment represents the stomach, small and large intestines, and pancreas as a single lumped compartment. Each tissue is further divided into vascular and interstitial subcompartments, as shown in Figure 4.2. Model variables and parameters are defined in Table 4.4.

With o labelling organ, the independent variables are the antibody concentrations in each of the compartments as a function of time, C_o and $\tilde{C}_o$ for the vascular and interstitial organ subcompartments, respectively. Antibodies enter each tissue vascular compartment, representing the intra-organ blood, from the extra-organ blood compartment (denoted by *blood*). A fraction of molecules extravasates from the vascular space into the interstitial subcompartment, while the remaining antibodies return to the blood compartment. Within vascular subcompartments, antibodies are also taken up by the vascular endothelial cells at a tissue-specific clearance rate, $f_{CL_o}CL_{\text{tot}}$, where f_{CL_o} is the tissue-specific fractional contribution to the systemic clearance, CL_{tot}. The rate of change in the number of antibodies in the vasculature of

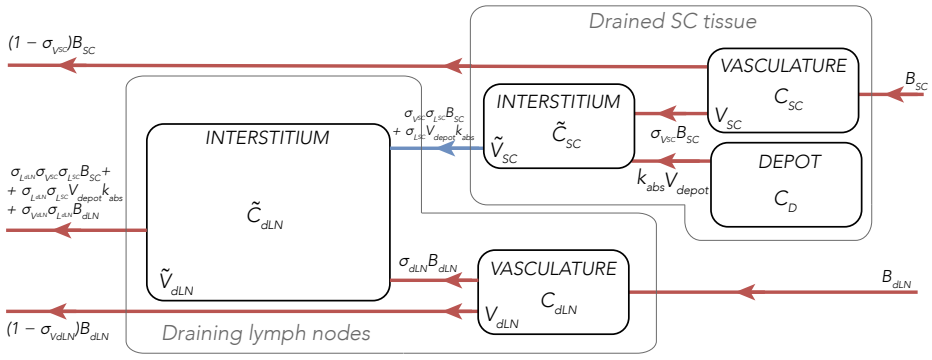


Figure 4.3: Draining lymph nodes are represented in the model as a separate compartment and denoted with a suffix, *dLN*. The draining lymph node compartment is represented by vascular and interstitial subcompartments, and drains antibodies from the local SC tissue compartment. A SC administration is modelled through the depot compartment, from where antibodies flow to the interstitial subcompartment of the SC tissue at a rate $k_{\text{abs}}V_{\text{depot}}$, and, subsequently a proportion of antibodies is transported to the draining lymph node compartment, at a rate of $\sigma_{L_{\text{SC}}}\sigma_{V_{\text{SC}}}B_{\text{SC}} + k_{\text{abs}}V_{\text{depot}}$ per unit time. A fraction of those antibodies is returned to the systemic circulation (at a rate of $\sigma_{L_{\text{dLN}}}\sigma_{L_{\text{SC}}}\sigma_{V_{\text{SC}}}B_{\text{SC}} + \sigma_{L_{\text{dLN}}}k_{\text{abs}}V_{\text{depot}}$. Some antibodies reenter the vascular subcompartment of the SC tissue at a rate $\sigma_{V_{\text{SC}}}B_{\text{SC}}$ per unit time from the extra-organ blood compartment, and similarly the vascular compartment of draining lymph nodes at a rate $\sigma_{V_{\text{dLN}}}B_{\text{dLN}}$. They are then drained into the interstitial draining lymph node subcompartment at a rate of $\sigma_{L_{\text{SC}}}\sigma_{V_{\text{SC}}}B_{\text{SC}} + \sigma_{V_{\text{dLN}}}B_{\text{dLN}}$ per unit time, from where they are returned to the extra-organ blood compartment at a rate of $\sigma_{L_{\text{dLN}}}\sigma_{L_{\text{SC}}}\sigma_{V_{\text{SC}}}B_{\text{SC}} + \sigma_{L_{\text{dLN}}}\sigma_{V_{\text{dLN}}}B_{\text{dLN}}$ per unit time. Molecules that have not extravasated to the interstitium of the SC administration site tissue and the draining lymph nodes are returned to the systemic circulation at a rate of $(1-\sigma_{V_{\text{dLN}}})B_{\text{dLN}}$ and $(1-\sigma_{V_{\text{SC}}})B_{\text{SC}}$.

organ, o, is given by:

$$V_o\frac{dC_o}{dt} = B_o(C_{\text{blood}} - C_o) - f_{CL_o}CL_{\text{tot}}C_o, \tag{4.1}$$

where V_o is the intra-organ blood volume of organ, o, B_o is the blood flow of the organ, o, and C_{blood} is the concentration of antibodies in the extra-organ blood compartment.

A fraction of antibodies in the vasculature of organ, o, denoted σ_{V_o}, enters the interstitial subcompartment of the organ, o, so that the rate of extravasation is proportional to the flow of antibodies through the vasculature subcompartment: $\sigma_{V_o}B_oC_o$. Similarly, the return parameter, σ_{L_o}, defines the lymphatic clearance rate, which proportional to the flow of antibodies through the interstitium ($\sigma_{V_o}B_o\tilde{C}_o$ per unit time). The lymphatic clearance rate is, as a result, equal to $\sigma_{V_o}\sigma_{L_o}B_o\tilde{C}_o$ per unit time, and the rate of change in the number of antibodies in the interstititum of organ, o, is given by:

$$\tilde{V}_o\frac{d\tilde{C}_o}{dt} = \sigma_{V_o}B_o(C_o - \sigma_{L_o}\tilde{C}_o), \tag{4.2}$$

Symbol	Definition	Unit
C_o	Free antibody vasculature concentration in organ, o	molecules / L
$\tilde{C}_o$	Free antibody interstitial volume concentration in organ, o	molecules / L
R_o	Free target cell vasculature concentration in organ, o	molecules / L
$\tilde{R}_o$	Free target cell interstitial volume concentration in organ, o	molecules / L
RC_o	Antibody-target cell complex vasculature concentration in organ, o	molecules / L
$\widetilde{RC}_o$	Antibody-target cell complex interstitial volume concentration in organ, o	molecules / L
B_o	Blood flow (volume of blood per unit time) in organ, o	L / min
V_{blood}	Extra-organ blood volume	L
V_o	Intra-organ blood volume of organ, o	L
$\tilde{V}_o$	Total volume of organ, o	L
σ_{V_o}	Fraction of antibodies extravasating into the interstitial space of organ, o	-
σ_{L_o}	Fraction of antibodies leaving the interstitial space of organ, o	-
ABC_o	Antibody biodistribution coefficient for organ, o	-
CL_{tot}	Antibody systemic clearance	L / min
f_{CL_o}	Organ, o, fractional contribution to the systemic clearance	-
k_{on}	Antibody binding association rate constant	L /(molecules·min)
k_{off}	Antibody binding dissociation rate constant	1 /min
k_{prod}	Target cell synthesis rate constant	cells / (L·min)
k_{elim_o}	Target cell degradation rate constant	1 /min
S_{max}	Maximal antibody-target cell complex elimination rate	L /(min)
SC_{50}	Half-maximal antibody-target cell complex elimination rate concentration	molecules / L
k_{abs}	Antibody absorption rate following SC administration	1 / min
D_{SC}	Subcutaneous injection antibody dose	molecules
D_{IV}	Intravenous infusion antibody dose	molecules
T_{admin}	Intravenous infusion time	min

Table 4.4: Definitions and units of parameters and variables in the model described in Section 4.2.1. See Figures 4.1–4.3 for a schematic of an exemplar organ and the associated parameters.

where $\tilde{V}_o$ is the volume of the organ.

Equations (4.1) and (4.2) apply to all organs except the liver and lymph node compartments. Equations for the liver are modified to capture the distinct anatomical arrangement of the hepatic circulation, where the liver receives blood exiting the mesenteric organ compartments, the spleen and the gut:

$$\begin{aligned} V_{\text{liver}}\frac{dC_{\text{liver}}}{dt} &= B_{\text{liver}}C_{\text{blood}} + \sigma_{V_{\text{spleen}}}\sigma_{L_{\text{spleen}}}B_{\text{spleen}}\tilde{C}_{\text{spleen}} + B_{\text{gut}}(1-\sigma_{V_{\text{gut}}})C_{\text{gut}} \\ &\quad - \left(B_{\text{liver}} + \sigma_{V_{\text{spleen}}}\sigma_{L_{\text{spleen}}}B_{\text{spleen}} + B_{\text{gut}}(1-\sigma_{V_{\text{gut}}})\right)C_{\text{liver}} - f_{CL_{\text{liver}}}CL_{\text{tot}}C_{\text{liver}}. \end{aligned} \tag{4.3}$$

Analogously, the equation for the number of antibodies in the liver interstitium is adjusted to account for the specific anatomy of hepatic blood and lymph circulation, and changes in time

according to:

$$\begin{aligned}\tilde{V}_{\text{liver}}\frac{d\tilde{C}_{\text{liver}}}{dt} &= \sigma_{V_{\text{liver}}}\left(B_{\text{liver}} + \sigma_{V_{\text{spleen}}}\sigma_{L_{\text{spleen}}}B_{\text{spleen}} + B_{\text{gut}}(1-\sigma_{V_{\text{gut}}})\right)C_{\text{liver}} \\ &\quad - \sigma_{V_{\text{liver}}}\sigma_{L_{\text{liver}}}\left(B_{\text{liver}} + \sigma_{V_{\text{spleen}}}\sigma_{L_{\text{spleen}}}B_{\text{spleen}} + B_{\text{gut}}(1-\sigma_{V_{\text{gut}}})\right)\tilde{C}_{\text{liver}}.\end{aligned} \tag{4.4}$$

Lymph nodes are represented in the model as two distinct compartments: the draining lymph nodes compartment, representing the group of lymph nodes draining the subcutaneous tissue at the SC administration site and denoted by *dLN*, and the remaining lymph nodes compartment, denoted by *LN*. Both lymph node compartments are represented as vasculature (the intra-organ blood space) and interstitial subcompartments, where antibodies from the drained organ compartments are directed via lymphatics.

The lumped remaining lymph node compartment (*LN*) drains all organ compartments, except the spleen and the SC administration site tissue. The rate of change in the number of antibodies in the blood supply compartment to the lymph nodes, analogously to Equation (4.1), is given by:

$$V_{\text{LN}}\frac{dC_{\text{LN}}}{dt} = B_{\text{LN}}(C_{\text{blood}} - C_{\text{LN}}) - f_{CL_{\text{LN}}}CL_{\text{tot}}C_{\text{LN}}. \tag{4.5}$$

The rate of change of antibody concentration in the interstitial lymph node subcompartment accounts for the contribution from the lymph node vasculature and, additionally, the flow of interstitium drained antibodies from the connected organs:

$$\begin{aligned}\tilde{V}_{\text{LN}}\frac{d\tilde{C}_{\text{LN}}}{dt} &= \sigma_{V_{\text{LN}}}B_{\text{LN}}(C_{\text{LN}} - \sigma_{L_{\text{LN}}}\tilde{C}_{\text{LN}}) + \sum_i \sigma_{V_i}\sigma_{L_i}B_i\tilde{C}_i - \sum_i \sigma_{L_{\text{LN}}}\sigma_{V_i}\sigma_{L_i}B_i\tilde{C}_{\text{LN}} \\ &\quad + \sigma_{V_{\text{liver}}}\sigma_{L_{\text{liver}}}\left(B_{\text{liver}} + \sigma_{V_{\text{spleen}}}\sigma_{L_{\text{spleen}}}B_{\text{spleen}} + (1-\sigma_{V_{\text{gut}}})B_{\text{gut}}\right)\tilde{C}_{\text{liver}} \\ &\quad - \sigma_{L_{\text{LN}}}\sigma_{V_{\text{liver}}}\sigma_{L_{\text{liver}}}\left(B_{\text{liver}} + \sigma_{V_{\text{spleen}}}\sigma_{L_{\text{spleen}}}B_{\text{spleen}} + (1-\sigma_{V_{\text{gut}}})B_{\text{gut}}\right)\tilde{C}_{\text{LN}},\end{aligned} \tag{4.6}$$

where $i \in \{\text{gut, bone marrow, remaining organs}\}$.

In contrast to the lumped lymph node compartment, the draining lymph nodes receive antibodies only from the local SC tissue, as shown in Figure 4.3. The local SC tissue is represented by vascular and interstitial SC tissue subcompartments, as well as a depot compartment, used to model the SC administration of antibodies. The rate of change in the

antibody concentration in the vascular and interstitial SC tissue subcompartments is given by:

$$V_{\mathrm{SC}}\frac{dC_{\mathrm{SC}}}{dt} = B_{\mathrm{SC}}(C_{\mathrm{blood}} - C_{\mathrm{SC}}) - f_{CL_{\mathrm{SC}}}CL_{\mathrm{tot}}C_{\mathrm{SC}}, \tag{4.7}$$

and

$$\tilde{V}_{\mathrm{SC}}\frac{d\tilde{C}_{\mathrm{SC}}}{dt} = \sigma_{V_{\mathrm{SC}}}B_{\mathrm{SC}}C_{\mathrm{SC}} - \sigma_{L_{\mathrm{SC}}}(\sigma_{V_{\mathrm{SC}}}B_{\mathrm{SC}} + k_{\mathrm{abs}}V_{\mathrm{depot}})\tilde{C}_{\mathrm{SC}} + k_{\mathrm{abs}}V_{\mathrm{depot}}C_{\mathrm{depot}}, \tag{4.8}$$

analogously to Equations (4.2) and (4.1). Antibodies can be administered SC to the depot compartment as modelled by an initial condition and then they are drained with a constant removal rate, k_{abs}:

$$V_{\mathrm{depot}}\frac{dC_{\mathrm{depot}}}{dt} = -k_{\mathrm{abs}}V_{\mathrm{depot}}C_{\mathrm{depot}}. \tag{4.9}$$

The rate of change in the number of antibodies in the draining lymph node blood supply compartment is analogous to Equation (4.5) and given by:

$$V_{\mathrm{dLN}}\frac{dC_{\mathrm{dLN}}}{dt} = B_{\mathrm{dLN}}(C_{\mathrm{blood}} - C_{\mathrm{dLN}}) - f_{CL_{\mathrm{dLN}}}CL_{\mathrm{tot}}C_{\mathrm{dLN}}. \tag{4.10}$$

The rate of change of antibodies in the interstitial subcompartment of the draining lymph nodes accounts for the drainage of antibodies from the local SC tissue and the removal of antibodies from the depot compartment:

$$\begin{aligned}\tilde{V}_{\mathrm{dLN}}\frac{d\tilde{C}_{\mathrm{dLN}}}{dt} &= \sigma_{V_{\mathrm{dLN}}}B_{\mathrm{dLN}}(C_{\mathrm{dLN}} - \sigma_{L_{\mathrm{dLN}}}\tilde{C}_{\mathrm{dLN}}) \\ &\quad + \sigma_{L_{\mathrm{SC}}}\left(\sigma_{V_{\mathrm{SC}}}B_{\mathrm{SC}} + k_{\mathrm{abs}}V_{\mathrm{depot}}\right)\tilde{C}_{\mathrm{SC}} \\ &\quad - \sigma_{L_{\mathrm{SC}}}\sigma_{L_{\mathrm{dLN}}}(\sigma_{V_{\mathrm{SC}}}B_{\mathrm{SC}} + k_{\mathrm{abs}}V_{\mathrm{depot}})\tilde{C}_{\mathrm{dLN}},\end{aligned} \tag{4.11}$$

where each term in order describes: (i) antibody extravasating into the lymph node through the blood supply to the lymph node; (ii) a proportion of the antibody that has extravasated from the lymph node's blood supply being returned to the systemic circulation; (iii, iv) antibody drained from the SC tissue compartment; and (v,vi) a proportion of the antibody that has been drained from the SC tissue compartment and has been returned to the systemic circulation.

Antibodies that have not extravasated from the organs' vasculatures return to the extra-

organ blood compartment, combined with the lymph node compartments outflow:

$$
\begin{aligned}
V_{\text{blood}}\frac{dC_{\text{blood}}}{dt} = {} & \underbrace{f_{IV}}_{(i)} - \underbrace{f_{CL_{\text{blood}}} C L_{\text{tot}} C_{\text{blood}}}_{(ii)} - \underbrace{B_{\text{tot}} C_{\text{blood}}}_{(iii)} \\
& + \underbrace{\sum_{i \notin \{\text{liver, gut, spleen}\}} (1-\sigma_{V_i}) B_i C_i}_{(iv)} \\
& + \underbrace{(1-\sigma_{V_{\text{liver}}})\left(B_{\text{liver}} + \sigma_{V_{\text{spleen}}}\sigma_{L_{\text{spleen}}} B_{\text{spleen}} + (1-\sigma_{V_{\text{gut}}})B_{\text{gut}}\right) C_{\text{liver}}}_{(v)} \\
& + \underbrace{(1-\sigma_{V_{\text{LN}}}) B_{\text{LN}} C_{\text{LN}}}_{(vi)} + \underbrace{(1-\sigma_{V_{\text{dLN}}}) B_{\text{dLN}} C_{\text{dLN}}}_{(vii)} \\
& + \underbrace{\sigma_{L_{\text{dLN}}}\sigma_{V_{\text{dLN}}} B_{\text{dLN}} \tilde{C}_{\text{dLN}}}_{(viii)} + \underbrace{\sigma_{L_{\text{dLN}}}\sigma_{L_{\text{SC}}}(\sigma_{V_{\text{SC}}} B_{\text{SC}} + k_{\text{abs}} V_{\text{depot}}) \tilde{C}_{\text{dLN}}}_{(ix)} \\
& + \underbrace{\sigma_{L_{\text{LN}}}\sigma_{V_{\text{LN}}} B_{\text{LN}} \tilde{C}_{\text{LN}}}_{(x)} + \underbrace{\sum_{i \notin \{\text{liver, spleen, SC, LN, dLN}\}} \sigma_{L_{\text{LN}}}\sigma_{V_i}\sigma_{L_i} B_i \tilde{C}_{\text{LN}}}_{(xi)} \\
& + \underbrace{\sigma_{L_{\text{LN}}}\sigma_{V_{\text{liver}}}\sigma_{L_{\text{liver}}}\left(B_{\text{liver}} + \sigma_{V_{\text{spleen}}}\sigma_{L_{\text{spleen}}} B_{\text{spleen}} + (1-\sigma_{V_{\text{gut}}})B_{\text{gut}}\right) \tilde{C}_{\text{LN}}}_{(xii)},
\end{aligned}
\tag{4.12}
$$

where $B_{\text{tot}} = \sum_i B_i$ where $i \in \{$ spleen, bone marrow, gut, liver, SC administration site compartment, draining lymph nodes, remaining lymph nodes, remaining organs $\}$, and (i) the term f_{IV} is a function describing intravenous administration of antibodies and the remaining terms represent in order: (ii) clearance of antibodies; (iii) the flow of antibodies into and (iv - vii) the return of antibodies from the vasculatures of the organ and lymph node compartments; (viii - ix) the return of antibodies from the draining lymph node compartment; and (x - xii) the return of antibodies from the lumped lymph node compartment (remaining lymph nodes). Equation (4.12) closes the system and completes the flow circuit.

4.2.1.2 Monoclonal antibody binding and target cell interactions (PK-PD) submodel

The PK-PD submodel of the framework, depicted in Figure 4.4, describes the interaction of antibodies with specific affinity against antigens expressed on cell surfaces with the target cells. The binding scheme, together with target cell production and degradation, as well as target

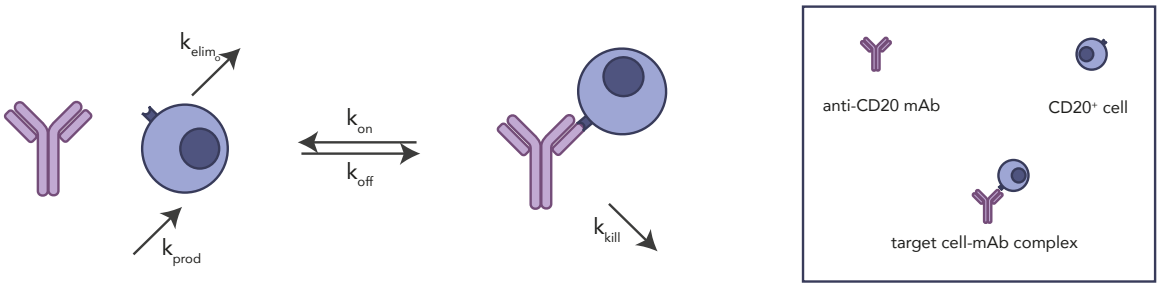


Figure 4.4: The PK-PD submodel describes the interactions of antibodies with specific affinity against antigens expressed on cell surfaces with the target cells. The binding scheme is embedded within the PBPK submodel, as described in Section 4.2.1.2, to simulate the kinetics of mAb binding *in vivo*. Anti-CD20 mAb binds reversible to a $CD20^+$ cell, with the binding constant k_{on} and unbinding rate constant k_{off}. The antibody- B cell complex is eliminated at the rate k_{kill}. The target cells are produced at the rate k_{prod} and degraded at the rate k_{elim_o}.

cell-antibody complexes elimination is given by:

$$\begin{aligned} C_o + R_o &\underset{k_{\text{off}}}{\overset{k_{\text{on}}}{\rightleftharpoons}} RC_o \\ RC_o &\xrightarrow{k_{\text{kill}}} \emptyset \\ \emptyset &\xrightarrow{k_{\text{prod}}} R_o \\ R_o &\xrightarrow{k_{\text{elim}_o}} \emptyset, \end{aligned} \tag{4.13}$$

where C_o, R_o and RC_o are the concentrations of unbound antibody, unbound target cell and antibody-target cell complexes in the organ, o, vascular compartment respectively. In the remainder of the text, an *unbound* or *free* antibody refers to an antibody not bound to a target cell (C_o). When referring to a *target cell*, we consider a target cell not bound to an antibody (R_o), while bound target cells or bound antibodies are quantified through the antibody-target cell complex variable (RC_o).

Antibodies interact with cells expressing the target antigen and bind to target cell reversibly with the association and dissociation constants, k_{on} and k_{off}, respectively. Target cells are produced at a rate, k_{prod}, and degraded at a rate, k_{elim_o}, the value of which was assumed as the ratio of target production rate constant, k_{prod}, and the initial target concentration in each compartment, *i.e.*, $k_{\text{elim}_o} = k_{\text{prod}}/(R_o V_o)$ and $k_{\text{elim}_{\tilde{o}}} = k_{\text{prod}}/(\tilde{R}_o \tilde{V}_o)$, for the vascular and interstitial subcompartments, respectively. Antibodies are assumed to reduce the number of target cells by stimulating cellular destruction, through elimination of antibody-target cell

complexes at a rate, k_{kill}, which depends on the antibody concentration [108, 109, 110]:

$$k_{\text{kill}} = \frac{S_{\text{max}} C_o}{SC_{50} + C_o}, \tag{4.14}$$

where S_{max} and SC_{50} are pharmacodynamic parameters describing the maximal killing rate and the free antibody concentration resulting in a half-maximal effect of the complexes elimination. The mathematical form of the killing rate, k_{kill}, accounts for the cross-talk between antibodies and different immune cells involved in the effector mechanisms, and subsequent activation of the engaged effector cells, which may impact the efficacy of cell elimination [106]. A saturating functional form of the term ensures that that there is a limit to the size of the possible effects of antibody concentration on the resulting cell elimination. In the model, we depict the target cell population, as opposed to the concentration of the target antigen, which in the context of the presented work is the CD20 receptor. As CD20 is a membrane-bound target that does not internalise upon ligand binding [111], the choice of the target variable does not impact our simulations, as we do not have to consider the process of target internalisation.

The resulting kinetic scheme, given by reactions (4.13) and Equation (4.14), is embedded within the PBPK submodel to simulate the kinetics of mAb binding and target cell elimination *in vivo*. The PBPK and PK-PD submodels are coupled through the ODEs given by Equations (4.1) - (4.12), which are modified according to Equations (4.13) and (4.14). For instance, Equation (4.1) is modified to account for the presence of the target cells as follows:

$$\frac{dC_o}{dt} = \frac{B_o}{V_o}(C_{\text{blood}} - C_o) - \frac{f_{CL_o} CL_{\text{tot}}}{V_o} C_o - k_{\text{on}} R_o C_o + k_{\text{off}} RC_o, \tag{4.15}$$

where C_o, R_o and RC_o are the concentrations of unbound antibodies, unbound target cells and antibody-target complexes in the vascular space of organ, o, respectively. Furthermore, the concentration of the target cells and target cell-antibody complexes changes according to:

$$\frac{dR_o}{dt} = -k_{\text{on}} R_o C_o + k_{\text{off}} RC_o + k_{\text{prod}} - k_{\text{elim}_o} R_o, \tag{4.16}$$

and

$$\frac{dRC_o}{dt} = k_{\text{on}} R_o C_o - k_{\text{off}} RC_o - \frac{S_{\text{max}} C_o}{SC_{50} + C_o} RC_o. \tag{4.17}$$

Equation (4.2), describing the rate of change in the concentration of antibody in the

interstitial space of organ, o, is extended analogously:

$$\frac{d\tilde{C}_o}{dt} = \frac{\sigma_{V_o} B_o}{\tilde{V}_o} \left(C_o - \sigma_{L_o} \tilde{C}_o\right) - k_{\text{on}} \tilde{R}_o \tilde{C}_o + k_{\text{off}} \widetilde{RC}_o, \tag{4.18}$$

where the rate of change in the interstitial concentration of the free target cells, $\tilde{R}_o$, and the antibody-target cell complexes, $\widetilde{RC}_o$, changes according to:

$$\frac{d\tilde{R}_o}{dt} = -k_{\text{on}} \tilde{R}_o \tilde{C}_o + k_{\text{off}} \widetilde{RC}_o + k_{\text{prod}} - k_{\text{elim}_{\tilde{o}}} \tilde{R}_o, \tag{4.19}$$

and

$$\frac{d\widetilde{RC}_o}{dt} = k_{\text{on}} \tilde{R}_o \tilde{C}_o - k_{\text{off}} \widetilde{RC}_o - \frac{S_{\text{max}} \tilde{C}_o}{SC_{50} + \tilde{C}_o} \widetilde{RC}_o. \tag{4.20}$$

The remaining ODEs are modified analogously and the ODE system describing the antibody deposition introduced in Section 4.2.1.1 represents a specific case of the PBPK-PD framework with no target present in the system.

4.2.2 Parameterisation

Blood flows, blood and organ volumes in the model were parameterised based on the physiological reference data on cynomolgus monkeys [112, 8]. Blood volumes and blood flows for each organ compartment were expressed through fractions of the total blood volume, $V_o = f_{V_o} V_{\text{blood,tot}}$, and cardiac output, $B_o = f_{B_o} CO$, values reported for cynomolgus monkeys [112]. Due to the lack of cynomolgus monkey reference data for the parameters of the bone marrow compartment, we assumed that the bone marrow comprises approximately the same fraction of total body volume as in human (5% [113]), while the values for the blood flow and blood volume in the compartment were based on the skeletal tissue reference data in cynomolgus monkeys [112, 8]. The baseline values of the extravasation parameters, σ_{V_o}, were estimated using a fit-by-eye of the model simulations and the preclinical data [107]. The values of the return parameters, σ_{L_o}, were based on antibody biodistribution coefficients, ABC_o, reported by Shah and Betts, who quantified antibody concentration in major tissues relative to blood concentration across various species [114]. Contributions of the individual compartments to the systemic clearance, $f_{CL_{\text{tot}}}$, were based on the catabolic activity reported by Eigenmann et al. [104], and scaled by tissue weight to cynomolgus monkey. Parameters within the PBPK framework are summarised in Table 4.5 [94, 97, 96]. Initial $CD20^+$ cell distribution across model compartments was estimated based on the work by Westermann and

Compartment	f_{B_o} [112]	f_{V_o} [112]	$\tilde{V}_o$ [L] [8]	f_{CL_o} [104]	σ_{L_o} [114]	σ_{V_o}
Spleen	7.9E-3	1.28E-3	3.9E-3	5.6E-3	7.81	5E-6
Bone Marrow	8.0E-4	0.02	0.4	0.11	13.76	5E-6
Gut	0.14	0.07	0.16	2.4E-2	19.00	5E-6
SC tissue	5.0E-4	4.8E-4	4.4E-3	1.2E-3	6.37	5E-6
Liver	7.3E-3	0.06	0.14	9.9E-2	8.26	5E-6
Draining LNs	1.0E-4	1.5E-5	2.0E-4	2.0E-4	11.82	5E-6
Remaining LNs	1.2E-2	1.5E-3	2.5E-5	2.4E-5	11.82	5E-6
Remaining organs	0.77	0.25	3.3	0.69	18.93	5E-6
Extra-organ blood	-	0.6	-	4.6E-2	-	-
$V_{\text{blood,tot}}$ [L]	0.189 [112]					
CO [L/min]	0.884 [112]					
CL_{tot} [L/min]	1.2E-5 [116, 117]					

Table 4.5: Cynomolgus monkey anatomical parameter values used for the PBPK submodel parameterisation. Blood flows, blood and organ volumes in the model were parameterised based on the physiological reference data [112, 8]. Blood volumes and blood flows for each organ compartment were expressed through fractions of the total blood volume, $V_o = f_{V_o} V_{\text{blood,tot}}$, and cardiac output, $B_o = f_{B_o} CO$, values reported for cynomolgus monkeys [112]. Draining lymph nodes were assumed to comprise 1% of all lymph nodes, and the parameterisation of the draining lymph node compartment was scaled accordingly. Local SC tissue at the site of SC administration was parameterised under the assumption that a proportion of the lymph nodes affected by lesions drains a corresponding proportion of the skin, *i.e.* 1% of the skin tissue, and the lack of sensitivity of the model to the assumed value was confirmed. Tissue-intrinsic clearance rates were calculated based on the catabolic activity of each tissue, as reported by Eigenmann et al. [104], and scaled by an organ's weight. The values of the return parameters, σ_{L_o}, were based on antibody biodistribution coefficients, ABC_o, reported by Shah and Betts [114], while the extravasation parameters, σ_{V_o}, were assumed equal across all the compartments and the listed values estimated based on initial simulations prior to data fitting, described in Section 4.2.7.

Pabst [115]. Reported organ B cell numbers were mapped to the compartments represented in the model and scaled by tissue weight to cynomolgus monkey. The B cell numbers in the extra- and intra-organ blood compartments were calculated based on the relative blood volume of each compartment and scaling the number of B cells in the blood reported by Westermann and Pabst [115]. PK-PD parameters of anti-CD20 antibodies were sourced from the literature, and are summarised in Tables 4.6.

4.2.2.1 Parameterising lumped compartments

Lumping is a model reduction method aiming to reduce the dimensionality and complexity of a mathematical model of a dynamical system [18]. Due to the complexity of whole-body PBPK models, this model reduction method has been examined in the context of PBPK models applied to both small-molecule drugs [17] and macromolecules, such as monoclonal antibodies [92]. The practicality of model reduction has also been demonstrated for Bayesian inference methods in drug development, where parameter estimation with clinical data might not be tractable or too time-consuming due to the complexity of the system [123].

Parameter	Value	Equivalent value	References
T_{admin}	13 - 20 min	-	[1]
D_{IV}	30 - 50 mg	1.2×10^{17} - 2×10^{17} molecules	[2] [107]
D_{SC}	30 - 50 mg	1.2×10^{17} - 2×10^{17} molecules	[2] [107]
V_{depot}	0.012 L	-	[3]
k_{abs}	0.0025 1/min	-	[4]
k_{on}	10^6 1/(Ms)	9.96×10^{-17} L/(molecules·min)	[118]
k_{off}	0.0052 1/s	-	[5]
k_{prod}	0.019 cells/(L·day)	1.32×10^{-5} cells/(L·min)	[119]
S_{max}	0.042 1/min	-	[6]
SC_{50}	9.198 ng/mL	3.68×10^{13} molecules/L	[6]

Table 4.6: Antibody-specific parameterisation used in the PK-PD submodel. Parameter values were sourced from the literature and available regulatory documentation. For each organ compartment, B cell elimination rate constant, k_{elim_o}, was assumed as the ratio of the B cell production rate constant, k_{prod}, and the initial B cell number in each compartment, *i.e.* $k_{\text{elim}_o} = k_{\text{prod}}/(R_o V_o)$ and $k_{\text{elim}_{\tilde{o}}} = k_{\text{prod}}/(\tilde{R}_o \tilde{V}_o)$. [1]Estimated based on the administration time in the clinic; [2]Ranges based on the doses reported as 10 mg/kg, body weight of cynomolgus monkeys in the study ($3 - 5$ kg). Equivalent value calculated based on the molecular weight conversion factor ($MW = 4 \times 10^{15}$ molecules/mg) for Rituximab (145 kDa [120]); [3]Calculated based on the dose, D_{SC}, for an anti-CD20 mAb, SC Rituximab; [4]Estimated based on comparison with the preclinical data [107]; [5]Calculated based on the Rituximab dissociation constant, $K_D = 5.2$ nM [121]; [6]Estimated based on a real-time cytotoxicity assay study [122].

In the PBPK submodel, described in Section 4.2.1.1, the gut and the remaining organs compartments represent two lumped compartments which comprise distinct tissues (*e.g.*, the gut compartment depicts the stomach, pancreas, small and large intestines). We, therefore, mapped the parameters associated with the distinct tissues within each lumped compartment onto the parameters that describe the lumped compartments in the model (see Figure 4.5).

Consider a lumped compartment, L, representing n individual organs or tissues, with the organ, $\tilde{V}_L$, and blood volumes, V_L, of the lumped compartment, L, equal to the sum of the corresponding parameters of the individual organs or tissues:

$$\begin{aligned} V_L &= \sum_{i=1}^{n} V_i, \\ \tilde{V}_L &= \sum_{i=1}^{n} \tilde{V}_i. \end{aligned} \tag{4.21}$$

Let N_L and C_L be the number and concentration of antibodies in the lumped compartment, L. Mapping between the parameters of the lumped and individual compartments is derived from the constraint that the total numbers of antibodies in the lumped vascular and interstitial compartments (N_L and $\tilde{N}_L$, respectively) and across the vascular and interstitial organ

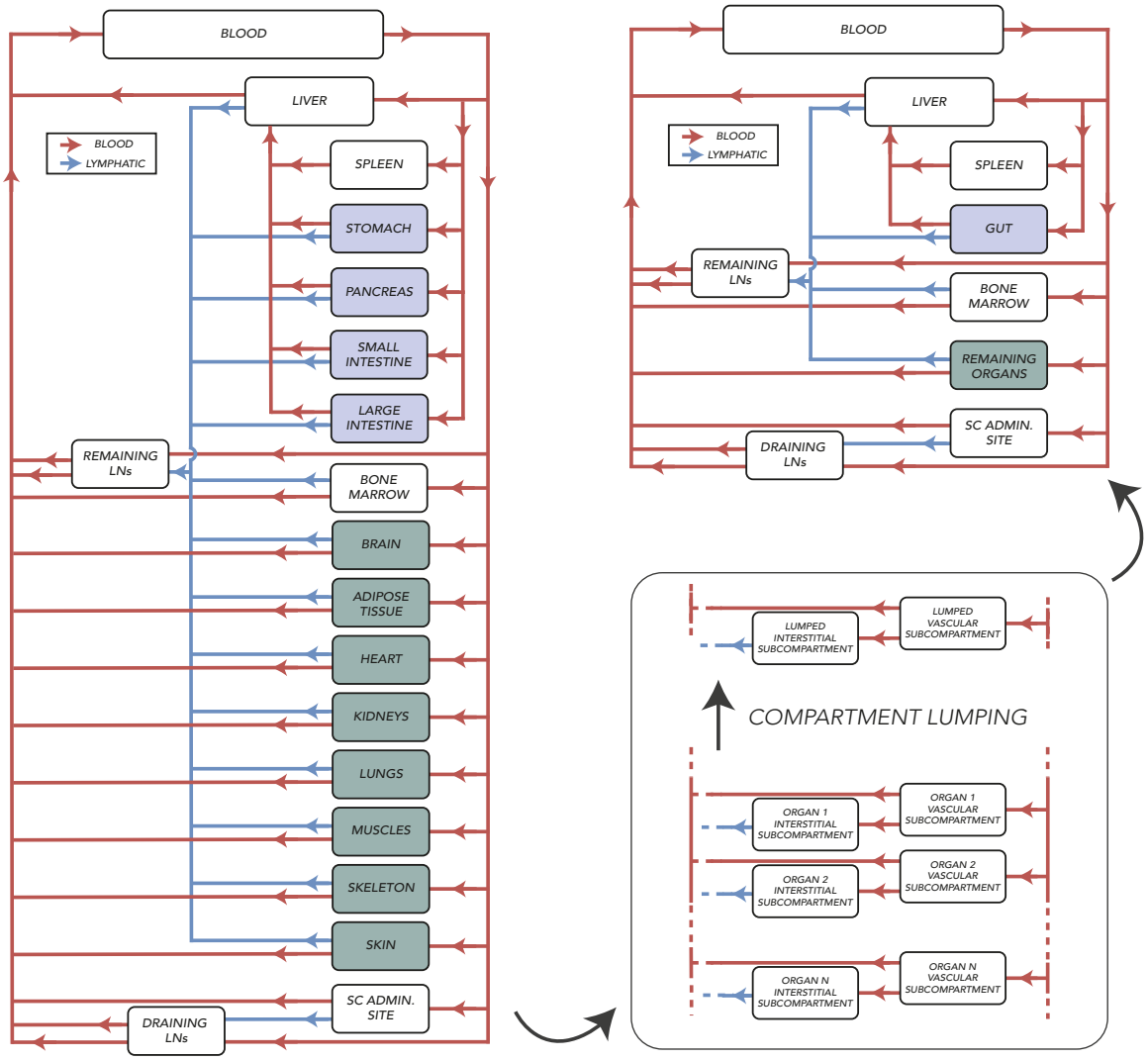


Figure 4.5: Full (left) vs lumped PBPK model (upper right) of monoclonal antibody deposition. The full PBPK model comprises 19 main compartments, each representing a distinct organ or a tissue. The complexity of the full model is reduced (9 compartments in the lumped PBPK model) through compartment lumping (lower right), where vascular and interstitial subcompartments are lumped together such that a lumped compartment represents multiple organs and tissues. Compartments lumped together are highlighted. For instance, the stomach, pancreas, and small and large intestine compartments are lumped as the gut compartment (purple).

compartments comprising the lumped compartment (N_i and $\tilde{N}_i$) are conserved:

$$\begin{aligned} N_L(t) &= \sum_{i=1}^{n} N_i(t), \\ \tilde{N}_L(t) &= \sum_{i=1}^{n} \tilde{N}_i(t), \end{aligned} \tag{4.22}$$

or equivalently:

$$C_L(t) = \frac{1}{V_L} \sum_{i=1}^{n} V_i C_i(t), \tag{4.23}$$

and

$$\tilde{C}_L(t) = \frac{1}{\tilde{V}_L} \sum_{i=1}^{n} \tilde{V}_i \tilde{C}_i(t). \tag{4.24}$$

Consider Equations (4.1) and (4.2) in steady state:

$$\frac{C_o}{C_{\text{blood}}} = \frac{B_o}{B_o + f_{CL_o} CL_{\text{tot}}}, \tag{4.25}$$

and

$$\frac{\tilde{C}_o}{C_o} = \frac{1}{\sigma_{L_o}}. \tag{4.26}$$

Since $f_{CL_o} CL_{\text{tot}} \ll B_o$ (see Table 4.5), Equation (4.25) implies:

$$\frac{C_o}{C_{\text{blood}}} \approx 1. \tag{4.27}$$

Equation (4.27), therefore, suggests that the antibody concentration in the extra- and intra-organ blood compartments is approximately equal in quasi-steady state, and the overall concentration in the blood pool is roughly homogeneous. However, all system equations are required to account for the transients in the model behaviour at early times, *i.e.*, the initial sharp increase, peak, and subsequent decay in the antibody concentration, as well as for the interaction of antibodies with target cells that we introduce in the PK-PD submodel.

Noting that an antibody biodistribution coefficient, ABC_o, quantifies antibody concentration in an organ, o, relative to blood concentration [114], we can also express the coefficient ABC_o using Equation (4.26):

$$ABC_o = \frac{\tilde{C}_o}{C_{\text{blood}}} = \frac{1}{\sigma_{L_o}}. \tag{4.28}$$

Dividing Equation (4.24) by C_{blood}:

$$\frac{\tilde{C}_L}{C_{\text{blood}}} = \frac{1}{\sigma_{L_L}} = \frac{1}{\tilde{V}_L}\sum_{i=1}^{n}\tilde{V}_i\frac{1}{\sigma_{L_i}}, \tag{4.29}$$

which defines the relation between the parameter σ_{L_L} and the parameters σ_{L_i} and ABC_i of the individual organs, we obtain:

$$\frac{1}{\sigma_{L_L}} = \frac{1}{\tilde{V}_L}\sum_{i=1}^{n}\tilde{V}_i\frac{1}{\sigma_{L_i}} = \frac{1}{\tilde{V}_L}\sum_{i=1}^{n}\tilde{V}_i ABC_i. \tag{4.30}$$

Differentiating Equation (4.23) with respect to time, t, and considering the vascular sub-compartments of the lumped organs (Equation (4.1)):

$$\begin{aligned} V_L\frac{dC_L}{dt} &= B_L(C_{\text{blood}} - C_L) - f_{CL_L}CL_{\text{tot}}C_L \\ &= \sum_{i=1}^{n}\left(B_i(C_{\text{blood}} - C_i) - f_{CL_i}CL_{\text{tot}}C_i\right) = \sum_{i=1}^{n}V_i\frac{dC_i}{dt}, \end{aligned} \tag{4.31}$$

we require

$$B_L C_{\text{blood}} = \sum_{i=1}^{n}B_i C_{\text{blood}}, \tag{4.32}$$

$$B_L C_L = \sum_{i=1}^{n}B_i C_i, \tag{4.33}$$

and

$$f_{CL_L}CL_{\text{tot}}C_L = \sum_{i=1}^{n}f_{CL_i}CL_{\text{tot}}C_i. \tag{4.34}$$

Equation (4.32) simplifies to:

$$B_L = \sum_{i=1}^{n}B_i, \tag{4.35}$$

which we can use to express Equation (4.33) as:

$$C_L = \frac{\sum_{i=1}^{n}B_i C_i}{\sum_{i=1}^{n}B_i}. \tag{4.36}$$

However, Equation (4.23), which defines the interstitial concentration in the lumped compart-

ment, L, also implies that

$$C_L = \frac{\sum_{i=1}^{n} V_i C_i}{\sum_{i=1}^{n} V_i}, \tag{4.37}$$

resulting in an equality that is not always true:

$$\frac{B_i}{\sum_{i=1}^{n} B_i} = \frac{V_i}{\sum_{i=1}^{n} V_i}, \tag{4.38}$$

as the above equality requires the ratio of the blood flow to the blood volume of each organ i in the lumped compartment to be equal to that of the lumped compartment:

$$\frac{B_i}{V_i} = \frac{\sum_{i=1}^{n} B_i}{\sum_{i=1}^{n} V_i}, \tag{4.39}$$

for the concentration-time profiles of the individual and lumped subcompartments to coincide. This discrepancy highlights that the lumping of the model compartments may generate errors, as the full and simplified models are not equivalent. Finally, using Equation (4.23) and noting that $C_o \approx C_{\text{blood}}$, Equation (4.34) gives:

$$f_{CL_L} = \frac{\sum_{i=1}^{n} f_{CL_i} C_i}{C_L} = \frac{\sum_{i=1}^{n} f_{CL_i} C_i}{\frac{\sum_{i=1}^{n} V_i C_i}{V_L}} \approx \frac{\sum_{i=1}^{n} f_{CL_i} C_{\text{blood}}}{\frac{\sum_{i=1}^{n} V_i C_{\text{blood}}}{V_L}} = \sum_{i=1}^{n} f_{CL_i}, \tag{4.40}$$

where the last equality follows from Equation (4.21).

Similarly, differentiating Equation (4.24) with respect to time, t, and considering the interstitial subcompartments of the lumped organs (Equation (4.2)):

$$\tilde{V}_L \frac{d\tilde{C}_L}{dt} = \sigma_{V_L} B_L (C_L - \sigma_{L_L} \tilde{C}_L) = \sum_{i=1}^{n} \sigma_{V_i} B_i (C_i - \sigma_{L_i} \tilde{C}_i) = \sum_{i=1}^{n} \tilde{V}_i \frac{d\tilde{C}_i}{dt}, \tag{4.41}$$

we require

$$\sigma_{V_L} B_L C_L = \sum_{i=1}^{n} \sigma_{V_i} B_i C_i, \tag{4.42}$$

and

$$\sigma_{L_L} \sigma_{V_L} B_L \tilde{C}_L = \sum_{i=1}^{n} \sigma_{L_i} \sigma_{V_i} B_i \tilde{C}_i. \tag{4.43}$$

Using Equation (4.23) and noting that $C_o \approx C_{\text{blood}}$, Equation (4.42) gives:

$$\sigma_{V_L} = \frac{\sum_{i=1}^{n} \sigma_{V_i} B_i C_i}{B_L C_L} = \frac{\sum_{i=1}^{n} \sigma_{V_i} B_i C_i}{B_L \frac{\sum_{i=1}^{n} V_i C_i}{V_L}} = \frac{\sum_{i=1}^{n} \sigma_{V_i} B_i C_{\text{blood}}}{B_L \frac{\sum_{i=1}^{n} V_i C_{\text{blood}}}{V_L}} = \frac{\sum_{i=1}^{n} \sigma_{V_i} B_i}{\sum_{i=1}^{n} B_i}, \tag{4.44}$$

where the last equality follows from Equations (4.21) and (4.35). On the other hand, Equation (4.43) gives:

$$\sigma_{L_L} = \frac{\sum_{i=1}^{n} \sigma_{L_i} \sigma_{V_i} B_i \tilde{C}_i}{\sigma_{V_L} B_L \tilde{C}_L}. \tag{4.45}$$

However, as $\tilde{C}_i$ and $\tilde{C}_L$ are dynamic variables, σ_{L_L} can be only be defined correctly as a constant once the system reaches quasi steady state and $\tilde{C}_i \approx C_{\text{blood}}/\sigma_{L_i}$ (see Equations (4.26) and (4.27)). In quasi steady state, the above expression can be simplified to give:

$$\sigma_{L_L} = \frac{\tilde{V}_L}{\sum_{i=1}^{n} \frac{\tilde{V}_i}{\sigma_{L_i}}}, \tag{4.46}$$

which is equivalent to Equation (4.30) derived previously.

The above derivation, therefore suggests that lumping organ compartments in a PBPK model may introduce an error due to the full and simplified models not being exact. However, we pursued this analysis to the extent that is necessary for the purpose of mapping the single organs and lumped compartment parameters in this chapter and we will comment on the issue in Section 4.4.4.

4.2.3 Simulating IV and SC administration of antibodies

The ODE system describing the antibody deposition (Sections 4.2.1.1 and 4.2.1.2) was solved numerically using the Matlab stiff $ode23tb$ solver with a variable time step, subject to initial conditions, where antibodies were administered *in silico* through an intravenous infusion and subcutaneous injection. The intravenous infusion was simulated by defining the input function, f_{IV}, in the blood compartment ODE (see Equation (4.12)) as:

$$f_{IV} = \begin{cases} \frac{D_{\text{IV}} MW}{T_{\text{admin}}} & t \leq T_{\text{admin}} \\ 0 & t \geq T_{\text{admin}} \end{cases}, \tag{4.47}$$

Organ compartment	Initial B cell numbers	
	Vascular space	Interstitial space
Spleen	3.2×10^6	3.5×10^{10}
Bone marrow	4.9×10^7	2.5×10^{10}
Gut	1.7×10^8	1.18×10^{10}
SC Site	1.2×10^6	2.3×10^5
Liver	1.5×10^8	1.1×10^{10}
Draining lymph nodes	3.8×10^4	3.8×10^8
Remaining lymph nodes	3.8×10^6	3.8×10^{10}
Remaining organs	6.2×10^8	6.4×10^9
Extra-organ blood	1.5×10^9	-

Table 4.7: Initial distribution of the B cell numbers across the model compartments, estimated based on data compiled by Westermann and Pabst [115].

where D_{IV} is the antibody dose in the IV formulation, MW is the molecular weight conversion factor ($MW = 4 \times 10^{15}$ molecules/mg) and T_{admin} is the duration of the infusion. Subcutaneous injection was assumed to occur instantaneously and was simulated through initial conditions, where the antibody dose in the SC formulation is administered to the depot compartment (see Figure 4.3):

$$C_{\text{depot}}(t = 0) = \frac{D_{\text{SC}} MW}{V_{\text{depot}}}, \tag{4.48}$$

where D_{SC} is the antibody dose in the SC formulation and V_{depot} is the volume of the injection. Table 4.7 shows the the initial number of B cells in the model compartments, $V_o R_o(t = 0)$ and $\tilde{V}_o \tilde{R}_o(t = 0)$, assumed to hold for both the IV and SC administration.

4.2.4 Structural identifiability analysis

Structural identifiability of the PBPK-PD framework was analysed using an analytical scaling method developed by Castro and de Boer [15], which allows an assessment of local structural identifiability of ODE models by considering the invariance of the model equations under the scaling transformation of the framework parameters [15]. Consider a general ODE model with n variables, $x_i(t)$, and m parameters, λ_j:

$$\frac{dx_i}{dt} = f_i(x_1, \cdots, x_n; \lambda_1, \cdots \lambda_m),$$

where $i = 1, \cdots, n$ and the functions f_i define the time evolution of the variables, $x_i(t)$. Variables, $x_i(t)$, are further categorised as either observed (*i.e.*, measured in an experiment) or latent (*i.e.*, variables which cannot be observed or for which data is not available). The scaling method is based on the decomposition of the functions, f_i, into a sum of M linear independent summands, f_{ik}:

$$\frac{dx_i}{dt} = f_i(x_1, \cdots, x_r, x_{r+1}, \cdots; \lambda_1, \cdots \lambda_m) = \sum_{k=1}^{M} f_{ik}(\tilde{x_k}, \tilde{\lambda_k}), \tag{4.49}$$

where a pair of summands f_{ik} and f_{il} is linear independent for $k \neq l$, all fixed i, and $\tilde{x_k}$ and $\tilde{\lambda}_k$ indicate the subset of variables and parameters present in the function f_{ik}. The analysis is then performed in the following steps:

1. All parameters (λ_i, $i = 1, \ldots, m$) are scaled by unknown scaling factors, u_{λ_i}. All observed variables (x_k, $k = 1, \ldots, r$, where $r < n$) remain unscaled, while all latent variables (x_j, $j = r + 1, \ldots, n$, where $r < n$) are scaled by unknown scaling factors, u_{x_j}

$$\lambda_i \rightarrow u_{\lambda_i} \lambda_i,$$

$$x_k \rightarrow x_k,$$

$$x_j \rightarrow u_{x_j} x_j,$$

   where $i = 1, \ldots, m$, $k = 1, \ldots, r$ and $j = r + 1, \ldots, n$. The scaled parameters and variables are then substituted into Equation (4.49).

2. Each linear independent function, f_{ik}, is equated to its scaled version, such that:

$$f_{ik}(\tilde{x}, \tilde{\lambda}) = \frac{1}{u_{x_i}} f_{ik}(u_{\tilde{x}} \tilde{x}, u_{\tilde{\lambda}} \tilde{\lambda}), \tag{4.50}$$

   where $u_{x_i} = 1$ for $1 \leq i \leq r$ (observed variables) and the factor, $\frac{1}{u_{x_i}}$, originates from the scaling of the derivative, *i.e.*, $\frac{dx_i}{dt} \rightarrow u_{x_i} \frac{dx_i}{dt}$.

3. Equation (4.50) is used to find combinations of the scaling factors, u, which leave the system invariant. These combinations define the identifiability equations of a given model.

4. Variables x_i with a solution $u_{x_i} = 1$ are observable, *i.e.*, it is theoretically possible to infer its state [124]. Parameters λ_i with a solution $u_{\lambda_i} = 1$ are structurally identifiable. Parameters whose scaling factors, u, are coupled form parameter groupings and cannot be identified independently.

The outlined method was used to investigate the local structural identifiability of the model applied to monoclonal antibodies (the full PBPK-PD framework in Section 4.2.1). Blood antibody concentration was assumed to be an observable variable, while the antibody concentrations in all the remaining compartments were treated as latent. Scaling factors were introduced for all latent variables and parameters in the model. The exceptions were the physiological parameters, such as organ ($\tilde{V}_o$), fractional blood volumes (f_{V_o}), fractional blood flows (f_{B_o}), cardiac output, (CO), and fractional tissue-intrinsic clearances (f_{CL_o}), which were assumed to be known. Identifiability equations were derived by considering linearly independent functions in the ODE system.

Consider Equations (4.15) – (4.20) and scale all latent variables and unknown parameters by scaling factors, u:

$$\begin{array}{ccc}
C_o \to u_{C_o} C_o & \tilde{C}_o \to u_{\tilde{C}_o} \tilde{C}_o & R_o \to u_{R_o} R_o \\
\tilde{R}_o \to u_{\tilde{R}_o} \tilde{R}_o & RC_o \to u_{RC_o} RC_o & \widetilde{RC}_o \to u_{\widetilde{RC}_o} \widetilde{RC}_o \\
V_{\text{blood,tot}} \to u_{V_{\text{blood,tot}}} V_{\text{blood,tot}} & CO \to u_{CO} CO & CL_{\text{tot}} \to u_{CL_{\text{tot}}} CL_{\text{tot}} \\
\sigma_{V_o} \to u_{\sigma_{V_o}} \sigma_{V_o} & \sigma_{L_o} \to u_{\sigma_{L_o}} \sigma_{L_o} & k_{\text{on}} \to u_{k_{\text{on}}} k_{\text{on}} \\
k_{\text{off}} \to u_{k_{\text{off}}} k_{\text{off}} & k_{\text{elim}_o} \to u_{k_{\text{elim}_o}} k_{\text{elim}_o} & k_{\text{elim}_{\tilde{o}}} \to u_{k_{\text{elim}_{\tilde{o}}}} k_{\text{elim}_{\tilde{o}}} \\
k_{\text{prod}} \to u_{k_{\text{prod}}} k_{\text{prod}} & S_{\max} \to u_{S_{\max}} S_{\max} & SC_{50} \to u_{SC_{50}} SC_{50},
\end{array} \tag{4.51}$$

where the subscript o applies to all organs in the model, *i.e.*, the spleen, bone marrow, gut, liver, SC administration site compartment, draining lymph nodes, remaining lymph nodes and remaining organs.

Expressing the blood flow (B_o) and the blood volume (V_o) parameters in Equation (4.15) using the fractional blood flow (f_{B_o}) and the cardiac output (CO) parameters as $B_o = f_{B_o} CO$, and using the fractional blood volume (f_{V_o}) and the total volume ($V_{\text{blood,tot}}$) parameters as $V_o = f_{V_o} V_{\text{blood,tot}}$, respectively, linearly independent functions appearing in Equation (4.15) are

given by:

$$f_{11} = \frac{f_{B_o} CO}{f_{V_o} V_{\text{blood,tot}}} C_{\text{blood}} \quad f_{12} = -\frac{f_{B_o} CO}{f_{V_o} V_{\text{blood,tot}}} C_o \quad f_{13} = -\frac{f_{CL_o} CL_{\text{tot}}}{f_{V_o} V_{\text{blood,tot}}} C_o$$
$$f_{14} = -k_{\text{on}} R_o C_o \qquad f_{15} = k_{\text{off}} R C_o. \tag{4.52}$$

In Equation (4.16), they are given by

$$f_{21} = -k_{\text{on}} R_o C_o \qquad f_{22} = k_{\text{off}} R C_o$$
$$f_{23} = k_{\text{prod}} \qquad f_{24} = -k_{\text{elim}_o} R_o; \tag{4.53}$$

and in Equation (4.17) by

$$f_{31} = k_{\text{on}} R_o C_o \quad f_{32} = -k_{\text{off}} R C_o$$
$$f_{33} = -\frac{S_{\max} C_o}{S C_{50} + C_o} \qquad f_{34} = R C_o. \tag{4.54}$$

Similarly, expressing the blood flow (B_o) in Equation (4.18) using the fractional blood flow (f_{B_o}) and the cardiac output (CO) parameters as $B_o = f_{B_o} CO$, linearly independent functions appearing in Equation (4.18) are given by

$$f_{41} = \frac{\sigma_{V_o} f_{B_o} CO}{\tilde{V}_o} C_o \quad f_{42} = -\frac{\sigma_{V_o} \sigma_{L_o} f_{B_o} CO}{\tilde{V}_o} \tilde{C}_o$$
$$f_{43} = -k_{\text{on}} \tilde{R}_o \tilde{C}_o \qquad f_{44} = k_{\text{off}} \widetilde{RC}_o, \tag{4.55}$$

in Equation (4.19) by

$$f_{51} = -k_{\text{on}} \tilde{R}_o \tilde{C}_o \qquad f_{52} = k_{\text{off}} \widetilde{RC}_o$$
$$f_{53} = k_{\text{prod}} \qquad f_{54} = -k_{\text{elim}_{\tilde{o}}} \tilde{R}_o, \tag{4.56}$$

and, finally, in Equation (4.20) by

$$f_{61} = k_{\text{on}} \tilde{R}_o \tilde{C}_o \quad f_{62} = -k_{\text{off}} \widetilde{RC}_o$$
$$f_{63} = -\frac{S_{\max} \tilde{C}_o}{S C_{50} + \tilde{C}_o} \qquad f_{65} = \widetilde{RC}_o. \tag{4.57}$$

Equating the linearly independent functions to their scaled versions, we obtain the following identifiability equations:

$$
\begin{aligned}
&f_{11} = \tfrac{f_{B_o} CO}{f_{V_o} V_{\text{blood,tot}}} C_{\text{blood}} = \tfrac{u_{CO}}{u_{C_o} u_{V_{\text{blood,tot}}}} \tfrac{f_{B_o} CO}{f_{V_o} V_{\text{blood,tot}}} C_{\text{blood}} && f_{12} = -\tfrac{f_{B_o} CO}{f_{V_o} V_{\text{blood,tot}}} C_o = -\tfrac{1}{u_{C_o} u_{V_{\text{blood,tot}}}} \tfrac{u_{CO} f_{B_o} CO}{f_{V_o} V_{\text{blood,tot}}} u_{C_o} C_o \\
&f_{13} = -\tfrac{f_{CL_o} CL_{\text{tot}}}{f_{V_o} V_{\text{blood,tot}}} C_o = -\tfrac{1}{u_{C_o} u_{V_{\text{blood,tot}}}} \tfrac{u_{CL_{\text{tot}}} f_{CL_o} CL_{\text{tot}}}{f_{V_o} V_{\text{blood,tot}}} u_{C_o} C_o && f_{14} = -k_{\text{on}} R_o C_o = -\tfrac{1}{u_{C_o}} u_{k_{\text{on}}} k_{\text{on}} u_{R_o} R_o u_{C_o} C_o \\
&f_{15} = k_{\text{off}} RC_o = \tfrac{1}{u_{C_o}} u_{k_{\text{off}}} k_{\text{off}} u_{RC_o} RC_o && f_{21} = -k_{\text{on}} R_o C_o = -\tfrac{1}{u_{R_o}} u_{k_{\text{on}}} k_{\text{on}} u_{R_o} R_o u_{C_o} C_o \\
&f_{22} = k_{\text{off}} RC_o = \tfrac{1}{u_{R_o}} u_{k_{\text{off}}} k_{\text{off}} u_{RC_o} RC_o && f_{23} = k_{\text{prod}} = \tfrac{1}{u_{R_o}} u_{k_{\text{prod}}} k_{\text{prod}} \\
&f_{24} = -k_{\text{elim}_o} R_o = -\tfrac{1}{u_{R_o}} u_{k_{\text{elim}_o}} k_{\text{elim}_o} u_{R_o} R_o && f_{31} = k_{\text{on}} R_o C_o = \tfrac{1}{u_{RC_o}} u_{k_{\text{on}}} k_{\text{on}} u_{R_o} R_o u_{C_o} C_o \\
&f_{32} = -k_{\text{off}} RC_o = -\tfrac{1}{u_{RC_o}} u_{k_{\text{off}}} k_{\text{off}} u_{RC_o} RC_o && f_{33} = -\tfrac{S_{\max} C_o}{SC_{50} + C_o} = -\tfrac{1}{u_{RC_o}} \tfrac{u_{S_{\max}} S_{\max} u_{C_o} C_o}{u_{SC_{50}} SC_{50} + u_{C_o} C_o} \\
&f_{34} = RC_o = \tfrac{1}{u_{RC_o}} u_{RC_o} RC_o && f_{41} = \tfrac{\sigma_{V_o} f_{B_o} CO}{\tilde{V}_o} C_o = \tfrac{u_{\sigma_{V_o}} u_{CO}}{u_{\tilde{C}_o}} \tfrac{\sigma_{V_o} f_{B_o} CO}{\tilde{V}_o} u_{C_o} C_o \\
&f_{42} = -\tfrac{\sigma_{V_o} \sigma_{L_o} f_{B_o} CO}{\tilde{V}_o} \tilde{C}_o = -\tfrac{u_{\sigma_{L_o}} u_{\sigma_{V_o}} u_{CO}}{u_{\tilde{C}_o}} \tfrac{\sigma_{V_o} \sigma_{L_o} f_{B_o} CO}{\tilde{V}_o} u_{\tilde{C}_o} \tilde{C}_o && f_{43} = -k_{\text{on}} \tilde{R}_o \tilde{C}_o = -\tfrac{1}{u_{\tilde{C}_o}} u_{k_{\text{on}}} u_{\tilde{C}_o} u_{\tilde{R}_o} k_{\text{on}} \tilde{C}_o \tilde{R}_o \\
&f_{44} = k_{\text{off}} \widetilde{RC}_o = \tfrac{1}{u_{\tilde{C}_o}} u_{k_{\text{off}}} u_{\widetilde{RC}_o} k_{\text{off}} \widetilde{RC}_o && f_{51} = -k_{\text{on}} \tilde{R}_o \tilde{C}_o = -\tfrac{1}{u_{\tilde{R}_o}} u_{k_{\text{on}}} u_{\tilde{C}_o} u_{\tilde{R}_o} k_{\text{on}} \tilde{C}_o \tilde{R}_o \\
&f_{52} = k_{\text{off}} \widetilde{RC}_o = \tfrac{1}{u_{\tilde{R}_o}} u_{k_{\text{off}}} u_{\widetilde{RC}_o} k_{\text{off}} \widetilde{RC}_o && f_{53} = k_{\text{prod}} = \tfrac{1}{u_{\tilde{R}_o}} u_{k_{\text{prod}}} k_{\text{prod}} \\
&f_{54} = -k_{\text{elim}_{\tilde{o}}} \tilde{R}_o = -\tfrac{1}{u_{\tilde{R}_o}} u_{k_{\text{elim}_{\tilde{o}}}} k_{\text{elim}_{\tilde{o}}} u_{\tilde{R}_o} \tilde{R}_o && f_{61} = k_{\text{on}} \tilde{R}_o \tilde{C}_o = \tfrac{1}{u_{\widetilde{RC}_o}} u_{k_{\text{on}}} u_{\tilde{C}_o} u_{\tilde{R}_o} k_{\text{on}} \tilde{C}_o \tilde{R}_o \\
&f_{62} = -k_{\text{off}} \widetilde{RC}_o = -\tfrac{1}{u_{\widetilde{RC}_o}} u_{k_{\text{off}}} k_{\text{off}} u_{\widetilde{RC}_o} \widetilde{RC}_o && f_{63} = -\tfrac{S_{\max} \tilde{C}_o}{SC_{50} + \tilde{C}_o} = -\tfrac{1}{u_{\widetilde{RC}_o}} \tfrac{u_{S_{\max}} S_{\max} u_{\tilde{C}_o} \tilde{C}_o}{u_{SC_{50}} SC_{50} + u_{\tilde{C}_o} \tilde{C}_o} \\
&f_{64} = \widetilde{RC}_o = -\tfrac{1}{u_{\widetilde{RC}_o}} u_{\widetilde{RC}_o} \widetilde{RC}_o.
\end{aligned}
\tag{4.58}
$$

Identifiability equations for the compartments which have different structure of the ODEs, *i.e.*, blood, spleen, the liver, the SC administration site, the depot, the draining lymph node and the remaining lymph node compartments, were derived analogously (which were not included here due to the high number of identifiability equations for the whole ODE system). The resulting identifiability equations can be solved for the scaling factors, u:

$$
\begin{aligned}
&u_{C_o} = u_{\tilde{C}_o} = u_{C_{\text{depot}}} = u_{R_o} = u_{RC_o} = u_{\tilde{R}_o} = u_{\widetilde{RC}_o} = 1, \\
&u_{k_{\text{on}}} = u_{k_{\text{off}}} = u_{k_{\text{prod}}} = u_{k_{\text{elim}_o}} = u_{k_{\text{elim}_{\tilde{o}}}} = u_{\sigma_{V_o}} = u_{\sigma_{L_o}} = \\
&u_{k_{\text{abs}}} = u_{S_{\max}} = u_{SC_{50}} = u_{V_{\text{blood,tot}}} = u_{CL_{\text{tot}}} = u_{CO} = 1,
\end{aligned}
\tag{4.59}
$$

where the subscript o applies to all organs in the model, *i.e.*, the spleen, bone marrow, gut, liver, SC administration site compartment, draining lymph nodes, remaining lymph nodes and remaining organs. As all parameters in the model have only one trivial solution ($u_{\lambda_i} = 1$) for any solution of the identifiability equations, all parameters are structurally identifiable by

definition. The analysis of the ODE system described in Section 4.2.1 yielded a system of identifiability equations with only one trivial solution, indicating that, given blood antibody concentration data, the model is structurally identifiable.

4.2.5 Local sensitivity analysis

A local sensitivity analysis of the PBPK-PD model was performed to identify the most influential parameters governing the free antibody blood concentration. A single IV and SC administration of antibody (with 40 mg dose for both administration routes) were simulated, and the sensitivity of the maximal free antibody blood concentration, C_{max}, defined as

$$C_{\text{max}} = max(C_{\text{blood}}(t)), \tag{4.60}$$

and the time taken to achieve it, T_{max}:

$$T_{\text{max}} : C_{\text{blood}}(t = T_{\text{max}}) = C_{\text{max}}, \tag{4.61}$$

was evaluated using a local one-at-a-time (OAT) method.

For both the IV and SC administration simulations, the parameters tested in the local sensitivity analysis included the extravasation parameters (σ_{V_o}), the return parameters (σ_{L_o}), total blood volume ($V_{\text{blood,tot}}$, cardiac output (CO), systemic antibody clearance rate (CL_{tot}), the PK-PD submodel parameters (k_{on}, k_{off}, S_{max}, SC_{50}, k_{prod}) and the initial B cell numbers across the model compartments ($\tilde{V}_o\widetilde{RC}_o(t = 0)$, $V_{\text{blood,tot}}RC_{\text{blood,tot}}(t = 0)$). The antibody administration site absorption rate (k_{abs}) was additionally analysed in the SC administration case. Each parameter value was varied one at a time by $\pm 10\%$, while keeping the rest of the parameters at their baseline levels, as given in Tables 4.5 and 4.6. The reference set of parameters was sourced from the literature, as detailed in Section 4.2.2, and the remaining unknown parameters were estimated to match the free antibody blood concentration predicted by the model to the data used for fitting, which we describe in more detail in Sections 4.2.6 and 4.2.7.

Sensitivity in the simulated outputs ($C_{\text{max,IV}}$, $C_{\text{max,SC}}$, $T_{\text{max,IV}}$ and $T_{\text{max,SC}}$) was measured by evaluating the change in each output using a local sensitivity index defined through a partial derivative of each output with respect to the varied parameter. The resulting derivatives were normalised for dimensional and scaling reasons to allow comparison. The sensitivity indices

were, thus, defined as:

$$S_i = \frac{\partial V}{\partial P_i} \Big/ \frac{V}{P_i}, \tag{4.62}$$

where V denotes the output variable analysed ($V \in \{C_{\text{max,IV}}, C_{\text{max,SC}}, T_{\text{max,IV}}, T_{\text{max,SC}}\}$), and P_i the varied parameter, with i running over all parameters included in the local sensitivity analysis.

4.2.6 Experimental data

Experimental data was obtained from the literature for the purpose of model fitting and practical identifiability analysis [107]. In the study by Mao et al., cynomolgus monkeys were treated with either IV or SC formulation of an anti-CD20 mAb, rituximab, and the efficacy, PK and PD were compared for the two administration routes. The aim of the study was to determine the feasibility of achieving equivalent B cell depletion and sustained CD20 target coverage of the SC formulation of rituximab compared to the intravenous dosing. Given the preclinical nature of the study, it offers a rich data set comprising not only peripheral blood but also lymph node samples, typically unavailable in the clinical setting.

Two groups of animals were treated twice (on day 0 and day 7) with either a SC or IV formulation of rituximab. Free antibody concentration was measured in the peripheral blood over 14 days (6 time points). Data on B cell depletion and free surface CD20 levels in the distal lymph nodes was taken before the treatment and on day 18. B cell depletion and CD20 target coverage in the peripheral blood were further monitored for up to 63 days. We digitised the peripheral blood antibody concentration data and utilised it in the practical identifiability analysis of the PBPK-PD framework applied in the context of anti-CD20 mAb, as described below in Sections 4.2.7 and 4.3.3. Peripheral blood and lymph node B cell depletion measurements were also used for qualitative comparison of the simulated model behaviour following the resulting data fitting.

4.2.7 Data fitting and practical identifiability

Although the structure of the proposed model is relatively simple compared to the previously published PBPK-type antibody deposition models (see Tables 4.2 and 4.3), the total number of model parameters yields the practical identifiability and data fitting infeasible without any further restrictions. We, therefore, utilised the local sensitivity analysis on the PBPK-PD framework, described in Sections 4.2.5 and 4.3.2, to guide the parameter selection for data fitting. Based on the results of the local sensitivity analysis, which we will discuss in

Section 4.3.2, we selected the following subset of parameters to be inferred with the use of the experimental data described in Section 4.2.6: total blood volume ($V_{\text{blood,tot}}$), total systemic antibody clearance CL_{tot}, extravasation parameters (σ_{V_o}), and additionally the antibody absorption rate from the SC administration site (k_{abs}) for the SC dataset. The number of the extravasation parameters, σ_{V_o}, was reduced to three, by assigning each organ one of the three parameters, according to the structure of the vascular endothelium: σ_{dis} for the organ compartments with discontinuous endothelial structure (liver, spleen), σ_{LN} for the lymph node compartments (draining lymph nodes, remaining lymph nodes) and σ_{other} for all the remaining compartments [100].

Finally, to account for the uncertainty in the data during parameter estimation, we introduce a noise model. As we expected the measurement error in the antibody concentration to scale with the magnitude, we assumed a multiplicative Gaussian noise. The antibody blood concentration simulated by the model, C_{blood} was corrected by the noise term according to:

$$C_{\text{noisy,blood}}(\theta, t) = C_{\text{blood}}(\theta, t) + \epsilon(t), \tag{4.63}$$

where the noise term, $\epsilon(t)$, was defined as:

$$\epsilon(t) = C_{\text{blood}}(\theta, t)^{\eta_{\text{noise}}} \upsilon(t), \tag{4.64}$$

where η_{noise} is the exponential power controlling the rate at which the noise scales with the output, and $\upsilon(t)$ is independent and identically distributed (*iid*) Gaussian:

$$\upsilon(t) \overset{iid}{\sim} \mathcal{N}(0, \sigma_{\text{noise}}), \tag{4.65}$$

with the baseline standard deviation σ_{noise}.

The following reasoning resulted in the choice of 7 parameters for the inference with the use of IV data set ($V_{\text{blood,tot}}$, CL_{tot}, $\sigma_{V,\text{dis}}$, $\sigma_{V,\text{LN}}$, $\sigma_{V,\text{other}}$, σ_{noise}, η_{noise}), and 8 parameters for the SC data set ($V_{\text{blood,tot}}$, CL_{tot}, $\sigma_{V,\text{dis}}$, $\sigma_{V,\text{LN}}$, $\sigma_{V,\text{other}}$, k_{abs}, σ_{noise}, η_{noise}). We utilised a Bayesian approach to fit the model to each of the two data sets using an open-source Python package, PINTS [125]. Uniform prior distributions were defined for the parameters included for the inference. The parameter variability was based on the value ranges reported in the literature (for the parameters $V_{\text{blood,tot}}$, CL_{tot} and k_{abs}, see Section 4.2.2), parameter definitions in the model (for the parameters $\sigma_{V,\text{dis}}$, $\sigma_{V,\text{LN}}$, $\sigma_{V,\text{other}} \in [0, 1]$) or estimates of the variability in the experimental data (for the parameters σ_{noise} and η_{noise}). The model output,

declared as the free antibody blood concentration at the measurement time points, with the assumed multiplicative Gaussian noise (Equation (4.63)) was simulated, and, together with the prior distributions, log-likelihood values were computed. The posterior distributions were estimated using the Differential Evolution Markov Chain Monte Carlo method (DE-MCMC) [126]. The sampler was assigned 8 and 9 chains for the IV and the SC data set, respectively, and each chain was run for 15,000 iterations. To account for the heterogeneity between the individual animals in the study, for each iteration, the values for the remaining parameters in the model were randomly sampled from normal distributions with means as defined in Tables 4.5 and 4.6 and 10% coefficient of variation, unless the variability ranges were known. Convergence was assessed by evaluating the $\hat{R}$ value, which gives a measure of convergence for the approximated posteriors, with $\hat{R} \to 1$ as the algorithm converges. To account for the bias in the initial parameter values specified in the algorithm, the first 6,000 iterations were discarded before further analysis. The resulting distributions of the parameter values were plotted as histograms, and the means, standard deviations and 95% confidence intervals were evaluated. Parameter distributions were sampled to simulate the antibody blood concentration and compare it to the original data. Means, 25%, 50% and 75% confidence intervals of the inferred free antibody concentrations for both administration routes were computed. Finally, the ODE system was solved based on the marginal posterior distributions and the behaviour of the full model was analysed. Median solutions for all variables in the model were computed, together with 25%, 50% and 75% confidence intervals to indicate the variability between single solutions.

4.3 Results

4.3.1 Structural identifiability

Structural identifiability of the proposed PBPK-PD framework was investigated to assess whether the structure of the constructed model allows parameter fitting. The analysis was performed using the scaling method, developed by Castro and de Boer [15], where the invariance of the system of ODEs was considered under the scaling transformation of the model parameters. For a model parameter, λ_i, to be structurally identifiable, the method requires that the system remains invariant under scaling of the parameter, λ_i, with a scaling factor, u_{λ_i}. Combinations of the scaling factors that preserve the invariance of the system solve the identifiability equations. Parameters with only one trivial solution ($u_{\lambda_i} = 1$) for any solution of the identifiability equations are structurally identifiable by definition. Identifiability equations

were derived in Section 4.2.4 for the model applied in the context of monoclonal antibodies. The blood antibody concentration was assumed to be an experimentally observable variable, and the implications of the blood concentration being the sole observable quantity on the feasibility of parameter estimation were investigated. The analysis of the ODE system yielded a system of identifiability equations with one trivial solution (see Equation (4.59)), indicating that, given only blood antibody concentration data, the model is structurally identifiable.

4.3.2 Local sensitivity analysis

The results of the structural identifiability analysis indicated that all the model parameters considered in the analysis were structurally identifiable. However, the total number of model parameters yields the practical identifiability and data fitting infeasible without any further assumptions to assist those techniques. We, therefore, performed a local sensitivity analysis to assess the relative sensitivity of the free antibody blood concentration, C_{blood} to the model parameters and to guide the process of fitting the model to the data. Varying one parameter at a time, we simulated a single IV and SC administration of anti-CD20 antibody and evaluated the change in the free antibody blood concentration due to each parameter. The impact on the concentration-time curve was quantified by measuring the change in two outputs: the maximal free antibody blood concentration, C_{max}, and the time taken since the administration for the maximal free antibody blood concentration to be achieved, T_{max}. Such choice of the investigated variables allowed us to assess the relative importance of the model parameters along two axes of the concentration-time curve.

The evaluated sensitivity indices, listed in Table 4.8, as a whole suggested that, for both IV and SC administrations, the maximal free antibody blood concentration, C_{max}, is primarily sensitive to the same few PBPK parameters. For the IV administration route, the C_{max} concentration showed the most prominent sensitivity to the total blood volume, $V_{\text{blood,tot}}$, the cardiac output, CO, and the total systemic clearance, CL_{tot} (sensitivity indices of the order of magnitude between 10^{-2} and 10^{-1}). Similarly, for the maximal antibody concentration associated with the SC administration route, the most significant parameters were: the total blood volume, $V_{\text{blood,tot}}$, the antibody absorption rate constant, k_{abs}, the total systemic clearance, CL_{tot} and the cardiac output, CO (sensitivity indices of the order of magnitude same as in the IV case). In contrast, the sensitivity of the variable, T_{max}, to the model parameters differed between the two administration routes. Compared to the, essentially negligible, sensitivity indices for the IV administration route (sensitivity indices of the orders of magnitude of 10^{-16}), the SC route showed much stronger sensitivity to the antibody absorption rate constant, k_{abs}, the cardiac output, CO, the total systemic clearance, CL_{tot} and the total blood volume, $V_{\text{blood,tot}}$

Parameter	Sensitivity indices			
	$C_{\text{max,IV}}$	$C_{\text{max,SC}}$	$T_{\text{max,IV}}$	$T_{\text{max,SC}}$
$\sigma_{V_{\text{spleen}}}$	-4.07E-05	-1.64E-04	6.32E-16	-8.68E-02
$\sigma_{V_{\text{bm}}}$	-1.55E-07	-1.82E-05	0	1.07E-04
$\sigma_{V_{\text{gut}}}$	-3.93E-05	-2.72E-03	0	6.40E-02
$\sigma_{V_{\text{SC}}}$	-1.43E-07	2.41E-04	4.02E-16	-7.90E-03
$\sigma_{V_{\text{liver}}}$	-6.08E-05	-3.04E-03	0	-7.21E-02
$\sigma_{V_{\text{LN}}}$	-2.77E-06	-4.45E-06	0	8.11E-06
$\sigma_{V_{\text{dLN}}}$	-2.91E-08	-9.14E-08	0	9.51E-06
$\sigma_{V\text{rem.org.}}$	-2.24E-04	-1.69E-02	0	-4.47E-01
$\sigma_{L_{\text{spleen}}}$	0	0	0	0
$\sigma_{L_{\text{bm}}}$	0	0	0	0
$\sigma_{L_{\text{gut}}}$	0	0	0	0
$\sigma_{L_{\text{SC}}}$	0	0	0	0
$\sigma_{L_{\text{liver}}}$	0	0	0	0
$\sigma_{L_{\text{LN}}}$	0	0	0	0
$\sigma_{L_{\text{dLN}}}$	0	0	0	0
$\sigma_{L_{\text{rem.org.}}}$	0	0	0	0
$VB_{\text{blood,tot}}$	6.78E-03	-3.92E-01	6.32E-16	1.63E+00
CO	-5.86E-03	-2.28E-02	0	-2.09E+00
CL_{tot}	-9.47E-04	-7.93E-02	0	-1.77E+00
k_{abs}	0	2.60E-01	0	-6.50E+00
k_{on}	-6.16E-05	5.49E-04	6.32E-16	-5.42E-01
k_{off}	7.48E-06	-5.09E-04	0	-6.58E-01
S_{max}	-3.82E-08	-5.38E-04	4.02E-16	-8.63E-01
SC_{50}	-3.70E-10	1.84E-07	0	2.24E-04
k_{prod}	-2.59E-05	-6.15E-06	0	7.98E-02
$V_{\text{spleen}}\widetilde{RC}_{\text{spleen}}(t=0)$	7.32E-13	5.42E-06	0	1.52E-01
$V_{\text{bm}}\widetilde{RC}_{\text{bm}}(t=0)$	-7.01E-11	-2.09E-07	0	-2.09E-05
$V_{\text{gut}}\widetilde{RC}_{\text{gut}}(t=0)$	-2.18E-07	-6.71E-05	-4.02E-16	-1.12E-01
$V_{\text{SC}}\widetilde{RC}_{\text{SC}}(t=0)$	0	-5.28E-08	0	-2.02E-04
$V_{\text{liver}}\widetilde{RC}_{\text{liver}}(t=0)$	-6.80E-05	-1.34E-04	9.20E-16	5.43E-01
$V_{\text{LN}}\widetilde{RC}_{\text{LN}}(t=0)$	0	0	0	0
$V_{\text{dLN}}\widetilde{RC}_{\text{dLN}}(t=0)$	0	0	0	0
$V_{\text{rem.org.}}\widetilde{RC}_{\text{rem.org.}}(t=0)$	0	0	0	0
$V_{\text{blood,tot}}RC_{\text{blood,tot}}(t=0)$	-1.45E-05	-7.86E-07	0	-5.13E-04

Table 4.8: Results of the local sensitivity analysis on the free antibody blood concentration simulated using the mAb PBPK-PD model, as described in Section 4.2.5. Sensitivity of the maximal free antibody blood concentration, C_{max}, and the time taken to reach the maximal free antibody blood concentration, T_{max}, to each input parameter (first column) was measured for the intravenous ($C_{\text{max,IV}}$, $T_{\text{max,IV}}$) and subcutaneous administration of antibodies ($C_{\text{max,SC}}$, $T_{\text{max,SC}}$). Selected parameters from the PBPK submodel (extravasation, σ_{V_o}, and return parameters, σ_{L_o}, total blood volume $VB_{\text{blood,tot}}$, cardiac output CO, and the systemic antibody clearance CL_{tot}, antibody administration site absorption rate k_{abs}), the PK-PD submodel (k_{on}, k_{off}, S_{max}, SC_{50}, k_{prod}) and initial B cell numbers across the model compartments ($\tilde{V}_o\widetilde{RC}_o(t=0)$, $V_{\text{blood,tot}}RC_{\text{blood,tot}}(t=0)$) were varied ±10% from their baseline values (see Table 4.5 and 4.6 and the resulting sensitivity indices were normalised to allow comparison between the variables. For reference, a normalised sensitivity index of 0.01 can be interpreted as: a 10% increase in the parameter value causes 0.1% increase in the output variable.

(all sensitivity indices of the order of magnitude of 10^0). Given that following a SC administration antibodies are transported though the SC administration site and draining lymph node compartments before they reach the systemic circulation, while in the IV case, antibodies are administered directly to the blood compartment at a constant (and known) rate, it is perhaps intuitive that that the sensitivity indices for $T_{\text{max,SC}}$ were much higher than the corresponding sensitivity indices in the IV administration route, $T_{\text{max,IV}}$.

The analysis of the model simulations of both administration routes also highlighted that the extravasation parameters of the organ compartments, σ_{V_o}, affect the free antibody blood concentration to a larger extent compared to the return parameters, σ_{L_o}, which both the C_{max} and T_{max} variables showed no sensitivity to. We, therefore, parameterised the return parameters, σ_{L_o}, based on the values of antibody biodistribution coefficients [114], as described in Section 4.2.2.1. While the absolute values of the evaluated sensitivity indices for the total blood volume, $V_{\text{blood,tot}}$, and the cardiac output parameters, CO, were comparable for both of those parameters, we expected the value of the total blood volume parameter, $V_{\text{blood,tot}}$, to play a more important role in the model. This observation was based on model simulations (see Figure 4.6), where we compared the impact of varying the total blood volume parameter, $V_{\text{blood,tot}}$ (Figure 4.6(a)), and the cardiac output, CO (Figure 4.6(b)). Changes in the value of the total blood volume parameter, $V_{\text{blood,tot}}$, resulted in higher variability of the free antibody blood concentration, particularly around the first data point taken shortly after the IV administration, and, therefore, close to the concentration maximal value, C_{max}. Due to the model simulating an IV administration as a direct administration of antibody into the blood compartment, the peak concentration, C_{max}, was predicted to be of the order of $D_{IV}/V_{\text{blood,tot}}$.

Additionally, the performed simulations suggested that the inference of both the cardiac output parameter, CO, and the extravasation parameters, σ_{V_o} might be impacted by the interactions of the parameters. This interaction can be seen, for instance, in terms $\sigma_{V_o} B_o = \sigma_{V_o} f_{B_o} CO$ (see Equation (4.18)). As local sensitivity techniques, by definition, cannot quantify the impact of parameter interaction on the model output, this cannot be directly concluded from Table 4.8 alone. Given that inference of the extravasation parameters, σ_{V_o}, was deemed as potentially more informative, as the knowledge of the values for those parameters facilitates predicting antibody biodistribution in specific tissues, the value of the cardiac output parameter, CO, was fixed and treated as a known parameter, while the value of the total blood volume parameter, $V_{\text{blood,tot}}$, and the extravasation parameters, σ_{V_o}, were inferred based on the fitting of the model to the data, which we describe in Section 4.3.3.

The free antibody blood concentration profile was significantly less sensitive to the target-related parameters, such as rate constants and the initial B cell distribution across the model

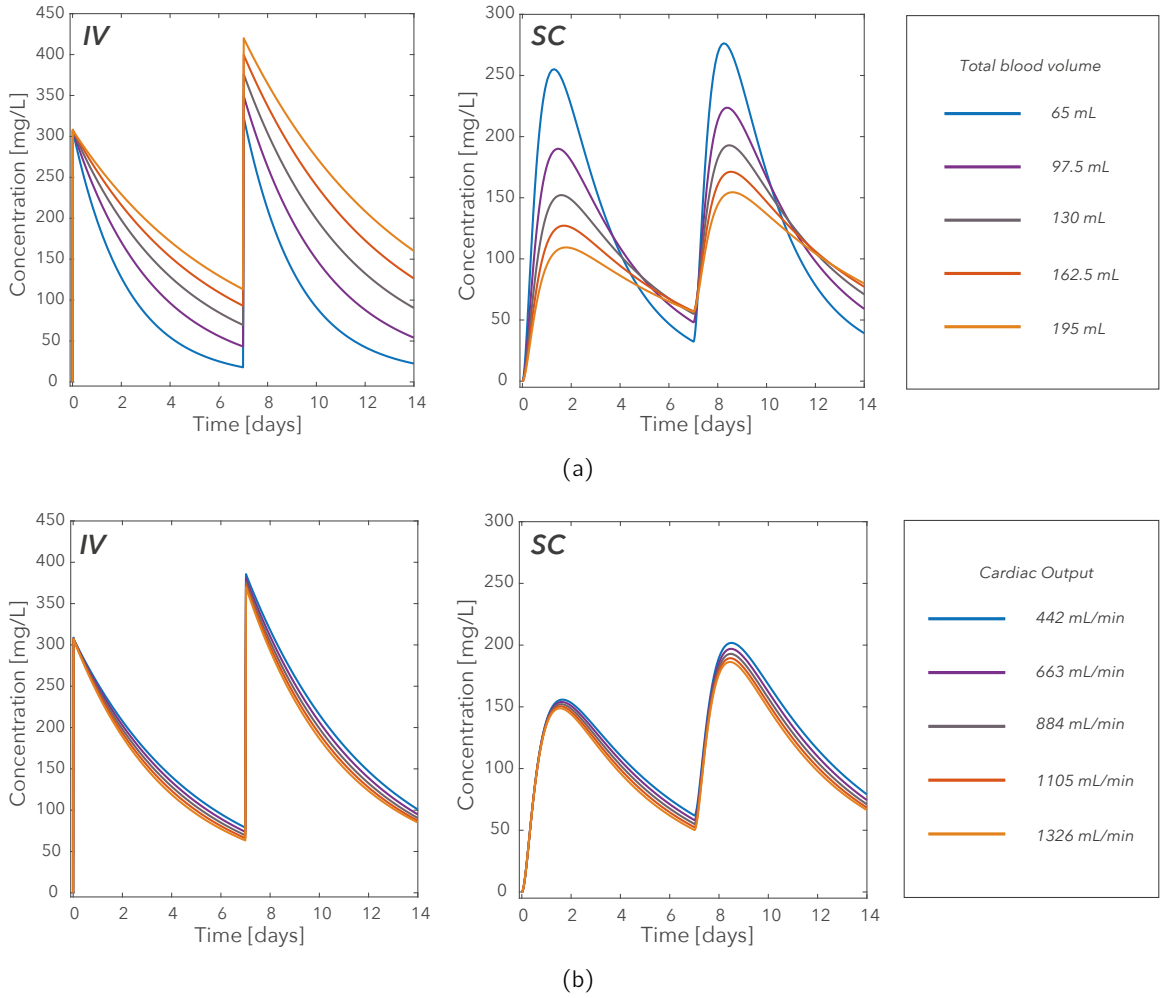


Figure 4.6: Free antibody concentration in blood simulated varying (a) total blood volume and (b) cardiac output. Solutions to the ODE describing the intravenous (left plots) and subcutaneous administration (right plots) of anti-CD20 antibody in cynomolgus monkeys in the PBPK-PD framework were evaluated varying the selected parameter between 50% and 150% from the baseline, $V_{\text{blood,tot}} = 130\,\text{mL}$ and $CO = 884\,\text{mL/min}$ (values indicated in the legends). The remaining parameters in the model, the values of which can be found in Tables 4.5 and 4.6 were kept constant.

compartments, suggesting that the uncertainty associated with those parameters may not be markedly restricting for the data fitting process. For this reason, PK-PD submodel parameters, listed in Table 4.6, and the initial B cell distribution across the model compartments (see Table 4.7), were treated as known parameters and their values were sourced from the literature, as described in Section 4.2.2.

4.3.3 Data fitting and practical identifiability analysis

We performed practical identifiability analysis by fitting the model to the Mao et al. data [107] using Bayesian inference and Monte Carlo methods, as described in Section 4.2.7. Given the

dimensionality of the PBPK-PD framework, inference of all model parameters is not feasible. We, therefore, utilised the results of the local sensitivity analysis (Section 4.3.2) to guide the selection of the parameters to be included in the parameter inference and data fitting process. The measurements of the free antibody blood concentration following the intravenous and subcutaneous administration of rituximab in two groups of cynomolgus monkeys were treated as independent data sets and the model was fitted independently to each data set.

The analysis yielded marginal posterior distributions for the model parameters $\sigma_{V,\text{dis}}$, $\sigma_{V,\text{LN}}$, $\sigma_{V,\text{other}}$, CL_{tot}, $V_{\text{blood,tot}}$ and the multiplicative Gaussian error parameters σ_{noise}, η_{noise} for the IV data set, shown in Figure 4.7, and for the model parameters $\sigma_{V,\text{dis}}$, $\sigma_{V,\text{LN}}$, $\sigma_{V,\text{other}}$, CL_{tot}, $V_{\text{blood,tot}}$, k_{abs} and the multiplicative Gaussian error parameters σ_{noise}, η_{noise} for the SC data set, shown in Figure 4.8. The summary statistics of the marginal posterior distributions and the measure of the convergence between MCMC chains is presented in Table 4.9. Most parameters were characterised by relatively narrow posterior distributions. The exceptions were the extravasation parameter $\sigma_{V,\text{LN}}$ for the lymph node compartment and the noise parameter η_{noise}, where the width of the posterior distribution spanned the considered variability range, indicating practical non-identifiability of those parameters for the model used to simulate both the IV and SC administration. The parameter $\sigma_{V,\text{LN}}$ was not determined by the algorithm because lymph nodes account for a small fraction of the total body volume in cynomolgus monkeys, and similarly are characterised much lower blood flow and blood volume than other model compartments. Thus, the fraction of antibody extravasating from lymph node vasculatures does not affect the free antibody blood concentration and the parameter value makes no difference to the fit compared to the other parameters. The estimated posterior distribution of the noise parameter η_{noise} additionally indicated that the model output is not sensitive to fine details of the noise model (see Section 4.2.7 for more details on the structure of the noise model).

Furthermore, most estimated posterior distributions were consistent between the IV and SC model applications. The only discrepancy was noted for the total blood volume parameter, the distribution of which was characterised by the mean of 87 mL and 95% confidence interval of 56 mL – 152 mL for the IV data set, while for the SC data set the corresponding marginal posterior distribution centred on the mean of 219 mL and the 95% confidence interval spanned the range of 135 mL to 285 mL.

Posterior estimates for the free antibody blood concentration were computed based on the marginal posterior distributions of the analysed parameters. The model simulated the intravenous administration of antibodies relatively well, as shown in Figure 4.9(a), albeit the mean of the inferred states slightly overestimated the free antibody concentration compared to the experimental data points, particularly during earlier times following the two IV administrations.

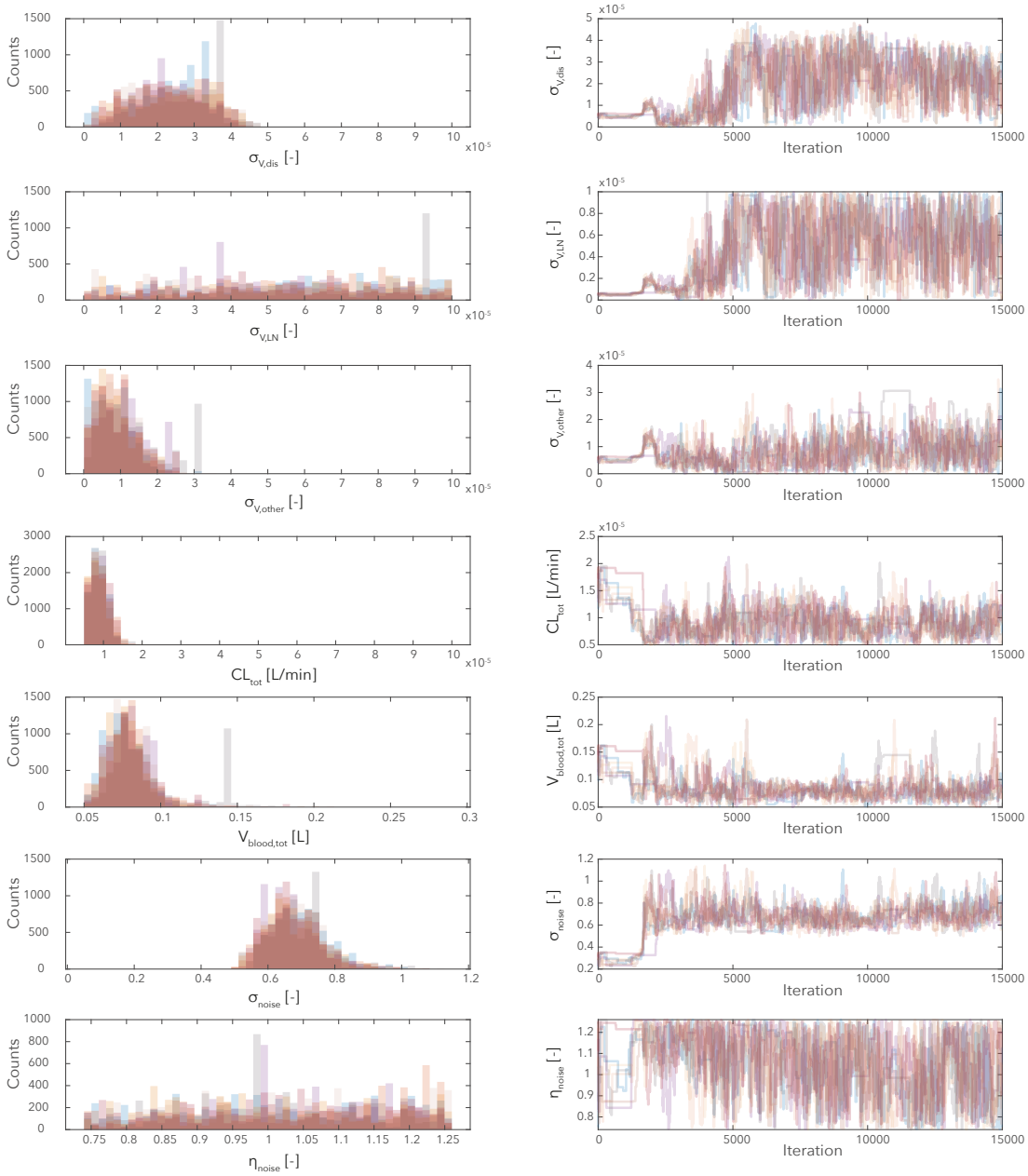


Figure 4.7: Marginal posterior distributions (left column) for the model parameters $\sigma_{V,\text{dis}}$, $\sigma_{V,\text{LN}}$, $\sigma_{V,\text{other}}$, CL_{tot}, $V_{\text{blood,tot}}$ and the multiplicative Gaussian error parameters σ_{noise}, η_{noise} and the trace plots of the 7 MCMC chains (right column), evaluated based on the free antibody blood concentration data following intravenous administration of rituximab in cynomolgus monkeys [107]. Most parameters were characterised by a relatively narrow posterior distribution. This was not the case for the parameter $\sigma_{V,\text{LN}}$ and η_{noise}, where the width of the posterior distribution spans the considered variability range, indicating practical non-identifiability of those parameters. The mean values and 95% confidence intervals of the resulting parameter distributions, as well as the measure of convergence between the MCMC runs ($\hat{R}$) are reported in Table 4.9.

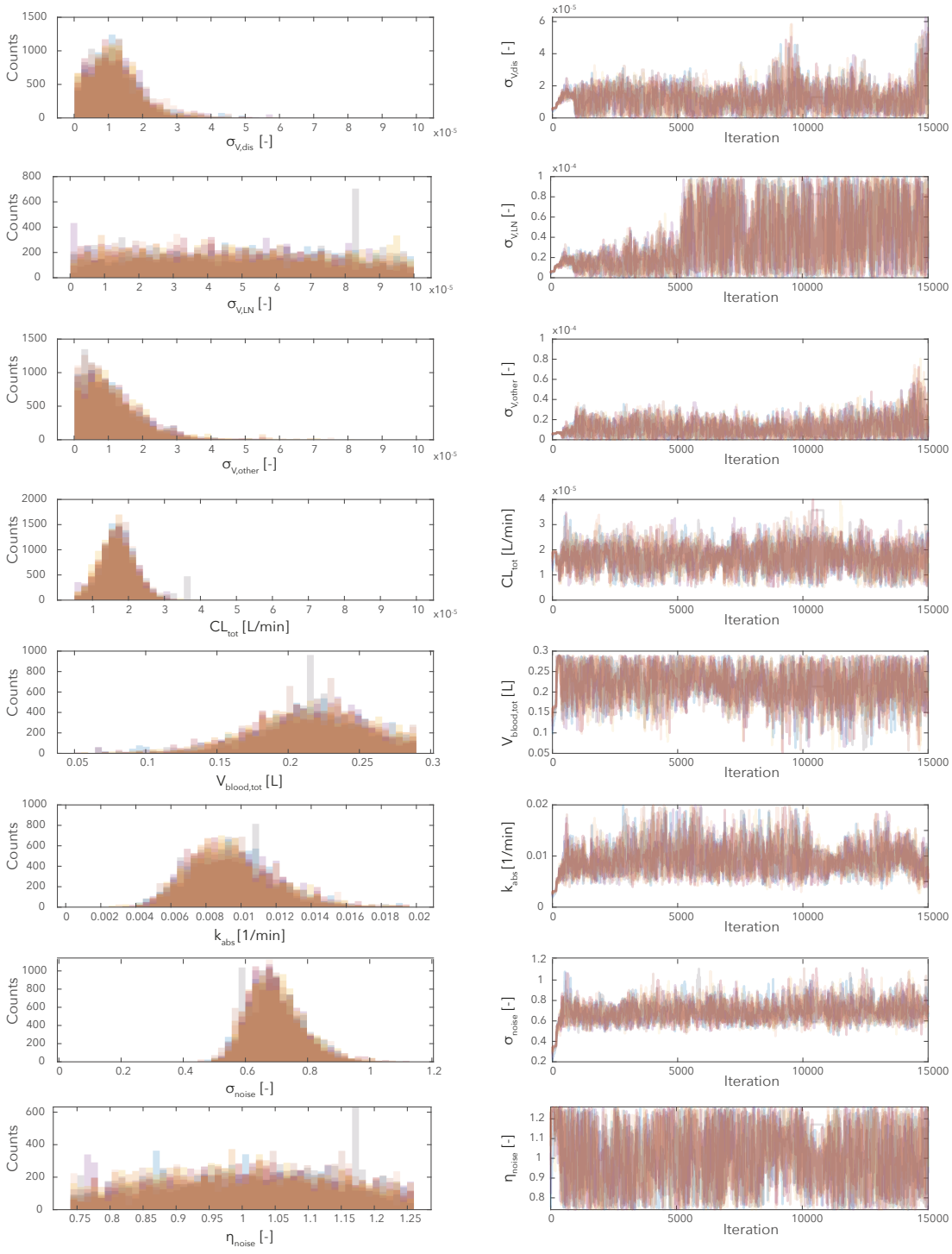
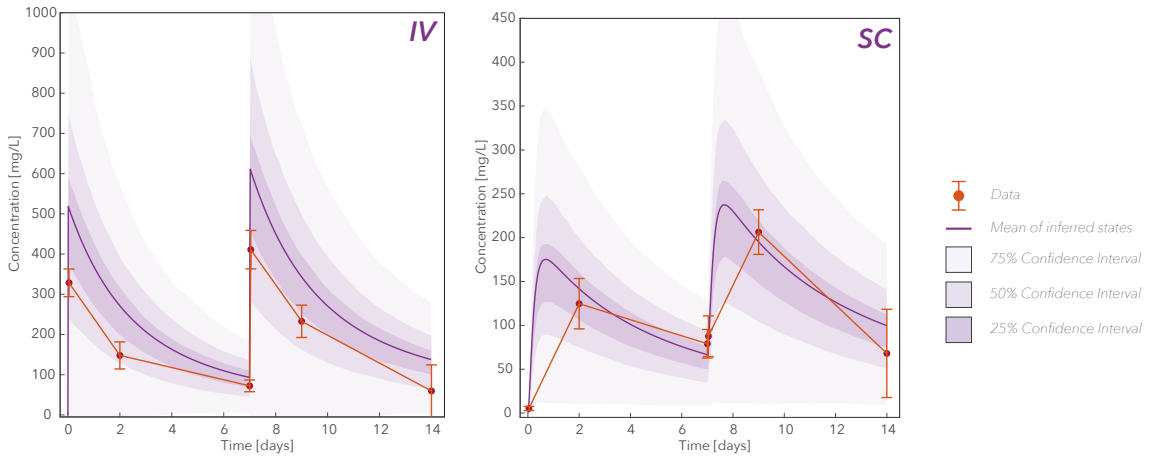


Figure 4.8: Marginal posterior distributions (left column) for the model parameters $\sigma_{V,\text{dis}}$, $\sigma_{V,\text{LN}}$, $\sigma_{V,\text{other}}$, CL_{tot}, $V_{\text{blood,tot}}$, k_{abs} and the multiplicative Gaussian error parameters σ_{noise}, η_{noise} and the trace plots of the 8 MCMC chains (right column), evaluated based on the free antibody blood concentration data following subcutaneous administration of rituximab in cynomolgus monkeys [107]. Most parameters were characterised by a relatively narrow posterior distribution. This was not the case for the parameter $\sigma_{V,\text{LN}}$ and η_{noise}, where the width of the posterior distribution spans the considered variability range, indicating practical non-identifiability of those parameters. The mean values and 95% confidence intervals of the resulting parameter distributions, as well as the measure of convergence between the MCMC runs ($\hat{R}$) are reported in Table 4.9.

		IV			SC		
Parameter	Units	Mean	95%CI	$\hat{R}$	Mean	95%CI	$\hat{R}$
$\sigma_{V,dis}$	-	1.8E-05	1.2E-06 – 4.0E-05	1.13	1.2E-05	9.7E-07 – 2.9E-05	1.00
$\sigma_{V,LNs}$	-	4.2E-05	2.9E-06 – 9.7E-05	1.10	3.6E-05	2.0E-06 – 9.5E-05	1.10
$\sigma_{V,other}$	-	7.9E-06	5.9E-07 – 2.3E-05	1.11	1.1E-05	5.6E-07 – 3.1E-05	1.01
CL_{tot}	[L/min]	9.5E-06	5.3E-06 – 1.7E-05	1.03	1.7E-05	7.8E-06 – 2.7E-05	1.01
$V_{\text{blood,tot}}$	[L]	0.087	0.056 – 0.152	1.05	0.219	0.135 – 0.285	1.01
k_{abs}	[1/min]	-	-	-	9.4E-03	5.0E-03 – 1.6E-02	1.00
σ_{noise}	-	0.64	0.24 – 0.90	1.06	0.68	0.53 – 0.88	1.01
η_{noise}	-	1.06	0.77 – 1.25	1.07	1.01	0.76 – 1.25	1.00

Table 4.9: Summary statistics of the marginal posterior distributions for the model parameters $\sigma_{V,\text{dis}}$, $\sigma_{V,\text{LN}}$, $\sigma_{V,\text{other}}$, CL_{tot}, $V_{\text{blood,tot}}$, k_{abs} and the multiplicative Gaussian error parameters σ_{noise}, η_{noise}. The posterior distributions were evaluated independently for the IV and SC datasets [107].



(a) (b)

Figure 4.9: Model simulations of the free antibody blood concentration following: (a) the intravenous; and (b) subcutaneous administration of rituximab in cynomolgus monkeys for the posterior parameter distributions. The mean of the inferred estimates was plotted with the solid purple line and the 25%, 50% and 75% confidence intervals were indicated by the shaded regions. The experimental data collected by Mao et al. [107] was shown in orange.

Similarly, the mean simulated antibody blood concentration following the two subcutaneous administrations of rituximab, plotted in Figure 4.9(b), represented the experimental data well. However, it is unclear whether the model captured the peak concentrations correctly given the temporal resolution of measurements.

Lastly, we analysed the behaviour of the full model by simulating a median solution to the ODE system for each administration route based on the resulting marginal posterior distributions. Figures 4.10 and 4.11 show the concentrations and localisations (defined as mass of antibody in a given compartment) of the free antibody, as well as the concentrations of unbound B cells, and antibody-B cell complexes across all model compartments following intravenous and subcutaneous administration of antibodies *in silico*. Based on the inferred parameter values, the model predicted higher antibody concentration in blood than in tissues

for both administration routes, which is consistent with the expected distribution of antibodies between the plasma and tissues [114]. The exceptions were the SC administration site and draining lymph node compartments in the simulation of the subcutaneous administration, where much higher antibody concentrations were simulated shortly following both SC administrations (see Figure 4.11, upper left and upper middle panels). This was not the case in the simulation of the intravenous administration, where both the draining and remaining lymph node compartments were characterised by very modest and comparable C_{max} concentrations. For both the intravenous and subcutaneous administration, the model predicted similar antibody concentration in the spleen, with the exception of the delayed peak in the concentration for the subcutaneous administration compared to the intravenous infusion.

The slower rate of antibodies reaching the blood compartment following the subcutaneous administration was reflected in a more gradual increase in antibody concentration in tissues compared to the intravenous route. Similarly, B cell depletion in tissues followed at a slightly slower rate following the SC than the IV administration, however for both routes B cell levels in the blood dropped rapidly and the depletion was sustained for the simulated time course, which is consistent with the data reported by Mao et al. [107]. Although the extravasation parameter of the lymph node compartments, $\sigma_{V,\text{LN}}$, was practically non-identifiable, the model suggests almost complete B cell depletion by day 14 in lymph nodes, though expectedly, much slower than in the blood. Similarly, model simulations resulted in relatively slow B cell number reduction in the bone marrow compartment. While the employed data set did not investigate the impact of rituximab on B cells in the bone marrow, the result was qualitatively consistent with the clinical data on patients with rheumatoid arthritis treated with rituximab [127]. We, however, note that the parameterisation used for the bone marrow compartment relied on the assumption that the bone marrow in cynomolgus monkeys comprises the same fraction of total body volume as in humans (see Section 4.2.2), and we are, hence, cautious about making any further conclusions regarding the predicted model behaviour in the tissue given the lack of appropriate data to parameterise it for the considered species. Simulated concentration profiles of the antibody-B cell complexes suggested that B cell binding occurs very rapidly after the first administration, and, as a single dose led to the depletion of the majority of B cells in the system, the complex concentration profile showed only a single peak. Interestingly, the simulated maximal concentration of the antibody and B cell complexes in the spleen was about five times higher for the intravenously-administered antibody compared to the subcutaneous route, which may highlight the distinct role of the spleen and lymph nodes in the IV and SC administration route for immunotherapy delivery. However, to the best of our knowledge, *in vivo* data that could be used to qualitatively compare to this model prediction has not been published.

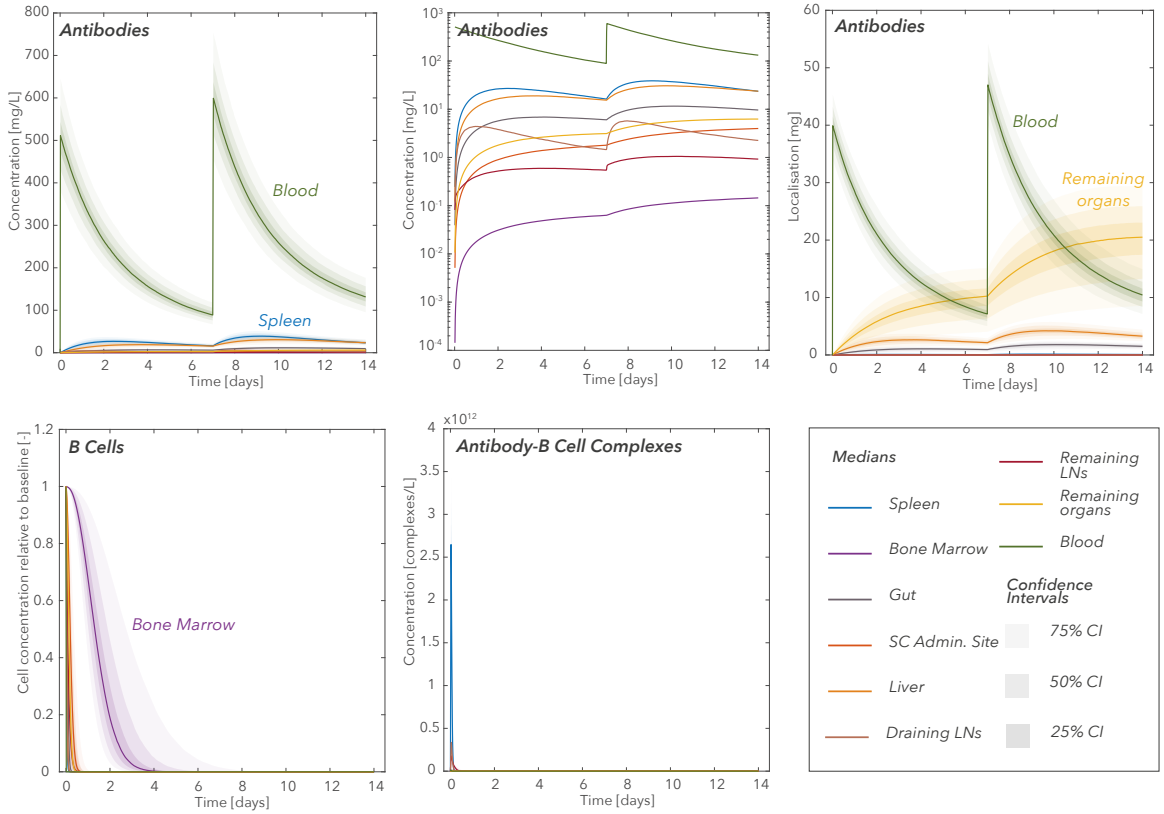


Figure 4.10: Solution to the ODE system describing the intravenous administration of anti-CD20 antibody in cynomolgus monkeys in the PBPK-PD framework based on the marginal posterior distributions of the parameters investigated in the parameter inference process (see Figure 4.7 and Table 4.9. Upper left panel: Free (not bound to B cell) antibody concentration. Upper middle panel: Median free (not bound to B cell) antibody concentration plotted on a logarithmic scale. Upper right panel: Free (not bound to B cell) antibody localisation, expressed as mass of free antibody in each compartment as a function of time. Lower left panel: Unbound (not bound to antibody) B cell concentration relative to baseline. Lower middle panel: Concentration of the antibody-B cell complexes. Median variables were plotted as lines, and 25%, 50% and 75% confidence intervals were indicated with the shaded regions. The most distinguishable curves were annotated. Note that *blood* represents the extra-organ and all intra-organ blood (vascular) compartments in the model.

4.4 Discussion

In this chapter, we proposed a novel PBPK-PD model describing the deposition and mechanism of action of monoclonal antibodies, applied in the context of anti-CD20 antibodies administered via two administration routes: an intravenous and subcutaneous delivery. The main aim of this research chapter was to assess whether the proposed model structure is appropriate to study the problem of the choice of the administration route in the clinical setting, where typically only blood data is available. We utilised structural identifiability analysis to investigate structural identifiability of the model parameters and applied local sensitivity analysis to quantify the relative sensitivity of the free antibody blood concentration to the model parameters. This methodology, in turn, informed the process of parameter selection for data fitting, which also

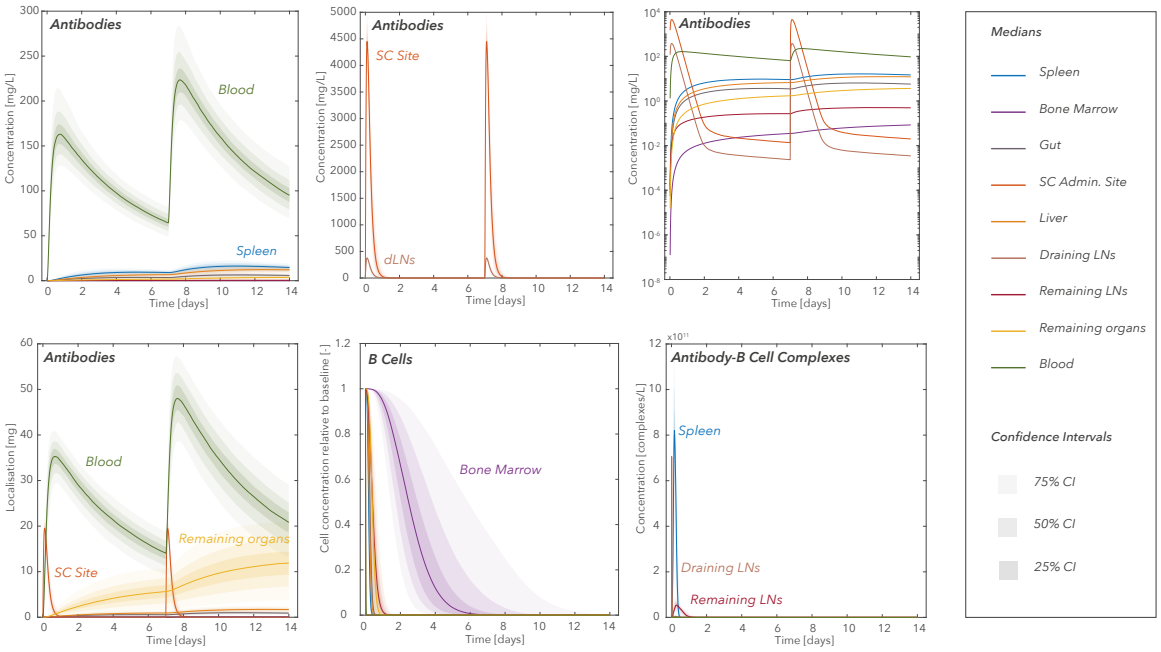


Figure 4.11: Solution to the ODE system describing the subcutaneous administration of anti-CD20 antibody in cynomolgus monkeys in the PBPK-PD framework based on the marginal posterior distributions of the parameters investigated in the parameter inference process (see Figure 4.7 and Table 4.9. Upper left and middle panel: Free (not bound to B cell) antibody concentration, with the concentration in the SC administration site compartment (*SC site*) and in the draining lymph node compartment (*dLNs*) plotted separately in the middle panel due to the difference in scale. Upper right panel: Median free (not bound to B cell) antibody concentration plotted on a logarithmic scale. Lower left panel: Free (not bound to B cell) antibody localisation, expressed as mass of antibody in each compartment as a function of time. Lower middle panel: Unbound (not bound to antibody) B cell concentration relative to baseline. Lower right panel: Concentration of the antibody-B cell complexes. Median variables were plotted as lines, and 25%, 50% and 75% confidence intervals were indicated with the shaded regions. The most distinguishable curves were annotated. Note that *blood* represents the extra-organ and all intra-organ blood (vascular) compartments in the model.

served as a basis for practical identifiability analysis of the framework. While the addressed research question is clinical in nature, we intentionally employed a preclinical study by Mao et al. in the process of practical identifiability [107]. The study compared the PK and PD for intravenously- and subcutaneously administered rituximab in cynomolgus monkeys, and, thus, offers a rich set of temporal data on antibody concentration and B cell depletion levels, both in the serum and in lymph nodes. As antibody concentration measurements are the typically collected data type in the clinical setting, this part of the data set was utilised in the model fitting and practical identifiability. B cell depletion data from the peripheral blood and distal lymph nodes, the latter of which would very rarely be available in the clinic, were, in contrast, incorporated into the qualitative assessment of the predicted model behaviour. As the additional B cell data was not directly used in the process of model fitting, this method, therefore, allowed us to examine the usability of the proposed framework with data availability similar to that in the clinic, while also granting a possibility of a better understanding of the

model behaviour.

4.4.1 The proposed framework can reproduce the antibody blood profile for both administration routes

By fitting five model and two noise parameters to the data, the model was able to capture the free antibody concentration in the blood following the intravenous administration relatively well. Although the mean of the inferred states slightly overestimated the concentration compared to the data reported by Mao et al. throughout the experiment, the shape of the concentration curve was captured accurately by the model, as depicted in Figure 4.9(a). Similarly, the fitting of the model to the subcutaneous dataset compared satisfactorily to the data (Figure 4.9(b)). However, due to the times at which the data was collected in the study, we cannot verify whether the peak concentration, C_{max} was captured correctly by the model. Overall, given the temporal resolution of the experimental data, our modelling of both intravenous and subcutaneous administration resulted in a close fit to the data.

4.4.2 Non-uniqueness of parameters

Our second goal was to investigate whether, in applications where only blood antibody concentration data is available, practical parameter non-identifiability occurs and what the immediate consequences of the parameter non-uniqueness might be in the context of use in the clinical setting. Specifically, we were interested in whether practical non-identifiability of the parameters might interfere with predicting antibody distribution across the model compartments, and whether the model can serve as a starting point in further research on the impact of the delivery route on efficacy and safety, for instance, by refining the model structure to represent a clinically relevant problem of a specific indication, such as Non-Hodgkin lymphoma. We showed that, under the considered assumptions, most parameters fitted to the data were practically identifiable.

One of the two practically unidentifiable parameters was the noise parameter η_{noise} (see Equation (4.64)). The roughly uniform marginal posterior distribution suggested that a simpler mathematical form of the noise term would be sufficient to describe the data.

The other practically unidentifiable parameter highlighted by the analysis was the lymph node extravasation parameter, $\sigma_{V,\text{LN}}$. In Sections 4.2.4 and 4.3.1, we showed that the organ, o, extravasation parameters, σ_{V_o} were structurally identifiable. However, due to the total number of the extravasation parameters in the model (8), we adopted a strategy based on the work by

Eigenmann et al. [100] to make the parameter inference tractable. We assigned one of three new extravasation parameters to each organ, according to the structure of the endothelium in each organ (discontinuous or non-discontinuous) and the organ type (lymph nodes or not lymph nodes). The liver and the spleen compartments were considered as tissues with discontinuous capillaries and were assigned the parameter $\sigma_{V,\text{dis}}$, lymph node compartments - $\sigma_{V,\text{LN}}$, and all the remaining compartments - $\sigma_{V,\text{other}}$. Out of the three new extravasation parameters, only the lymph node extravasation parameter $\sigma_{V,\text{LN}}$ was non-identifiable. As lymph node tissue accounts for a small fraction of the cardiac output, blood volume and total body volume, the impact of varying $\sigma_{V,\text{LN}}$ has very little if no effect on the antibody blood concentration profile, and, as a result, the algorithm cannot infer its value. In contrast, the liver, spleen and the remaining organ compartments represent a much more significant fraction of the cardiac output, total blood volume and body volume, and tend to show more defined marginal posterior distributions indicating identifiability.

4.4.3 The discrepancy in the total blood volume

The parameter inference on the whole produced consistent marginal posterior distributions between the IV and SC datasets. The exception was the total blood volume, $V_{\text{blood,tot}}$, with the mean 87 mL and 95% confidence interval of 56 - 152 mL for the IV dataset, and 219 mL and 135 - 285 mL for the SC dataset. The latter is much closer to the expected physiological values in cynomolgus monkeys, for which the total blood volume is estimated as 140 - 240 mL (47.7 mL/kg [112]). The most probable reason for the IV dataset resulting in a much lower inferred blood volume value is that the antibody blood concentration is predominantly sensitive to the blood volume parameter at times close to the first measurement following the first IV administration, when almost the entire dose of antibody is still present in the blood and the peak concentration is expected to be roughly equal to $D_{\text{IV}}/V_{\text{blood,tot}}$. An important factor contributing to the resulting discrepancy between the IV and SC datasets is the clear uncertainty in the data. As the blood volume scales with the body mass [128], and the dose used in the study scales with the body mass, the peak concentration, C_{max}, should, at least in theory be constant between the animals, however, the data suggests variability between 300 and 370 mg/L (see Figure 4.9(a)), thus evidencing sources of error. Interestingly, other authors reported similar observations, however, did not point towards uncertainty in data as a possible reason [129]. In their work, Overgaard et al. suggested that the discrepancy is due to stress-induced haemolysis due to sampling, and introduced the concept of *effective* blood volume [129]. As the study focused on red blood cells, and, therefore, their work is not directly

relevant to ours, we hypothesise that the observed difference in the inferred total blood volume value is due to the uncertainty in data.

4.4.4 Predicting tissue exposure

Another aim of this chapter was to understand the limitations that the extensive parameterisation of PBPK-based models imposes on the investigation of efficacy- and safety-related aspects of mAb therapeutics. The complexity of whole-body PBPK models may at times be prohibitive given the limited data available to parameterise them. In the model, we, therefore, depicted tissues and organs that are not directly relevant to the mechanism of action of anti-CD20 mAbs as a lumped compartment. We considered the problem of parameterising compartments representing multiple organs or tissues and, in Section 4.2.2.1, we presented a way of mapping the parameters of the lumped compartment onto the parameters of the separate organs, including the extravasation parameters, σ_{V_o}. As the antibody blood concentration showed no sensitivity to the return parameters, σ_{L_o}, in theory, identifiable parameters σ_{V_o} should allow the accurate prediction of the effect of the modelled modality on the specific organs. Being able to predict the accumulation of antibodies above certain thresholds in tissues such as skin could, for instance, highlight the potential of adverse events.

Given that, in our model, we incorporated organs not directly related to the mechanism of action of the antibody as a lumped compartment of *remaining organs*, we can only model the accumulation of antibodies in those organs as a whole. Furthermore, the *remaining organs* compartment comprises tissues that may be characterised by distinct PK profiles. Hence, we cannot draw conclusions applicable to specific tissues represented by the *remaining organs* compartment based on the inferred value of the parameter $\sigma_{V,\text{other}}$. To predict the antibody exposure of a single tissue or organ, tissue-specific data quantifying the PK of antibodies, such as data reported by Eigenmann et al. [100], for instance, is necessary. One could then either depict the tissue(s) of interest in a model as a distinct compartment(s) and base the relevant parameters σ_{V_o} and σ_{L_o} on the experimental data or use the derived mapping between the parameters of the lumped and distinguished compartments to correct the values of the parameters σ_{V_L} and σ_{L_L} for the lumped compartment. However, as we showed in Section 4.2.2.1, lumping organ compartments may result in a discrepancy between the full and simplified model. This problem has been, in fact, studied extensively, for instance, by Nestorov et al. [18], who examined the lumping model reduction method and proposed a set of principles that could serve as a guide in the method application. The authors concluded that in order to lump tissue compartments connected in the model in series, the compartments should equilibrate very rapidly with one another. Parallel tissue compartments, on the other

hand, should be characterised by timescales of a similar order. While the vascular subcompartments in the PBPK model described in this chapter, indeed, have very close timescales (due to $f_{\mathrm{CL}_o} CL_{\mathrm{tot}} \ll B_o$, see Equation (4.1)), it is not immediately clear whether the same is true for the interstitial subcompartments. The relative arrangement between the subcompartments being lumped is also more complex. Organs are connected in parallel relative to one another but each organ compartment is represented as vascular and interstitial subcompartments connected in series. By lumping organ compartments in the model described in Section 4.2.1, we combined the vascular subcompartments into a lumped vascular subcompartment, and, similarly, the interstitial subcompartments of individual organs were represented by a lumped interstitial subcompartment. Additionally, the PK-PD submodel introduces the description of the interactions between the antibodies and target cells, which makes the analysis even more complicated. However, we pursued this analysis to the extent that is necessary for the purpose of mapping the single organs and lumped compartment parameters, and we leave the examination of the consequences of the mapping to future work. As such, through this digression, we emphasise the importance of adjusting the structure of a model to fit the research question.

4.4.5 Antibody excess regime

Using the results of data fitting, we simulated an exemplar solution to the ODE system describing the PBPK-PD model (Section 4.2.1.2), while allowing the remaining model parameters to vary to account for the possible physiological differences between the individual animals. The model predicted very rapid and sustained depletion of B cells in the blood, consistent with the data collected in the study by Mao et al. [107]. In the remaining compartments, B cells also tended to be depleted relatively fast and a single dose was sufficient to practically deplete B cells in the system (except the bone marrow compartment). Even though almost no B cells were, therefore, present in the system at the time of the second administration, the PK of the second dose very closely resembled the PK after the first dose, suggesting that target binding does not influence the observed antibody profile in the blood. Further, the model exhibited very little sensitivity to the initial B cell distribution across the model compartments (see Table 4.8), and, in fact, setting the initial B cell numbers in all extra- and intra-organ blood compartments (which together comprise the largest reservoir of B cells in the model) resulted in an essentially identical antibody blood concentration profile. Our observations, therefore, imply that the profile of the free antibody concentration in the blood was almost entirely governed by the processes of antibody distribution rather than target interactions.

We attempted to explain this observation by comparing the absolute numbers of antibodies and target cells in the system. Doses chosen for the cynomolgus monkeys in the Mao et al.

study translate to the typical Rituximab doses in the clinic [107], and correspond to $\sim 10^{16}$ molecules of antibody. Meanwhile, the total number of B cells in the system is of the order of $\sim 10^{11}$. We also verified that the lowest antibody concentration after the peak (*i.e.*, on day 7) is always at least two orders of magnitude higher than the highest number of B cells (*i.e.*, on day 0). Thus the chosen dosing scheme falls within an antibody excess regime, where even instantaneous binding of all B cells would, in effect, have no impact on the antibody PK in the blood, in agreement with the clinical evidence showing that a single <1% of the typically administered rituximab doses depletes almost all circulating B lymphocytes in healthy individuals [130].

The concept of the *antibody in excess* regime also justifies one of the assumptions in our model, namely that only one antibody can bind to a single B cell. The CD20 density of the order of 10^5 receptors per cell implies that, in reality, multiple anti-CD20 antibodies can bind a single $CD20^+$ cell. The model proposed in this chapter quantifies B cell concentration, rather than CD20 concentration, and we parameterise the binding process using a single binding rate constant k_{on}, as opposed to an *effective* binding rate. Using the same framework allowing simple ion channel models to accommodate ion gating dynamics, we showed that the system is driven by single, rather than multiple, binding events. Furthermore, setting the unbinding rate constant, k_{off}, to zero does not change the antibody blood concentration profile, providing evidence to our conclusion. A more detailed explanation can be found in Appendix B.

4.4.6 Remarks on model complexity and comparison to previously developed models

In comparison to some of the previously developed PBPK-type models (see Tables 4.2 and 4.3), the proposed framework contains a relatively low level of detail. Given our aim to develop a model that facilitates clinically-useful predictions, we are, however, cautious of increasing the model complexity beyond what is necessary, particularly regarding processes where experimental data is lacking (and, hence, where parameterisation may be difficult). While, depending on the research question, a more detailed model structure may be necessary, we base the assumptions and simplifications in the proposed model structure on biological and mathematical arguments.

For instance, the PBPK-PD model does not explicitly represent the interactions of the therapeutic antibodies with the Fc receptor nor the competitive binding with endogenous IgG antibodies. To describe those processes, the introduction of a third, endosomal, subcompartment for each organ would be required, and, currently, there is no clear consensus in the modelling community on how to parameterise such spaces. However, Zhao et al. showed that

the percentage of antibodies transported to the endothelial spaces is 0.102% and 0.035% for skin and muscle, respectively [131]. Even ten fold higher levels would generally be difficult to resolve with the use of experimental data. Furthermore, although FcRn does impact the rate of antibody elimination [104], no substantial changes in plasma-to-tissue ratios or distribution kinetics have been demonstrated in animal models [114]. Finally, Fronton et al. illustrated that under most common conditions, it is not necessary to explicitly account for endogenous IgG and the competitive binding of endogenous and therapeutic antibodies to FcRn in the endosomal space of endothelial cells [92]. Assuming that the dissociation constants of therapeutic and endogenous antibodies to FcRn are similar and that the therapeutic antibody concentration in plasma is lower than that of endogenous IgG (both of which can generally be expected to hold for therapeutic antibodies, with only a few exceptions), the authors have demonstrated that a complex PBPK framework that incorporates both FcRn and endogenous IgG description can be reduced analytically to a much simpler model with a linear clearance rate, encompassing all catabolic mechanisms occurring in tissues. Given the outlined experimental evidence and the analytical arguments regarding model simplification and model equivalence, we did not directly consider antibody and Fc receptor interactions, and the competitive binding to FcRn with endogenous antibodies in the model.

Similarly, the description of the transport of antibodies from the blood to tissues is rather simple compared to the models reviewed in Tables 4.2 and 4.3, where the transcapillary exchange of antibodies was modelled in various ways (two- or one- pore formalism [101, 81, 102], diffusion and reflection coefficients [94, 95, 96, 97, 98], tissue partition coefficient description [92] or a combination of these methods [99]). Our approach most closely resembles the reflection coefficient description, where vascular ($\sigma_{V_{\text{refl,o}}}$) and lymphatic reflection coefficients ($\sigma_{L_{\text{refl,o}}}$) provide a measure of resistance to the antibody movement from the vascular and lymphatic vessels. We can draw an analogy between our model, where the number of antibodies crossing the vascular endothelium and entering the interstitial space of the tissue per unit time is equal to $\sigma_{V_o} B_o C_o$, and models employing the reflection coefficient approach, where the same quantity is expressed as $(1-\sigma_{V_{\text{refl,o}}}) J_o C_o$, with J_o being either parameterised as lymph or transcapillary fluid flow, depending on the exact approach. Similarly, the number of antibody leaving the tissue and entering the lymphatic vessels per unit time is equal to $\sigma_{L_o}\sigma_{V_o} B_o \tilde{C}_o$, while models incorporating the lymphatic reflection coefficient would express this quantity as: $(1-\sigma_{L_{\text{refl,o}}}) L_o \tilde{C}_o$, with L_o parameterised as lymph flow.

The typical assumed values of the vascular reflection coefficients lie between 0.8 and 0.95, and around 0.2 for the lymphatic reflection coefficients. The lower value for the lymphatic reflection coefficients reflects the fact that lymphatic vessels are wider and generally more fenestrated than blood vessels and, thus, restrict the movement of antibodies to a much lesser

degree. The estimated marginal posterior distributions of the σ_{V_o} parameters were characterised by means of the order of 10^{-5}. The difference in the order of magnitude compared to the vascular reflection coefficients used by other authors stems from the fact that, in our model, the transcapillary exchange of antibodies is parameterised through blood flow to the tissue, rather than lymph or transcapillary flow. Given that lymph or transcapillary flow tends to be several orders of magnitude lower than the blood flow to a tissue [101, 99], this difference in values was expected. In addition, we opted to parameterise the transcapillary antibody exchange in terms of blood flows since measuring lymph or transcapillary flow is difficult, and obtaining a reliable value for either of those quantities would introduce extensive further uncertainty.

4.4.7 Future work and concluding remarks

In this chapter, we proposed a mathematical model, combining the features of PBPK modelling with the traditional compartmental PK-PD approaches and simulating the intravenous and subcutaneous administration of anti-CD20 monoclonal antibodies. Utilising structural identifiability and local sensitivity analyses, we performed the initial assessment of the applicability of the model and determined a subset of parameters to which the model is most sensitive. Practical identifiability was investigated with the use of a preclinical dataset, from which we employed the antibody blood measurements in the data fitting process and the B cell depletion data in the qualitative model behaviour assessment and comparison. We showed that the model represented both the intravenous and subcutaneous administration of antibodies relatively well compared to the data and that the behaviour of the model is consistent with the current knowledge on the mechanism of action of anti-CD20 antibodies. We also concluded that in order for the framework to facilitate consideration of efficacy- and safety-related problems, which would require estimates of antibody localisation in on- and off-target tissues, *in vivo* data informing the kinetic parameters of antibody transport in and out of tissues is necessary.

As the work presented in this chapter focused on the initial development stages of the framework that could facilitate a comparison of the IV and SC administration routes, it offers many directions in terms of future work. The immediate next step could involve assessing whether the model captures the peak concentration following the SC administration accurately. This could be done with a richer dataset, for instance, a separate study included by Mao et al. [107], where the PK of a single SC dose of rituximab was analysed in a different group of monkeys. By adjusting the physiological parameterisation in the model to account for the

different characteristics of the animals in this study, it should be relatively straightforward to assess the accuracy of the model used to simulate the SC administration route.

Secondly, a more extensive data set would support further model and data fitting validation, as the preclinical data utilised in this work was relatively limited (4 animals per both IV and SC groups). Experimental PK *in vivo* data with a larger number of subjects in the study, be it preclinical or clinical, would allow more flexibility in terms of dedicating a part of the dataset for validation. *In vivo* experiments with labelled non-specific antibodies could facilitate informing the tissue-specific entry and exit rate parameter values. This, in turn, could allow the modelling of antibody localisation at the tissue level with higher confidence, which is of particular importance for predicting the accumulation of antibodies in tumours and the potential of adverse events. Introducing a tumour compartment in the model (for instance, lymphoma lesions in lymph nodes), together with the estimated tissue-specific entry and exit rate parameter values, and examination of the impact of compartment lumping on the model output, could make it feasible to address the question of the administration site of antibody-based therapies, such as: is an administration closer to the lesion more beneficial in terms of efficacy compared to a more distant administration site? Additionally, patient heterogeneity in response to treatment, due to, for instance, tumour microenvironment, could be represented by introducing a parameter describing patient sensitivity to the treatment and scaling the antibody-B cell complex killing rate, $k_{\text{kill}} \rightarrow pk_{\text{kill}}$, where the tumour lesion measurements could inform the parameter p. As a whole, the work presented in this chapter provides the foundation for natural next steps: representation of specific indications in the model, the prediction of antibody bioavailability and its relation to efficacy and safety, and the experimental validation of such predictions.

Chapter 5

Discussion

The work presented in this thesis considered the role of physiologically-based pharmacokinetic (PBPK) modelling in clinical drug development and examined the extent to which PBPK models can be usable in practice in the clinical setting, where appropriate data is sparse, contains a high level of uncertainty or is often lacking altogether. In particular, we have aimed to understand the strengths and limitations of whole-body PBPK models in regard to their complexity. We approached this objective by considering the problem from two angles: theory and application. Utilising model reduction and model simplification techniques, we explored how such methods can be used to obtain valuable information about the modelled biological system. Furthermore, we have aimed to understand how the complexity of whole-body PBPK models can be managed in practice. We, therefore, applied PBPK models to clinically relevant problems, through which we sought to; (i) examine the impact of splenectomy on T cell distribution, (ii) consider lymph node tissue compartmentalisation in PBPK models utilised for applications in immuno-oncology; and (iii) establish the foundation for the development of a mechanistic framework that could aid the identification of an administration route potentially resulting in superior efficacy and a more favourable safety profile for immunotherapeutic modalities. By considering the role of physiology and anatomy in the process of therapy deposition and their associated impact on the intravenous and subcutaneous delivery route, we aimed to identify factors that may determine the bioavailability, and thus the efficacy and toxicity, of a treatment administered via each of the administration routes. We further sought to examine what the implications of our conclusions are for the mathematical modelling approaches that can be used to address the problem of the optimal delivery route. As such, we investigated methods of extracting information from PBPK models in applications with limited or no data and how the complexity of a biological system, which gives rise to clinical observations, may be

handled or countervailed through careful consideration of its representation in a mathematical system. In this chapter, we will summarise the findings presented in the previous chapters in the context of the outlined goals, the rapidly growing field of mathematical modelling in drug development and the regulatory perspective.

5.1 Research summary

Chapter 1 provided a mathematical background to the thesis. Starting with a brief overview of the mathematical modelling approaches in drug development in oncology, we introduced PBPK modelling as one of the most established tools in the field. We argued that PBPK modelling offers a suitable approach to studying the problem of the optimal administration route, as it allows predicting the impact of physiological factors on the deposition of the studied modality, given a very intuitive model structure and physiologically interpretable parameters. While the structure of those models typically encompasses the whole body or major tissues and organs and, hence, results in a relatively high number of equations describing the system, we emphasised that the structure of those equations is mathematically relatively simple and fairly universal across various modality types, granting PBPK models their broad applicability. However, as we discussed throughout this thesis, in the clinical setting, a limited amount or type of data available for this class of modelling can also highlight the major weakness of PBPK models - their extensive parameterisation and complexity, which may give rise to problems with parameter identifiability and may limit our ability to draw biologically meaningful conclusions.

The second part of Chapter 1 provided biological context to the modelling applications considered through this thesis. We started by outlining the key concepts and components of the adaptive immune system and introduced cancer immunotherapy as a therapeutic intervention aiming to manipulate the immune system. We described how physiological and anatomical features support the generation of the adaptive immune response. In particular, we discussed how the structure of secondary lymphoid tissue (SLT), the spleen and lymph nodes, reflects the functions both of those organs serve in immunosurveillance mechanisms. We argued that, due to their structural and functional differences, intravenous and subcutaneous administration routes are associated with different initial exposure levels of the spleen and lymph nodes to the administered therapy. After providing an overview of the available literature on the effect of altering the administration route on the response to treatment, we hypothesised that the spleen and lymph nodes may contribute in different ways and to a different extent to the resulting efficacy, depending on the administration route and the specific indication.

In Chapter 2, we addressed the gaps in the quantitative understanding of the immunological role of the spleen, utilising splenectomy as a naturally fitting example. Based on the analysis of the clinical effects of the procedure in recent large cohort studies by Kristinsson et al. and Sun et al., which reported an increased risk of haematological malignancies and poorer outcomes to treatment in asplenic patients [47, 48], we hypothesised that the spleen may be a more efficient anatomical site to mobilise an immune response against blood-borne malignant cells, and potentially associated treatments. We refined a previously developed PBPK model of T cell trafficking and presented an application of the model, where we assessed the impact of *in silico* splenectomy on T cell distribution in humans, which, so far, has only been modelled in mice [53]. We showed that, while *in silico* splenectomy produced a minimal change in the SLT exposure, it significantly reduced the total number of T cells localising to SLT, and, thus, the number of possible T cell activation events. Based on the predicted lack of significant difference in the T cell concentration in SLT, we concluded that the remaining tissue is predicted to have insufficient cellular and trafficking capacity to compensate for immune functions normally mediated by the spleen. As the trafficking model can describe the recirculation of both endogenous and adoptively transferred T cells, our work, therefore, highlighted the impact of splenectomy and on the bioavailability of an administration of T cells in SLT, which is relevant to cell-based immunotherapy. Consequently, the results suggest that the spleen may play an important role in the efficacy of intravenously administered cell-based therapies.

Chapter 2 additionally presented an example of a PBPK modelling application, where clinical data was not available and, thus, where an alternative approach was necessary. The high complexity of the framework, due primarily to the detailed lymph node compartmentalisation, would otherwise be prohibitive in the process of data fitting. Despite the lack of data, it allowed us the possibility of examining the research question without any previous simplification of the model components that may have been necessary to understand the mechanism of splenectomy but would not have been captured in a simpler framework (for instance, the anatomy of the hepatic circulation). Furthermore, by utilising steady-state model reduction, we have gained structural and biological insight that would not have been possible from numerical simulations only. For example, the reduction in the size of the parameter space rendered a global sensitivity analysis feasible, again, without *a priori* assumptions regarding which model features would be relevant to the mechanism of T cell redistribution due to splenectomy. As a result, the model complexity still accommodated the physiological features of the biological system, while the accompanying disadvantages of the high dimensionality were eliminated.

Chapter 3 followed the question that arose in Chapter 2, namely: is such detailed lymph node compartmentalisation necessary to accurately depict T cell dynamics in a PBPK model? Even in the case of rich temporal data with minimal noise, practical and possibly structural

identifiability issues are to be expected for a PBPK model with 16 lymph node compartments (and, in our case, 37 compartments in total). Single lymph node compartment models have remained an established standard in drug development, as structurally simpler models are deemed more useful for the purposes of model identifiability and parameter estimation. We, however, argued that several applications relevant to immuno-oncology may require a more detailed description of the lymph node tissue. Of particular interest to us has been a modelling framework capable of representing a subcutaneous administration of a therapy, where lymph nodes draining the administration site are characterised by a completely different therapy exposure profile (as the modality localises there before it reaches the systemic circulation) than more distant lymph nodes, where the concentration of the modality increases much later (after it reaches the systemic circulation).

The aim of Chapter 3 was, therefore, to examine what constitutes a reasonable choice of lymph node compartmentalisation and how such a choice affects the model predictions and, in turn, its application. We addressed this question by comparing two immune cell trafficking models with opposing lymph node compartmentalisation: a multiple lymph node model from Chapter 2, and its simplified version with a single lumped lymph node compartment. Using analytical methods, we derived a mapping between various variables of the two models and characterised the difference in the predicted cell biodistribution by both models. Firstly, we showed that both models yield similar overall lymph node tissue concentration, which suggested that if predicting the whole-body lymph node exposure is relevant to the goal of the modelling work, a single lumped lymph node compartment is sufficient and introducing more detailed lymph node compartmentalisation is not necessary and there is no benefit in increasing the complexity of the model further. Secondly, we showed that the cell concentration in any organ-specific lymph node compartment can be related to the cell concentration in a single lumped lymph node compartment through a relationship that is close to linear with the inverse of a parameter determining the rate at which cells are drained from an organ. As the vast majority of PBPK models tend to be linear and are based on the mass conservation law, we suggested that a similar analytical method may be applied to models describing the deposition of other therapies involving macromolecules, such as antibodies. We, therefore, concluded that, if different kinetics and dynamics of a modality are expected within a particular lymph node group (*e.g.*, tumour-draining, administration site-draining, lesion-bearing lymph nodes), those lymph nodes should be compartmentalised separately in a model in order to allow meaningful interpretation, while the remaining lymph nodes can be depicted as a lumped compartment.

In Chapter 4, we presented an antibody deposition model, describing the distribution, pharmacokinetics and pharmacodynamics of anti-CD20 monoclonal antibodies (mAbs) administered intravenously and subcutaneously. The aim of the chapter was to assess whether the

constructed model structure may be appropriate to study the problem of the choice of the administration route in the clinical setting, where typically only blood antibody concentration data is available. Further, we sought to understand the limitations imposed by the extensive parameterisation of PBPK-type models on the investigation of efficacy- and safety-related aspects of antibody-based therapies. Having provided an overview of the previously developed PBPK-type models, applied in the context of antibody deposition in animal models, we reasoned that the complexity of such frameworks severely limits their usability in the clinical setting. We proposed a minimal model that combined the features of PBPK and pharmacokinetic-pharmacodynamic (PK-PD) models, and, hence, was intended to simulate the mechanism of action of anti-CD20 mAbs, while simultaneously maintaining a relatively low level of detail to facilitate its use with only antibody concentration data from blood samples. Our model is, therefore, the first to incorporate the description of the antibody-target interactions in a PBPK framework, as well as the delivery of antibodies via the intravenous and subcutaneous administration routes. The representation of the organs in the model was further considered in accordance with their role in the mechanism of action of anti-CD20 mAbs. For instance, the model included the lymph node tissue, given it is a target tissue for the B cell depletion, and the lymph node compartmentalisation facilitated the simulation of the subcutaneous administration of antibodies. In contrast, the organs not directly relevant to the mechanism of action were depicted in the model as a single lumped compartment, and we showed how such compartments may be parameterised based on parameters describing the single organs and tissues comprising the lumped compartment. Compared to the previously published frameworks, our model, however, did not explicitly consider binding to Fc receptors, nor did it account for the competitive binding to those receptors with endogenous IgG antibodies.

The structural identifiability of the framework was investigated using the scaling method by Castro and de Boer [15] and practical identifiability was assessed by determining posterior distributions for model parameters given preclinical data from the study by Mao et al. [107], who compared the pharmacokinetics and pharmacodynamics for the intravenous and subcutaneous administration of the anti-CD20 monoclonal antibody, rituximab, in cynomolgus monkeys. We firstly showed that, despite the relatively low level of detail compared to the previously published frameworks, our model provided a good fit to the free antibody concentration data in the peripheral blood for both the intravenous and subcutaneous administration routes. In addition, the model predicted the behaviour of B cells within the blood and lymph nodes compartment which was qualitatively consistent with the data included in the study. In the simulation of subcutaneous administration, the model further predicted significantly higher initial antibody concentration in the lymph nodes draining the subcutaneous administration site compared to both the remaining lymph nodes and the spleen. This was not the case in

the simulation of the intravenous administration, where both the draining and remaining lymph node compartments were characterised by very modest and comparable peak concentrations. For both the intravenous and subcutaneous administration, antibody levels in the spleen were predicted to be similar, with the exception of the (expected) delayed peak in the concentration for the subcutaneous administration compared to the intravenous infusion. The results, therefore, suggest that lymph nodes play a significant role in the subcutaneous administration route. In turn, this raises a question of whether the location of lesions (*e.g.*, Non-Hodgkin lymphoma lesions, as in the case of rituximab considered here) is important when considering the delivery method of anti-CD20 monoclonal antibodies and, furthermore, whether altering the administration site, depending on the lesion location, may be used to optimise the efficacy of such therapies.

Secondly, we determined that the model is structurally identifiable and two model parameters were practically non-identifiable. We, therefore, discussed what type of data or assumptions need to be incorporated to account for the aforesaid lack of practical identifiability. We proposed that in order for the framework to facilitate consideration of efficacy- and safety-related problems, which would require estimates of antibody localisation in on- and off-target tissues, any future modelling work need to implement *in vivo* data on the kinetics of the movement of antibodies in and out of tissues. Finally, the work presented in Chapter 4 suggested that the observed antibody concentration profile in the peripheral blood is mainly governed by the process of antibody distribution across the model compartments, rather than the antibody-target interactions. To provide context for this conclusion, we considered the absolute numbers of antibody molecules and target cells in the modelled system and described how therapeutic doses result in a modelling regime, which we referred to as *antibody excess* regime. The significantly higher number of antibody molecules compared to B cells ($> 10^5$ times higher) explained the relative importance of the antibody trafficking vs antibody binding processes and, therefore, the observed sensitivities of the model to its parameters. Our work, therefore, highlighted that, for the therapeutic dose levels, physiology and anatomy play a crucial role in the deposition of antibody-based therapy.

5.2 Research in context: previous and future work

The PBPK modelling approach undeniably offers several clear advantages. Firstly, the function PBPK models typically serve, that is to predict a systemic and tissue exposure of a modelled molecule, is highly relevant in the drug development field [6], but also beyond, for example, in toxicity and risk assessment studies [132]. Secondly, PBPK models provide a physiologically

meaningful framework for addressing research questions. As a result, both the structure of the model and the meaning of the model parameters can be intuitively understood and more easily communicated. Thirdly, the mathematical language on which such models are typically based (ordinary differential equations, the mass conservation law, *etc.*) is relatively simple, which makes PBPK models easy to implement and solve computationally, as well as grants the possibility to utilise mathematical techniques to further analyse the behaviour of a model.

For these reasons, PBPK models have become an integral part of drug discovery and development, where they have been extensively used to support the processes of new drug target selection, the rationalisation of molecule formats and the translation of pharmacological properties from preclinical species to first-in-human trials. The modelling approach has been extensively applied to small-molecule drugs. However, in recent years, we have witnessed increased investment in the development of biologics from pharmaceutical companies, and, particularly in the field of oncology, driven strongly by the encouraging progress in immunotherapy. The potential of PBPK simulations, and mathematical modelling as a whole, to facilitate clinical development has been acknowledged by the regulatory authorities and even explicitly encouraged by the U.S. Food and Drug Administration (FDA) in 2022 [133]. These trends naturally led to more interest in applying PBPK models to protein-based therapies, such as monoclonal antibodies, which comprise a major class of therapeutic agents on the market [134], but also more complex modalities such as bifunctional antibodies.

PBPK models have been widely applied to examine the processes involved in the pharmacokinetics of antibodies in various disease settings, such as tissue uptake, elimination, antibody-target binding in tissues and antibody recycling [135]. As described in Chapter 4, a lot of research has focused on incorporating different mechanistic factors into PBPK models of antibody deposition and, while whole-body PBPK models have been successfully applied to predict antibody systemic and tissue exposure, the usability of such models remains quite limited in the drug development field [135]. Due to the complexity and extensive parameterisation of full PBPK models, minimal PBPK models have been favoured in the context of preclinical and clinical research [135], as the reduction in their structural complexity is more appropriate given data availability, while still allowing examination of the antibody deposition in tissues of interest. We adopted a similar approach in Chapter 4, where we proposed a PBPK model describing the administration and deposition of monoclonal antibodies. We showed how a (pharmacokinetic-pharmacodynamic) PK-PD model depicting the mechanism of action of monoclonal antibodies can be incorporated into a PBPK model with a less granular tissue description, and simulated the expected antibody PK and PD.

While PBPK modelling has been mainly applied in the context of small-molecule drugs and antibodies, the methodology has also been utilised to describe the distribution and trafficking

dynamics of immune cells and cellular therapies. The majority of the research in this context has focused on investigating the possible mechanisms resulting in the limited delivery of effector cells to solid tumours [53, 69, 80, 52] and describing the kinetics of circulating immune cells or adoptively transferred cells [70, 69]. Additionally, a PBPK-PD model has been shown to accurately describe the biodistribution, expansion, and tumour engagement of CAR T cells in mouse models [79]. While mice or rat experimental data has been most often utilised to support the modelling work, *in silico* simulations alone have also been demonstrated to serve as a valuable tool in the effort to elucidate the potential reasons for the discrepancy between the efficacy in the clinic and preclinical solid tumour mice models [52]. In Chapter 2, we similarly illustrated how PBPK modelling can provide quantitative and mechanistic insight into the observed increase in haematological malignancy risk in asplenic patients in the absence of data. By applying a PBPK model of T cell trafficking and simulating splenectomy *in silico*, we assessed the impact of the procedure on T cell distributions in humans, which, to the best of our knowledge, has not been studied before.

The physiologically meaningful framework of the PBPK models, the double-edged sword, that grants their wide applicability can also be a source of difficulties, particularly when the modelling process requires the integration of experimental data. The high dimensionality and complexity relative to the amount and type of data available for the modelling purpose may give rise to issues with model identifiability and parameter estimation. In applications where parameter identifiability is of importance for the objectives of a study, this necessitates simplifications to the model structure. Therefore, even though PBPK models aim to faithfully represent whole-body physiology and anatomy, a certain level of inaccuracy in the way certain tissues are depicted, for instance, due to compartment lumping, in the model is unavoidable. While the lack of exactness is inherent to every mathematical model describing a complex system, this problem is particularly interesting in the context of PBPK models, as the modelling results are fundamentally based on the way the physiology is represented in the model. Compartment lumping as a model reduction method was first described in 1969 [136] and since then has been utilised in a variety of modelling approaches, including PBPK modelling. Nestorov et al. examined the lumping method in a theoretical manner and proposed a set of principles that could serve as a guide in the application of this method [18]. In Chapter 3, we focused on one specific example of structural simplification in PBPK models, namely the choice of the lymph node compartmentalisation, which can drastically impact the complexity of a model. We considered if and to what extent the choice of lymph node tissue description impacts the predictions of a PBPK model, and how models with different lymph node compartment numbers are related. Chapter 4, on the other hand, considered how lumped compartments may be parameterised based on physiological parameters for the organs comprising them. In

both chapters, we showed that, in general, the full and simplified models are not equivalent. A certain trade-off with a model simplification is, therefore, inevitable - reduced structure and dimensionality of a model may indeed make it more usable in practice, but some information is ultimately lost.

What constitutes the most appropriate structure of a reduced model for a given system depends on the overall research question and the scope of the modelling work, as well as on what level of error or uncertainty is deemed acceptable. Nonetheless, simplifications, such as compartment lumping, may in some instances be necessary, as the complexity of PBPK models relative to the amount and type of data that can be used to parameterise them often defines the limitations of the modelling work. In Chapter 2, we illustrated how this problem may be circumvented through analytical considerations of the model structure and application of sensitivity techniques. The question we examined in Chapter 2, however, regarded a possibility for a compensation mechanism to exist - *What are the bounds for a certain quantity?*, rather than - *What is the most probable value of a quantity?*, as may often be the case in applications where PBPK models are employed (for instance, *What is the residency time of an immune cell in lymph nodes?*). Chapter 4, on the other hand, provided an example of PBPK-based model development in circumstances where data is available, but, given the nature of the research question, is also limited. We then presented how model structure can be analysed to verify whether the model is identifiable with the type of data available for the modelling purpose.

Chapter 4 also illustrated how preclinical data can be incorporated into clinically focused modelling and simulations to enhance our understanding of the system described by the model and support the development of mathematical frameworks for clinical purposes. In fact, a similar approach is oftentimes employed in the field of quantitative systems pharmacology (QSP), which has recently gained a lot of interest. QSP aims to bridge the fields of system biology (highly mechanistic but often too complex to incorporate data) and pharmacometrics and PK-PD modelling (facilitates the integration of real-world data but offers limited mechanistic insight). As such, QSP combines the computational modelling of drug deposition with mechanistic descriptions of target-scale dynamics and has already proven as a valuable modelling approach, given the complexity of studied diseases and the cost of traditional approaches in drug development [137].

The difficulty to measure, test or validate the level of detail incorporated in whole-body PBPK models remains one of the most pertinent criticisms of such mechanistic models. However, with encouraging progress in medical imaging, including techniques like positron emission tomography (PET) and single-photon emission computed tomography (SPECT), current limitations relating to model validation may slowly be overcome. The improvement in data acquisition, both in terms of the quality of data (*e.g.*, spatial and temporal resolution) and the

overall amount of data generated, highlights the potential for increased relevance of PBPK modelling. The growing availability and variety of healthcare and clinical data may in the future help us elucidate the impact of splenectomy on immune cell biodistribution and understand its potential significance for the response to immunotherapy. More generally, PBPK models, which already serve as an indispensable tool enabling predictions at a subpopulation level, may facilitate predictions on an individual level, thus, aiding the design of more tailored therapies.

The development in data acquisition may also allow the development of more sophisticated mechanistic models. Not only may structural model simplification, such as compartment lumping, become less of a *sine qua non*, but inferring the mechanism of action of more complex modalities may also become attainable. New immunotherapeutics, such as cell-based therapies, including T cells and dendritic cells (DCs), bifunctional T cell engagers (BiTEs), fusion proteins and checkpoint inhibitors, have shown potential as powerful lines of treatment for many types of cancers but their mechanism of action is equally more complicated. Models, such as the one presented in Chapter 4, may provide the foundation for future application of the modelling framework by incorporating the disease description in the model, potentially expanding the PK-PD submodel beyond the monoclonal antibody mechanism of action, as the analysis presented in the chapter adds to the confidence in the model. As a result, if appropriate clinical data become available, model optimisation and *in silico* experiments could support the generation of predictions and insight for treatment efficacy and safety.

5.3 Outlook and concluding remarks

As cancer immunotherapy has been transforming the field of oncology, the questions regarding various aspects of those therapies which have been addressed with mathematical modelling have also continued to evolve. During the previous decades, predicting the toxicity of therapy and how to control it has been a major focus in clinical research. Questions, such as *What is the maximum tolerable dose?*, *How should the dosing scheme be designed for specific subpopulations?*, or *How can mathematical modelling facilitate predictions of drug-drug interactions?*, shaped a very classic view on the role of mathematical modelling in drug development.

However, since the growing success of immunotherapy for various cancer indications in the clinic, there has been a notable shift towards efficacy optimisation. Mathematical modelling has supported the examination of critical factors contributing to the observed efficacy of treatments but also therapies failing in the clinic despite promising preclinical results. Mechanistic models may aid further predictions of the on- and off-target tissue distribution of a given

modality, optimal method of administration or dose schedules for both existing and prospective therapeutics.

One of the most notable recent examples of the increasingly growing role of mathematical modelling in drug development and regulation is Project Optimus, an initiative put forward by the U.S. regulatory body, the FDA, to reform the dose optimisation and dose selection paradigm in oncology [138]. The maximum tolerated dose standard (*more is better*), based on cytotoxic chemotherapeutics, has been observed to lead to inappropriately characterised doses and dosing schedules for several targeted drugs and biologic therapies after their approval [139]. As poorly characterised doses and schedules may lead to an increased risk of toxicity without additional efficacy, the FDA aimed to develop strategies for dose optimisation from the earliest stages of drug development [138]. In particular, the published guidelines outlined how approaches like PK-PD, PBPK and QSP modelling can inform analyses of nonclinical and early clinical data, and, in turn, serve as supporting evidence for the proposed dose schedule [138].

Advancements in the development of novel biologics, such as bi- and trispecific antibodies or antibody-drug conjugates, also prompt questions regarding the most optimal delivery of such therapies and whether the answers to those questions depend on the specific mechanism of action and function of the investigated modality. While such considerations provide a great opportunity to incorporate mathematical modelling in the research process, they also highlight the urgent need for systematic studies that could serve as reliable and standardised sources for model parameterisation. Interdisciplinary efforts will most likely become a necessary element in the integration of *in silico* approaches in drug development in order to make the prospects of testing the mechanism of action in humans *in silico* and conducting *in silico* clinical trials more attainable.

Unique features and complexity in the mechanism of action of the novel modalities blur the boundary between pharmacokinetics and pharmacodynamics in a way that we not only seek predictions of a molecule's deposition but also of the cells involved in the mechanism of action of the treatment. Understanding the dynamics of the treatment components becomes, therefore, essential in navigating the deposition, safety and overall efficacy of those treatments. The progress in physiologically-based modelling, which can provide valuable input into those considerations, is, thus, driven by the improvement in data acquisition, in turn, further guiding the process of data collection. Such a synergistic cycle of experimental and modelling approaches is highly instrumental in the field of drug and therapy development. Obtaining data is a costly venture, requiring financial resources, time and often ethical considerations. Mechanistic physiology-based modelling, such as PBPK modelling, while at times more laborious than simpler non-mechanistic modelling approaches, can facilitate quantitative analysis prior

to and post-data acquisition. The complexity of such models can, indeed, be leveraged - with the careful use of biological and mathematical assumptions and considerations, we can blunt one of the sword's edges, which, in turn, can contribute toward insight and decision support for therapeutic development.

Appendix A

Blood flow changes in the systemic circulation post-splenectomy

Given that a body tends to maintain the same cardiac output following splenectomy [140], a fraction of blood volume received by an organ, and, as a result, the blood flow through an organ, is expected to increase in the absence of the spleen. Hence, we seek to quantify the change in the blood flow of an organ post-splenectomy for the lymphocyte trafficking framework.

To proceed, we consider a circulation model based on the fundamental assumption of proportionality between the pressure drop across the arterioles, capillary bed and venules associated with an organ, o, and the blood flow through the organ, o, that is

$$\Delta P = R_o B_o, \tag{A.1}$$

where ΔP is the pressure drop, B_o is the blood flow through the organ, o, (defined to include the associated venules and arterioles in this context) and R_o is the resistance of the organ, o. This proportionality stems from the linear relationship between pressure drop and blood flow inherent in the Poiseuille flow through the smaller arterial and venule vessels, and also in vessel models of the capillary beds [141, 142] or more recent homogenised Darcy models of the capillary bed [143]. Validation of this model does require the additional physics of the Fahraeus effect and the Fahraeus-Lindqvist effect, which summarise a complex relation between vessel size, haematocrit and effective blood viscosity, as well as the phase-separation

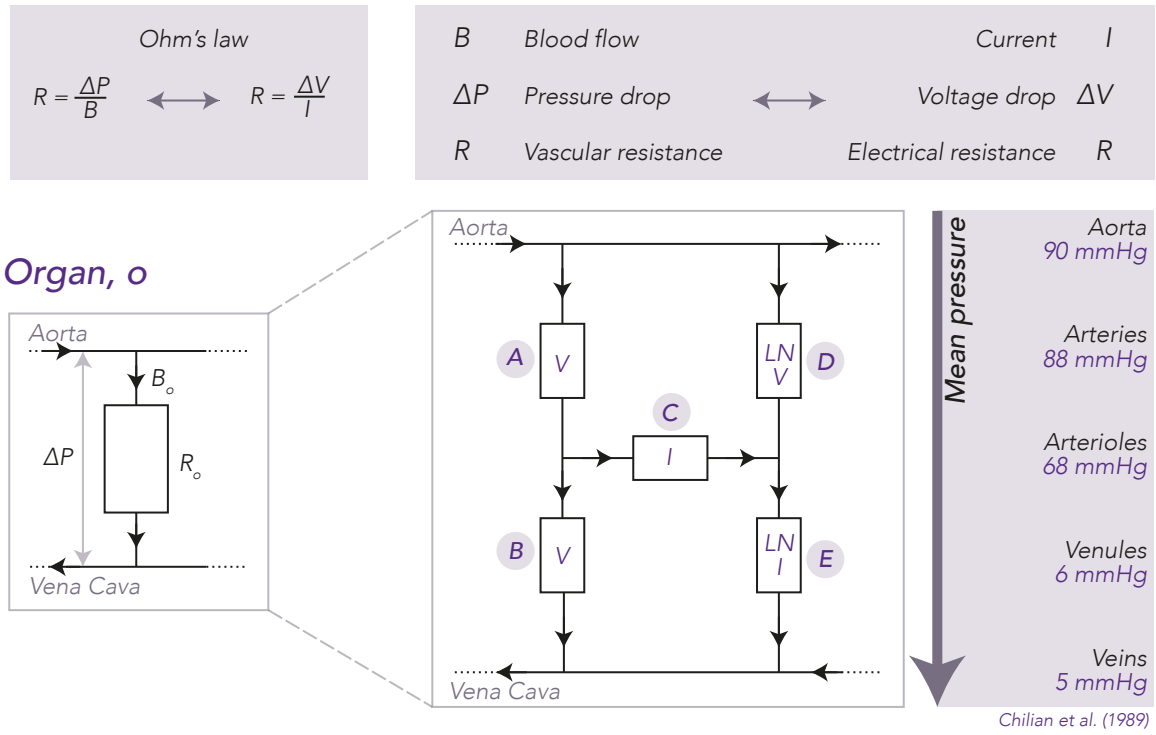


Figure A.1: The representation of organ, o, in the circulation model as a part of a Kirchhoff's circuit, with Kirchhoff's law of charge conservation, and thus a balance of currents, at nodes of the electric circuit analogous to a balance of flows at nodes in the circulation flow circuit. Continuing the analogy, the blood flow B_o, pressure drop ΔP and vascular resistance R_o, an organ o can be thought of as an Ohm's law resistor, where the blood flow, pressure drop and vascular resistance correspond to the current flowing through the "resistor", the voltage across the "resistor" and its resistance (left). In general, each organ will experience different pressure drops across different points in the circulation due to the different circulatory lengths and lymphatic drainage — from aorta and large arteries, between arterioles and venules (across capillary bed), to veins and vena cava (right). However, the pressure drops across the aorta and arteries (2 mmHg [144]), across arteries and arterioles (20 mmHg [144]), and across venules and veins (1 mmHg [144]) are small compared to the pressure drop from arterioles to venules (62 mmHg [144])and are, therefore, neglected. As a result, resistance associated with each organ represents the contributions from the vascular resistance of the organ before (A) and after (B) lymphatic drainage, the vascular resistance across the interstitium of the organ (C), the vascular resistance of the organ-draining lymph nodes (D) and the vascular resistance across the interstitium of the organ-draining lymph nodes (E), though this level of resolved detail is not required in the modelling presented here.

effect, encapsulating the redistribution of haematocrit at vessel bifurcations [142]. However, such physics governs the complex relation between the network geometry of an organ and its resistance to blood flow, R_o, rather than violating the proportionality between pressure drop and blood flow in the microcirculation.

An important caveat in the use of Equation (A.1) concerns the level of vasodilation, which changes regionally and temporally, for example, with exercise or after a meal, and is anticipated to substantially alter organ resistance simply by the fact that resistance to flow is exceptionally sensitive to vessel dilation, scaling with the fourth power of the reciprocal of vessel diameter for simple fluids such as water. Hence, it is implicitly assumed below in comparisons of pre- and post- splenectomy blood flows that the body is in the same state of vasodilation. We

also note that different organs will have different circulatory routes from, and back to, the heart and thus will experience different pressure drops due to the different circuit lengths of the feeding large arteries and draining large veins completing the cardiovascular circuit. However, the pressure drop across large arteries and large veins is subdominant compared to the arterioles, capillary beds and venules of the circulatory system (see Figure A.1) [144] and thus organ-specific variation in this subdominant contribution to the pressure drop across the cardiovascular circuit is also neglected below.

With these modelling assumptions in place, let the pressure difference between the large arteries and large veins with the spleen present (without the spleen) be denoted by ΔP (ΔP^*) and the blood flow through an organ, o, other than the spleen, liver and mesentery, when the spleen is present (without the spleen) be denoted by B_o (B_o^*). Then we have

$$R_o = \frac{\Delta P}{B_o} = \frac{\Delta P^*}{B_o^*}, \tag{A.2}$$

with analogous relations for the spleen, mesenteric organs and liver once the topology of the circulation is accommodated, as summarised in Figure A.2.

In particular, an organ, o, in the model can be thought of as a "resistor", where the blood flow, pressure drop and vascular resistance correspond to the current flowing through a resistor, the voltage across a resistor and its resistance. Hence, we can construct an electrical circuit (composed of resistors, battery and wires connecting all the components), which corresponds to the model compartments, arterial-venous pressure drop and major blood vessels connecting the organs. Such a circuit is shown in Figure A.2 (upper plane), where the mesenteric "circulation" is shown explicitly in the lower plane, and resistors corresponding to the remaining organs are represented in a simplified manner for clarity. The liver receives blood both from the hepatic artery (direct blood supply to the liver) and the hepatic portal vein, which drains from the mesenteric organs: the spleen, stomach, pancreas, small and large intestines. However, hepatic venous pressure gradient (HVPG), the pressure drop between the hepatic portal vein and the hepatic vein, is between $1 - 5\,\mathrm{mmHg}$ [145]. As a result, the contribution of the hepatic portal vein to the pressure drop across the cardiovascular circuit can be neglected, when compared to the dominant pressure drop across arterioles and venules associated with each mesenteric organ. Under such assumptions, an electrical circuit representing the circulation model simplifies to the circuit presented in Figure A.2 (lower plot).

To quantify the change in the blood flow through an organ o post-splenectomy, B_o^*, we consider the resistance of the circuit shown in Figure A.2 with the resistor R_{spleen} present and removed from the circuit. We make two assumptions: (i) the cardiac output remains

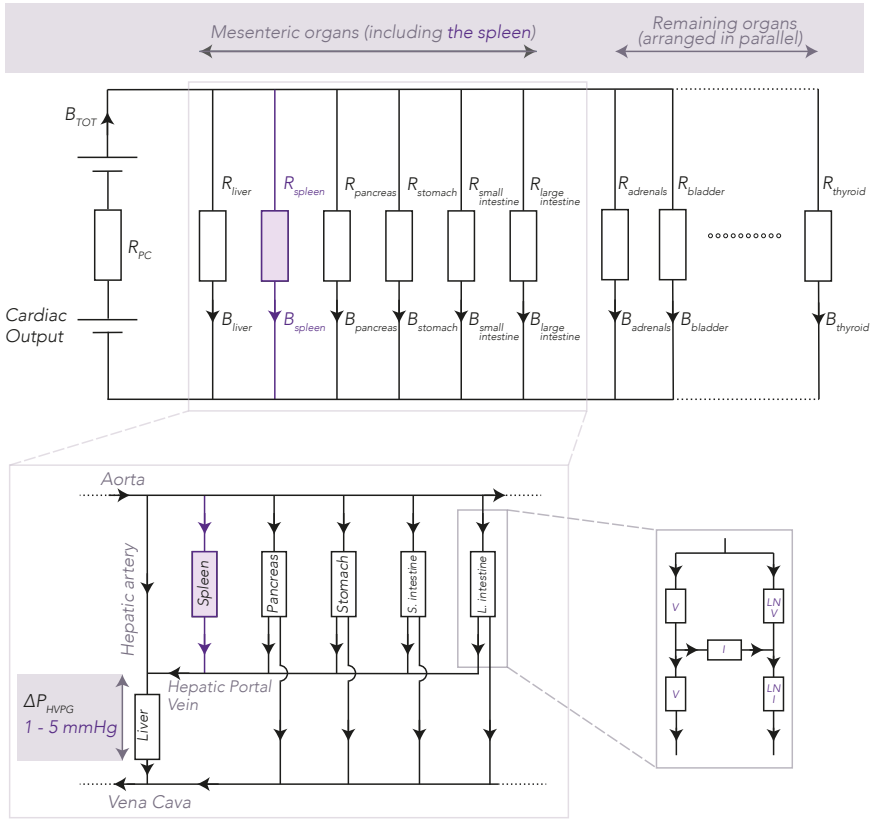


Figure A.2: The ODE model represented as a Kirchhoff circuit with Kirchhoff's law of charge conservation, and thus a balance of currents, at nodes of the electric circuit analogous to a balance of flows at nodes in the circulation flow circuit (upper). The liver receives blood both from the hepatic artery (direct blood supply to the liver) and the hepatic portal vein, which drains from the mesenteric organs: the spleen, stomach, pancreas, small and large intestines. However, since hepatic venous pressure drop ($HVPD$) is comparatively small compared to the pressure drop across arterioles and venules of any mesenteric organ, the contribution of the hepatic portal vein to the balance between fluxes and pressures is small, resulting in the modelling approximation of the circuit shown on the lower left. Note that the spleen lacks lymphatic drainage and that resistance associated with each organ (lower right) represents the contributions from the vascular resistance of the organ before and after lymphatic drainage, the vascular resistance across the interstitium of the organ, the vascular resistance of the organ-draining lymph nodes and the vascular resistance across the interstitium of the organ-draining lymph nodes, as indicated in Figure A.1, though this level of detail is not required in the modelling presented here.

constant after splenectomy ($B_{\mathrm{TOT}} = B^*_{\mathrm{TOT}}$), and (ii) splenectomy does not affect the vascular resistance of each organ ($R_o = R^*_o$).

By flow conservation, analogous to Kirchhoff's law in electric circuits, the cardiac output pre- and post splenectomy, B_{TOT} and B^*_{TOT}, can be expressed as a sum of the total blood flow through the spleen, B_{spleen}, and the remaining organs:

$$B_{\mathrm{TOT}} = B_{\mathrm{spleen}} + \sum_{o \notin \{\mathrm{PC},\ \mathrm{spleen}\}} B_o = \sum_{o \notin \{\mathrm{PC},\ \mathrm{spleen}\}} B^*_o = B^*_{\mathrm{TOT}}. \tag{A.3}$$

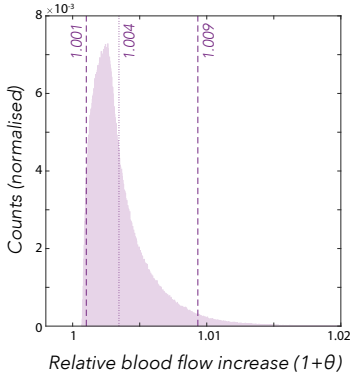


Figure A.3: Distribution of the relative blood flow increase, $1+\theta$, Equation (A.7)), where the dotted and dashed lines correspond to the mean and the 95% confidence interval of the plotted distribution, respectively.

Using Equation (A.1):

$$\frac{\Delta P}{R_{\text{spleen}}} + \sum_{o \notin \{\text{PC, spleen}\}} \frac{\Delta P}{R_o} = \sum_{o \notin \{\text{PC, spleen}\}} \frac{\Delta P^*}{R_o}, \tag{A.4}$$

and hence:

$$\frac{\Delta P^*}{\Delta P} = 1 + \frac{1}{R_{\text{spleen}} \sum_{o \notin \{\text{spleen, PC}\}} \frac{1}{R_o}} = 1 + \frac{B_{\text{spleen}}}{\sum_{o \notin \{\text{spleen, PC}\}} B_o} = \frac{B_{\text{TOT}}}{B_{\text{TOT}} - B_{\text{spleen}}}. \tag{A.5}$$

Using Equation (A.2), the blood flow through the organ o post-splenectomy can be expressed as:

$$\frac{B_o^*}{\Delta P^*} = \frac{B_o}{\Delta P}, \tag{A.6}$$

and substituting Equation (A.5) leads to the sought result:

$$B_o^* = \frac{B_{\text{TOT}}}{B_{\text{TOT}} - B_{\text{spleen}}} B_o = \left(1 + \frac{B_{\text{spleen}}}{B_{\text{TOT}} - B_{\text{spleen}}}\right) B_o = (1+\theta)\, B_o, \tag{A.7}$$

where θ describes the fractional increase in the blood flow through the organ o, in terms of blood flows measured in the presence of the spleen. Blood flow parameter values were randomly sampled 1,000,000 times for each organ compartment from uniform probability distributions, defined by the variability ranges, as described in Section 2.2.3. The relative blood flow increase, $1+\theta$, was evaluated for each sampled parameter set, and convergence was confirmed as noted in Section 2.2.5.1, with the resulting distribution plotted in Figure A.3. The distribution was characterised by a mean of 1.004 and 95% confidence interval 1.001 – 1.009, indicating that splenectomy does not increase blood flow through the remaining organs considerably within the framework.

Appendix B

Effective vs single binding and unbinding rate constants

The PBPK-PD model, introduced in Chapter 4, represents the transport, pharmacokinetics and pharmacodynamics of anti-CD20 monoclonal antibodies. Such antibodies are designed with specific affinity against CD20 antigens expressed on surfaces of B cells. As a single B cell expresses multiple CD20 receptors on its surface and CD20 receptor density is highly variable (between 10^3 to 10^5 receptors per cell [146]), in reality, multiple anti-CD20 antibodies can bind a single $CD20^+$ cell. In the model, however, we depict the concentration of the target cell population (B cells) as a time-dependent variable, as opposed to the concentration of the target antigen (CD20). The process of antibody and B cell binding is also parameterised using a single binding rate constant k_{on}, as opposed to an *effective* binding rate. We, therefore, aimed to estimate the effective binding rate in the system.

Using the same framework that allows simple ion channel models to accommodate ion gating dynamics [147], we start by drawing a parallel between an ion channel with multiple identical subunits, each of which can be in either closed or open state, and a B cell with multiple CD20 receptors on each surface, each of which can be bound or unbound to an antibody molecule. For instance, an ion channel consisting of two identical subunits can take any of four possible states: N_{00}, N_{01}, N_{10} or N_{11}, where the subscripts denote the two subunits, with 0 and 1 representing the closed and open state, respectively. Because the subunits are identical, we cannot distinguish between the states N_{01}, N_{10}. We, therefore, represent the states with exactly i open subunits as N_i. Let α and β be the opening and closing rate constant

of a single subunit, respectively. The kinetics of the ion channel states is given by the following reaction scheme:

$$N_0 \underset{\beta}{\overset{2\alpha}{\rightleftharpoons}} N_1 \underset{2\beta}{\overset{\alpha}{\rightleftharpoons}} N_2, \tag{B.1}$$

where the factor of 2 results from the fact that either of the two identical subunits can become open or closed. The above reaction scheme can be written through differential equations as follows:

$$\begin{aligned} \frac{dx_0}{dt} &= -2\alpha a x_o + \beta x_1, \\ \frac{dx_1}{dt} &= 2\alpha a x_o - \beta x_1 - \alpha a x_1 + 2\beta x_2, \\ \frac{dx_2}{dt} &= \alpha a x_1 - 2\beta x_2, \end{aligned} \tag{B.2}$$

where x_i denotes the proportion of channels in state N_i and a is the ion concentration.

Let us now consider a B cell with m CD20 receptors on its surface, each of which can be either unbound or bound to an antibody molecule, and denote a state in which a B cell has exactly i CD20 receptors bound to antibodies as N_i. An antibody binds reversibly to the receptor with a single binding and unbinding constant, α and β, respectively. The kinetics of the changes between the B cell states is then given by the following reaction scheme:

$$N_0 \underset{\beta}{\overset{m\alpha}{\rightleftharpoons}} N_1 \underset{2\beta}{\overset{(m-1)\alpha}{\rightleftharpoons}} N_2 \underset{3\beta}{\overset{(m-2)\alpha}{\rightleftharpoons}} N_3 \rightleftharpoons \ldots \rightleftharpoons N_{m-1} \underset{m\beta}{\overset{\alpha}{\rightleftharpoons}} N_m. \tag{B.3}$$

Let x_i denote the proportion of B cells in state N_i and let a be the unbound (free) antibody concentration. In Chapter 4, we showed that for the doses considered in our work, the total number of antibody molecules is 10^5-fold higher than the total number of B cells in the system. The free antibody concentration can be, therefore, assumed as approximately constant, $a \approx$ const. Under this assumption, the kinetic scheme (B.3) can be represented

through $m+1$ differential equations as:

$$\begin{aligned}
\frac{dx_0}{dt} &= -m\alpha a x_o + \beta x_1, \\
\frac{dx_1}{dt} &= m\alpha a x_o - \beta x_1 - (m-1)\alpha a x_1 + 2\beta x_2, \\
\frac{dx_2}{dt} &= (m-1)\alpha a x_1 - 2\beta x_2 - (m-2)\alpha a x_2 + 3\beta x_3, \\
&\vdots \\
\frac{dx_m}{dt} &= \alpha a x_{m-1} - m\beta x_1.
\end{aligned} \tag{B.4}$$

An effective binding rate constant determining the transition of B cell from the state N_i to the state N_{i+1} is, therefore:

$$k_{\text{binding}_i} = (m-i)a\alpha, \tag{B.5}$$

where $i \in \{0, 1, \ldots, m-1\}$, and, similarly, an effective unbinding rate constant describing the transition of B cell from the state N_{i+1} to the state N_i it given by:

$$k_{\text{unbinding}_i} = (i+1)\beta, \tag{B.6}$$

where $i \in \{0, \ldots, m-1\}$.

As CD20 receptor density can reach values of 10^5 receptors per cell [146], solving 10^5+1 ODEs is not numerically feasible. However, it is still informative to consider systems with lower numbers of B cell receptors per cell, m. Taking the value of the single binding rate constant, k_{on}, as α, and the single unbinding rate constant, k_{off}, as β:

$$\begin{aligned}
\alpha = k_{\text{on}} &\sim 10^{-16}\frac{\text{L}}{\text{molecules}\cdot\text{min}} \\
\beta = k_{\text{off}} &\sim 10^{-1}\frac{1}{\text{min}},
\end{aligned} \tag{B.7}$$

and estimating the free antibody concentration, a, as the total number of antibody molecules in a single 40 mg dose of rituximab divided ($D \sim 10^{17}$molecules) by total blood volume ($V_{\text{blood,tot}} \sim 10^{-1}$L) in cynomolgus monkeys, a is given by:

$$a \sim 10^{18}\frac{\text{molecules}}{\text{L}}, \tag{B.8}$$

where the sources for those parameters have been described in Section 4.2.2. The system of ODEs (Equations (B.4)) was solved for $m \in \{10, 100, 1000\}$ subject to initial conditions:

$$x_i(t=0) = \begin{cases} 1 & i = 0 \\ 0 & i \in \{1, \ldots, m\} \end{cases} . \tag{B.9}$$

The resulting solutions for $m \in \{10, 100, 1000\}$ were plotted in Figure B.1(a). The distributions of steady state occupancy (the distribution of the fraction of B cells in state N_i in steady state, where $i \in \{0, 1, \ldots, m\}$, were plotted in Figure B.1(b). The effective binding (Equation (B.5)) and unbinding constant rates (Equation (B.6)) associated with each state N_i were plotted in Figure B.1(c).

The behaviour of the system was consistent for all three cases of the total number of receptors per cell, $m \in \{10, 100, 1000\}$. In all three cases, the system reached steady state in less than one minute (see Figure B.1(a)) and the distributions of the relative number of cells across all the possible states in steady state showed that the majority of cells result in a nearly full receptor occupancy (see Figure B.1(b)). The comparison of the effective binding and unbinding constant rates also revealed that for the vast majority of the allowed states, the effective binding rate constant is higher than the effective unbinding rate constant (see Figure B.1(c)).

The time behaviour plots, shown in Figure B.1(a), indicate that the system undergoes a very fast initial decay, on a timescale of approximately $\tau = 0.1\,\text{min}$. The associated relaxation timescale, $1/\tau = 1\,\text{min}^{-1}$, is approximately equal to the product of the single binding rate constant, α, and the estimated antibody concentration, a: $a\alpha \sim 1\,\text{min}^{-1}$. This result, in turn, suggests that the initial behaviour of the system is driven by single, rather than multiple, binding events. This conclusion can additionally be explained by considering the relative antibody and B cell levels as follows. For a system of B cells with m CD20 receptors per cell, all cells are initially in the state N_0, with no occupied receptors. In the presence of antibodies, the majority of m receptors on each cell become bound very quickly, as the binding of antibodies to receptors occurs on a much faster timescale than unbinding ($\alpha \ll a\beta$). When the majority of cells occupy states N_i with higher i (with the majority of the receptors bound to antibodies), the effective unbinding rate constant, $k_{\text{unbinding}_i}$ becomes comparable to the effective binding rate constant, k_{binding_i}, meaning that single unbinding events occur more often for cells in states N_i with higher values of i, than for the states with small values of i. However, although the unbinding events become more frequent as more cells move to states N_i with a higher proportion of occupied receptors, due to the excess of antibodies in the system, as soon as

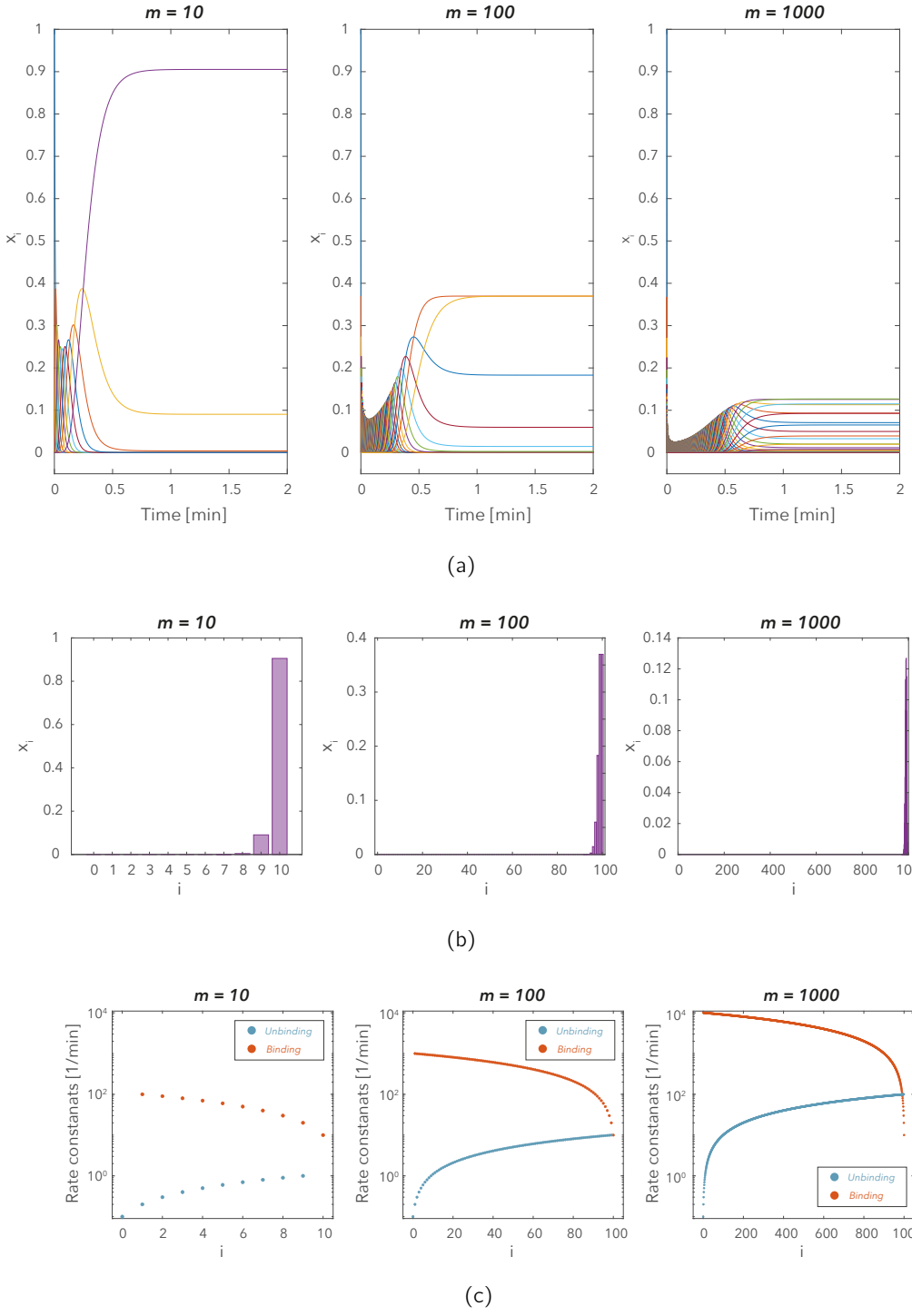


Figure B.1: Solutions to the ODE system given in Equations (B.4) describing reversible binding of antibodies to receptors expressed on cell surfaces, as depicted in Reaction Scheme (B.3), for $m = 10$, $m = 100$ and $m = 1000$ receptors per cell. (a) Time behaviour of the solutions to the ODE system for different values of receptor density. Each curve represents the fraction of cells, x_i, in state N_i, where i denotes the total number of receptors bound to antibodies, $i \in \{0, 1, \ldots, m\}$. (b) The distribution of steady-state occupancy, plotted as the distribution of the fraction of cells, x_i, in state N_i in steady state. (c) The effective binding (Equation (B.5)) and unbinding constant rates (Equation (B.6)) as for each state N_i.

an antibody unbinds from one of the receptors on a cell surface, another molecule quickly occupies the free receptor again. This results in a steady state where the majority of the cells in the system occupy states N_i with higher values of i.

The following framework, therefore, justifies the use of single binding rate constants in the PBPK-PD model in Chapter 4. While this simple approach does not accommodate the other processes depicted in the model, such as antibody transport and clearance, the comparison of the absolute numbers of antibodies and B cells in the system supports the conclusions presented in this appendix. The doses chosen in the preclinical study considered in Chapter 4 [107] correspond to $\sim 10^{16}$ molecules of antibody, while the total number of B cells in the system is of the order of $\sim 10^{11}$ cells. Furthermore, we verified that, except for early times following the administration, the lowest antibody concentrations predicted by the model were at least two orders of magnitude higher than the highest number of B cells across all model compartments during the timespan modelled in our simulations. However, as the first time measurement in the preclinical study was taken 60 min following antibody administration, which provides sufficient time for the binding processes to reach a quasi-steady state, the consequences of our assumption on the antibody-B cell binding kinetics are expected to have a negligible effect on the system behaviour during later times.

Bibliography

[1] A. E. Kmieciak, L. V. Brown, M. C. Coles, J. Wagg, A. Phipps, and E. A. Gaffney. "Predicted limited redistribution of T cells to secondary lymphoid tissue correlates with increased risk of haematological malignancies in asplenic patients." In: *Scientific reports* 11.1 (2021), p. 16394. ISSN: 2045-2322. DOI: 10.1038/s41598-021-95225-x.

[2] T. J. Snowden, P. H. van der Graaf, and M. J. Tindall. "Methods of Model Reduction for Large-Scale Biological Systems: A Survey of Current Methods and Trends." In: *Bulletin of Mathematical Biology* 79.7 (2017), pp. 1449–1486. ISSN: 1522-9602. DOI: 10.1007/s11538-017-0277-2.

[3] J. Lohmueller and O. Finn. "Current modalities in cancer immunotherapy: Immunomodulatory antibodies, CARs and vaccines." In: *Pharmacology & Therapeutics* 178 (2017), pp. 31–47. ISSN: 1879-016X. DOI: 10.1016/j.pharmthera.2017.03.008.

[4] Y. Togashi, K. Shitara, and H. Nishikawa. "Regulatory T cells in cancer immunosuppression - implications for anticancer therapy." In: *Nature Reviews. Clinical Oncology* 16.6 (2019), pp. 356–371. DOI: 10.1038/s41571-019-0175-7.

[5] M. Sauerborn, V. Brinks, W. Jiskoot, and H. Schellekens. "Immunological mechanism underlying the immune response to recombinant human protein therapeutics". In: *Trends in Pharmacological Sciences* 31.2 (2010), pp. 53–59. DOI: 10.1016/j.tips.2009.11.001.

[6] K. McNally, R. Cotton, and G. Loizou. "A Workflow for Global Sensitivity Analysis of PBPK Models". In: *Frontiers in Pharmacology* 2 (2011), p. 31. DOI: 10.3389/fphar.2011.00031.

[7] R. L. Lalonde, K. G. Kowalski, M. M. Hutmacher, W. Ewy, D. J. Nichols, P. A. Milligan, B. W. Corrigan, P. A. Lockwood, S. A. Marshall, L. J. Benincosa, T. G. Tensfeldt, K. Parivar, M. Amantea, P. Glue, H. Koide, and R. Miller. "Model-based drug development." In: *Clinical Pharmacology and Therapeutics* 82.1 (2007), pp. 21–32. ISSN: 0009-9236. DOI: 10.1038/sj.clpt.6100235.

[8] S. A. Peters. *Physiologically-based pharmacokinetic (PBPK) modeling and simulations: principles, methods, and applications in the pharmaceutical industry*. Oxford: Wiley-Blackwell, 2012. ISBN: 9780470484067.

[9] T. Teorell. "Kinetics of distribution of substances administered to the body, I: The extravascular modes of administration". In: *Archives internationales de pharmacodynamie et de therapie* 57 (1937), pp. 205–225.

[10] A. Saltelli and R. Bolado. "An alternative way to compute Fourier amplitude sensitivity test (FAST)". In: *Computational Statistics & Data Analysis* 26.4 (1998), pp. 445–460. ISSN: 0167-9473. DOI: 10.1016/S0167-9473(97)00043-1.

[11] S. Marino, I. Hogue, C. Ray, and D. Kirschner. "A methodology for performing global uncertainty and sensitivity analysis in systems biology". In: *Journal Of Theoretical Biology* 254.1 (2008), pp. 178–196. ISSN: 0022-5193. DOI: 10.1016/j.jtbi.2008.04.011.

[12] A. Saltelli, K. Chan, and E. Scott. *Sensitivity analysis*. Chichester: Wiley, 2008, pp. 167–197. ISBN: 9780470743829.

[13] A. Saltelli, S. Tarantola, and K. Chan. "A Quantitative Model-Independent Method for Global Sensitivity Analysis of Model Output". In: *Technometrics* 41.1 (1999), pp. 39–56. DOI: 10.1080/00401706.1999.10485594.

[14] J. H. A. Guillaume, J. D. Jakeman, S. Marsili-Libelli, M. Asher, P. Brunner, B. Croke, M. C. Hill, A. J. Jakeman, K. J. Keesman, S. Razavi, and J. D. Stigter. "Introductory overview of identifiability analysis: A guide to evaluating whether you have the right type of data for your modeling purpose". In: *Environmental Modelling & Software* 119 (2019), pp. 418–432. ISSN: 1364-8152. DOI: 10.1016/j.envsoft.2019.07.007.

[15] M. Castro and R. J. de Boer. "Testing structural identifiability by a simple scaling method". In: *PLOS Computational Biology* 16.11 (2020), pp. 1–15. DOI: 10.1371/journal.pcbi.1008248.

[16] B. Ribba, H. P. Grimm, B. Agoram, M. R. Davies, K. Gadkar, S. Niederer, N. van Riel, J. Timmis, and P. H. van der Graaf. "Methodologies for Quantitative Systems Pharmacology (QSP) Models: Design and Estimation". In: *CPT: Pharmacometrics & Systems Pharmacology* 6.8 (2017), pp. 496–498. DOI: 10.1002/psp4.12206.

[17] S. Pilari and W. Huisinga. "Lumping of physiologically-based pharmacokinetic models and a mechanistic derivation of classical compartmental models." In: *Journal of Pharmacokinetics and Pharmacodynamics* 37.4 (2010), pp. 365–405. ISSN: 1573-8744. DOI: 10.1007/s10928-010-9165-1.

[18] I. A. Nestorov, L. J. Aarons, P. A. Arundel, and M. Rowland. "Lumping of whole-body physiologically based pharmacokinetic models." In: *Journal of Pharmacokinetics and Biopharmaceutics* 26.1 (1998), pp. 21–46. ISSN: 0090-466X. DOI: 10.1023/a:1023272707390.

[19] N. Aide, R. Hicks, C. Le Tourneau, S. Lheureux, S. Fanti, and E. Lopci. "FDG PET/CT for assessing tumour response to immunotherapy". In: *European Journal of Nuclear Medicine and Molecular Imaging* 46.1 (2019), pp. 238–250. ISSN: 1619-7089. DOI: 10.1007/s00259-018-4171-4.

[20] K. Murphy, C. Weaver, A. Mowat, L. Berg, D. D. Chaplin, and C. Janeway. *Janeway's immunobiology*. 9th Edition. 2017, pp. 11–35. ISBN: 9780815345510.

[21] D. Tough and J. Sprent. "Life span of naive and memory T cells." In: *Stem Cells (Dayton, Ohio)* 13.3 (1995), pp. 242–249. ISSN: 1066-5099. DOI: 10.1002/stem.5530130305.

[22] M. Miyasaka, E. Hata, K. Tohya, and H. Hayasaka. "Lymphocyte Recirculation". In: *Encyclopedia of Immunobiology* (2016). DOI: 10.1016/B978-0-12-374279-7.07013-2.

[23] E. Butcher and L. Picker. "Lymphocyte homing and homeostasis." In: *Science (New York, N.Y.)* 272.5258 (1996), pp. 60–66. ISSN: 0036-8075.

[24] W Weninger, M A Crowley, N Manjunath, and U H von Andrian. "Migratory properties of naive, effector, and memory $CD8^+$ T cells." In: *The Journal of experimental medicine* 194.7 (2001), pp. 953–966. ISSN: 0022-1007. DOI: 10.1084/jem.194.7.953.

[25] U. von Andrian and C. Mackay. "T-cell function and migration. Two sides of the same coin." In: *The New England Journal of Medicine* 343.14 (2000), pp. 1020–1034. ISSN: 0028-4793. DOI: 10.1056/NEJM200010053431407.

[26] H. Suami and M. Scaglioni. "Anatomy of the Lymphatic System and the Lymphosome Concept with Reference to Lymphedema." In: *Seminars in Plastic Surgery* 32.1 (2018), pp. 5–11. ISSN: 1535-2188. DOI: 10.1055/s-0038-1635118.

[27] S. Lewis, A. Williams, and S. Eisenbarth. "Structure and function of the immune system in the spleen." In: *Science Immunology* 4.33 (2019). ISSN: 2470-9468. DOI: 10.1126/sciimmunol.aau6085.

[28] M. Cesta. "Normal structure, function, and histology of the spleen." In: *Toxicologic Pathology* 34.5 (2006), pp. 455–465. ISSN: 0192-6233. DOI: 10.1080/01926230600867743.

[29] M. Cataldi, C. Vigliotti, T. Mosca, M. Cammarota, and D. Capone. "Emerging Role of the Spleen in the Pharmacokinetics of Monoclonal Antibodies, Nanoparticles and Exosomes". In: *International Journal of Molecular Sciences* 18.6 (2017). ISSN: 1422-0067. DOI: 10.3390/ijms18061249.

[30] "Basic anatomical and physiological data for use in radiological protection: reference values. A report of age- and gender-related differences in the anatomical and physiological characteristics of reference individuals. ICRP Publication 89." In: *Annals of the ICRP* 32.3-4 (2002), pp. 5–265. ISSN: 0146-6453.

[31] A. Waldman, J. Fritz, and M. Lenardo. "A guide to cancer immunotherapy: from T cell basic science to clinical practice". In: *Nature Reviews Immunology* 20.11 (2020), pp. 651–668. ISSN: 1474-1741. DOI: 10.1038/s41577-020-0306-5.

[32] M. Wang, B. Yin, H. Wang, and R.-F. Wang. "Current advances in T-cell-based cancer immunotherapy." In: *Immunotherapy* 6.12 (2014), pp. 1265–1278. ISSN: 1750-7448. DOI: 10.2217/imt.14.86.

[33] A. Huehls, T. Coupet, and C. Sentman. "Bispecific T-cell engagers for cancer immunotherapy". In: *Immunology & Cell Biology* 93.3 (2015), pp. 290–296. DOI: 10.1038/icb.2014.93.

[34] A. Trabolsi, A. Arumov, and J. Schatz. "T Cell-Activating Bispecific Antibodies in Cancer Therapy". In: *The Journal of Immunology* 203.3 (2019), pp. 585–592. ISSN: 0022-1767. DOI: 10.4049/jimmunol.1900496.

[35] A. Im and S. Pavletic. "Immunotherapy in hematologic malignancies: past, present, and future". In: *Journal of Hematology & Oncology* 10.1 (2017), p. 94. ISSN: 1756-8722. DOI: 10.1186/s13045-017-0453-8.

[36] K. M. van Pul, J. C. L. Notohardjo, M. F. Fransen, B. D. Koster, A. G. M. Stam, D. Chondronasiou, S. M. Lougheed, J. Bakker, V. Kandiah, M. P. van den Tol, K. Jooss, R. J. C. L. M. Vuylsteke, A. J. M. van den Eertwegh, and T. D. de Gruijl. "Local delivery of low-dose anti-CTLA-4 to the melanoma lymphatic basin leads to systemic T_{reg} reduction and effector T cell activation". In: *Science Immunology* 7.73 (2022), eabn8097. DOI: 10.1126/sciimmunol.abn8097.

[37] P. Sridhar and F. Petrocca. "Regional Delivery of Chimeric Antigen Receptor (CAR) T-Cells for Cancer Therapy." In: *Cancers* 9.7 (2017). ISSN: 2072-6694. DOI: 10.3390/cancers9070092.

[38] M.-V. Mateos, H. Nahi, W. Legiec, S. Grosicki, V. Vorobyev, I. Spicka, V. Hungria, S. Korenkova, N. Bahlis, M. Flogegard, J. Bladé, P. Moreau, M. Kaiser, S. Iida, J. Laubach, H. Magen, M. Cavo, C. Hulin, D. White, V. De Stefano, P. Clemens, T. Masterson, K. Lantz, L. O'Rourke, C. Heuck, X. Qin, D. Parasrampuria, Z. Yuan, S. Xu, M. Qi, and S. Usmani. "Subcutaneous versus intravenous daratumumab in patients with relapsed or refractory multiple myeloma (COLUMBA): a multicentre, open-label, non-inferiority, randomised, phase 3 trial". In: *The Lancet Haematology* 7.5 (2020), e370–e380. ISSN: 2352-3026. DOI: 10.1016/S2352-3026(20)30070-3.

[39] A. Salar, I. Avivi, B. Bittner, R. Bouabdallah, M. Brewster, O. Catalani, G. Follows, A. Haynes, F. Hourcade-Potelleret, A. Janikova, J.-F. Larouche, C. McIntyre, M. Pedersen, J. Pereira, P. Sayyed, O. Shpilberg, and G. Tumyan. "Comparison of subcutaneous versus intravenous administration of rituximab as maintenance treatment for follicular lymphoma: results from a two-stage, phase IB study." In: *Journal of Clinical Oncology: Official Journal of the American Society of Clinical Oncology* 32.17 (2014), pp. 1782–1791. ISSN: 1527-7755. DOI: 10.1200/JCO.2013.52.2631.

[40] A. Y. Krishnan, M. C. Minnema, J. G. Berdeja, A. Oriol, N. W. C. J. van de Donk, P. Rodriguez-Otero, E. Askari, M.-V. Mateos, L. J. Costa, R. I. Verona, X. Ma, S. Girgis, S. Yang, B. W. Hilder, J. Russell, J. D. Goldberg, and A. Chari. "Updated Phase 1 Results from MonumenTAL-1: First-in-Human Study of Talquetamab, a G Protein-Coupled Receptor Family C Group 5 Member D x CD3 Bispecific Antibody, in Patients with Relapsed/Refractory Multiple Myeloma". In: *Blood* 138 (2021), p. 158. ISSN: 0006-4971. DOI: 10.1182/blood-2021-146868.

[41] A. Y. Krishnan, A. L. Garfall, M.-V. Mateos, N. W. C. J. van de Donk, H. Nahi, J. F. San-Miguel, A. Oriol, L. Rosiñol, A. Chari, M. Bhutani, L. Karlin, L. Benboubker, L. Pei, R. Verona, S. Girgis, T. Stephenson, J. D. Goldberg, A. Banerjee, and S. Z. Usmani. "Updated phase 1 results of teclistamab, a B-cell maturation antigen (BCMA) × CD3 bispecific antibody, in relapsed/refractory multiple myeloma (MM)." In: *Journal of Clinical Oncology* 39.15 (2021), p. 8007. DOI: 10.1200/JCO.2021.39.15_suppl.8007.

[42] J. G. Berdeja, A. Y. Krishnan, A. Oriol, N. W. C. J. van de Donk, P. Rodríguez-Otero, E. Askari, M.-V. Mateos, M. C. Minnema, L. J. Costa, R. Verona, S. Girgis, T. Prior, B. Hilder, J. S. Russell, J. D. Goldberg, and A. Chari. "Updated results of a phase 1, first-in-human study of talquetamab, a G protein-coupled receptor family C group 5 member D (GPRC5D) × CD3 bispecific antibody, in relapsed/refractory multiple myeloma (MM)." In: *Journal of Clinical Oncology* 39.15 (2021), p. 8008. DOI: 10.1200/JCO.2021.39.15_suppl.8008.

[43] D. M. Francis, M. P. Manspeaker, A. Schudel, L. F. Sestito, M. J. O'Melia, H. T. Kissick, B. P. Pollack, E. K. Waller, and S. N. Thomas. "Blockade of immune checkpoints in lymph nodes through locoregional delivery augments cancer immunotherapy." In: *Science Translational Medicine* 12.563 (2020). ISSN: 1946-6242. DOI: 10.1126/scitranslmed.aay3575.

[44] F. Dammeijer, M. van Gulijk, E. E. Mulder, M. Lukkes, L. Klaase, T. van den Bosch, M. van Nimwegen, S. P. Lau, K. Latupeirissa, S. Schetters, Y. van Kooyk, L. Boon, A. Moyaart, Y. M. Mueller, P. D. Katsikis, A. M. Eggermont, H. Vroman, R. Stadhouders, R. W. Hendriks, J. Thüsen, D. J. Grünhagen, C. Verhoef, T. van Hall, and J. G. Aerts. "The PD-1/PD-L1-Checkpoint Restrains T cell Immunity in Tumor-Draining Lymph Nodes." In: *Cancer Cell* 38.5 (2020), 685–700.e8. ISSN: 1878-3686. DOI: 10.1016/j.ccell.2020.09.001.

[45] F. Baharom, R. Ramirez-Valdez, K. Tobin, H. Yamane, C.-A. Dutertre, A. Khalilnezhad, G. Reynoso, V. Coble, G. Lynn, M. Mulè, A. Martins, J. Finnigan, X. M. Zhang, J. Hamerman, N. Bhardwaj, J. Tsang, H. Hickman, F. Ginhoux, A. Ishizuka, and R. Seder. "Intravenous nanoparticle vaccination generates stem-like TCF1$^+$ neoantigen-specific CD8$^+$ T cells". In: *Nature Immunology* 22.1 (2021), pp. 41–52. ISSN: 1529-2916. DOI: 10.1038/s41590-020-00810-3.

[46] S. Crary and G. Buchanan. "Vascular complications after splenectomy for hematologic disorders." In: *Blood* 114.14 (2009), pp. 2861–2868. ISSN: 1528-0020. DOI: 10.1182/blood-2009-04-210112.

[47] S. Kristinsson, G. Gridley, R. Hoover, D. Check, and O. Landgren. "Long-term risks after splenectomy among 8,149 cancer-free American veterans: a cohort study with up to 27 years follow-up". In: *Haematologica* 99.2 (2014), pp. 392–398. DOI: 10.3324/haematol.2013.092460.

[48] L. Sun, H. Chen, L. Jeng, T. Li, S. Wu, and C. Kao. "Splenectomy and increased subsequent cancer risk: a nationwide population-based cohort study." In: *American Journal of Surgery* 210.2 (2015), pp. 243–251. DOI: 10.1016/j.amjsurg.2015.01.017.

[49] H. Becher and V. Winkler. "Estimating the standardized incidence ratio (SIR) with incomplete follow-up data." In: *BMC Medical Research Methodology* 17.1 (2017), p. 55. ISSN: 1471-2288. DOI: 10.1186/s12874-017-0335-3.

[50] A. Marzo, R. Lake, D. Lo, L. Sherman, A. McWilliam, D. Nelson, B. Robinson, and B. Scott. "Tumor antigens are constitutively presented in the draining lymph nodes." In: *Journal of Immunology (Baltimore, Md.: 1950)* 162.10 (1999), pp. 5838–5845. ISSN: 0022-1767.

[51] A. McDonnell, A. Currie, M. Brown, K. Kania, B. Wylie, A. Cleaver, R. Lake, and B. Robinson. "Tumor cells, rather than dendritic cells, deliver antigen to the lymph node for cross-presentation." In: *Oncoimmunology* 1.6 (2012), pp. 840–846. ISSN: 2162-4011. DOI: 10.4161/onci.20493.

[52] L. V. Brown, E. A. Gaffney, A. Ager, J. Wagg, and M. C. Coles. "Quantifying the limits of CAR T-cell delivery in mice and men". In: *Journal of The Royal Society Interface* 18.176 (2021), p. 20201013. DOI: 10.1098/rsif.2020.1013.

[53] R. Melder, L. Munn, B. Stoll, E. Marecos, L. Baxter, R. Weissleder, and R. Jain. "Systemic Distribution and Tumor Localization of Adoptively Transferred Lymphocytes in Mice: Comparison with Physiologically Based Pharmacokinetic Model". In: *Neoplasia (New York, N.Y.)* 4 (2002), pp. 3–8. DOI: 10.1038/sj/neo/7900209.

[54] M. Cazaux, C. Grandjean, F. Lemaître, Z. Garcia, R. Beck, I. Milo, J. Postat, J. Beltman, E. Cheadle, and P. Bousso. "Single-cell imaging of CAR T cell activity in vivo reveals extensive functional and anatomical heterogeneity". In: *Journal of Experimental Medicine* 216.5 (2019), pp. 1038–1049. ISSN: 0022-1007. DOI: 10.1084/jem.20182375.

[55] P. Kulkarni, M. Bennett, A. Constantinescu, V. Arora, M. Viguet, P. Antich, R. Parkey, D. Mathews, R. Mason, and O. Oz. "Imaging Lung Clearance of Radiolabeled Tumor Cells to Study Mice with Normal, Activated or Depleted Natural Killer (NK) Cells". In: *AIP Conference Proceedings* 680 (2003). DOI: 10.1063/1.1619906.

[56] W. Muller. "Getting leukocytes to the site of inflammation." In: *Veterinary Pathology* 50.1 (2013), pp. 7–22. ISSN: 1544-2217. DOI: 10.1177/0300985812469883.

[57] W. Snyder, M. Cook, E. Nasset, L. Karhausen, and G. Parry Howells. *Report on the Task Group on Reference Man*. Tech. rep. ICRP No. 23, 1974.

[58] M. Abramowitz, C. Hall, A. Amodu, D. Sharma, L. Androga, and M. Hawkins. "Muscle mass, BMI, and mortality among adults in the United States: A population-based cohort study." In: *PloS one* 13.4 (2018), e0194697. ISSN: 1932-6203. DOI: 10.1371/journal.pone.0194697.

[59] L. Spenst, A. Martin, and D. Drinkwater. "Muscle mass of competitive male athletes." In: *Journal of Sports Sciences* 11.1 (1993), pp. 3–8. ISSN: 0264-0414. DOI: 10.1080/02640419308729956.

[60] K. Friedl, R. Moore, L. Martinez-Lopez, J. Vogel, E. Askew, L. Marchitelli, R. Hoyt, and C. Gordon. "Lower limit of body fat in healthy active men". In: *Journal of Applied Physiology* 77.2 (1994), pp. 933–940. DOI: 10.1152/jappl.1994.77.2.933.

[61] R. Baumgartner, S. Wayne, D. Waters, I. Janssen, D. Gallagher, and J. Morley. "Sarcopenic Obesity Predicts Instrumental Activities of Daily Living Disability in the Elderly". In: *Obesity Research* 12.12 (2004), pp. 1995–2004. DOI: 10.1038/oby.2004.250.

[62] M. Joyner and D. Casey. "Regulation of Increased Blood Flow (Hyperemia) to Muscles During Exercise: A Hierarchy of Competing Physiological Needs". In: *Physiological Reviews* 95.2 (2015), pp. 549–601. ISSN: 0031-9333. DOI: 10.1152/physrev.00035.2013.

[63] M. Levitzky. "Pulmonary physiology". In: 7th. Lange physiology series. McGraw-Hill Medical, 2007. ISBN: 9780071437752.

[64] C. Norryd, H. Denker, A. Lunderquist, T. Olin, and U. Tylen. "Superior mesenteric blood flow during digestion in man." In: *Acta Chirurgica Scandinavica* 141.3 (1975), pp. 197–202. ISSN: 0001-5482.

[65] N. Charkoudian. "Skin Blood Flow in Adult Human Thermoregulation: How It Works, When It Does Not, and Why". In: *Mayo Clinic Proceedings* 78.5 (2003), pp. 603–612. ISSN: 0025-6196. DOI: 10.4065/78.5.603.

[66] Kirschner Lab. *Matlab functions for PRCC and eFAST*. URL: http://malthus.micro.med.umich.edu/lab/usadata/ (visited on 07/08/2020).

[67] M. Sappey, A. Karmanski, É. Beau, and A. Bry. *Anatomie, physiologie, pathologie des vaisseaux lymphatiques considérés chez l'homme et les vertébrés*. Adrien Delahaye, Imprimerie de E. Martinet., 1874.

[68] A. Perelson and F. Wiegel. "Scaling aspects of lymphocyte trafficking." In: *Journal of Theoretical Biology* 257.1 (2009), pp. 9–16. ISSN: 1095-8541. DOI: 10.1016/j.jtbi.2008.11.007.

[69] A. Khot, S. Matsueda, V. Thomas, R. Koya, and D. Shah. "Measurement and Quantitative Characterization of Whole-Body Pharmacokinetics of Exogenously Administered T Cells in Mice." In: *The Journal of Pharmacology and Experimental Therapeutics* 368.3 (2019), pp. 503–513. ISSN: 1521-0103. DOI: 10.1124/jpet.118.252858.

[70] V. Ganusov and J. Auerbach. "Mathematical Modeling Reveals Kinetics of Lymphocyte Recirculation in the Whole Organism". In: *PLOS Computational Biology* 10.5 (2014), pp. 1–15. DOI: 10.1371/journal.pcbi.1003586.

[71] J. Westermann, R. Schwinzer, P. Jecker, and R. Pabst. "Lymphocyte subsets in the blood. The influence of splenectomy, splenic autotransplantation, ageing, and the site of blood sampling on the number of B, T, $CD4^+$, and $CD8^+$ lymphocytes in the rat." In: *Scandinavian Journal of Immunology* 31.3 (1990), pp. 327–334. ISSN: 0300-9475. DOI: 10.1111/j.1365-3083.1990.tb02775.x.

[72] T. Seabrook, W. Hein, L. Dudler, and A. Young. "Splenectomy selectively affects the distribution and mobility of the recirculating lymphocyte pool". In: *Blood* 96.3 (2000), 1180 LP –1183. DOI: 10.1182/blood.V96.3.1180.

[73] R. Pabst and F. Trepel. "The Predominant Role Of The Spleen In Lymphocyte Recirculation". In: *Cell Proliferation* 9.2 (1976), pp. 179–189. DOI: 10.1111/j.1365-2184.1976.tb01265.x.

[74] *Physiologically Based Pharmacokinetic Analyses - Format and Content. Guidance for Industry*. U.S. Department of Health and Human Services Food, Drug Administration, Center for Drug Evaluation, and Research (CDER), 2018.

[75] *Clinical Drug Interaction Studies - Study Design, Data Analysis and Clinical Implications. Guidance for Industry*. U.S. Department of Health and Human Services Food, Drug Administration, Center for Drug Evaluation, and Research (CDER), 2017.

[76] *Clinical Drug Interaction Studies - Cytochrome P450 Enzyme- and Transporter-Mediated Drug Interactions. Guidance for Industry*. U.S. Department of Health and Human Services Food, Drug Administration, Center for Drug Evaluation, and Research (CDER), 2020.

[77] *Guideline on the reporting of physiologically based pharmacokinetic (PBPK) modelling and simulation*. European Medicines Agency, Committee for Medicinal Products for Human Use, 2018.

[78] M. Grimstein, Y. Yang, X. Zhang, J. Grillo, S. Huang, I. Zineh, and Y. Wang. "Physiologically Based Pharmacokinetic Modeling in Regulatory Science: An Update From the U.S. Food and Drug Administration's Office of Clinical Pharmacology." In: *Journal of Pharmaceutical Sciences* 108.1 (2019), pp. 21–25. ISSN: 1520-6017. DOI: 10.1016/j.xphs.2018.10.033.

[79] A. Singh, X. Zheng, X. Lin-Schmidt, W. Chen, T. Carpenter, A. Zong, W. Wang, and D. Heald. "Development of a quantitative relationship between CAR-affinity, antigen abundance, tumor cell depletion and CAR-T cell expansion using a multiscale systems PK-PD model." In: *mAbs* 12.1 (2020), p. 1688616. ISSN: 1942-0870. DOI: 10.1080/19420862.2019.1688616.

[80] H. Zhu, R. Melder, L. Baxter, and R. Jain. "Physiologically based kinetic model of effector cell biodistribution in mammals: Implications for adoptive immunotherapy". In: *Cancer Research* 56 (1996), pp. 3771–3781.

[81] S. Friedrich, S. Lin, B. Stoll, L. Baxter, L. Munn, and R. Jain. "Antibody-Directed Effector Cell Therapy of Tumors: Analysis and Optimization Using a Physiologically Based Pharmacokinetic Model". In: *Neoplasia (New York, N.Y.)* 4 (2002), pp. 449–463. DOI: 10.1038/sj.neo.7900260.

[82] H. Suami. "Lymphosome concept: Anatomical study of the lymphatic system." In: *Journal of Surgical Oncology* 115.1 (2017), pp. 13–17. ISSN: 1096-9098. DOI: 10.1002/jso.24332.

[83] A. Rostami-Hodjegan and S. Toon. "Physiologically Based Pharmacokinetics as a Component of Model-Informed Drug Development: Where We Were, Where We Are, and Where We Are Heading". In: *The Journal of Clinical Pharmacology* 60.S1 (2020), S12–S16. DOI: 10.1002/jcph.1654.

[84] J.-F. Jin, L. Zhu, M. Chen, H.-M. Xu, H.-F. Wang, X.-Q. Feng, X.-P. Zhu, and Q. Zhou. "The optimal choice of medication administration route regarding intravenous, intramuscular, and subcutaneous injection." In: *Patient Preference and Adherence* 9 (2015), pp. 923–942. ISSN: 1177-889X. DOI: 10.2147/PPA.S87271.

[85] B. Bittner, W. Richter, and J. Schmidt. "Subcutaneous Administration of Biotherapeutics: An Overview of Current Challenges and Opportunities". In: *BioDrugs* 32.5 (2018), pp. 425–440. ISSN: 1179-190X. DOI: 10.1007/s40259-018-0295-0.

[86] J. Gabriel. "Intravenous versus subcutaneous access for palliative care patients." In: *British Journal of Nursing (Mark Allen Publishing)* 23.2 (2014), S20, S22. ISSN: 0966-0461. DOI: 10.12968/bjon.2014.23.Sup1.S20.

[87] K. Stoner, H. Harder, L. Fallowfield, and V. Jenkins. "Intravenous versus Subcutaneous Drug Administration. Which Do Patients Prefer? A Systematic Review." In: *The Patient* (2014). ISSN: 1178-1661. DOI: 10.1007/s40271-014-0075-y.

[88] *Antibody Society. Antibody Therapeutics Approved or in Regulatory Review in the EU or US.* URL: https://www.antibodysociety.org/resources/approved-antibodies/ (visited on 10/15/2022).

[89] A. Pitiot, N. Heuzé-Vourc'h, and T. Sécher. "Alternative Routes of Administration for Therapeutic Antibodies - State of the Art". In: *Antibodies* 11.3 (2022). ISSN: 2073-4468. DOI: 10.3390/antib11030056.

[90] A. Trivedi, S. Stienen, M. Zhu, H. Li, T. Yuraszeck, J. Gibbs, T. Heath, R. Loberg, and S. Kasichayanula. "Clinical Pharmacology and Translational Aspects of Bispecific Antibodies." In: *Clinical and Translational Science* 10.3 (2017), pp. 147–162. ISSN: 1752-8062. DOI: 10.1111/cts.12459.

[91] P. M. Glassman and J. P. Balthasar. "Physiologically-based pharmacokinetic modeling to predict the clinical pharmacokinetics of monoclonal antibodies." In: *Journal of Pharmacokinetics and Pharmacodynamics* 43.4 (2016), pp. 427–446. ISSN: 1573-8744. DOI: 10.1007/s10928-016-9482-0.

[92] L. Fronton, S. Pilari, and W. Huisinga. "Monoclonal antibody disposition: a simplified PBPK model and its implications for the derivation and interpretation of classical compartment models." In: *Journal of Pharmacokinetics and Pharmacodynamics* 41.2 (2014), pp. 87–107. ISSN: 1573-8744. DOI: 10.1007/s10928-014-9349-1.

[93] D. C. Roopenian and S. Akilesh. "FcRn: the neonatal Fc receptor comes of age". In: *Nature Reviews Immunology* 7.9 (2007), pp. 715–725. ISSN: 1474-1741. DOI: 10.1038/nri2155.

[94] A. Garg and J. P. Balthasar. "Physiologically-based pharmacokinetic (PBPK) model to predict IgG tissue kinetics in wild-type and FcRn-knockout mice." In: *Journal of Pharmacokinetics and Pharmacodynamics* 34.5 (2007), pp. 687–709. ISSN: 1567-567X. DOI: 10.1007/s10928-007-9065-1.

[95] S. R. Urva, V. C. Yang, and J. P. Balthasar. "Physiologically based pharmacokinetic model for T84.66: A monoclonal anti-CEA antibody". In: *Journal of Pharmaceutical Sciences* 99.3 (2010), pp. 1582–1600. ISSN: 0022-3549. DOI: 10.1002/jps.21918.

[96] L. Abuqayyas and J. P. Balthasar. "Application of PBPK modeling to predict monoclonal antibody disposition in plasma and tissues in mouse models of human colorectal cancer". In: *Journal of Pharmacokinetics and Pharmacodynamics* 39.6 (2012), pp. 683–710. ISSN: 1573-8744. DOI: 10.1007/s10928-012-9279-8.

[97] Y. Chen and J. P. Balthasar. "Evaluation of a catenary PBPK model for predicting the in vivo disposition of mAbs engineered for high-affinity binding to FcRn." In: *The AAPS Journal* 14.4 (2012), pp. 850–859. ISSN: 1550-7416. DOI: 10.1208/s12248-012-9395-9.

[98] D. Shah and A. Betts. "Towards a platform PBPK model to characterize the plasma and tissue disposition of monoclonal antibodies in preclinical species and human." In: *Journal of Pharmacokinetics and Pharmacodynamics* 39.1 (2012), pp. 67–86. ISSN: 1573-8744. DOI: 10.1007/s10928-011-9232-2.

[99] D. G. Covell, J. Barbet, O. D. Holton, C. D. Black, R. J. Parker, and J. N. Weinstein. "Pharmacokinetics of monoclonal immunoglobulin G1, F(ab')2, and Fab' in mice." In: *Cancer Research* 46.8 (1986), pp. 3969–3978. ISSN: 0008-5472.

[100] M. J. Eigenmann, T. V. Karlsen, B.-F. Krippendorff, O. Tenstad, L. Fronton, M. B. Otteneder, and H. Wiig. "Interstitial IgG antibody pharmacokinetics assessed by combined in vivo- and physiologically-based pharmacokinetic modelling approaches." In: *The Journal of Physiology* 595.24 (2017), pp. 7311–7330. ISSN: 1469-7793. DOI: 10.1113/JP274819.

[101] L. Baxter, H. Zhu, D. Mackensen, and R. Jain. "Physiologically based pharmacokinetic model for specific and nonspecific monoclonal antibodies and fragments in normal tissues and human tumor xenografts in nude mice." In: *Cancer Research* 54.6 (1994), pp. 1517–1528. ISSN: 0008-5472.

[102] G. Z. Ferl, A. M. Wu, and J. J. 3rd DiStefano. "A predictive model of therapeutic monoclonal antibody dynamics and regulation by the neonatal Fc receptor (FcRn)." In: *Annals of Biomedical Engineering* 33.11 (2005), pp. 1640–1652. ISSN: 0090-6964. DOI: 10.1007/s10439-005-7410-3.

[103] B. Rippe and B. Haraldsson. "Fluid and protein fluxes across small and large pores in the microvasculature. Application of two-pore equations." In: *Acta Physiologica Scandinavica* 131.3 (1987), pp. 411–428. ISSN: 0001-6772. DOI: 10.1111/j.1748-1716.1987.tb08257.x.

[104] M. J. Eigenmann, L. Fronton, H. P. Grimm, M. B. Otteneder, and B.-F. Krippendorff. "Quantification of IgG monoclonal antibody clearance in tissues." In: *mAbs* 9.6 (2017), pp. 1007–1015. ISSN: 1942-0870. DOI: 10.1080/19420862.2017.1337619.

[105] J. Golay, G. Semenzato, A. Rambaldi, R. Foà, G. Gaidano, E. Gamba, F. Pane, A. Pinto, G. Specchia, F. Zaja, and M. Regazzi. "Lessons for the clinic from rituximab pharmacokinetics and pharmacodynamics". In: *mAbs* 5.6 (2013), pp. 826–837. DOI: 10.4161/mabs.26008.

[106] T. M. Pierpont, C. B. Limper, and K. L. Richards. "Past, Present, and Future of Rituximab—The World's First Oncology Monoclonal Antibody Therapy". In: *Frontiers in Oncology* 8 (2018). DOI: 10.3389/fonc.2018.00163.

[107] C.-P. Mao, M. R. Brovarney, K. Dabbagh, H. F. Birnböck, W. F. Richter, and C. J. Del Nagro. "Subcutaneous versus intravenous administration of rituximab: pharmacokinetics, CD20 target coverage and B-cell depletion in cynomolgus monkeys." In: *PloS one* 8.11 (2013), e80533. ISSN: 1932-6203. DOI: 10.1371/journal.pone.0080533.

[108] A. Sharma, C. B. Davis, L. A. Tobia, D. C. Kwok, M. G. Tucci, E. R. Gore, D. J. Herzyk, and T. K. Hart. "Comparative pharmacodynamics of keliximab and clenoliximab in transgenic mice bearing human CD4." In: *The Journal of Pharmacology and Experimental Therapeutics* 293.1 (2000), pp. 33–41. ISSN: 0022-3565.

[109] A. Betts, N. Haddish-Berhane, D. K. Shah, P. H. van der Graaf, F. Barletta, L. King, T. Clark, C. Kamperschroer, A. Root, A. Hooper, and X. Chen. "A Translational Quantitative Systems Pharmacology Model for CD3 Bispecific Molecules: Application to Quantify T Cell-Mediated Tumor Cell Killing by P-Cadherin LP DART®". In: *The AAPS Journal* 21.4 (2019), p. 66. ISSN: 1550-7416. DOI: 10.1208/s12248-019-0332-z.

[110] X. Jiang, X. Chen, T. J. Carpenter, J. Wang, R. Zhou, H. M. Davis, D. L. Heald, and W. Wang. "Development of a Target cell-Biologics-Effector cell (TBE) complex-based cell killing model to characterize target cell depletion by T cell redirecting bispecific agents." In: *mAbs* 10.6 (2018), pp. 876–889. ISSN: 1942-0870. DOI: 10.1080/19420862.2018.1480299.

[111] D. A. Einfeld, J. P. Brown, M. A. Valentine, E. A. Clark, and J. A. Ledbetter. "Molecular cloning of the human B cell CD20 receptor predicts a hydrophobic protein with multiple transmembrane domains." In: *The EMBO Journal* 7.3 (1988), pp. 711–717. ISSN: 0261-4189.

[112] D. Mandikian, I. Figueroa, A. Oldendorp, H. Rafidi, S. Ulufatu, M. G. Schweiger, J. A. Couch, N. Dybdal, S. B. Joseph, S. Prabhu, G. Z. Ferl, and C. A. Boswell. "Tissue Physiology of Cynomolgus Monkeys: Cross-Species Comparison and Implications for Translational Pharmacology." In: *The AAPS Journal* 20.6 (2018), p. 107. ISSN: 1550-7416. DOI: 10.1208/s12248-018-0264-z.

[113] C. Hindorf, G. Glatting, C. Chiesa, O. Lindén, and G. Flux. "EANM Dosimetry Committee guidelines for bone marrow and whole-body dosimetry". In: *European Journal of Nuclear Medicine and Molecular Imaging* 37.6 (2010), pp. 1238–1250. ISSN: 1619-7089. DOI: 10.1007/s00259-010-1422-4.

[114] D. K. Shah and A. M. Betts. "Antibody biodistribution coefficients: inferring tissue concentrations of monoclonal antibodies based on the plasma concentrations in several preclinical species and human." In: *mAbs* 5.2 (2013), pp. 297–305. ISSN: 1942-0870. DOI: 10.4161/mabs.23684.

[115] J. Westermann and R. Pabst. "Distribution of lymphocyte subsets and natural killer cells in the human body". In: *The Clinical Investigator* 70.7 (1992), pp. 539–544. ISSN: 1432-1440. DOI: 10.1007/BF00184787.

[116] M. B. Regazzi, I. Iacona, M. A. Avanzini, L. Arcaini, G. Merlini, V. Perfetti, F. Zaja, M. Montagna, E. Morra, and M. Lazzarino. "Pharmacokinetic Behavior of Rituximab: A Study of Different Schedules of Administration for Heterogeneous Clinical Settings". In: *Therapeutic Drug Monitoring* 27.6 (2005). ISSN: 0163-4356.

[117] C. T. Liu and G. A. Higbee. "Determination of body surface area in the rhesus monkey." In: *Journal of Applied Physiology* 40.1 (1976), pp. 101–104. ISSN: 0021-8987. DOI: 10.1152/jappl.1976.40.1.101.

[118] J. Foote and H. N. Eisen. "Kinetic and affinity limits on antibodies produced during immune responses." In: *Proceedings of the National Academy of Sciences of the United States of America* 92.5 (1995), pp. 1254–1256. ISSN: 0027-8424. DOI: 10.1073/pnas.92.5.1254.

[119] D. C. Macallan, D. L. Wallace, Y. Zhang, H. Ghattas, B. Asquith, C. de Lara, A. Worth, G. Panayiotakopoulos, G. E. Griffin, D. F. Tough, and P. C. L. Beverley. "B-cell kinetics in humans: rapid turnover of peripheral blood memory cells". In: *Blood* 105.9 (2005), pp. 3633–3640. ISSN: 0006-4971. DOI: 10.1182/blood-2004-09-3740.

[120] *Rituxan (rituximab) Label*. URL: https://www.accessdata.fda.gov/drugsatfda_docs/label/2006/103705s5230-s5231lbl.pdf.

[121] European Medicines Agency. "Mabthera - Scientific Discussion". In: *Mabthera, Scientific Discussion*. 2005. URL: https://www.ema.europa.eu/en/documents/scientific-discussion/mabthera-epar-scientific-discussion_en.pdf.

[122] J. Fassy, K. Tsalkitzi, M. Goncalves-Maia, and V. M. Braud. "A Real-Time Cytotoxicity Assay as an Alternative to the Standard Chromium-51 Release Assay for Measurement of Human NK and T Cell Cytotoxic Activity". In: *Current Protocols in Immunology* 118.1 (2017), pp. 7.42.1–7.42.12. DOI: 10.1002/cpim.28.

[123] T. Wendling, N. Tsamandouras, S. Dumitras, E. Pigeolet, K. Ogungbenro, and L. Aarons. "Reduction of a Whole-Body Physiologically Based Pharmacokinetic Model to Stabilise the Bayesian Analysis of Clinical Data." In: *The AAPS Journal* 18.1 (2016), pp. 196–209. ISSN: 1550-7416. DOI: 10.1208/s12248-015-9840-7.

[124] A. F. Villaverde, N. Tsiantis, and J. R. Banga. "Full observability and estimation of unknown inputs, states and parameters of nonlinear biological models". In: *Journal of The Royal Society Interface* 16.156 (2019), p. 20190043. DOI: 10.1098/rsif.2019.0043.

[125] M. Clerx, M. Robinson, B. Lambert, C. L. Lei, S. Ghosh, G. R. Mirams, and D. J. Gavaghan. "Probabilistic Inference on Noisy Time Series (PINTS)". In: *Journal of Open Research Software* 7.1 (2019), p. 23. DOI: 10.5334/jors.252.

[126] C. J. F. T. Braak. "A Markov Chain Monte Carlo version of the genetic algorithm Differential Evolution: easy Bayesian computing for real parameter spaces". In: *Statistics and Computing* 16.3 (2006), pp. 239–249. ISSN: 1573-1375. DOI: 10.1007/s11222-006-8769-1.

[127] T. H. Ramwadhdoebe, L. G. M. van Baarsen, M. J. H. Boumans, S. T. G. Bruijnen, M. Safy, F. H. Berger, J. F. Semmelink, C. J. van der Laken, D. M. Gerlag, R. M. Thurlings, and P. P. Tak. "Effect of rituximab treatment on T and B cell subsets in lymph node biopsies of patients with rheumatoid arthritis". In: *Rheumatology* 58.6 (2019), pp. 1075–1085. ISSN: 1462-0324. DOI: 10.1093/rheumatology/key428.

[128] S. Lindstedt and P. Schaeffer. "Use of allometry in predicting anatomical and physiological parameters of mammals". In: *Laboratory Animals* 36 (2002), pp. 1–19. DOI: 10.1258/0023677021911731.

[129] R. Overgaard, M. Karlsson, and S. Ingwersen. "Pharmacodynamic model of interleukin-21 effects on red blood cells in cynomolgus monkeys". In: *Journal of Pharmacokinetics and Pharmacodynamics* 34 (2007), pp. 559–574. DOI: 10.1007/s10928-007-9059-z.

[130] C. Schoergenhofer, M. Schwameis, C. Firbas, J. Bartko, U. Derhaschnig, R. M. Mader, R. S. Plaßmann, P. Jilma-Stohlawetz, K. Desai, P. Misra, U. Jäger, and B. Jilma. "Single, very low rituximab doses in healthy volunteers - a pilot and a randomized trial: implications for dosing and biosimilarity testing." In: *Scientific Reports* 8.1 (2018), p. 124. ISSN: 2045-2322. DOI: 10.1038/s41598-017-17934-6.

[131] L. Zhao, P. Ji, Z. Li, P. Roy, and C. G. Sahajwalla. "The antibody drug absorption following subcutaneous or intramuscular administration and its mathematical description by coupling physiologically based absorption process with the conventional compartment pharmacokinetic model." In: *Journal of Clinical Pharmacology* 53.3 (2013), pp. 314–325. ISSN: 1552-4604. DOI: 10.1002/jcph.4.

[132] J. C. Lipscomb, S. Haddad, T. Poet, and J. Krishnan. "Physiologically-based pharmacokinetic (PBPK) models in toxicity testing and risk assessment." In: *Advances in Experimental Medicine and Biology* 745 (2012), pp. 76–95. ISSN: 0065-2598. DOI: 10.1007/978-1-4614-3055-1_6.

[133] K. Venkatakrishnan and P. H. van der Graaf. "Toward Project Optimus for Oncology Precision Medicine: Multi-Dimensional Dose Optimization Enabled by Quantitative Clinical Pharmacology". In: *Clinical Pharmacology & Therapeutics* 112.5 (2022), pp. 927–932. DOI: 10.1002/cpt.2742.

[134] R.-M. Lu, Y.-C. Hwang, I.-J. Liu, C.-C. Lee, H.-Z. Tsai, H.-J. Li, and H.-C. Wu. "Development of therapeutic antibodies for the treatment of diseases". In: *Journal of Biomedical Science* 27.1 (2020), p. 1. ISSN: 1423-0127. DOI: 10.1186/s12929-019-0592-z.

[135] Y. Tang and Y. Cao. "Modeling pharmacokinetics and pharmacodynamics of therapeutic antibodies: Progress, challenges, and future directions". In: *Pharmaceutics* 13.3 (2021). ISSN: 19994923. DOI: 10.3390/pharmaceutics13030422.

[136] J. Wei and J. C. W. Kuo. "Lumping Analysis in Monomolecular Reaction Systems. Analysis of the Exactly Lumpable System". In: *Industrial & Engineering Chemistry Fundamentals* 8.1 (1969), pp. 114–123. ISSN: 0196-4313. DOI: 10.1021/i160029a019.

[137] J. P. F. Bai, J. C. Earp, D. G. Strauss, and H. Zhu. "A Perspective on Quantitative Systems Pharmacology Applications to Clinical Drug Development". In: *CPT: Pharmacometrics & Systems Pharmacology* 9.12 (2020), pp. 675–677. DOI: 10.1002/psp4.12567.

[138] Friends of Cancer Research Annual Meeting 2021. *Optimizing Dosing in Oncology Drug Development*. 2021. URL: https://friendsofcancerresearch.org/wp-content/uploads/Optimizing_Dosing_in_Oncology_Drug_Development.pdf.

[139] M. Shah, A. Rahman, M. R. Theoret, and R. Pazdur. "The Drug-Dosing Conundrum in Oncology - When Less Is More." In: *The New England journal of medicine* 385.16 (2021), pp. 1445–1447. ISSN: 1533-4406. DOI: 10.1056/NEJMp2109826.

[140] D. Ffoulkes-Crabbe, R. Creighton, G. Volgyesi, D. Steward, and H. Nisbet. "The effect of splenectomy on circulatory adjustments to hypoxaemia in the anaesthetized dog." In: *British Journal of Anaesthesia* 48.7 (1976), pp. 639–641. ISSN: 0007-0912. DOI: 10.1093/bja/48.7.639.

[141] H. Lipowsky and B. Zweifach. "Network analysis of microcirculation of cat mesentery." In: *Microvascular Research* 7.1 (1974), pp. 73–83. ISSN: 0026-2862. DOI: 10.1016/0026-2862(74)90038-7.

[142] A. Pries, T. Secomb, P. Gaehtgens, and J. Gross. "Blood flow in microvascular networks. Experiments and simulation." In: *Circulation Research* 67.4 (1990), pp. 826–834. ISSN: 0009-7330. DOI: 10.1161/01.res.67.4.826.

[143] R. Shipley, A. Smith, P. Sweeney, A. Pries, and T. Secomb. "A hybrid discrete–continuum approach for modelling microcirculatory blood flow". In: *Mathematical Medicine and Biology: A Journal of the IMA* 37.1 (2020), pp. 40–57. ISSN: 1477-8599. DOI: 10.1093/imammb/dqz006.

[144] W. Chilian, S. Layne, E. Klausner, C. Eastham, and M. Marcus. "Redistribution of coronary microvascular resistance produced by dipyridamole." In: *The American Journal of Physiology* 256.2 Pt 2 (1989), H383–90. ISSN: 0002-9513. DOI: 10.1152/ajpheart.1989.256.2.H383.

[145] A. Kumar, P. Sharma, and S. Sarin. "Hepatic venous pressure gradient measurement: time to learn!" In: *Indian Journal of Gastroenterology: Official Journal of the Indian Society of Gastroenterology* 27.2 (2008), pp. 74–80. ISSN: 0254-8860.

[146] J. Golay, M. Lazzari, V. Facchinetti, S. Bernasconi, G. Borleri, T. Barbui, A. Rambaldi, and M. Introna. "CD20 levels determine the in vitro susceptibility to rituximab and complement of B-cell chronic lymphocytic leukemia: further regulation by CD55 and CD59". In: *Blood* 98.12 (2001), pp. 3383–3389. ISSN: 0006-4971. DOI: 10.1182/blood.V98.12.3383.

[147] J. P. Keener and J. Sneyd. *Mathematical physiology*. 2nd Edition. Interdisciplinary applied mathematics; 8. New York: Springer, 2009. ISBN: 9780387793887.